UNIVERSITY OF PADUA

DOCTORAL THESIS

Scientific and Technological Advancements in Microwave and Radiofrequency Engineering: from Safety in Food Heating and in Bioelectromagnetics to Assisted Chemical Processing

Series:	*Ph.D Candidate:*
XXX	Christian BIANCHI
Curriculum:	*Coordinator:*
Electrical Energy ENGINEERING	Prof. Roberto TURRI
Department:	*Supervisor:*
Dept. of Industrial ENGINEERING	Prof. Fabrizio DUGHIERO
Head Office:	*Director of the Doctoral School:*
Università degli Studi di PADOVA	Prof. Paolo COLOMBO

Laboratory of Electroheat

Department of Industrial Engineering

January 14, 2018

Declaration of Authorship

I, Christian BIANCHI, declare that this thesis titled, "Scientific and Technological Advancements in Microwave and Radiofrequency Engineering: from Safety in Food Heating and in Bioelectromagnetics to Assisted Chemical Processing" was submitted in fulfillment of the requirements for the degree of Doctor of Philosophy. I confirm that:

- This work was done while in candidature for a research degree at the University of Padua.
- Where I have consulted the published work of others, this is always clearly attributed.
- Where I have quoted from the work of others, the source is always given.
- I have acknowledged all main sources of help.

Signed:

_____

Date:

_____

"*The truth is rarely pure and never simple.*"

Oscar Wilde

University of Padua

Abstract

Electrical Engineering

Department of Industrial Engineering

Doctor of Philosophy

Scientific and Technological Advancements in Microwave and Radiofrequency Engineering: from Safety in Food Heating and in Bioelectromagnetics to Assisted Chemical Processing

by Christian BIANCHI

The research activity carried out during the Ph. D. course can be divided in several sub-topics related to radiofrequency and microwave engineering. The projects are characetrized by different aims, technical-scientific complexities and application sectors. All the projects can be gathered by the same physical aspects which characterize the studied phenomena. The common background is related to dielectric polarization due to alternating electric field in resonant or propagation conditions. Particular attention was turned to phenomenological theory and numerical computing. The findings of the current work can be useful for microwave oven users and manufacturers, since safety implications on responsible use and design are provided. A theoretical mechanistic understanding of arcing in microwave ovens is given, analysing electromagnetics, heat-transfer, moisture-transfer and electrodynamics, in an unified framework. Findings related to bioelectromagnetics can facilitate the CE marking approval of an inovative equipment to treat patients subjected to Disfunctional Tear Syndrome. Based on the obatined data, physicians can define new protocols in terms of length and intensity of the electromagnetic stimulation under safe conditions. Regarding chemical processes that are assisted by microwave radiation, a rigourous demonstration that solid-state technology improves the quality of the heating pattern with respect to magnetron based technology is provided. An original probabilistic algorithm to pilot solid-state based reactors was developed and tested to show the improved capabilities in terms of uniform heating with respect to traditional techniques.

Acknowledgements

Voglio ringraziare la mia famiglia per avermi sempre sostenuto (ed anche sopportato) negli anni fino al raggiungimento di questo importante traguardo, a partire da mamma, papà, Erika, Lele, Thomas, zio Lele, Jacq, Daniele ed il nuovo arrivato della famiglia Mattia. Un pensiero va ai nonni, che da quando ero bambino, hanno sempre provveduto a premiarmi per ogni promozione e traguardo scolastico. Un grazie speciale va a tutti i membri della famiglia Raveri (Plus) per l'aiuto dato in questi anni, e per avermi accolto da subito come un nuovo membro. Ringrazio gli amici dell'infanzia di Sant'Elena, del liceo Benedetti, del liceo Foscarini e i compagni di Università, con i quali, tra partite di calcio, spritz nei campi di Venezia o nelle piazze di Padova, e quaderni di appunti (spesso pieni zeppi di errori), mi hanno dato (e continuano a darmi) la spensieratezza di tutti i giorni. Tra i ringraziamenti più sentiti figurano gli amici del LEP e InovaLab (e se dimentico qualcuno gli offrirò da bere): Marco Bullo, Betta, Lele, Teo, Spezz, Tolo, Nic Sempreboni, Spec, Tony, Pino Basso, Angelo, Gambaz, Simone Turetta, Lancer, Galendino, Pippo Callegari, Durigon, Marco Vinante, Chiara de Massari, Cristina, Marcello, Lanza e tesisti vari passati di qua (potrei scrivere una seconda tesi di dottorato solo citandoli). Un particolare ringraziamento ai tesisti Paolo Bonato, Pietro Tommanin, Fabio Paccanaro e Filippo Amadio. Ringrazio le macchinette del caffe del DII per avermi tenuto sveglio in tutti questi anni (anche se penso di aver già ricambiato con una frazione consistente dello stipendio mensile), e ringrazio la Vilma e Franceso della portineria per avermi permesso di entrare in dipartimento anche quando dimenticavo il badge a casa. Ringrazio Paolo Nobili che mi ha salvato informaticamente in molte occasioni. Grazie a Pizzeria al Porteo, al bar Tre scalini, Verba Volant, Antico desiderio e a tutte le mense di Padova (in particolare la Pio X per l'apertura serale), che mi hanno sfamato nonostante il non propriamente lauto stipendio da dottorando.

Un sentito ringraziamento al Professore Alfredo Ruggeri, all'Ingegnere Alessandro Pozzato, a TELEA Electronic Engineering e alla Fondazione Banca degli Occhi del Veneto, per il fondamentale aiuto ricevuto. Un caloroso ringraziamento all'Ing. Prof. Michele Forzan per essere sempre stato disponibile nell' aiutarmi in qualsiasi evenienza durante l'arco del dottorato. Un sentito ringraziamento va ai Professori, Paolo Di Barba, Paolo Canu e Michele Maggini per avermi dato stimolanti e preziosi spunti di ricerca.

Ed un grazie speciale al Professor Dughiero per aver sempre creduto in me, e per avermi dato l'opportunità di intraprendere questo percorso, contagiandomi col suo spirito energico.

Infine, un grazie a Chiara, che con la sua presenza mi da un senso a tutto.

I would like to thank Prof. Datta, who gave me the opportunity to work at Cornell University, supporting my research activities in many ways and helping me to have a great experience in U.S.. I am also extremely grateful to Mina and Mohsen because they made me feel like family. And special thanks to Nancy for getting me curious about America and much more.

Contents

List of Figures

List of Tables

List of Abbreviations

BC	Boundary Condition
BET	Brunauer Emmett and Teller
BSF	Based on the Specific Function
BSM	Based on the Specific Model
CV	Control Volume
DC	Direct Current
DE(S)	Dry Eye (Syndrome)
DTS	Disfunctional Tear Syndrome
DUT	Device Under Test
ED	ElectroDynamics
EM	ElectroMagnetic
EMC	ElectroMagnetic Compatibility
FCC	(American) Federal Communications Commission
FDA	Food and Drug Administration
FDTD	Finite Difference Time Domain
FE	Finite Element
FEM	Finite Element Method
HT	Heat Transfer
ICNIRP	International Commission on Non-Ionizing Radiation Protection
ICOP	International Center of Ocular Physiopatology
ISM	Industrial Scientific and Medical
IT	Information Technology
LFU	Lacrimal Functiona Unit
MBS	Magnetron Based System
MT	Moisture Transfer

MW	Microwave
PDE	Partial Differential Equation
PEC	Perfect Electric Conductor
PML	Perfect Matched Layer
RF	RadioFrequency
RMS	Root Mean Square
RQM	Risonanza Quantica Molecolare
R&D	Research and Development
SAR	Specific Absorption Rate
SBC	Scattering Boundary Condition
SBS	Solid state Based System
SE	Shielding Effect
SEC	Single European Code
SIP	SuperImposition Principle
TE	Transverse Electric
TEM	Transverse Electric and Magnetic
VHP	Visible Human Project
VNA	Vector Network Analyser

Physical Constants

Avogadro's constant	$N_a = 6.02 \times 10^{-23}\,\mathrm{mol}^{-1}$
Boltzmann's constant	$k_b = 1.380\,648\,52 \times 10^{-23}\,\mathrm{m}^2\,\mathrm{kg}\,\mathrm{s}^{-2}\,\mathrm{K}^{-1}$
electrical permittivity in free space	$\epsilon_0 = 8.854\,187\,817 \times 10^{-12}\,\mathrm{F}\,\mathrm{m}^{-1}$
electron charge	$e = 1.602\,176\,62 \times 10^{-19}\,\mathrm{C}$
electron mass	$m_e = 9.109\,383\,56 \times 10^{-31}\,\mathrm{kg}$
gas constant	$R_b = 8.314\,472\,\mathrm{J}\,\mathrm{K}^{-1}\,\mathrm{mol}^{-1}$
latent heat of evaporation of water	$\Delta H_m = 2264.705\,\mathrm{kJ}\,\mathrm{kg}^{-1}$
magnetic permeability in free space	$\mu_0 = 4\,\pi 10^{-7}\,\mathrm{H}\,\mathrm{m}^{-1}$
speed of light	$c = 2.997\,924\,58 \times 10^{8}\,\mathrm{m}\,\mathrm{s}^{-1}$
standard atmospheric pressure	$P_0 = 101\,325\,\mathrm{Pa}$
weight of atomic nitrogen	$W_N = 14.0007\,\mathrm{u}$
weight of atomic oxigen	$W_O = 15.9994\,\mathrm{u}$

List of Symbols

Chapter 2

$\boldsymbol{B}$	magnetic induction	T
c_b	specific heat at constant pressure of blood	J $\mathrm{kg}^{-1}\mathrm{K}^{-1}$
c_p	specific heat at constant pressure	J $\mathrm{kg}^{-1}\mathrm{K}^{-1}$
d_*	the maximum extension of the region under investigation	m
d_{el}	distance between the electrodes	m
d_{ij}	distance between node i and node j	m
$\boldsymbol{D}$	electric induction	C m^{-2}
$\boldsymbol{E}$	electric field	V m^{-1}
f_j	frequency of the j-th armonic	Hz
h	convective heat transfer coefficient	W $\mathrm{m}^{-2}\mathrm{K}^{-1}$
$\boldsymbol{H}$	magnetic field	A m^{-1}
I_{rms}	root mean square current	A
$\boldsymbol{J}$	current density field	A m^{-2}
k	thermal conductivity	W $\mathrm{m}^{-1}\mathrm{K}^{-1}$
k_0	propagation constant in free space	m^{-1}
k_{mat}	number of material properties	$-$
m	number of tissues	$-$
M	matrix to derive the ripartition coefficient	$-$
M_1	body matrix	m, m, m, $-$
M_2	air matrix	m, m, m, $-$
M_{nod}	nodes outside the phantom	$-$
n	number of armonics	$-$
$\hat{n}$	normal unit vector	$-$
n_h	number of the computed harmonics	$-$

n_{nod}	nodes inside the phantom	$-$
p	number of interface elements	$-$
p_i	i-th material function	BSF
P_{abs}	overall absorbed power by the load	W
P_i	supplied power at the i-th armonic	W
$P_{load\ i}$	absorbed power by the load at the i-th armonic	W
P_{max}	maximum output power	W
P_{tot}	overall supplied power	W
PF	power factor	$-$
$\boldsymbol{q}$	heat flux	$\mathrm{W\ m^2}$
Q_{blood}	thermal regulation due too blood perfusion	$\mathrm{W\ m^{-3}}$
Q_{em}	elettromagnetic thermal source	$\mathrm{W\ m^{-3}}$
$Q_{em\ i}$	electromagnetic thermal source due to the i-th armonic	$\mathrm{W\ m^{-3}}$
Q_{met}	metabolic heat source	$\mathrm{W\ m^{-3}}$
Q_{source}	overall thermal source	$\mathrm{W\ m^{-3}}$
R_{int}	internal resistance of the generator	Ω
R_{load}	resistance of the load	Ω
t	time	s
t_*	tolerance threshold	$-$
T_0	room temperature	K
T_*	metabolic temperature	K
T_b	undisturbed arterial temperature	K
V_{rms}	root mean square voltage	V
x	spacial coordinate along x axis	m
x_i	supplied power at the i-th armonic in dBm	W
y	spacial coordinate along y axis	m
z	spacial coordinate along z axis	m
Z_{int}	internal impedance	Ω
Z_{load}	impendance of the load	Ω
α_i	ripartition coefficient of the i-th armonic	$-$
γ_{ij}	conductive over dielectrical behaviour	$-$

	at the j-th armonic for the i-th tissue	
δ_{ij}	dielectric penetration depth at	m
	the j-th armonic for the i-th tissue	
ϵ	dielectric permettivity	$\mathrm{F\ m^{-1}}$
ϵ'	real relative electrical permittivity	$-$
ϵ''	imaginary relative electrical permittivity	$-$
$\dot{\epsilon}$	complex electrical permittivity	$\mathrm{F\ m^{-1}}$
ϵ_0	electrical permittivity in free space	$\mathrm{F\ m^{-1}}$
ϵ_i	dielectric permettivity of the i-th tissue	$\mathrm{F\ m^{-1}}$
ϵ_r	relative electrical permittivity	$-$
$\dot{\epsilon_r}$	complex relative electrical permittivity	$-$
λ_0	wavelength in free space	m
λ_{0j}	wavelength in free space of the j-th armonic	m
μ	magnetic permeability	$\mathrm{H\ m^{-1}}$
μ_0	magnetic permeability in free space	$\mathrm{H\ m^{-1}}$
μ_r	relative magnetic permeability	$-$
ω_i	angular frequency at the i-th armonic	rad
ρ	mass density	$\mathrm{kg\ m^{-3}}$
σ	electrical conductivity	$\mathrm{S\ m^{-1}}$
σ_i	electrical conductivity of the i-th tissue	$\mathrm{S\ m^{-1}}$
ω_b	perfusion rate	$\mathrm{s^{-1}}$

Chapter 3

A_1	input surface	$\mathrm{m^2}$
A_2	output surface	$\mathrm{m^2}$
$\tilde{A}_1$	reduced input surface	$\mathrm{m^2}$
$\tilde{A}_2$	reduced output surface	$\mathrm{m^2}$
$\boldsymbol{d}$	general domain vector	BSM
$\boldsymbol{d_0}$	central vector of analysis domain	BSM
C^j	normalized computed sensitivity	$-$
D_j	j-th domain of analysis	BSM

$\boldsymbol{E}$	electric field	$\mathrm{V\ m^{-1}}$
f	frequency of electromagnetic fiel	Hz
$\boldsymbol{H}$	magnetic field	$\mathrm{A\ m^{-1}}$
$\langle H^j \rangle$	mean of j-th response function	BSM
H^j_{max}	maximum of j-th response function	BSM
H^j_{min}	minimum of j-th response function	BSM
$\boldsymbol{J}_1$	sign of the gradient of the response function	BSM
$\boldsymbol{J}_2$	sign of the gradient of the reduced response function	BSM
m	number of domains of analysis	$-$
n	number of indipendent optimization parameters	$-$
$\hat{n}$	normal unit vector	$-$
p	choke-cavity gap	m
P_1	input power	W
P_2	output power	W
S_{21}	scattering parameter at the port 2 due to port 1	$-$
$\tilde{S}_{21}$	reduced scattering parameter at the port 2 due to port 1	$-$
$\boldsymbol{x}$	indipendent optimization parameters	BSM
x_*	optimal final design	BSM
$\tilde{x}_*$	reduced optimal solution	BSM
$\boldsymbol{x_0}$	central vector of indipendent parameters	BSM
$\boldsymbol{x_{max}}$	maximum constrain of optimization parameters	BSM
$\boldsymbol{x_{min}}$	minimum constrain of optimization parameters	BSM
y	functional	BSM
$\tilde{y}$	reduced model functional	BSM
Δd_j	j-th analysis domain step	BSM
Δx_i	investigation step	BSM
Ω	computational domain	$\mathrm{m^3}$
$\tilde{\Omega}$	reduced computational domain	$\mathrm{m^3}$

Chapter 4

A_2	equivalent surface of leakage	$\mathrm{m^2}$

c_b	specific heat at constant pressure of blood	$\mathrm{J\ kg^{-1}K^{-1}}$
c_p	specific heat at constant pressure	$\mathrm{J\ kg^{-1}K^{-1}}$
$\boldsymbol{E}$	electric field	$\mathrm{V\ m^{-1}}$
d	choke-cavity displacement	m
f	frequency of electromagnetic filed	Hz
h	relative height of the appliance	m
$\boldsymbol{H}$	magnetic fiel	$\mathrm{A\ m^{-1}}$
k	thermal conductivity	$\mathrm{W\ m^{-1}K^{-1}}$
k_0	propagation constant in free space	$\mathrm{m^{-1}}$
l	distance between the phantom and the oven door	m
$\hat{n}$	unit normal vector	$-$
P_{int}	input power	W
P_{out}	output power	W
R	statistical linear correlation coefficient	$-$
Q_{blood}	thermal regulation due too blood perfusion	$\mathrm{W\ m^{-3}}$
Q_{em}	elettromagnetic thermal source	$\mathrm{W\ m^{-3}}$
Q_{met}	metabolic heat source	$\mathrm{W\ m^{-3}}$
S_{ij}	scattering parameter at the port i due to port j	$-$
t	time	s
T	temperature	K
T_b	undisturbed arterial temperature	K
v	volume	$\mathrm{m^3}$
α	angular rotation around z axis	rad
Δx_i	i-th displacement along x direction	m
Δz_i	i-th displacement along z direction	m
ϵ''	imaginary relative electrical permittivity	$-$
ϵ_r	relative electrical permittivity	$-$
$\dot{\epsilon_r}$	complex relative electrical permittivity	$-$
λ_0	wavelenght in air	m
μ_r	relative magnetic permeability	$-$
ρ	mass density	$\mathrm{kg\ m^{-3}}$

ω_b	perfusion rate	s^{-1}

Chapter 5

c_0	room concentration of humidity	m^{-3}
c_p	specific heat at constant pressure	$\mathrm{J\ kg^{-1}\ K^{-1}}$
c_{vap}	concentration of saturated vapor	$\mathrm{mol\ m^{-3}}$
D_{air}	diffusivity in air	$\mathrm{m^2\ s^{-1}}$
D_e	electron diffusivity	$\mathrm{m^2\ s^{-1}}$
$\boldsymbol{E}$	electric field	$\mathrm{V\ m^{-1}}$
E_{eff}	effective magnitude of electric field	$\mathrm{V\ m^{-1}}$
E_{rms}	root medium square of electric field	$\mathrm{V\ m^{-1}}$
f	frequency	Hz
g	gap between halves	m
h	convective heat transfer coefficient	$\mathrm{W\ m^{-2}\ K^{-1}}$
$\vec{\mathbf{j}}_{\mathbf{vap}}$	flux of water vapor	$\mathrm{kg\ m^{-2}\ s^{-1}}$
k	thermal conductivity	$\mathrm{W\ m^{-1}\ K^{-1}}$
k_0	propagation constant in free space	$\mathrm{m^{-1}}$
$(K_e)_{gas}$	electron mobility in the gas per unit length	$\mathrm{m^2\ V^{-1}\ s^{-1}}$
m_{avg}	normalized modulation of average power	$-$
m_i	ion mass	kg
m_m	molecular mass	kg
n	amount of substance of gas	mol
n_e	electron density	$\mathrm{m^{-3}}$
n_i	ion density	$\mathrm{m^{-3}}$
$\hat{n}$	unit normal vector	$-$
p_{air}	partial pressure of dry air	Pa
p_{vap}	partial pressure of vapor	Pa
P_{air}	partial pressure of dry air	Pa
P_{avg}	average power	W
P_{em}	dissipated electromagnetic power	$\mathrm{W\ m^{-3}}$
P_{sat}	saturation vapor pressure	Pa

P_{peaks}	peaks power	W
$\boldsymbol{q}$	heat flux	$\mathrm{W\ m^{-2}}$
Q	heat source	$\mathrm{W\ m^{-3}}$
r	peaks to average factor	$-$
t	time	s
T	temperature	K
T_e	electron temperature	K
T_i	ion temperature	K
T_0	room temperature	K
$(v_e)_{gas}$	electron velocity in the gas	$\mathrm{m\ s^{-1}}$
$(v_e)_{th}$	electron thermal velocity	$\mathrm{m\ s^{-1}}$
$(v_i)_{th}$	ion thermal velocity	$\mathrm{m\ s^{-1}}$
$(V_i)_{gas}$	ionizing potential in the gas	V
W_i	molecular weight of the i-th gaseous component	$\mathrm{kg\ mol^{-1}}$
x_i	normalized fraction of the i-th gaseous component	$-$
$(\alpha)_{gas}$	ionizing collisions in the gas per unit lenght	$\mathrm{m^{-1}}$
ΔH_m	latent heat of evaporation	$\mathrm{kJ\ kg^{-1}}$
ϵ	electrical permittivity	$\mathrm{F\ m^{-1}}$
ϵ'	real relative electrical permittivity	$-$
ϵ''	imaginary relative electrical permittivity	$-$
$(\eta)_{gas}$	attaching collisions in the gas per unit length	$\mathrm{m^{-1}}$
$\dot{\epsilon_r}$	complex relative electrical permittivity	$-$
θ	angular rotation of the sample	rad
$(\lambda_e)_{gas}$	electron mean free path in the gas	m
μ	magnetic permeability	$\mathrm{H\ m^{-1}}$
μ_r	relative magnetic permeability	$-$
ν_{att}	attachment rate	$\mathrm{s^{-1}}$
ν_c	collision frequency	$\mathrm{s^{-1}}$
ν_{ion}	ionization rate	$\mathrm{s^{-1}}$
ξ_i	i-th boundary	$\mathrm{m^2}$
ρ	mass density	$\mathrm{kg\ m^{-3}}$

ρ_{ch}	charge density	$\mathrm{C\ m^{-3}}$
σ	electrical conductivity	$\mathrm{S\ m^{-1}}$
σ_{coll}	cross section for inelastic collisions	$\mathrm{m^2}$
ω	angular frequency	rad
Ω_i	i-th subdomain	$\mathrm{m^3}$

Chapter 6

c_p	specific heat at constant pressure	$\mathrm{J\ kg^{-1}K^{-1}}$
$\boldsymbol{E}$	electric field vector	$\mathrm{V\ m^{-1}}$
E_{rms}	electric field root medium square	$\mathrm{V\ m^1}$
f	frequency of the electromagnetic field	Hz
k	thermal conductivity	$\mathrm{W\ m^{-1}K^{-1}}$
l_c	cut-off radius for TE_{10} in circular waveguides	m
m_i	i-th mass of the load	$\mathrm{m^3}$
P_{abs}	absorbed power	W
P_{em}	electromagnetic power density	$\mathrm{W\ m^3}$
P_{int}	input power	W
P_{load}	overall load power	W
P_{loss}	power losses	W
P_{min}	minimum power at each port	W
P_{max}	maximum power at each port	W
P_{porti}	power at the i-th port	W
P_{ref}	reference power	W
P_{refl}	reflected power	W
P_{tot}	total generated power	W
$\boldsymbol{q}$	thermal flux	$\mathrm{W\ m^{-2}}$
$\boldsymbol{S}$	Scattering matrix	$-$
S_{ij}	scattering parameter at the port i due to port j	$-$
T	temperature	K
u_e	field non-uniformity	$-$
V_i	i-th volume of the load	$\mathrm{m^3}$

α_i	electric field modulation at the port i-th	$-$
ΔP	Power step of the analysis	W
Δt	heating period	s
$\Delta\phi$	phase step of the analysis	rad
ϵ_r'	real relative permittivity	$-$
ϵ_r''	imaginary relative permittivity	$-$
$\dot{\epsilon}_g$	complex permittivity of the granular material	$-$
$\dot{\epsilon}_l$	complex permittivity of the inserted material	$-$
$\dot{\epsilon}_r$	complex permittivity of the background material	$-$
ϵ_{sic}	emissivity of silicon carbide	$-$
η	efficiency	$-$
θ_i	initial phase of the electric field at the port i-th	rad
μ_r	relative magnetic permeability	$-$
ν_b	grade of porosity	$-$
ϕ_i	phase at the port i	rad
ϕ_{ref}	Reference phase	W
ρ	mass density	$\mathrm{kg\ m^{-3}}$

Chapter 7

c_p	specific heat at constant pressure	$\mathrm{J\ kg^{-1}K^{-1}}$
dl	infinitesimal lenght along x axis	m
dV	infinitesimal volume	$\mathrm{m^3}$
$d\delta$	infinitesimal lenght along z axis	m
$d\rho$	infinitesimal lenght along y axis	m
$\boldsymbol{E}$	electric field	$\mathrm{V\ m^{-1}}$
$\dot{\boldsymbol{E}}$	superimposed phasorial electric field	$\mathrm{V\ m^{-1}}$
$\dot{E_{0i}}$	phasorial field amplitude due to the i-th port	$\mathrm{V\ m^{-1}}$
$\dot{\boldsymbol{E_i}}$	phasorial electric field due to the i-th port	$\mathrm{V\ m^{-1}}$
$\boldsymbol{E_j}$	electric field due to the j-th configuration	$\mathrm{V\ m^{-1}}$
$\boldsymbol{E_j^i}$	discretized electric field due to the j-th configuration	$\mathrm{V\ m^{-1}}$
E_{rms}	root medium square of electric field	$\mathrm{V\ m^{-1}}$

f	frequency of electromagnetic filed	Hz
f^i	weight related to the i-th node	$-$
h	convective heat transfer coefficient	$\mathrm{W\ m^{-2}\ K^{-1}}$
k	number of ports	$-$
k_0	propagation constant in free space	$\mathrm{m^{-1}}$
k_{th}	thermal conductivity	$\mathrm{W\ m^{-1}K^{-1}}$
l	number of electromagnetic termal steps forming one termal step	$-$
m	number of nodes forming Ω	$-$
m_i	j-th material property function	based on the specific material
n	number of degrees of freedom of electric field patterns	$-$
$\hat{n}$	unit normal vector	$-$
p	number pf material properties	$-$
p_j	overall probability of the j-th configuration	$-$
p_j^i	probability of the j-th configuration due to the i-th node	$-$
$\boldsymbol{P}$	complete set of power inputs	W
$\boldsymbol{q}$	heat flux	$\mathrm{W\ m^{-3}}$
Q	overall termal source	$\mathrm{W\ m^{-3}}$
Q_{em}	dissipated electromagnetic power	$\mathrm{W\ m^{-3}}$
t	time	s
T	temperature	K
T_*	target temperature	K
T_*^i	discretized target temperature	K
$\dot{T}_\dagger$	desired temperature raise	$\mathrm{K\ s^{-1}}$
T_0	initial temperature	K
T^i	discretized temperature	K
$\boldsymbol{V}$	velocity field	$\mathrm{m\ s^{-1}}$
w	electromagnetic power dissipation	$\mathrm{W\ m^{-3}}$
w_c^i	computed power density at the c-th probabilistic extraction	$\mathrm{W\ m^{-3}}$
w_j	electromagnetic power dissipation	$\mathrm{W\ m^{-3}}$
w_*^i	discretized target power dissipation	$\mathrm{W\ m^{-3}}$

w_j^i	discretized electromagnetic power	$\mathrm{W\ m^{-3}}$
w_r^i	computed power density at the r-th probabilistic extraction	$\mathrm{W\ m^{-3}}$
	dissipation related to the j-th configuration	
x	spacial coordinate along x axis	m
y	spacial coordinate along y axis	m
z	spacial coordinate along z axis	m
$\boldsymbol{\alpha}$	complete set of modultion coefficients	$-$
α_i	modulation coefficient of the i-th port	$-$
δ	convective superficial layer	m
δ_{mat}	loss angle of material	rad
Δt_{em}	electromagnetic time step	s
Δt_{th}	termal time step	s
$\Delta\phi_{ij}$	phase shift between ports i and j	rad
ϵ'	real relative electrical permittivity	$-$
ϵ''	imaginary relative electrical permittivity	$-$
$\dot{\epsilon_r}$	complex relative electrical permittivity	$-$
θ_i	phasorial field phase due to the i-th port	rad
μ	magnetic permeability	$\mathrm{H\ m^{-1}}$
$\boldsymbol{\phi}$	complete set of phases	rad
ϕ_i	phase shift of port i	rad
ρ	mass density	$\mathrm{kg\ m^{-3}}$
ω	angular frequency	rad
Ω	spacial region of the load	$\mathrm{m^3}$

Dedicated to Chiara,
who lights me up everyday.

1 Introduction

1.1 Scientific background

Interaction between electromagnetic fields with matter (solid, liquid, gas) depends on the frequency of the propagating waves and on the material properties of the object exposed to radiation (e.g., metallic, ceramic, plastic, etc.). Restricting to radiofrequency (RF) and microwave (MW) frequencies (from 3 MHz up to 300 GHz), electromagnetic radiation can be reflected by metals since the electrons in the conduction band can freely move, creating a rippling wave pattern in the spatial distribution. Oscillation of electrons generates another electromagnetic field which is out of phase with the incident field (reflection). Electrons cannot respond instantaneously to the motion of the incident electromagnetic wave and therefore a fraction of the incident energy is deposited into a thin layer of the metallic material (converted heat). This phenomenon at RF/MW frequencies is typically employed to melting and sintering metallic nanoparticles since the thickness of the deposition layer is comparable with the size of the sample [1]. In case of RF/MW radiation to a dielectric material, the involved phenomena are much different. Materials can be transparent to the radiation, which means that the incident energy is completely transferred without energy absorption (ideal glasses and ceramics), and the incident wave can be polarized avoiding thermal losses. Otherwise, materials can be dissipative and several phenomena like volumetric, dipolar, ionic and electronic polarization can become source of heating within the exposed matter [2]. All the different mechanisms implicate heating as a consequence of an intrinsic or extrinsic charge unbalance which strives the oscillating dipoles to follow the external electromagnetic field. These phenomena are associated to molecular friction within matter, since the dipoles are obstructed by collisions with neighboring molecules and atoms. This agitation or motion generates heat, and this can be mathematically quantified considering that the lag of the oscillating dipoles with respect to the incident field ensures a current density component in phase with the applied electric field [3]. When RF/MW radiation is applied to a gas, the provided heating is actually negligible since molecular and atomic friction is dramatically smaller because of the random and

more sparse arrangement of molecules. In case of highly intense radiation, the electric field accelerates the free electrons (derived mostly from cosmic radiation and photo-ionization), providing high kinetic energy [4]. These electrons impinge neutral atoms and molecules by mean of random collisions. Detailed phenomena that regulate the collisions are based on quantum mechanic principles (out of the purpose of the current work), and the main resulting effects can be classified as elastic or inelastic [5]. In the first case, the internal energy of the impinged atoms or molecules does not change. In the second case, the impinged atoms or molecules change their internal energy levels, inducing excitation, electromagnetic radiation and/or ejection of energized charged particles (ionization). If the ionization rate is sufficiently high to balance the rate of electron losses, a stable plasma channel is generated. At MW frequencies the electron losses are mostly due to electron attachment and diffusion [6]. Electrically triggered plasma is commonly utilized for many applications: (a few examples) welding, lightning, ignition of combustion, and even more exotic applications like nuclear fusion and aerospace propulsion [7]. Sometimes, plasma formation can be considered as a dangerous side-effect like in the case of telecommunications or electric power systems. The intensity of the generated electric field can induce involuntarily breakdown phenomena. This phenomenological picture is at the basis of many events of everyday life, and new mechanistic explanations and quantitative assessments of the involved physical quantities can be fundamental to improve knowledge and to gain benefits for the society.

1.2 Microwave and Radiofrequency safety: general aspects

One of the purposes of this doctoral thesis is to maximize user safety in the use of radio frequency and microwave technology. Leaving aside the topics related to electrical safety, biological safety and food safety, this thesis deals mainly with the issue of electrothermal safety. What are the most typical situations in which a user can be exposed to non-ionizing radiation? First of all, the most widespread source is represented by telecommunications standards, such as cell phones (microwave band) and Internet access systems, such as routers and modems. The study of non-ionizing radiation related to these devices is subject to many controversies. Mainly, the reason why it is not possible to determine their possible toxicity is due to the fact that the main induced effect, that is electromagnetic heating, is so low that it can be neglected when compared to other sources of metabolic heat. Toxicity studies about non-thermal effects are very complex and easily exposed to criticism. To cite some

examples, the length of observation periods should be in the order of years, since people are normally exposed to electromagnetic fields for whole portions of life; the impossibility of distinguishing any electromagnetic toxicity from other sources of toxicity through long-term in vivo analysis, and the possible difference in physiological behavior of cells in vivo compared to cells in vitro in the long run. So, what can be further sources of exposition to RF and MW that can be scientifically analyzed and at the same time highly widespread? These sources are RF medical equipment and microwave ovens. One of the main effects induced is the rise in temperature by dielectric polarization, and from a physiological point of view it is known that cells go into apoptosis (programmed cell death) when the temperature is in a range between 42 and 43 degrees Celsius. How is it possible to limit the risks of excessive exposure in these cases? With regard to exposure in the therapeutic field, an accurate dosimetric evaluation is necessary with experimental and numerical techniques. In this way, it is possible to help the manufacturers of microwave and radiofrequency equipment in improving the products and also to help the doctors in the identification of safety protocols. With regard to the domestic environment, an improvement in the protection systems, and a quantitative assessment of the safety conditions must be developed taking into account the high variability of the conditions of use. For example, the mechanical displacements due to aging, the relative user-source position, the user's absolute distance and the mass of the thermal load are factors that greatly influence the level of risk. An important role must also be played by mass media that must inform consumers without creating alarmism, but with the constructive intent of guaranteeing maximum satisfaction in the use of technology in a safe environment. This is why it is important to provide information with ethics on issues concerning technology, but a good deal of criticality is also needed in correctly assessing the cost-benefit balance in the third millennium era.

1.3 New challenges

The classic advantages of microwave heating compared to conventional heating are now well known: ability to heat the material from the inside, speed, selectivity, reduced inertia and even cheapness, thanks to the low cost of Magnetrons. Equally known are the typical disadvantages which apparently make microwave heating a lower quality thermal process than conventional convection and thermal conduction. Just think that no restaurant proudly presents the use of microwaves for cooking. But

what is a physical reason behind these qualitative considerations? The main responsible are the stationary resonating waves. There is an analogy between the electromagnetic case and vibrations generated in guitar strings, where there are constraints at the ends, tension of the rope and elastic stiffness of the strings which determine the wavelengths of the pressure waves. Based on this characteristics, a certain harmonic resonates by exciting a specific sonic note. Similarly, any microwave oven has some constraints that are imposed by the walls (the electric field must be normal to the metal surface), propagation frequency that corresponds to the note emitted by the guitar, dielectric permittivity that corresponds to the rigidity of strings and the wavelength that separates two successive peaks in complete acoustic analogy. This distribution of the peaks and nodes determines the configuration of the electric field and the consequent distribution of the power density in the material. Therefore, given a fixed configuration, the material is subject to an inhomogeneous overheating that can strongly compromise the quality of the process. To overcome this problem, stirrers have been invented that allow the system to vary the distribution of the electric field inside the material. Among the most common, there are moving elements positioned in front of the waveguide (element that injects the electric field into the cavity), or the turntable that allows a variation of the position of the maximum and minimum peaks within the material. What are the limits of these strategies? Basically, we can identify two: the inability to adapt the behavior of the stirrer to the specific thermal load, which can vary in geometry and materials; the inability to manage the new degrees of freedom of the system in terms of reconfiguration of the electric field in a controlled manner. Returning to the acoustic analogy, we are using Vienna's symphony as a fireproof siren, and it works badly. But then the question arises: how is it possible to make the best use of microwave heating by enhancing its physical nature? Thanks to the development of new generation solid-state high-frequency and high-power electronics, multiple electromagnetic inputs can be controlled in phase and amplitude. In this way it is possible to reconfigure the system adapting it to the specific needs of the process. Using an appropriate sensor-system, an adaptive automatic control system can be created to customize the heating pattern. Thus, processes in the chemical, pharmaceutical, food and other sectors can widely benefit from this technological innovation. How can we increase the quality of solid-state processes? We must invest resources in two categories: the development of intelligent algorithms for the management of electromagnetic ports; the development of innovative reactors/cavities that allow to increase the degrees of freedom in terms of electrical field configurations. When these two strands have reached the technical-scientific maturity, it will be possible to involve RF and MW processes in applications requiring stringent standards

on the quality of the heating pattern, and at the same time needing all the characteristic advantages of volumetric processes.

1.4 Interrelation between the treated sub-topics

In many processes, non-ionizing dielectric polarization can be considered as the primary desired effect, or at the opposite, as the main side-effect. In the first case, the processes that employ mainly this kind of radiation are microwave cooking and microwave assisting of chemical reactions. The main open challenge is controlling the heating pattern avoiding problems related to the presence of resonant standing waves. Indeed, standing waves impede both uniform distribution of power density and highly focused radiation. Thanks to recent developments of new microwave sources based on solid state electronics, it is possible to change the radiated field pattern just exploiting constructive and destructive interference. A lot of interesting and unexplored scenarios are now available, renovating the potential of microwave heating.

In chapter 6, the analysis is particularized to the case of steam reforming of methane, which is a largely used chemical process for the production of hydrogen. This process operates at high temperature since a catalytic bed must be hold at 700 °C (this temperature is related to chemical kinetics) to promote the reaction. Conventional heating of tubular reactors based on gas combustion is regularly adopted in industrial scale, but some problems occur to heat thoroughly the core. Microwave heating based on magnetron can provide heat directly inside the material, but strong non-uniformities rise axially because of the resonant standing waves. Therefore, a rigorous investigation on the capability of improving the heating uniformity by mean of MW solid state electronics becomes fundamental. Considering the new degrees of freedom available in terms of controlling the electric field patterns, it is important to determine the new suitable algorithms to control the MW source. The development of such control algorithm can increase effectiveness on improving process quality. In chapter 7, an original probabilistic algorithm is presented, showing that some drawbacks of traditional processing can be overcome.

Sometimes, non-ionizing dielectric polarization can be considered as a side-effect. These problems usually belong to the category of Electromagnetic Compatibility (EMC). One of the most delicate cases of EMC problems concerns with the exposure of human body in the near field region of a radiating source. In general, if the temperature within the body overcomes a certain threshold value,

there are associated damages for organs and tissues. In case of therapeutic treatments, the assessment of induced thermal effects requires high-end numerical and experimental analysis. In chapter 2, an innovative therapy to treat Dry Eye Syndrome is considered. An in depth investigation of the associated thermal effects was made to provide new therapeutic protocols under safe operative conditions. If the exposure is passively endured, determination of a security state and development of new protections can be achieved properly just considering high-performance numerical techniques. Given that MW ovens are the most diffused high power microwave source, in chapter 3, a new strategy to develop performing MW shields for domestic ovens is presented. Particular attention was turned to reduce computational burden. A detailed analysis of the effects associated to usage of the appliance, considering the mechanical slackness of door hinges and hooks was performed in chapter 4. Considering international guidelines, safety levels were estimated.

It is common knowledge that the insertion of a metallic object in a microwave oven can induce arcing. Unfortunately, this phenomenon occurs even without presence of metals but just between dielectrics. A theoretical mechanistic understanding is not available although the potential risks are well documented. In chapter 5, the development of such phenomenological framework is provided, and threshold conditions to avoid arcing are given.

All the research activities that have been accomplished in the current thesis have been carried out theoretically, numerically and experimentally; and the specific weight of each component was calibrated based upon the specific needs of any research projects.

1.5 Instructions for the reader

This thesis is structured according to the anglo-saxon schema: at any chapter corresponds the related article. Therefore, the chapters can be considered as standalone entities with minimal overlapping, despite of the reader is acknowledged about the common background. Some articles have been already published, while others have been recently submitted to journals. In order to keep the nomenclature as compact as possible, avoiding the abuse of subscripts, the list of symbols of any chapter has been defined independently. The list of symbols in the front matter was created by assembling.

2 Assessment of Electrothermal Compatibility for a New Radiofrequency Therapy to Treat Dry Eye Disease

2.1 Abstract

An innovative therapy based upon radiofrequency radiation has been recently adopted to treat patients subjected to dry eye disease. The disease is related to a malfunctioning of the lacrimal glands, which are not able to secrete the normal lacrimation, and therefore changing the fluid viscosity or the production rate of tears. A recent research has demonstrated the efficacy into giving relief to the patients who were treated by radiofrequency, but further investigations are necessary to evaluate electromagnetic and thermal effects which are associated to radiation. In particular, because of the low blood perfusion within eyes, it is important to avoid dangerous overheating that can induce side-effects like cataracts. The purpose of the current work is to assess these induced side-effects, considering two possible applicators: patch electrodes and eyelid electrodes. The dosimetric evaluation was performed by mean of a finite element software considering a realistic human body phantom, after a validation stage of the model at the International Center of Ocular Physiopatology (Venice, Italy). The experimental tests were conducted analyzing the physical behavior of real eyes which were placed on an agar-gel support. Reproducing the tested clinical conditions, the temperature within the eyeball never overpassed the value of 39°C, considering the effective transferred power of 7.8 W, with a duty-cycle of 0.5. Analyzing in the range of power from 4 W to 20 W, with duty-cycle of 0.5, and stimulation-period of 20 minutes, new operative conditions are available in terms of intensity and length of the treatment under safe conditions.

2.2 Introduction

The current work provides a quantitative thermal evaluation of an innovative treatment, based on electromagnetic stimulation, to treat patients subjected to the Disfunctional Tear Syndrome (DTS), also known as Dry Eye Syndrome (DES). According to the Report of the International Dry Eye Workshop (2007), the definition of such disease is provided [8] – Dry-Eye Syndrome is a multi factorial disease of the tears and ocular surface that results in symptoms of discomfort, visual disturbances and tears film instability with potential damage to the ocular surface ... accompanied by increased osmolarity of tear film and inflammation of the ocular surface. This disease is related to a dysfunction of the Lacrimal Functional Unit (LFU): lacrimal glands, ocular surface, eyelid and involved sensorial nerves. The syndrome can be iposecretive, related to the reduced production of aqueous tears, or evaporative, related to a low tears quality [9]. Nowadays, the existing therapies can be pharmacological, surgical, based on contact-lens or based on ophtalmic creams [10]. These therapies are palliative since they are not able to restore the physiological lacrimal secretion [11]. Therapies that treat the entire superficial structure of the eye seem to be more promising than classical techniques [12]. Among these emerging therapies there are: application of new drugs to stimulate the entire lacrimal unit, mechanical stimulation (e.g., vibration, massages) and thermo-therapies [13, 14, 15]. An experimental study has demonstrated the effectiveness on improving the conditions of patients who were treated by electromagnetic stimulation, considering the induced heat as side-effect. In this study, the patients (27) were treated considering 12 sessions over 2 months, in particular, 2 sessions per week during the first month, and 1 session per week during the second month. The analytical indexes (e.g, OSDI, TBUT, Oxford score, Schrimer I) proved the capability to improve the conditions of patients that were treated with the electromagnetic therapy, with no complications [16]. Considering that the induced heat is the main side-effect, new quantitative evaluations must be done to improve the efficacy of the treatment, but taking care of avoiding dangerous overheating [17]. The current work aims to provide numerical thermal assessments of this electromagnetic therapy, considering the same clinical conditions during the treatment: harmonic distribution, power levels and shape of applicators. By mean of Finite Element (FE) software, a numerical model was developed to reproduce in-silico the therapeutic conditions. The model was validated by mean of ex-vivo experiments at the International Center of Ocular Physipoatology, considering a real human eyeball placed on an agar-gel support. Then, the model was adopted to analyze the temperature evolution (max, min, range) within the eyeball during the experimented treatments, and the induced Specific Absorption Rate (SAR) in the eye components

(cornea, lens, sclera-wall, humor aqueous). Also, sensitivity analysis was performed to determine the increase of the maximum temperature in relation to the power level. Thus, the results can be used as reference-data to define new protocols in terms of power and time-period of stimulation.

2.3 Materials and Methods

2.3.1 In silico setup

Reconstruction of the phantom

The purpose of this section is to describe the steps which have been adopted to achieve a reliable customized phantom. In the current work there are three important needs that are strongly related to computational cost:

- For the electromagnetic simulation, the phantom was limited at the position of the pelvis. During the therapy, the electrodes were placed on the eyes and at the pelvis. Therefore, the bottom part of the body is not of interest for the current analysis.
- For the thermal simulation, the phantom was limited at the position of the neck. The thermal simulation can be run only over the head domain, since the remaining part of the body remains at physiological temperature.
- Accuracy of the surface reconstruction has to be properly set, considering that the implementation of a curvilinear closed surface into a finite element software occurs by mean of a discretization process. Any insertion of nodes increases the rank of the stiffness matrix, thus, as well as computational burden. At the same time, nodal overpopulation to fit the geometry does not correspond to an improvement of computational accuracy.

At the Visible Human Project (VHP) website there is a database regarding the topology of the human body tissues [18]. The starting point to reconstruct the human model is the knowledge of all the anatomical information of different organs and tissues, and the list of tissues with a corresponding numerical code. The raw file is characterized by a 3-order tensor (196 x 114 x 626 cells) corresponding to the 3 dimensional space axes, where each row-index identifies the position with respect to the relative axis. The value inside the cell defines which kind of tissue is present in the specific position. The tissue 0 corresponds to air. The reconstruction strategy is based upon the identification of the surface-interface between air and the body, in order to create a volume which can be directly imported into

the Finite Element (FE) software. First, two matrices ($n_{nod} \times 4$ matrix M_1 and $m_{nod} \times 4$ matrix M_2) were defined considering M_1 as the body matrix (only information regarding body elements) and M_2 the air matrix (only information regarding m_{nod} air elements). n_{nod} is the number of body nodes. Each row of the matrix defines the position along x, y and z. Then, an assessment of the relative distances between the elements in M_1 and M_2 was done, in order to identify all the border elements. A new matrix was defined considering the Euclidean distance and inserting the value in the position d_{ij} between the i-th and the j-th elements with $i = 1, ..., n_{nod}$ and $j = 1, ..., m_{nod}$.

$$d_{ij} = \sqrt{(x_j - x_i)^2 + (y_j - y_i)^2 + (z_j - z_i)^2} \tag{2.1}$$

The elements having a value that is equal to the spatial resolution distance correspond to the interface surface. All these elements are characterized by the row index, which defines the i-th element of the matrix M_1 as body-interface element, and similarly for the column index, which defines the j-th element of the matrix M_2. Then, a new $p \times 3$ (p is the number of interface elements) matrix containing the topological positions of the body interface was constructed and further elaborated. Following this procedure, a dataset of cloud-points with no faces was available. The normals of the vertices of a mesh was computed without exploiting the triangle connectivity. Here, the Poisson surface reconstruction algorithm was adopted to reconstruct the actual surface [19]. When the surface was created, a simplification algorithm was performed. This operation was done applying the Quadric-Edge Collapse Decimation to the already reconstructed surface, imposing the percentage of accuracy reduction [20]. The last operation has been repeated several times until the proper simplification is achieved. In Fig. 2.1 we can observe two phantom portions that were used for the electromagnetic analysis and thermal analysis respectively. In Fig. 2.2, the geometries that have been achieved by mean of the simplification process are reported. For more details about the eye anatomy and its implementation, the reader is addressed to [21].

Material properties of the tissues

The desired final result, regarding the implementation of the material properties, is a series of k functions (this number is related to the total number of material properties required to reproduce single-physics or multiphysics analysis), which depend on the spatial position: $p_1 = f_1(x, y, z), ..., p_k =$

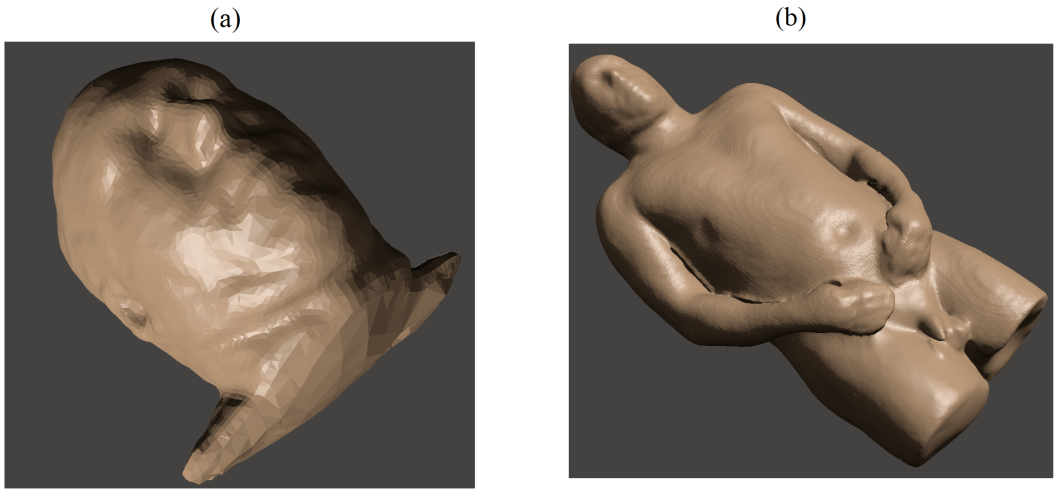

FIGURE 2.1: (a) Head of the pahntom (thermal domain). (b) Body of the phantom (electromagnetic domain).

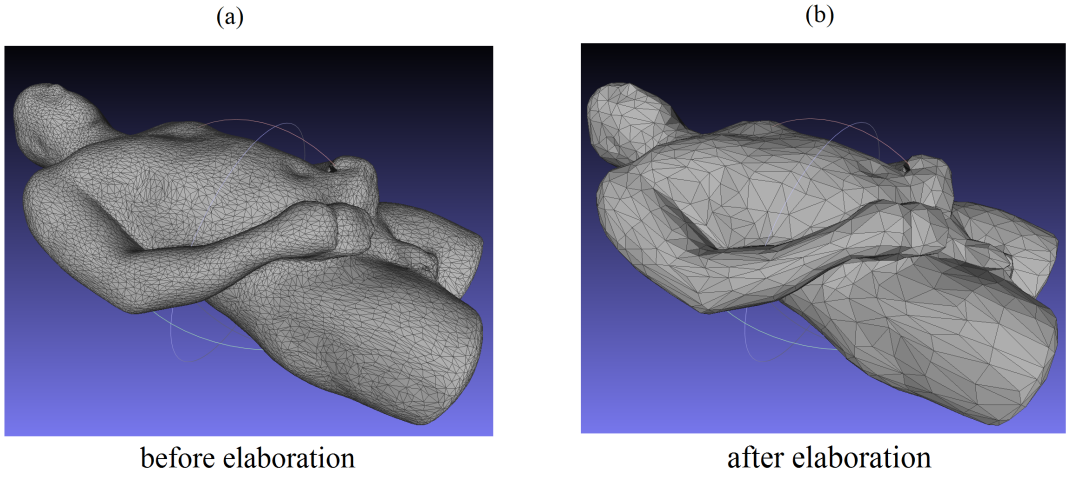

FIGURE 2.2: (a) Topological domain before algorithmic simplification. (b) Simplified domain suitable to be imported into the finite element software.

$f_k(x, y, z)$. The available initial data was a 3-order tensor of the tissue topology (the same considered in the section 2.3.1), and a material properties database. Regarding the database, the material properties available at the IT'IS foundation website were adopted, considering the main physical components: heat transfer and electromagnetics (frequency dependent charts) [22]. Then, for each node, the appropriate material property in any position was associated, relating any nodes to the corresponding specific tissues. A general schema of the procedure is depicted in Fig. 2.3 and the implemented material functions are reported in Fig. 2.4.

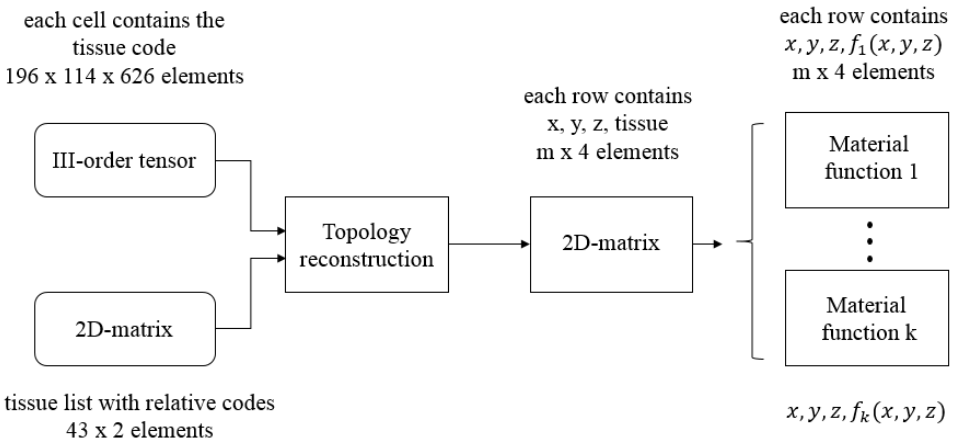

FIGURE 2.3: Flow chart depicting the general schema to computing the non-uniform material property functions.

2.3.2 Ex vivo setup

The experiments were conducted to achieve the two following results: first, the validation of the implemented numerical model, to improve reliability on predictions; second, a preliminary assessment of the thermal effects in real eyes under therapy for high power levels, to identify threshold conditions for significant temperature rise.

Human eyeballs and agar-gel support

The experimental analysis was conducted onto intact ex-vivo eyeballs, which were identified by Single European Code (SEC) [23]. The eyeballs were inserted in an agar-gel support. In this way it was possible to reproduce dielectric properties similar to a real body. The temperature variations were measured in three positions:

- At the corneal surface, close to the placement of the applicator;

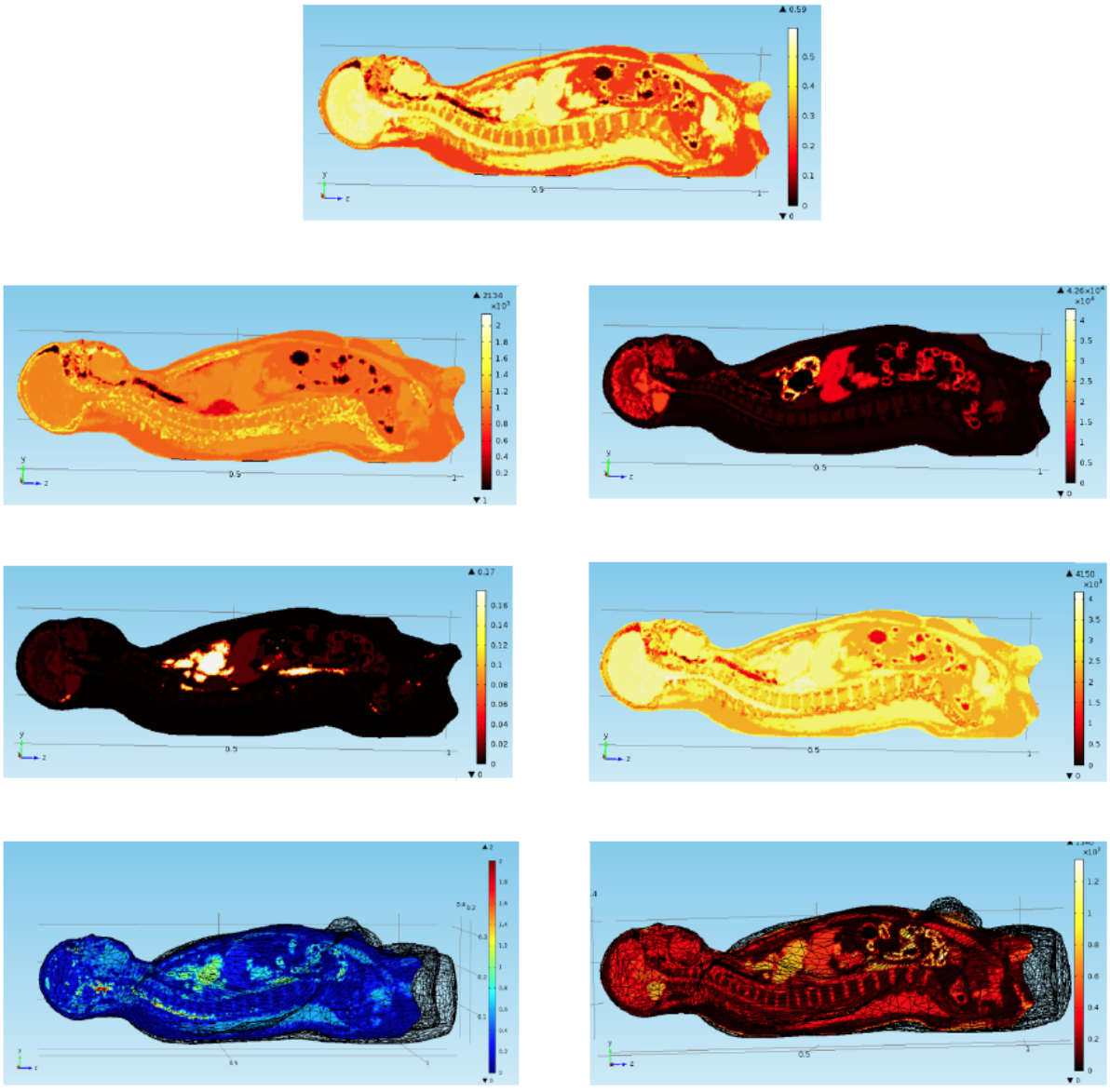

FIGURE 2.4: Material properties were implemented considering 40 different tissues, characterizing the non-uniformity of the phantom.

- In the anterior chamber, where the iris and the crystalline lens are located;
- In the bottom position of eyeball.

The donors were previously classified as not medical fitness compliant. The eyeballs were conserved individually in an ad-hoc container, which was filled by conservation fluid, and they were maintained at the room temperature for three hours before the start of the experiments. At the moment of running the tests, the eyeballs did not show any abnormalities that can be attributed to conservation or transport. Consistency was normal and transparency was at a normal level. In order to guarantee the maintenance of the structural resistance of the eyeballs during the tests, the tone was previously augmented by mean of injections of hyaluronic acid in the vitreous chamber.

Thermal sensors

Temperature measurements during the ex-vivo experiments were made by the internal sensor, which were integrated in the mask, and other internal sensors by mean of optic fibers. The integrated sensors were digital-chip thermometers IC DS18B20, MAXIM Integrated, that can operate in the range $T \in [-55, 125]$ °C with a resolution of 0.5 °C. The optic fibers were TS/3 FOTEMP1-H, Ampere, that can operate in the range $T \in [-200, 300]$ °C with a resolution of 0.2 °C.

RF generator and electrodes

The used generators were Rexon-eye-1 (used for clinical trials [16]) and Rexon-eye-2 (used for validation and sensitivity analysis), characterized respectively from internal impedance $Z_{int} = 400\ \Omega$ and $Z_{int} = 100\ \Omega$, maximum output power $P_{tot} = 25$ W and $P_{tot} = 80$, and different harmonic distributions (Tab.2.1, Tab.2.2, Tab.2.3, Tab.2.4). The generators are based upon the Risonanza Quantica Molecolare (RQM) technology made by TELEA Electronic Engineering. The generators were connected to two electrodes: the active ocular applicator and the neutral grounded plate. The considered active electrodes had two different shapes: first, the patch applicator placed in periocular position; second, the eyelid applicator, placed above the eyelid. The eyelid electrode was inside the mask, which contained internal temperature sensors to provide real-time superficial measurements. In the validation stage, the tests were conducted using impermeable cloths to separate the electrodes from the eyeballs, considering that during the therapy the patient kept the eyes closed.

Experimental procedures

The experimental tests were conducted utilizing three eyeballs. In order to make internal temperature measurements, it was necessary to create accesses by mean of perforation of the scleral matrix through a sterile needle such that to preserve the material inside the eyeball and avoiding the emptying. These operations and the insertion of the thermal sensors were made with the assistance of an optic microscope. The frequencies of the related spectrum were fixed over time during experiments.

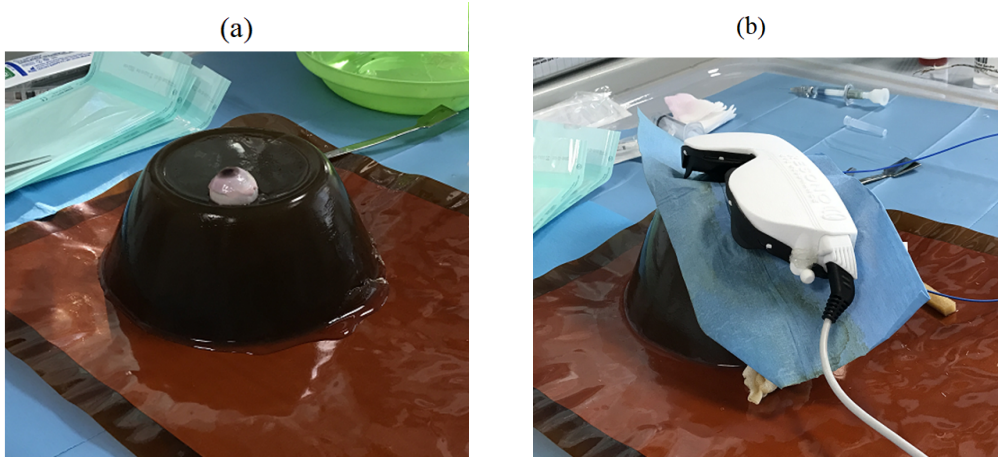

FIGURE 2.5: (a) Eyeball placed on the agar-gel support. (b) Impermeable tissues between the electrode and the eyeball.

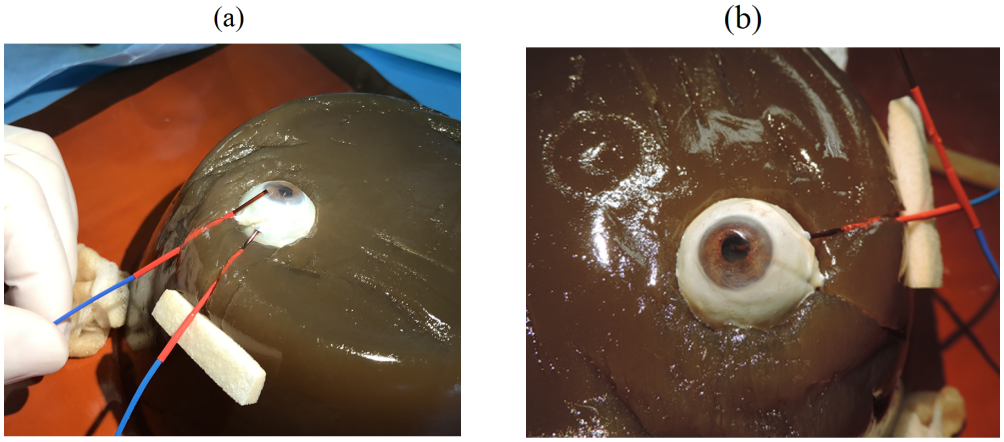

FIGURE 2.6: (a) Placement of the optic fiber on the corneal surface. (b) Placement of the optic fiber inside the eyeball.

2.4 Theory and numerical computation

2.4.1 Mathematical formulation given the therapeutic conditions

The materials that constitute all the tissues of the human body do not maintain the same behavior when subjected to an electromagnetic radiation at different propagating wavelengths. We consider the dielectric permittivity ϵ and the electrical conductivity σ (relative magnetic permeability is uniformly $\mu_r = 1$) as constitutive material functions of the physics under investigation. In Fig. 2.7 we report the electromagnetic response of vitreous humor when subjected to radiation in the range $f \in [4, 64]$ MHz. Fig. 2.7 shows that the higher the frequency and the smaller the permittivity, thus, the capability of

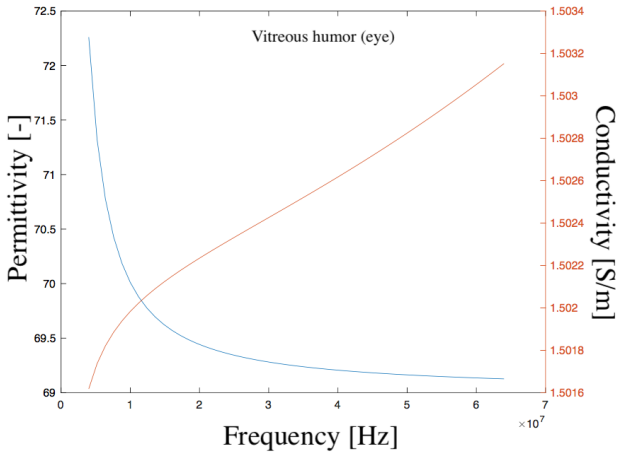

FIGURE 2.7: Electromagnetic response of an organic tissue (vitreous humor) in the frequency domain from 4 MHz to 64 MHz.

penetrating the body increases. Moreover, the electrical conductivity raises at higher frequencies, so the dissipation augments. This behavior has an important consequence regarding simulation. If the electromagnetic radiation is characterized by a frequency that is lower than 500 kHz, an human body can be well approximated as a real electrical conductor. In this case, the mathematical formulation is quasi-static, which is very cost effective from a computational point of view. In order to apply the quasi-static formulation, it is important to check three conditions. These conditions are related to material properties, propagating wavelength, distance between electrodes, and extension of the propagating medium [24]. Considering a system characterized by several harmonics $j = 1, ..., n$, the first condition is:

$$\lambda_{0j} = \frac{c}{f_j} = \frac{1}{f_j\sqrt{\epsilon_0\mu_0}} >> d_* \quad j = 1, ..., n \tag{2.2}$$

where d_* is the maximum extension of the region under investigation. This condition is valid even at the highest frequency included in the model (see section 2.5.3) $f = 36$ MHz. The corresponding value of $\lambda_{0\ 3} \approx 8.3$ m is much bigger than the maximum distance $d_* = 2$ m. The other condition that must be verified regards the penetration depth, which is related to the induced micro-currents within the human body. This condition should be verified for all the propagation frequencies $j = 1, ..., n$ and for all the body tissues $i = 1, ..., m$:

$$\delta_{ij} = \frac{c}{2\pi f_j \sqrt{\frac{\epsilon_i}{2}\left[\sqrt{1+\left(\frac{\sigma_i}{2\pi f_j \epsilon_i}\right)}-1\right]}} > d_{el} \quad i = 1, ..., m \quad j = 1, ..., n \tag{2.3}$$

where $d_{el} = 1.2$ m is the distance between the electrodes. The third condition is related to the predominance of conductive behaviour over dielectric behavior. We consider the parameter γ:

$$\gamma_{ij} = \frac{\sigma_i}{2\pi f_j \epsilon_i} >> 1 \quad i = 1, ..., m \quad j = 1, ..., n \tag{2.4}$$

The condition presented in Eq. 2.3 and Eq. 2.4 were tested for the case under investigation, and the results are reported in Fig. 2.8 for the 4 MHz harmonics (fundamental). The red lines indicate the reference conditions for acceptance or rejection. The plot in Fig. 2.8 (a) shows that the condition related to the penetration depth is verified by all the tissues. On the other hand, the condition related to conductive predominance ((b) in Fig. 2.8) is rejected by 36 tissues. Thus, the full-Maxwell formulation must be considered for the current study for all the harmonics, since criticality increases when harmonic order augments. Consequently, it is necessary to adopt the full-Maxwell's formulation, where the electrical conductivity, electrical permittivity and the magnetic permeability must be treated with a mutually coupled approach. Therefore, the computational cost is necessarily higher than for the quasi-static formulation. The material properties are linear with respect to temperature, since the expected temperature rise is limited. On the other hand, the material properties are not linear with respect to frequency as already mentioned above. Therefore, we shall compute as many frequency-domain analysis as many as the number of the harmonics, and then we should apply the Super Imposition Principle (SIP) to sum up the power density contributions into the overall power density source for a time-domain analysis. In general, during the therapy, the functioning is pulsed, therefore, a duty-cycle is introduced in the thermal model. A general schema about the here presented computational strategy is reported in Fig. 2.9.

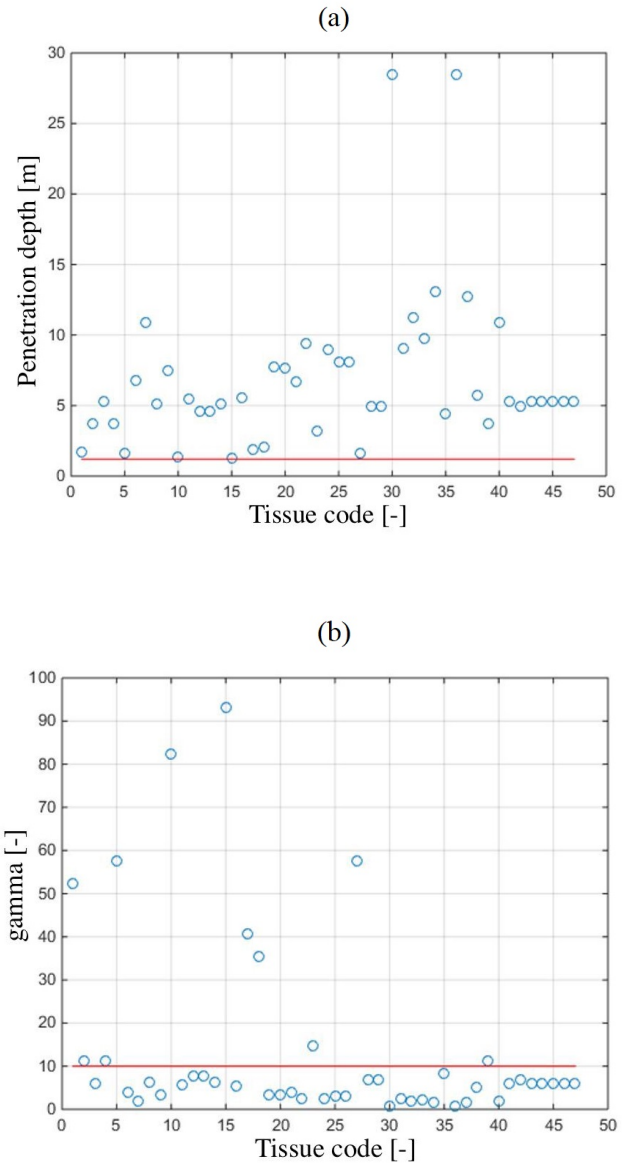

FIGURE 2.8: (a) The condition expressed in equation 2.3 is reported for all the tissues. (b) The condition in equation 2.4 is also reported.

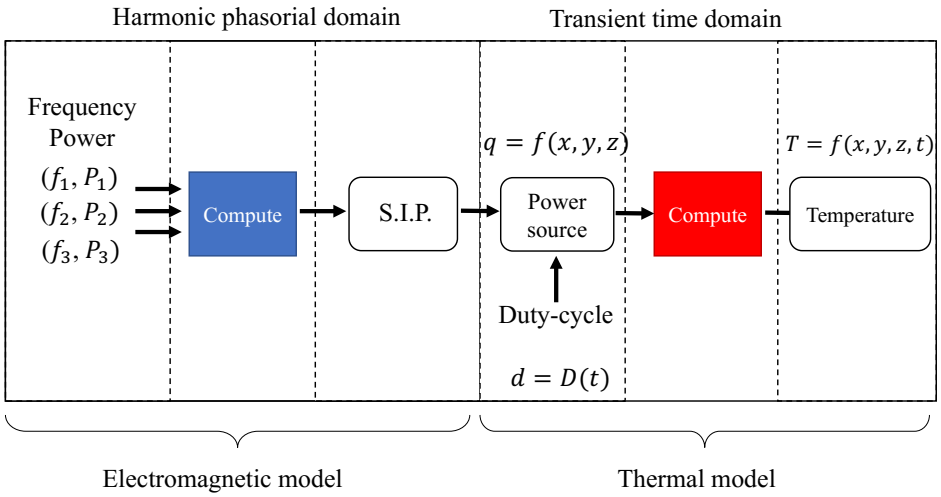

FIGURE 2.9: Computational strategy to simulate the transient thermal evolution due to the pulsed simulation, given a fixed harmonic electromagnetic distribution of power.

2.4.2 Implemented physics

The therapeutic conditions can be studied through many electromagnetic frequency-domain analysis as many as the number of the harmonics, and one transient heat transfer analysis over the time domain.

Electromagnetics

As already discussed in the section 2.4.1, we must consider the full Maxwell's equations. Let us consider the curl equations in the phasor form [25]:

$$\nabla \times \boldsymbol{E} = -j\omega \boldsymbol{B} \tag{2.5}$$

$$\nabla \times \boldsymbol{H} = \boldsymbol{J} + j\omega \boldsymbol{D} \tag{2.6}$$

and the material properties are characterized by the constitutive laws:

$$\boldsymbol{J} = \sigma \boldsymbol{E} \tag{2.7}$$

$$\boldsymbol{B} = \mu \boldsymbol{H} \tag{2.8}$$

$$\boldsymbol{D} = \epsilon \boldsymbol{E} \tag{2.9}$$

By substitution of Eq. 2.7 and Eq. 2.9 into Eq. 2.6 we derive as follows:

$$\nabla \times \boldsymbol{H} = \sigma \boldsymbol{E} + j\omega\epsilon \boldsymbol{E} = (\sigma + j\omega\epsilon)\boldsymbol{E} \tag{2.10}$$

and considering the equivalent complex permittivity as follows:

$$\sigma + j\omega\epsilon = j\omega\dot{\epsilon} \tag{2.11}$$

$$\rightarrow \dot{\epsilon} = \epsilon + \frac{\sigma}{j\omega} = \epsilon - \frac{j\sigma}{\omega} \tag{2.12}$$

so, we can express Eq. 2.12 in relative terms:

$$\dot{\epsilon_r} = \epsilon_r - \frac{j\sigma}{\omega\epsilon_0} = \epsilon' - j\epsilon'' \tag{2.13}$$

by substitution of Eq. 2.12 into Eq. 2.6 we get the compact form of the curl equation including the term related to dissipation:

$$\nabla \times \boldsymbol{H} = j\omega\dot{\epsilon}\boldsymbol{E} \tag{2.14}$$

now, considering the other curl equation we can write down:

$$\mu^{-1}\nabla \times \boldsymbol{E} = -j\omega\boldsymbol{H} \tag{2.15}$$

And applying the curl to both the sides of Eq. 2.15:

$$\begin{aligned} \nabla \times \mu^{-1}\nabla \times \boldsymbol{E} &= -j\omega\nabla \times \boldsymbol{H} \\ &= -j\omega(j\omega\dot{\epsilon}\boldsymbol{E}) \\ &= \omega^2\dot{\epsilon}\boldsymbol{E} \end{aligned} \tag{2.16}$$

Introducing the propagation constant in free space:

$$k_0 = \omega\sqrt{\mu_0\epsilon_0} \tag{2.17}$$

we can derive the final form of the governing law of the electromagnetic physics, which can be actually implemented in the finite element model

$$\nabla \times \mu^{-1} \nabla \times \boldsymbol{E} - k_0 \epsilon_r \boldsymbol{E} = 0 \tag{2.18}$$

Heat transfer

If we consider the classical heat transfer equation and the Pennes equation for the thermo regulation of the body[1], we can write down [26]:

$$\rho c_p \frac{\partial T}{\partial t} = \nabla \cdot (k \nabla T) + Q_{source} \tag{2.19}$$

where the term Q_{source} can be divided in three components: the heat generated by the external applied field, the thermal regulation due to blood perfusion, and the metabolic heat source which is related to the specific tissues and organs.

$$Q_{source} = Q_{em} + Q_{blood} + Q_{met} \tag{2.20}$$

$$Q_{em\ i} = 2\pi f_i \epsilon_i'' \left| \boldsymbol{E_i} \right|^2 \tag{2.21}$$

$$Q_{em} = \sum_i Q_{em\ i} = \sum_i 2\pi f_i \epsilon_i'' \left| \boldsymbol{E_i} \right|^2 \tag{2.22}$$

$$Q_{met} = f_{met}(x, y, z) \tag{2.23}$$

$$Q_{blood} = \rho c_b \omega_b (T_b - T) \tag{2.24}$$

where T_b is the undisturbed arterial temperature.

Initial and boundary conditions

The electromagnetic physics is analyzed over the frequency domain, and therefore the initial conditions are actually irrelevant from the physical point of view (they can play a role just for computational convergence). Instead, regarding the boundary conditions, the model is characterized by scattering toward the external environment (no reflection). The diffusion scattering boundary conditions are

[1] There are several existing formulations of body thermo-regulation. The model used in the current thesis is the classical formulation made by Pennes which presents some limitations like absence of large artery-vessels. This assumption is precautionary for the current research since the primary neglected effect is local cooling.

imposed over the external faces of the computational domain as follows:

$$\hat{n} \times (\nabla \times \boldsymbol{E}) - jk_0 \hat{n} \times (\boldsymbol{E} \times \hat{n}) = 0 \tag{2.25}$$

This imposition derives from the Sommerfeld condition at a finite distance from a radiating source. Therefore, in order to truncate the computational domain, imposing the absence of reflection, we can approximate properly in this way. This imposition is a numerical approximation of the Sommerfeld radiation (e.g. tangential components of the electric field cannot be totally scattered). For more details, any interested reader can be addressed to the following reference [27]. Regarding the heat transfer physics, since the analysis is over the time domain, we have to consider the initial conditions. Considering that the body is at metabolic temperature level in equilibrium with the environment, we can derive the initial condition as the solution of the heat equation in case of absence of external fields $Q_{em} = 0$, and other thermal sources. So, considering the steady state condition:

$$T_*(x, y, z): \quad \rho c_p \frac{\partial T_*}{\partial t} = \nabla \cdot (k \nabla T_*) + Q_{met} + Q_{blood} \tag{2.26}$$

Regarding the boundary conditions, the heat convection is imposed over the external surface of the body (actually in correspondence of the skin).

$$\boldsymbol{q} = h\,(T - T_0)\,\hat{n} \tag{2.27}$$

where $h \approx 15$ W/(m^2 K) defines the condition of limited natural air convection. Fig. 2.10 shows the superficial metabolic temperature before the start of the therapy.

2.4.3 Determination of the input power

Harmonic distribution

The RF-therapy operates injecting certain amounts of power at different propagating frequencies. Therefore, any harmonic is characterized by a specific overall amount of supplied power that depends on the impedance of the system. Considering that the variability of the impedance is quite big, since it depends on many conditions (e.g. the position of the grounded electrode, the physique of the patient, the dielectric properties of the tissues, etc.), it is appropriate to analyze the harmonic distribution experimentally in laboratory, using the used generator and adopting two impedances as reference

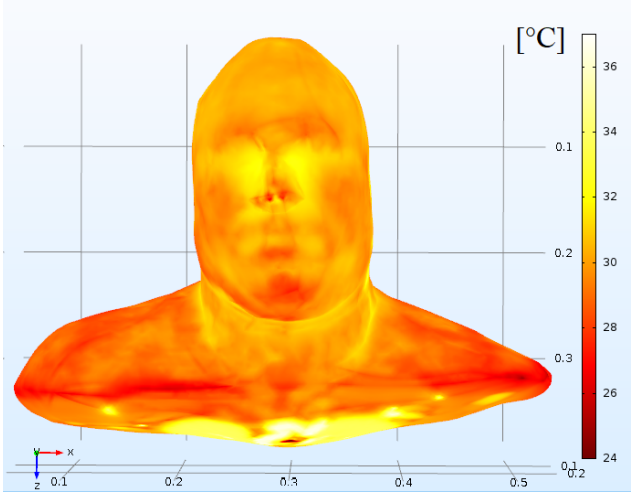

FIGURE 2.10: Metabolic temperature is the initial condition for the thermal transient analysis.

bounds. In this way, it is possible to compute the repartition coefficients $\alpha_1 = (P_1/P_{tot}), ..., \alpha_n = (P_n/P_{tot})$ which are related to the n provided harmonics. The procedure to determine the repartition coefficients that were implemented in the in-silico analysis can be done as follows. Let us point out explicitly the expression for the conversion of power from linear scale (P_i) to dBm scale (x_i):

$$x_i = 30 + 10\text{Log}\left(\frac{P_i}{1[\text{W}]}\right) \tag{2.28}$$

therefore we get the ratio between any two following harmonics:

$$\frac{P_i}{P_{i+1}} = 10^{\left(\frac{x_i - x_{i+1}}{10}\right)} \tag{2.29}$$

considering that we have defined the repartition coefficients as $\alpha_i = P_i/P_{tot}$, we derive as follows:

$$P_{tot} = \sum_{i=1}^{n} P_i = \sum_{i=1}^{n} \alpha_i P_{tot} \tag{2.30}$$

$$\rightarrow \quad \sum_{i=1}^{n} \alpha_i = 1 \tag{2.31}$$

Therefore, we can derive:

$$\frac{P_i}{P_{i+1}} = \frac{\alpha_i}{\alpha_{i+1}} \tag{2.32}$$

So, if we consider Eq. 2.31 and Eq. 2.32 with $i = 1, ..., n-1$, we derive a full rank system:

$$\begin{cases} \sum_{i=1}^{n} \alpha_i = 1 \\ \frac{P_1}{P_2} = 10^{\left(\frac{x_1 - x_2}{10}\right)} \\ \vdots \\ \frac{P_{n-1}}{P_n} = 10^{\left(\frac{x_{n-1} - x_n}{10}\right)} \end{cases} \tag{2.33}$$

The system in Eq. 2.33 can be much more conveniently rewritten in the matricial form for numerical implementation:

$$m_{1,j} = 1 \quad j = 1, ..., n \tag{2.34}$$

$$m_{j+1,j} = 1 \quad j = 1, ..., n-1 \tag{2.35}$$

$$m_{j+1,j+1} = -10^{\left(\frac{x_i - x_{i+1}}{10}\right)} \quad j = 1, ..., n-1 \tag{2.36}$$

$$m_{l,m} = 0 \quad l, m \text{ elsewhere} \tag{2.37}$$

$$M_{n\times n} = \begin{bmatrix} m_{11} & m_{12} & \cdots & m_{1n} \\ m_{21} & m_{22} & \cdots & m_{2n} \\ \vdots & \vdots & \ddots & \vdots \\ m_{n1} & m_{n2} & \cdots & m_{nn} \end{bmatrix}, \tag{2.38}$$

$$e_1 = [1, 0, ..., 0], \quad \boldsymbol{\alpha} = [\alpha_1, ..., \alpha_n] \tag{2.39}$$

$$\boldsymbol{\alpha} = \left[M^{-1}\right] \cdot e_1 \tag{2.40}$$

Total absorbed power

The generator is characterized by an internal impedance Z_{int}, and the system (cables, electrodes and body) is characterized by an impedance Z_{load}. Depending on the specific values of Z_{int} and Z_{load}, the overall power can span different values. Fig. 2.11 shows experimental results that are always confined between 200 Ω and 400 Ω. Therefore, these values can be assumed as the limiting bounds for the impedances at the different harmonics. For the current analysis, it is possible to consider the following assumptions:

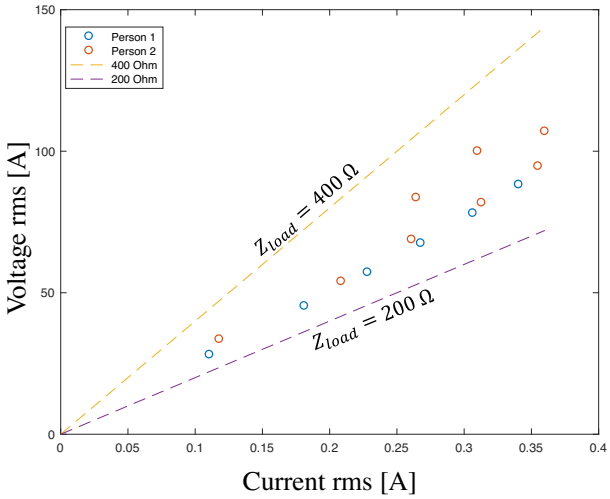

FIGURE 2.11: Impedance of the system under the therapeutic conditions.

- The imaginary components of the system can be neglected because they can be compensated electronically.
- The load impedance is fixed for all the harmonics. This assumption is well posed under the current therapeutic conditions, because the spectral power distribution is strongly decreasing monotonically. Therefore, the related error decreases proportionally.

We define the equivalent electrical circuit of the system as presented in Fig. 2.12. The input power

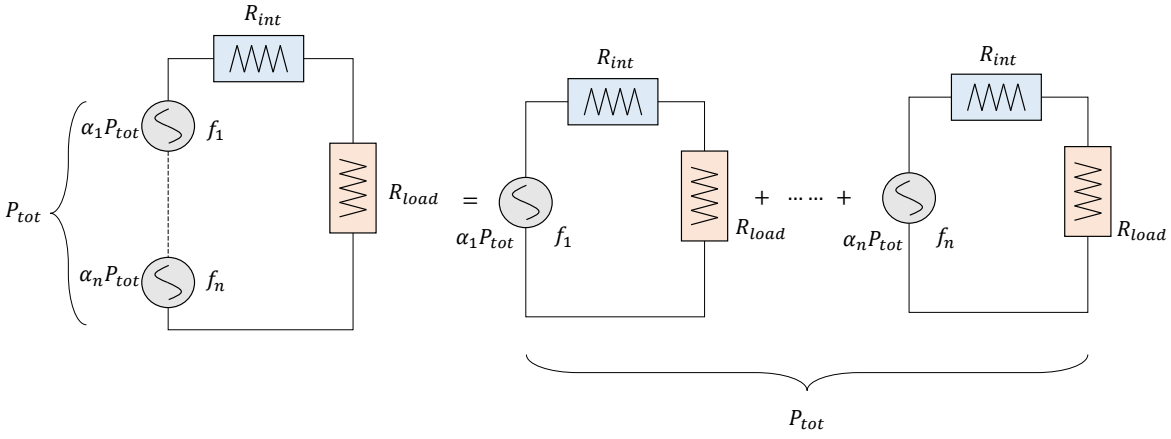

FIGURE 2.12: Equivalent linear electrical circuit to determine the transferred power.

can be derived as follows:

$$P_{load\ i} = \alpha_i P_{tot} \frac{4R_{load}R_{int}}{(R_{load}+R_{int})^2} \tag{2.41}$$

$$\sum_i P_{load\ i} = P_{abs} \tag{2.42}$$

$$\begin{aligned} \rightarrow \sum_i P_{load\ i} &= \sum_i \left[\alpha_i P_{tot} \frac{4R_{load}R_{int}}{(R_{load}+R_{int})^2} \right] \\ &= P_{tot} \frac{4R_{load}R_{int}}{(R_{load}+R_{int})^2} \sum_i \alpha_i \end{aligned} \tag{2.43}$$

$$\rightarrow P_{abs} = P_{tot} \frac{4R_{load}R_{int}}{(R_{load}+R_{int})^2} \tag{2.44}$$

The value of P_{tot} depends on the setting of the medical device, $R_{load} \in [200, 400]\ \Omega$ and R_{int} is given by the data-sheet of the medical device. Another important aspect that must be considered is the the the actual number of the implemented harmonics in the model (truncation). This evaluation is strictly related to the harmonic power. Assuming a tolerance threshold t_* (normalized), we can consider the following criterion to truncate the computation at the n_h-th harmonic.

$$n_h = \min(j), \quad j = 1, ..., n : \quad \sum_{i=1}^{n_h} \alpha_i \geq 1 - t_* \tag{2.45}$$

2.5 Results and discussion

2.5.1 Experimental validation

Validation was performed considering a truncated cone support made in agar gel, a real human eyeball on the top, and the generator Rexon-eye-2. The repartition coefficients were assumed as in the section 2.5.3 for the smaller load impedance. The truncated cone was characterized by height $h = 0.1$ m, bottom radius $r_{bottom} = 0.09$ m, equivalent top radius $r_{top} = 0.02$ m (this is related to the equivalent circular size of the eyelid electrode). The adopted agar support had dielectric permittivity $\epsilon_r = 450$, and the electrical conductivity was $\sigma_{agar} = 0.9$ S/m. The electrical resistance of the truncated cone can be computed as follows [28]:

$$R_{agar} = \frac{\rho_{agar} h}{\pi r_{top} r_{bottom}} \approx 16\ \Omega \tag{2.46}$$

Considering equation 2.44, and assuming the experimental conditions: power level of 7 over a full-scale of 10, with maximum power supply of 80 W, and duty-cycle of 0.5

$$P_{abs} = P_{tot}\frac{4R_{load}R_{int}}{(R_{load}+R_{int})^2} \approx 56\frac{4\cdot 16\cdot 100}{(16+100)^2} \approx 27 \text{ W}$$

The value $P_{abs} = 27$ W is the input value for the overall deposited power in the thermal load. In Fig. 2.13 there are two pictures related the electromagnetic and the thermal models. Fig. 2.14 shows that the observations made experimentally were well numerically predicted, thus validating the model.

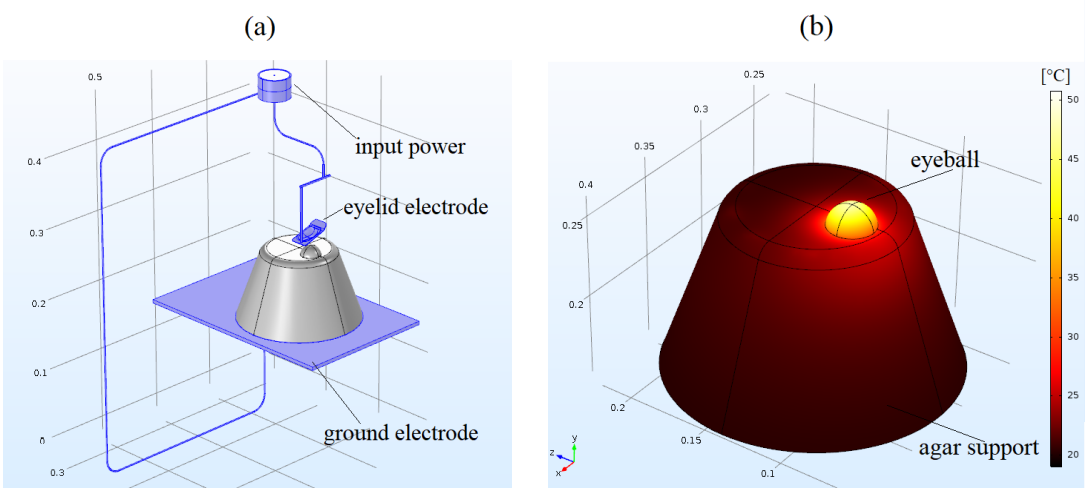

FIGURE 2.13: Implemented models: (a) Main elements of the electromagnetic simulation, (b) Main elements of the heat transfer simulation.

2.5.2 Patch applicator: reproduction of experimental trials

The purpose of this section is to analyze numerically the temperature and the SAR distributions within the eyeball, considering the therapeutic conditions of the experimental trials [16]. Two patch electrodes were applied close to each eye, one over the temporal area and one under the lower lid, and activated each of them for 60 seconds in sequence. The cycle was repeated 4 times, for a total stimulation length of 16 minutes. To determine the repartition coefficients, the power was experimentally measured in laboratory, using equivalent test-impedances $Z_{load} = 200\ \Omega$ and $Z_{load} = 400\ \Omega$. The harmonic distribution was provided by Rexon-eye-1. The results are reported in Table 2.1 and Table 2.2. The computation of the repartition coefficients derives from the resolution of the linear system presented in Eq. 2.40. The normalized cumulative error was estimated assuming $t_* = 0.05$. Fig. 2.15 shows that we must consider 4 harmonics for the impedance bound $Z_{int} = 200\ \Omega$ and 2 harmonics for

Ranking	Frequency [MHz] f	Power [dBm] x_i	Repartition coeff. [-] α_i	Absolute power [W] $P_i = \alpha_i P_{abs\ (200\ \Omega)}$
1	4.01	-24.94	0.7971	15.77
2	8.01	-33.96	0.0999	1.98
3	12.00	-38.18	0.0378	0.75
4	16.03	-39.04	0.0310	0.61
5	20.02	-41.98	-	-
6	24.01	-42.18	-	-
7	32.00	-49.35	-	-
8	3.19	-63.88	-	-
9	28.07	-65.45	-	-
10	2.43	-66.42	-	-
11	6.36	-67.46	-	-
12	14.11	-67.46	-	-
13	17.05	-67.61	-	-
14	24.51	-67.82	-	-
15	19.23	-67.88	-	-
16	33.88	-68.25	-	-
17	21.27	-69.18	-	-
18	18.27	-69.50	-	-
19	6.55	-69.71	-	-
20	10.05	-69.76	-	-

TABLE 2.1: Ranking and specific power for each harmonics utilizing a test-impedance $Z_{load} = 200\ \Omega$, Rexon-eye-1 and the patch applicator. The missing values can be neglected following the criterion expressed in Eq. 2.45.

Ranking	Frequency [MHz] f	Power [dBm] x_i	Repartition coeff. [-] α_i	Absolute power [W] $P_i = \alpha_i P_{abs\ (400\ \Omega)}$
1	4.01	-19.62	0.8758	19.49
2	8.01	-29.24	0.0956	2.13
3	12.00	-37.14	-	-
4	15.99	-42.54	-	-
5	20.02	-42.97	-	-
6	24.01	-43.86	-	-
7	32.03	-48.70	-	-
8	3.39	-65.55	-	-
9	20.48	-65.71	-	-
10	33.42	-66.28	-	-
11	2.53	-67.65	-	-
12	22.66	-67.66	-	-
13	33.85	-68.14	-	-
14	5.30	-68.34	-	-
15	23.38	-68.43	-	-
16	28.14	-68.43	-	-
17	4.84	-68.47	-	-
18	10.18	-68.95	-	-
19	29.79	-69.26	-	-
20	32.72	-69.38	-	-

TABLE 2.2: Ranking and specific power for each harmonics utilizing a test-impedance $Z_{load} = 400\ \Omega$, Rexon-eye-1 and the patch applicator. The missing values can be neglected following the criterion expressed in Eq. 2.45.

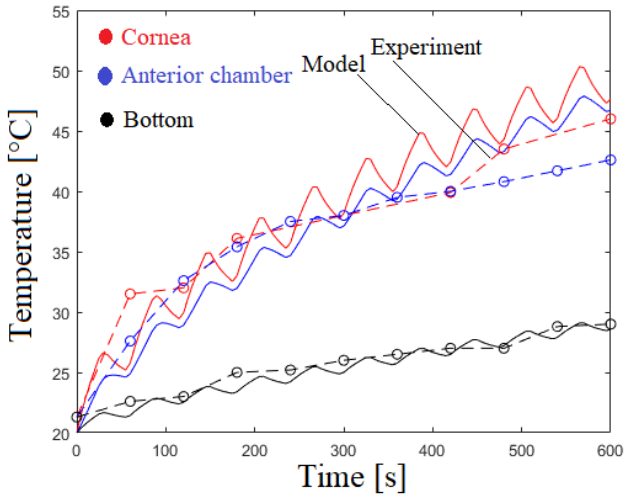

FIGURE 2.14: Comparison between the numerically predicted temperature evolutions at the corneal surface, at the anterior chamber, and at the bottom of the eyeball, with the measurements. Temperature was measured with 60 seconds of sampling time.

the impedance bound $Z_{int} = 400\ \Omega$. The rms current, the rms voltage, the power factor and the total supplied power from the generator was experimentally measured during the therapy: $I_{rms} = 190$ mA, $V_{rms} = 44.36$ V, $PF = 0.92$ and $P = V_{rms} \cdot I_{rms} \cdot PF \approx 7.8$ W. In Fig. 2.16, the geometry and the positioning of the patch electrodes were reported. Fig. 2.17 shows the superficial temperature at the the end of the treatment of the head and of the eyeball. Fig. 2.18 depicts the evolution of the maximum temperature and minimum temperature over time. The histograms presented in Fig. 2.19 report the Specific Absorption Rate (SAR) of all the tissues forming the eye: cornea, lens, sclera wall and aqueous humor. The results show that the therapy induced very limited overheating since the maximum temperature within the eyeball was below 39 °C. This value is compatible with the perception of the treated patients, considering that they were able to feel the heating with no associated pain. We can observe in Fig. 2.18 that the therapy did not achieve the thermal steady state, thus for longer stimulation, given the clinical conditions of the experimental trials, the temperature increases further. Fig. 2.19 shows the SAR levels of the elements forming the eye: cornea, lens, sclera wall and aqueous humor. The minimum, the most frequent level and the maximum were respectively in W/kg: $\{6, 6, 19\}$ for cornea, $\{6, 6, 10\}$ for lens, $\{4, 10, 80\}$ for sclera wall and $\{6, 11, 58\}$ for aqueous humor.

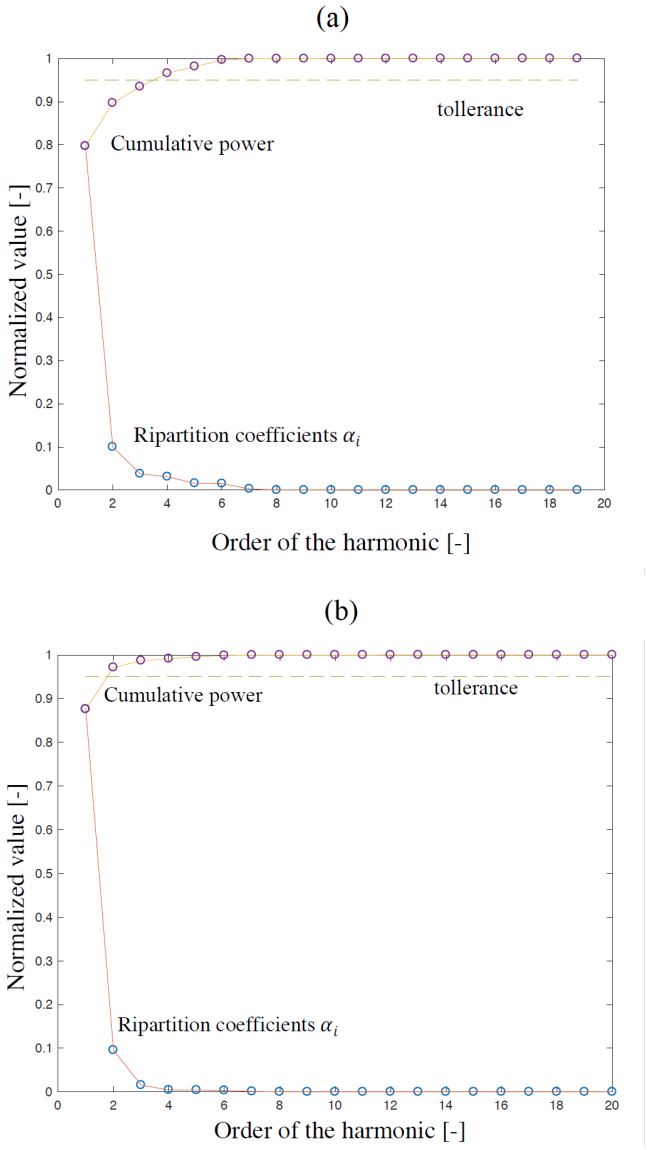

FIGURE 2.15: Ripartition coefficients and cumulative power for the patch applicator case: (a) $Z_{int} = 200\ \Omega$, (b) $Z_{int} = 400\ \Omega$.

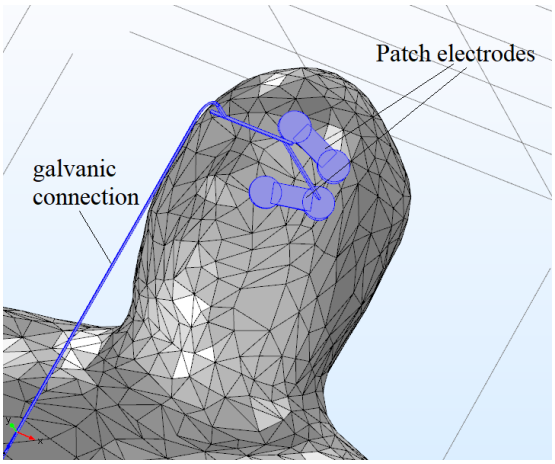

FIGURE 2.16: Representation of the implemented geometry of the patch applicator.

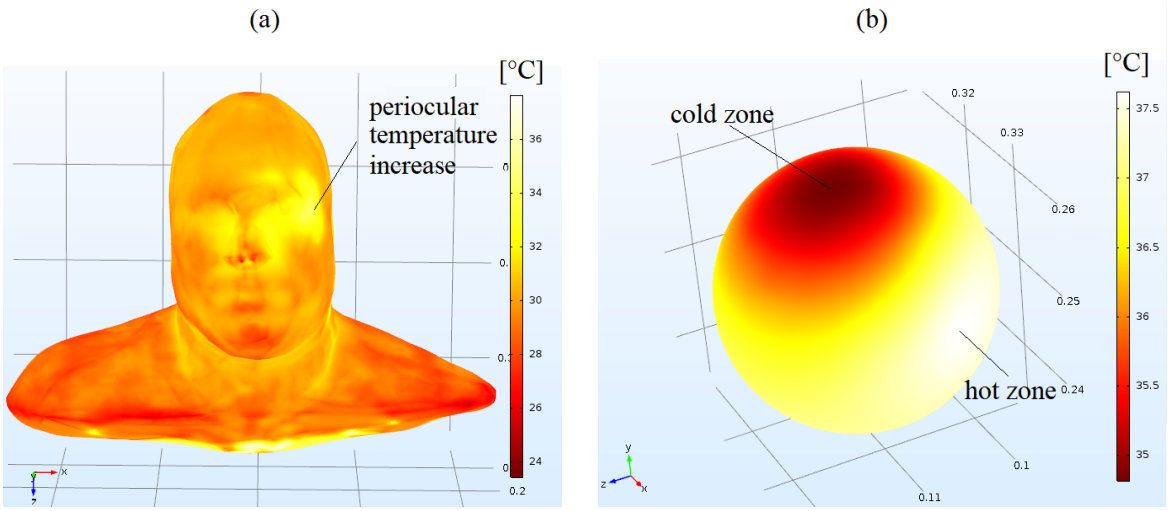

FIGURE 2.17: Superficial temperature related to the treatment with the patch applicator, after 960 seconds, with total absorption of 8 W and duty-cycle of 0.5: (a) head and neck, (b) eyeball.

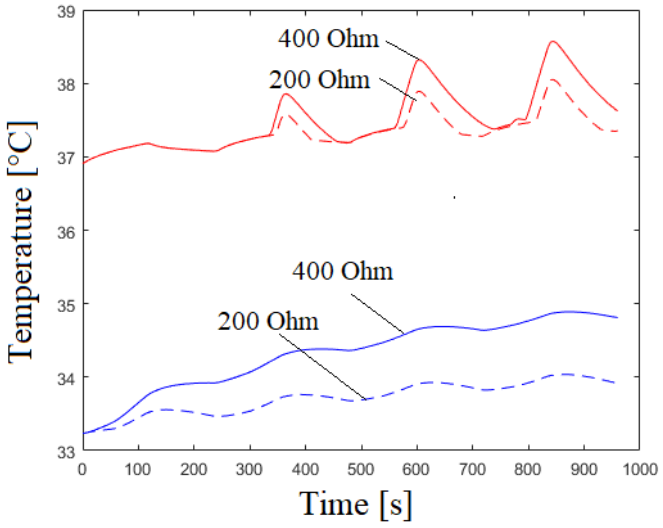

FIGURE 2.18: Maximum and minimum temperature, given the tested clinical conditions in [16]. The bounds are related to the load impedance variability which can span values in the range $[200, 400]\Omega$.

2.5.3 Eyelid applicator: sensitivity analysis

The current analysis has been performed considering the generator Rexon-eye-2 as the power supplier. The maximum temperature within the eyeball was computed in relation to different levels of the applied power. Indirectly, this analysis determines the maximum acceptable power, given a fixed maximum temperature. The power distributions were experimentally measured in laboratory, using the equivalent test-impedances $Z_{load} = 200\ \Omega$ and $Z_{load} = 400\ \Omega$. The distributions are reported in Table 2.3 and Table 2.4. The repartition coefficients are computed solving the linear system presented in Eq. 2.40. The results are reported in Fig. 2.20. Fig. 2.20 shows that we must consider 7 harmonics for the impedance bound $Z_{int} = 200\ \Omega$ and 4 harmonics for $Z_{int} = 400\ \Omega$. Since this is a precautionary analysis, we make the following assumptions hold:

- The generator is matched ($Z_{int} = Z_{load}$): maximum power transfer condition.
- The entire power is deposited into the head region. In general, depending on the shapes of the electrodes, the absorbed power is divided in two regions: around the applicator, and around the ground electrode.

The maximum output power of the analysis was 20 W. This value was modulated by a factor l ($l \in [0, 1]$). The considered stimulation had a duty cycle of 0.5 and a cycle-period of 1 minute (30 seconds

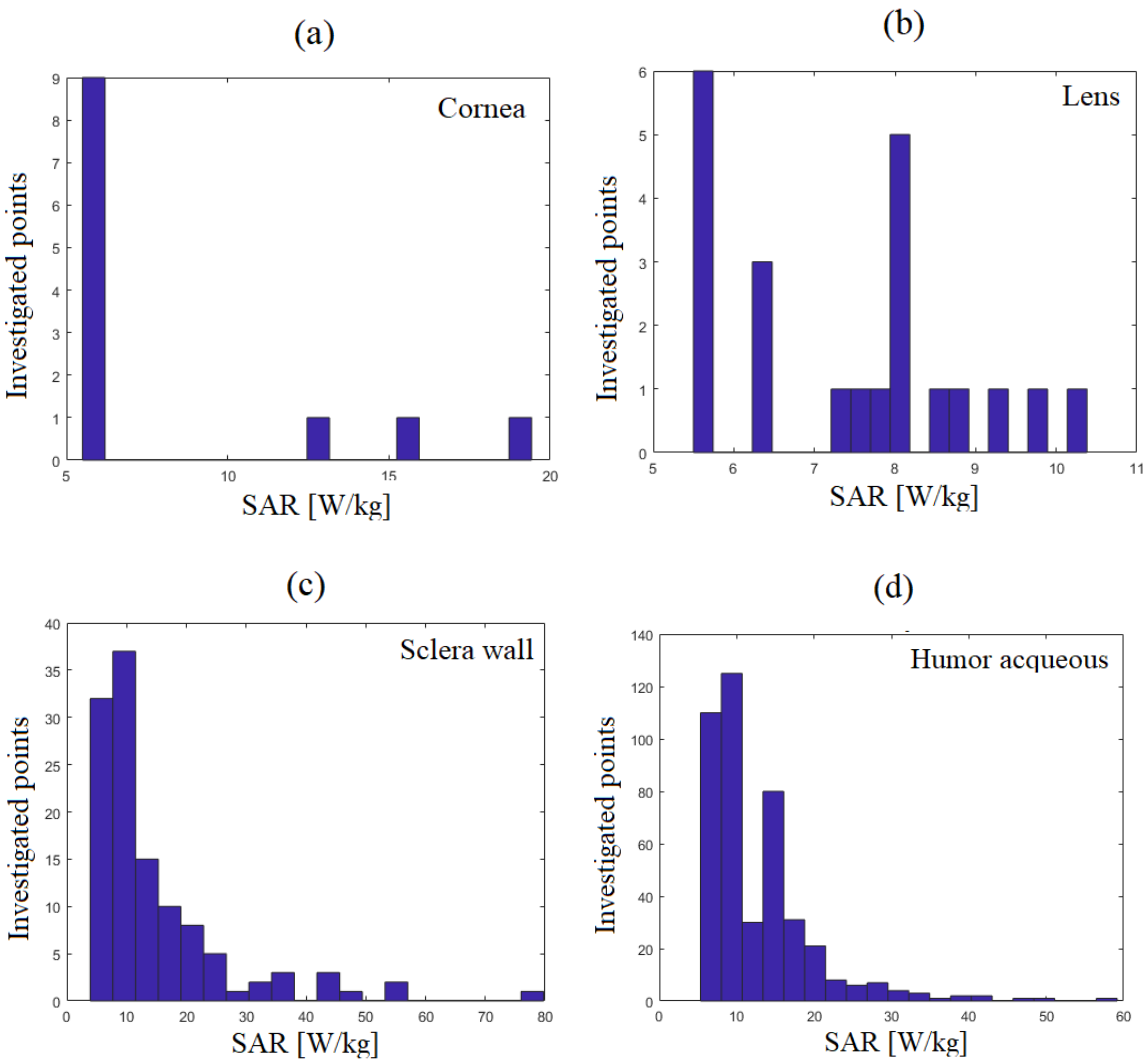

FIGURE 2.19: Specific Absorption Rate (SAR) in the main elements composing the eyeball.

Ranking	Frequency [MHz] f	Power [dBm] x_i	Repartition coeff. [-] α_i	Absolute power [W] $P_i = \alpha_i P_{abs\ (200\ \Omega)}$
1	16.01	-20.95	0.3340	$l \cdot 23.75$
2	8.02	-22.70	0.2229	$l \cdot 15.85$
3	4.02	-23.53	0.1844	$l \cdot 13.11$
4	12.02	-26.47	0.0937	$l \cdot 6.66$
5	20.01	-28.23	0.0624	$l \cdot 4.44$
6	35.99	-29.88	0.0427	$l \cdot 3.04$
7	24.00	-32.14	0.0254	$l \cdot 1.81$
8	40.04	-32.37	-	-
9	32.00	-39.12	-	-
10	28.00	-39.68	-	-
11	44.04	-50.09	-	-
12	48.03	-51.88	-	-
13	52.03	-53.76	-	-
14	21.63	-62.80	-	-
15	21.74	-63.52	-	-
16	14.01	-63.55	-	-
17	17.52	-64.85	-	-
18	17.42	-65.70	-	-
19	19.04	-66.28	-	-
20	18.71	-66.36	-	-

TABLE 2.3: Ranking and specific power for each harmonics utilizing a test-impedance $Z_{load} = 200\,\Omega$, Rexon-eye-2 and the eyelid applicator. The missing values can be neglected following the criterion expressed in Eq. 2.45.

Ranking	Frequency [MHz] f	Power [dBm] x_i	Repartition coeff. [-] α_i	Absolute power [W] $P_i = \alpha_i P_{abs\ (400\ \Omega)}$
1	8.02	-19.95	0.4446	$l \cdot 22.76$
2	4.02	-21.91	0.2826	$l \cdot 14.47$
3	16.01	-24.94	0.1406	$l \cdot 7.20$
4	12.02	-26.98	0.0881	$l \cdot 4.51$
5	20.01	-32.84	-	-
6	24.00	-38.10	-	-
7	36.05	-38.86	-	-
8	40.04	-39.19	-	-
9	28.00	-43.74	-	-
10	32.05	-47.52	-	-
11	47.98	-49.49	-	-
12	51.98	-53.45	-	-
13	43.98	-60.75	-	-
14	17.96	-70.40	-	-
15	17.31	-71.11	-	-
16	18.82	-71.21	-	-
17	19.04	-72.27	-	-
18	18.39	-72.73	-	-
19	18.50	-72.72	-	-
20	18.28	-72.79	-	-

TABLE 2.4: Ranking and specific power for each harmonics utilizing a test-impedance $Z_{load} = 400\,\Omega$, Rexon-eye-2 and the eyelid applicator. The missing values can be neglected following the criterion expressed in Eq. 2.45.

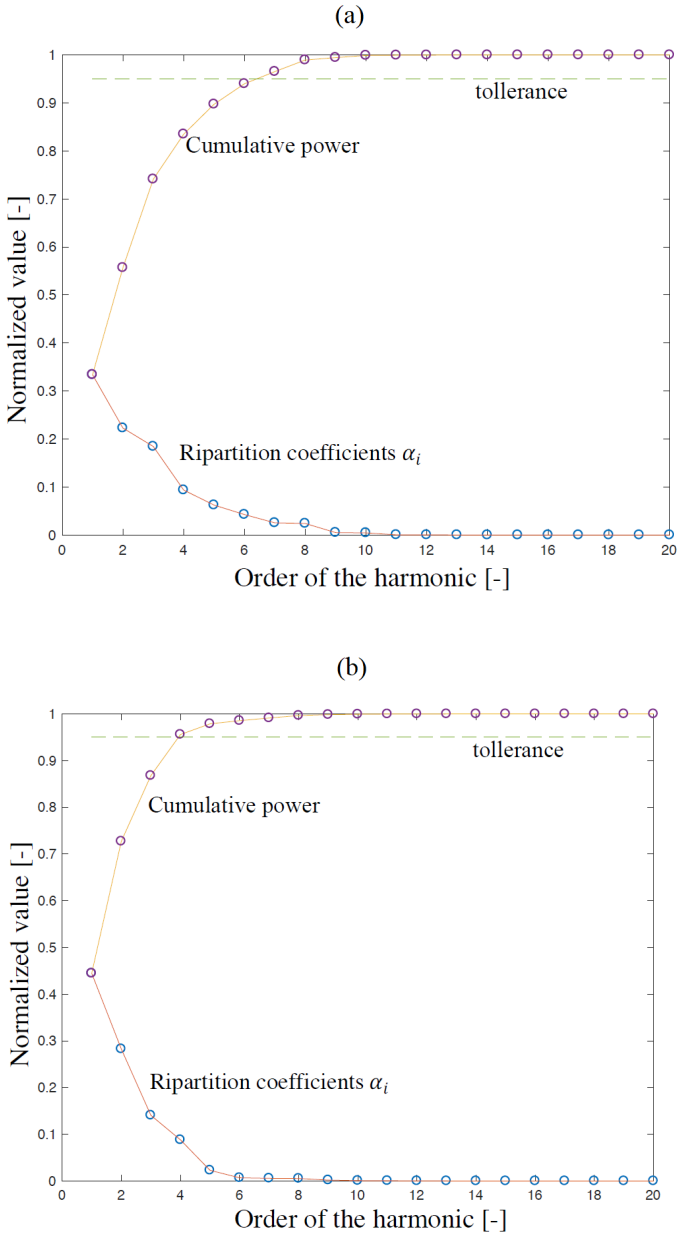

FIGURE 2.20: Repartition coefficients and cumulative power for the patch applicator case: (a) $Z_{int} = 200\ \Omega$, (b) $Z_{int} = 400\ \Omega$.

on and 30 seconds off). The analysis was done over the time domain of 1200 seconds. In Fig. 2.21, the geometry and the positioning of the patch electrodes are reported. Fig. 2.22 shows the superficial temperature of the head and of the eyeball, after 16 minutes of treatment. Fig. 2.23 shows the evolution of the maximum temperature for five power levels: 4 W, 8 W, 12 W, 16 W and 20 W. From

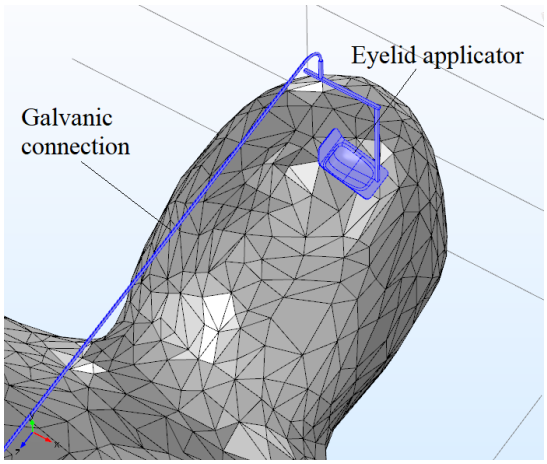

FIGURE 2.21: Representation of the implemented geometry of the eyelid applicator.

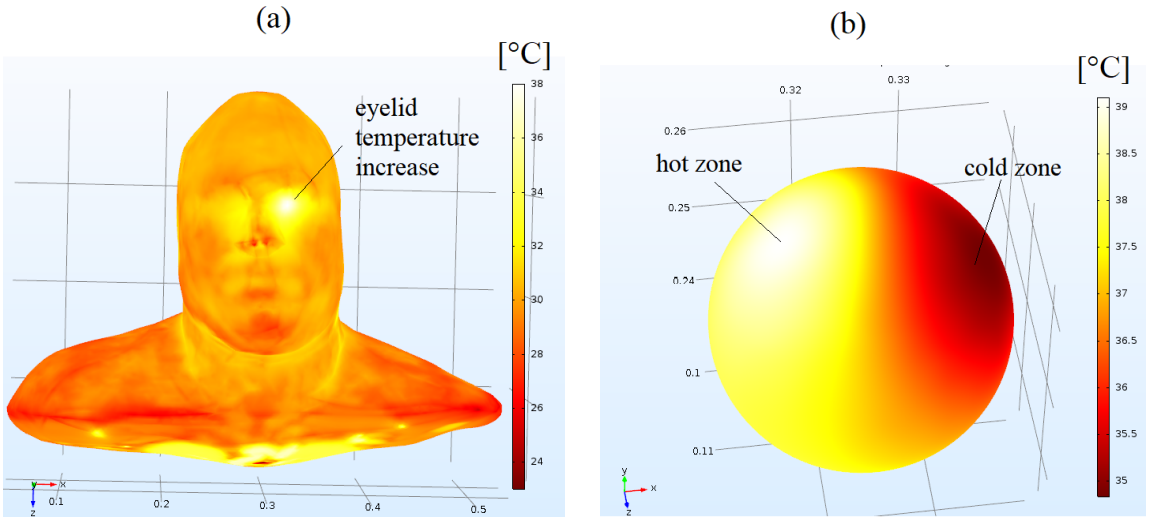

FIGURE 2.22: Superficial temperature related to the treatment with the eyelid applicator, after 960 seconds, with total absorption of 8 W: (a) head and neck, (b) eyeball.

the results, when the power level is higher than 8 W, then the overheating can be dangerous for time periods around 20 minutes. Considering a power level of 12 W, the maximum temperature achieves 42 °C which can induce cataracts and other side-effects. In case of shorter stimulation periods, higher power levels can be considered. The optimal therapeutic setting must be determined based on medical

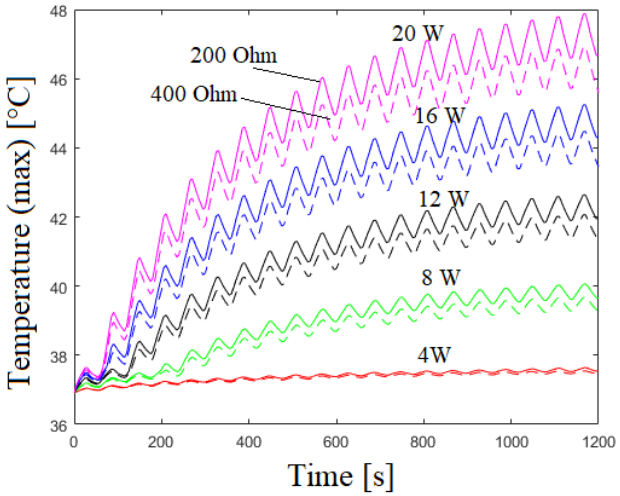

FIGURE 2.23: Maximum temperature within the eyeball in different cases of overall deposited power in the head: 4 W, 8 W, 12 W, 16 W and 20 W.

evaluations, and using Fig. 2.23 as reference for the maximum induced temperature. In order to obtain a reference-data plot and a reference-chart, it is more convenient to depict the results as presented in Fig. 2.24 and Tab.2.5. The results can be utilized by the physicians to define optimal intensity and length of the treatment under safe operative conditions.

2.6 Conclusions

From a methodological point of view, the work is based on the development of a numerical phantom, reconstructing geometry and material properties at several electromagnetic frequencies. The mathematical formulation was derived considering the specific conditions of the therapy. The model was experimentally validated ex-vivo, using a real eyeball and an agar-gel support. Then, the model was used to predict temperature and SAR in the elements forming the eye. Reproducing the tested clinical conditions in [16], the temperature within the eyeball never overpassed the value of 39°C, considering the effective transferred power of 7.8 W, with a duty-cycle of 0.5. New operative conditions are available in terms of intensity of the treatment and length of the treatment, under safe conditions that can be controlled "a priori". The results were derived through a sensitivity analysis, considering that the power level swept from 4 W to 20 and duty-cycle of 0.5, for a total period of 20 minutes. Clinical evaluations made by the physicians, combined with the here presented thermal constraints in terms of

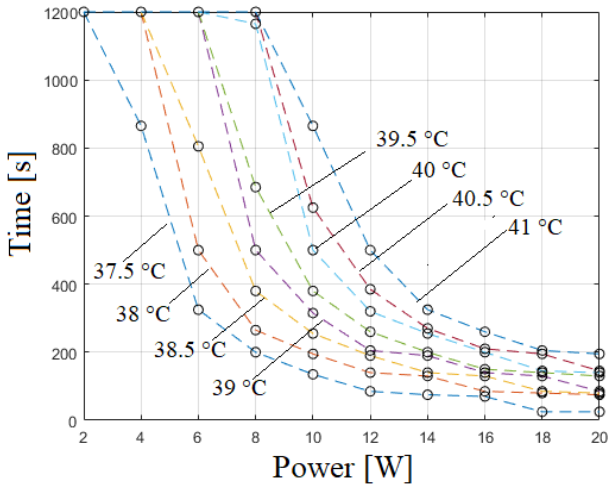

FIGURE 2.24: Given fixed values of acceptable maximum temperature, the corresponding power-time curves of stimulation are reported. The adopted duty cycle to derive the data in this chart is 0.5.

Power	2 W	4 W	6 W	8 W	10 W	12 W	14 W	16 W	18 W	20 W
Temperature					Time [s]					
37.50 °C	1200	865	325	200	135	85	75	70	25	25
37.75 °C	1200	1200	380	210	145	130	85	80	75	70
38.00 °C	1200	1200	500	265	195	140	130	85	80	75
38.25 °C	1200	1200	565	320	200	145	135	90	80	75
38.50 °C	1200	1200	805	380	255	190	140	130	85	80
38.75 °C	1200	1200	1045	390	260	200	145	135	90	85
39.00 °C	1200	1200	1200	500	315	205	190	140	130	85
39.25 °C	1200	1200	1200	565	325	255	195	145	135	130
39.50 °C	1200	1200	1200	685	380	260	200	150	140	130
39.75 °C	1200	1200	1200	810	440	270	205	195	140	135
40.00 °C	1200	1200	1200	1165	500	320	255	200	145	140
40.25 °C	1200	1200	1200	1200	560	330	260	200	190	140
40.50 °C	1200	1200	1200	1200	625	385	270	210	195	145
40.75 °C	1200	1200	1200	1200	740	440	320	255	200	150
41.00 °C	1200	1200	1200	1200	865	500	325	260	205	195

TABLE 2.5: Reference chart to define the time extension of the stimulation, given the maximum temperature rise and the power setting from the generator, with duty cycle of 0.5.

total electromagnetic deposited energy into the body, can improve the efficacy of the electromagnetic stimulation, giving the possibility to define new protocols.

3 Novel Efficient Strategy to Design an Optimized Microwave Shield

3.1 Abstract

In this paper a novel approach to numerically design a MW shield is proposed. The strategy is based upon the interplay between a reduced model, formed by three periodical elements "teethes" in a waveguide, and a full model composed by an entire shield, a metallic cavity and the open space. A correlation criterion is implemented to avoid the divergence between the physical responses of the models. In order to save computational time, evaluation of less influent design variables is included, and a pre-optimization is performed. The compact range method has been experimentally applied to test the optimized MW shield. A comparison between computed and measured EM leakages is presented and discussed. Measured scattering parameter S_{21} is lower than -30 dB over the ISM frequency band, confirming the adequacy of the strategy.

3.2 Introduction

The first patent of a MW shield has been made in 1950, and the first paper was published in 1956 [29]. From that period on, many other publications and patents have been derived improving the shielding capability. Recently, issues related to EM risks for public health have been increasingly concerned about. An in-depth study of the thermal effects caused by the exposure to a microwave oven can be found in [30], also induced thermal effects inside the human body, due to EM radiation is analyzed in [31]. Actually, the effectiveness of the shielding is due to a trade-off between computational velocity and required precision to calculate the leakages. Similar problems are involved in fields not directly related to MW shield design. An interesting work shows the possibility to apply reduced modal analysis techniques for electromagnetic calculations, typically used in structural mechanics [32]. Also,

simplification of FEM and Finite Difference Time Domain (FDTD) models, limited by certain hypothesis on the geometry but including non-linearity of materials, can be found in [33]. Moreover, many efforts have been devoted to model order reduction like in [34], especially in the field of control theory. Up to date, advanced design strategies to develop MW shields are based, on the one hand, upon the optimization of a periodic element "teeth", reducing the computational complexity, but not considering the full extent of the device; on the other hand, upon the implementation of accurate and complete models, especially using FDTD algorithms, but not primary concerning the computational burden [35]. An intrinsic difficulty that must be faced for MW shield designing, regards the achievement of precise computation with small mesh elements in the air-gap regions, but these elements are extended onto a very long border. In this paper a novel cost-effective strategy to design MW shields has been formally considered, eliminating less influent design variables, pre-optimizing a reduced model, which is related to a full one by a correlation criterion, and then centering the research domain at a pre-optimized setting of parameters. Experimental validation has confirmed the reliability of this novel algorithmic strategy.

3.3 Design process as a formal problem

Let us assume that we want to design a device, whose performances are maximized when a functional y is made as small as possible. The device is characterized by a series of parameters $\boldsymbol{x} = [x_1, ..., x_n]$ with the design constraints $\boldsymbol{x_{min}} = [x_{min\ 1}, ..., x_{min\ n}]$, $\boldsymbol{x_{max}} = [x_{max\ 1}, ..., x_{max\ n}]$, while Δx_i is the investigation step and $i = 1, ..., n$. The domain of the analysis is defined by a series of intervals $D_j = [d_{min\ 1}, ..., d_{min\ n}]$ where $j = 1, ..., m$, $\Delta d_j$is the analysis domain step and $\boldsymbol{d} = d_1, ..., d_m$ is the general domain vector. The central vectors of the considered system are $\boldsymbol{x_0}$ and $\boldsymbol{d_0}$. The influence of $\boldsymbol{x}$ on the physical quantity y is evaluated by the scalar function $h : \mathbb{R}^{n+m} \rightarrow \mathbb{R}$, $y = h(\boldsymbol{x}, \boldsymbol{d})$. First, a preliminary evaluation of the sensitivity of each x_i is computed as reported in Table 3.1. Sensitivity function indicates how a specific design variable influences the functional, considering all the fixed design ranges for any variable, after normalization: Once the model has been defined, we have to create a simpler and more compact model, which has to maintain a similar physical behavior of the previous one. The new model can be mathematically represented by $\tilde{y} = \tilde{h}(\boldsymbol{x}, \boldsymbol{d})$. the reduced model must satisfy a correlation condition that can be computed in three steps as presented in Table 3.2. When the correlation condition is satisfied, a parametrical sweep analysis or an algorithmic optimizer,

Sensitivity-chart computation

Action	Object	Condition	Note
evaluate	$H^j(\boldsymbol{x_j}) = h^j(\boldsymbol{x_{0j}}, \boldsymbol{d})$	$\boldsymbol{x_{oj}} = \boldsymbol{x_o}$	$\boldsymbol{x_{oj}}(j)$ is free
find	$H^j_{min}, H^j_{max}, \langle H^j \rangle$		
compute	$C^j = (H^j_{max} - H^j_{min})/\langle H^j_{max} \rangle$		
sort	C^j		high $\rightarrow$ low

TABLE 3.1: This computational procedure has to be performed with $j = 1, ...m$.

Correlation condition

Action	Object	Condition	Note
evaluate	$\nabla h = \left[\frac{\partial h}{\partial x_n}, ..., \frac{\partial h}{\partial x_1}\right]$ $\nabla \tilde{h} = \left[\frac{\partial \tilde{h}}{\partial x_1}, ..., \frac{\partial \tilde{h}}{\partial x_n}\right]$	$\boldsymbol{x} = \boldsymbol{x_o},\ \boldsymbol{d} = \boldsymbol{d_o}$	
compute	$\boldsymbol{J_1} = sgn(\nabla h), \boldsymbol{J_2} = sgn(\nabla \tilde{h})$		
check if	$\boldsymbol{J_1} = \boldsymbol{J_2}$		$\rightarrow$ ok

TABLE 3.2: The consistency between the models can be verified with this procedure.

as deeply and extensively described in [36] can be applied to the reduced model. An optimal solution $\tilde{\boldsymbol{x}}_*$ of the simple model can be obtained, and it has to be used to create a full model of the device. This full model should be actually close to an optimum final design $\boldsymbol{x}_*$, reachable by a final low-cost computation. Two different computational strategies can be adopted in the optimization phase. On one hand, the acknowledgment of the relation between x and y can be the main scope itself; therefore a parametric sweep analysis should be applied. On the other hand, the main interest can be turned to the maximization of the performances, so an algorithmic optimizer should be preferred. In this work, a sweep analysis approach has been adopted. In case of numerous n and m the computation can be expensive, therefore only an algorithmic optimizer can be applied. When the reduced device is optimized, the optimization research domain of the full model is composed by an initial population, centered at the best reduced setting. The final design is achieved running two optimizations, the first one fast and approximated with many iterations, and the second one slow and accurate with very few iterations. A schematic representation of the overall decision algorithm is depicted in Fig. 3.1.

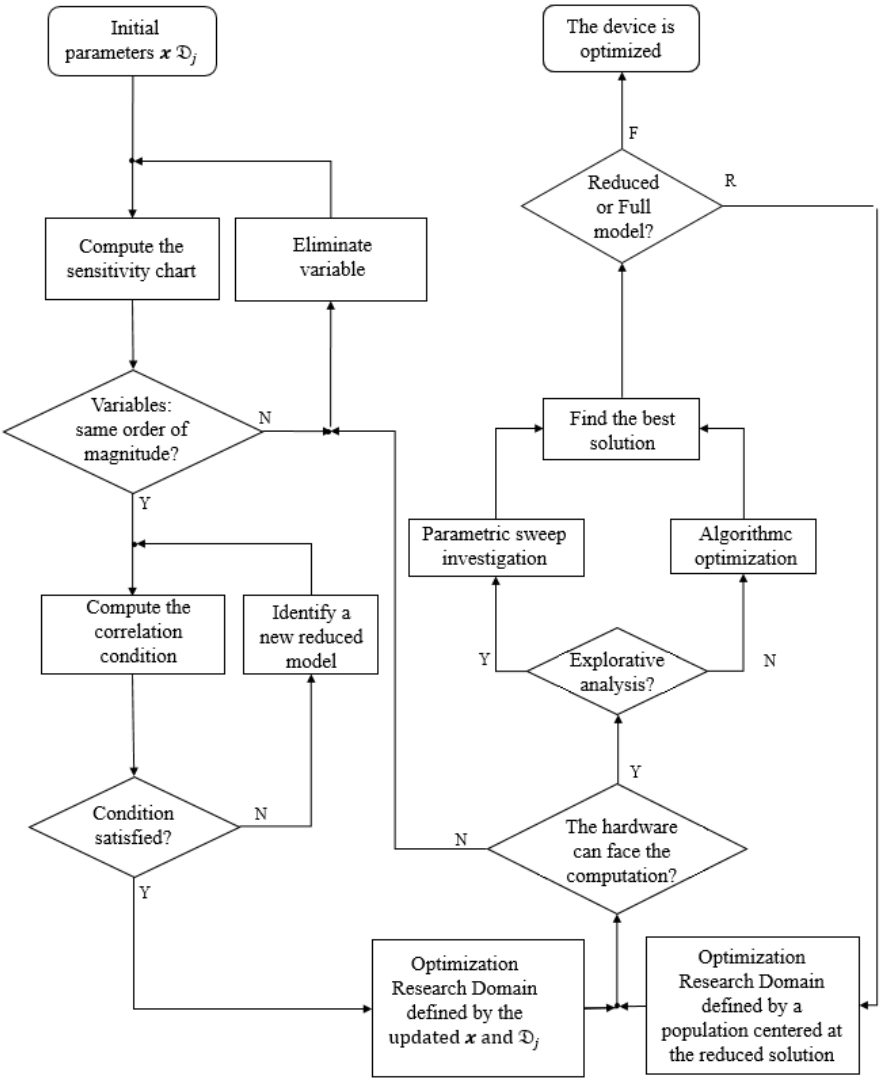

FIGURE 3.1: Decision algorithm in a flowchart form: computation of the sensitivity chart, reduced and full optimizations.

3.4 Implementation of the model

3.4.1 Physical setting

The governing Partial Differential Equations (PDEs) are the full Maxwell equations expressed in phasorial form. Reduced model: boundaries have been set as Perfect Electric Conductors (PEC), since the borders are made by a metallic waveguide. Defining metallic components as PEC is a good approximation in the MW frequency range [37]. Full model: boundaries have been defined by scattering condition to reproduce the radiation in open space. Usually, in EM propagation, the Perfect Matched Layer (PML) is implemented to facilitate the algorithmic convergence, but in this case the PML has not been included to avoid influencing S_{21}. Both models: the mean of propagation is air and the electromagnetic ports are rectangular, with EM mode TE_{10}. Implementing TE_{10} instead of representing the actual radiating antenna is an efficient technique, which does not affect the reliability of the model [38].

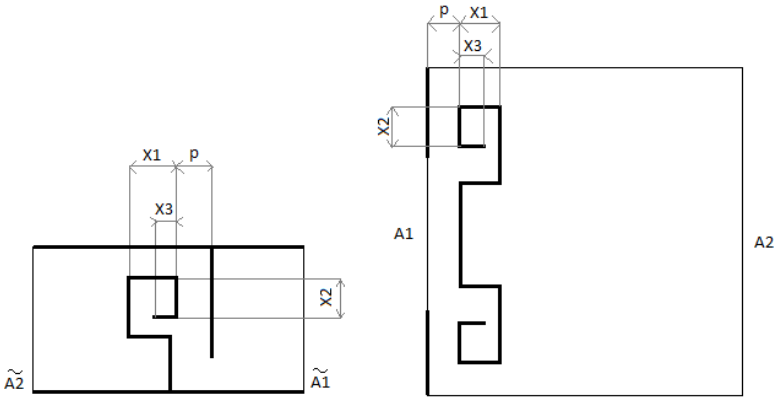

FIGURE 3.2: 2D-view schema of the reduced and full model of the systems on the (zy) cut-plane.

3.4.2 Parameters of the analysis and numerical results

In Fig. 3.2 we observe the 2D-views of the 3D reduced and full models. The EM input power crossings the input area $\tilde{A}_1$ is $P_1 = 2000$ W. The leakage is represented by P_2, going out from the surface $\tilde{A}_2$. The reduced response function is $y = \tilde{S}_{21} = \sqrt{P_2/P_1}$ which physically represents the scattering parameter between port 1 and 2. The reduced computational domain is $\tilde{\Omega}$, while the full

model is defined in Ω. The full response function can be computed as follows:

$$y = \sqrt{\left[\int_{A_2} \Re(\boldsymbol{E} \times \boldsymbol{H^*}) \cdot \hat{n}\, dA\right] / P_1} \tag{3.1}$$

The other parameters of the analysis have been set as $\boldsymbol{x} = [x_1, x_2, x_3]$, $\boldsymbol{x_{min}} = [30, 30, 5]$ mm, $\boldsymbol{x_{max}} = [50, 50, 15]$ mm, $\boldsymbol{x_0} = [35, 40, 10]$ mm, $f = d_1 \in D_1 = [902; 928]$ MHz (Industrial Scientific and Medical ISM frequency band), $p = d_2 \in D_2 = [3; 5]$ mm, $\Delta d_1 = 2$ MHz, and $\Delta d_2 = 1$ mm. The computed results are $\nabla \tilde{h} = [-3.89, -1.50, -2.88] \rightarrow \boldsymbol{J_1} = [-1, -1, -1]$ and $\nabla h = [-8.19, -4.42, -10.91] \rightarrow \boldsymbol{J_2} = [-1, -1, -1]$, therefore the correlation condition is satisfied. The computed sensitivity chart is presented in Table 3.3. We can observe that the design

Computed sensitivity chart for the design variables

j	$S_{21\ min}$	$S_{21\ max}$	$\langle S_{21} \rangle$	C^j
1	3.98×10^{-5}	2.09×10^{-8}	8.19×10^{-7}	3.32
2	1.43×10^{-1}	1.24×10^{-1}	6.14×10^{-2}	4.15
3	4.30×10^{-2}	2.99×10^{-2}	1.53×10^{-2}	4.02

TABLE 3.3: The appearing values derive from a preliminary parametric analysis to assess the impact on the scattering parameter for each design variable x_i.

variables have the same order of magnitude ($C^1 \approx C^2 \approx C^3$). Therefore, none of them can be neglected. Finally, after a parametric sweep optimization we have obtained the set of design variables $\tilde{x}_* = [26, 30, 5]$ mm, and the final close solution for the full model $x_* = [30, 28, 6]$ mm. In Fig. 3.3 we can observe the electric field distributions for the reduced and the full models at the condition of lower EM radiation, $p = 5$ mm, $f = 905$ MHz and $p = 4mm$, $f = 910$ MHz respectively. The views on the zy and xy planes show where eventual EM leakages are located. In Fig. 3.4 the objective functions for the reduced model, over the domain analysis D_1 and D_2, have been reported respectively. Over the entire ISM band $S_{21\ dB}$ is lower than -30 dB so it means that the shielding effect (SE) is higher than 99%, therefore the novel algorithmic design strategy has worked properly.

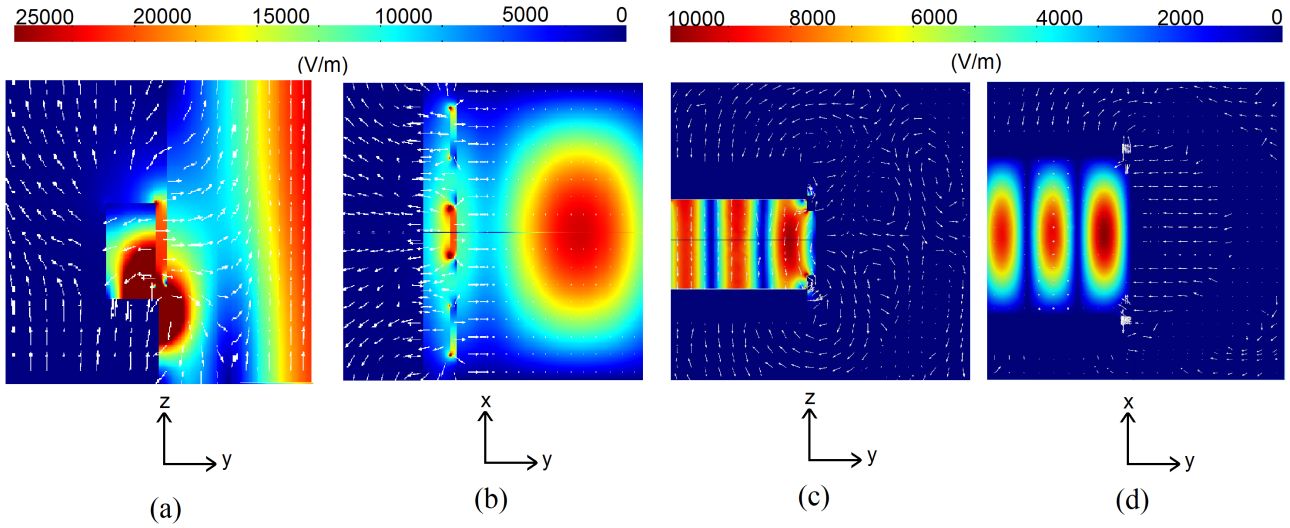

FIGURE 3.3: Electric field magnitude for different cut-planes on (zy) directions (a)-(c) and (xy) directions (b)-(d). The reduced model has been depicted in (a)-(b) while the full model in (c)-(d). The dark areas are the less subjected to EM radiation thanks to the effect of the shield.

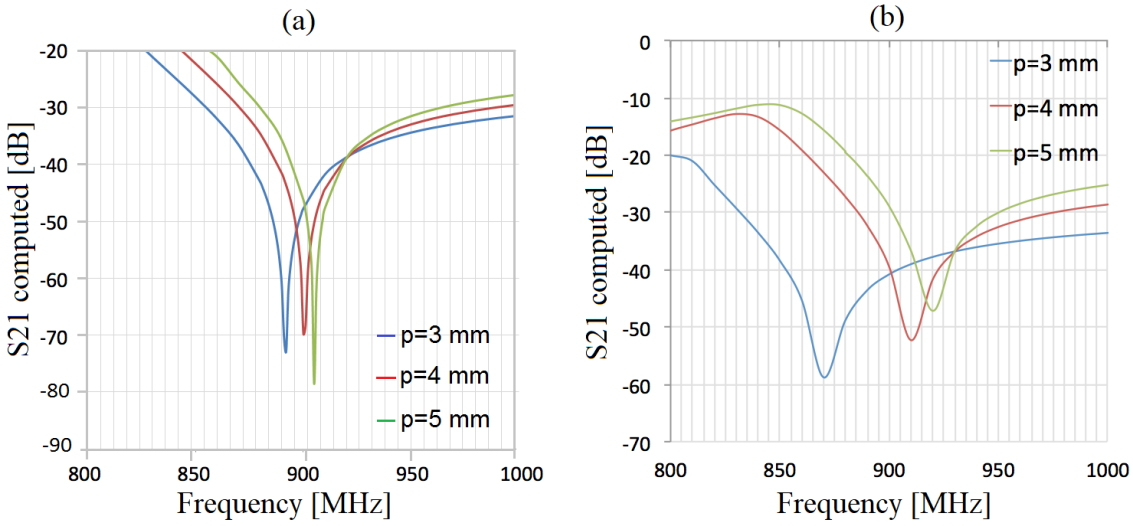

FIGURE 3.4: Reduced model (a) and full model (b): Objective function over the frequency domain parameterized by different values of p. The computation is made using FEM software.

3.5 EMI testing and validation

3.5.1 Experimental setup

In order to confirm the design and simulations, testing must be performed. A method that will give indications that the Device Under Test (DUT) will pass requirements at 3 or 10 meter range is to fabricate a compact range. The compact range must be large enough to measure only far-fields. The range must also be lined with absorbing material to attenuate reflections so only the "line of sight" measurements are made. Measurements can be conducted with a network analyzer to determine the attenuation or gain of the DUT or a signal generator-spectrum analyzer combination. The receive antenna is a wide band double ridge waveguide horn for frequencies greater than GHz and up to GHz. For receive antennas making measurements at frequencies lower than GHz patch antennas have been utilized, which are very space efficient. The experimental setup that has been prepared in laboratory has been reported in Fig. 3.5

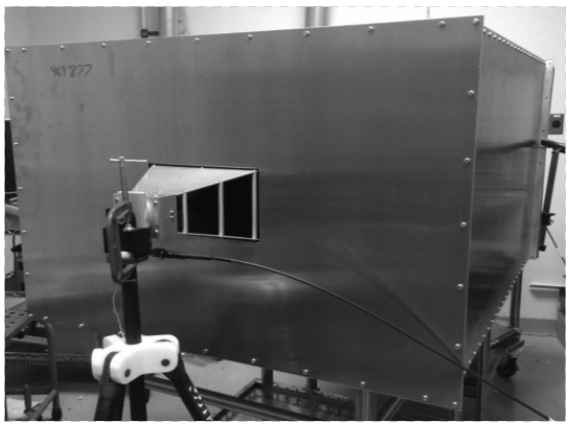

FIGURE 3.5: Experimental setup that has been implemented in laboratory to testing the actual performances of the microwave shield over the 912 MHz ISM band.

3.5.2 Discussion

The experimental measurements presented in Fig. 3.6 are compatible with the computed results, confirming the effectiveness of the computational strategy based on the reduced model analysis. The Shielding Effect (SE) is always lower than -30 dB in the ISM frequency band $[902; 928]$ MHz. The main difference between the computed results is related to the width of the shielding bands; the reduced model presents the narrowest band. The experimental curves are characterized by two minims instead of just one minimum of the computed curves. From Fig. 3.4 and Fig. 3.5 we observe that

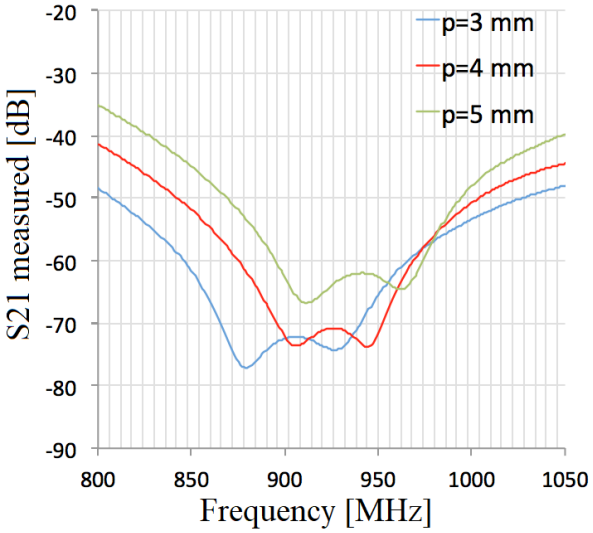

FIGURE 3.6: Experimental measurements obtained in the laboratory to verify the actual values of the scattering parameters over the analysis domain.

there is a specific frequency which induces the same SE independently from the air-gap size. The explorative analysis shows the possibility to obtain a shield able to satisfy the project requirements without any influence from the variable p. This phenomenon could be very interesting in order to develop new-generation shields, which maintain the same shielding capability at different air-gaps.

3.6 Conclusions

The application of the computational strategy presented in this work, successfully satisfied the required algorithmic performances: design effectiveness and low computational cost. The interplay between a reduced and a full model is a key point to adopt this novel design method; moreover the ease of implementation can be exploited creating a personalized homemade version of the presented strategy. The logical schema is quite general so the procedure can be extended to other types of devices. The only difficult aspect that has to be handled carefully regards the choice of the reduced model. If the device is formed by periodical elements (e.g. electrical machines, antennas, thermoelectric generators, etc.), the identification can be simple, but in general, the best choice of the reduced model can be less intuitive. Future developments can be done analyzing lower order reduced models in a multi-scale framework, but considering that the real challenge is to maintain the required computational resources as low as possible, in order to derive new strategies which can be broadly appealing

for the academic and the industrial sectors.

4 Influence of the Damage of a 2.45 GHz Microwave Choke: Electromagnetic and Thermal Evaluation on a 3D Human Body Phantom

4.1 Abstract

The purpose of this work is to evaluate the temperature rise in radiated human tissues under exposure from microwave oven. A realistic 2.45 GHz choke (which satisfies the international guidelines: 2 mW/cm^2 at 5 cm distance for a brand-new appliance) was considered, and the effects of the gradual damage of its hooks and hinges was evaluated over the frequency domain, assessing the actual response of the shielding capability. The analysis was conducted considering different absorbing masses inside the oven and different relative positions which influence the electromagnetic leakage. The maximum Specific Absorption Rate (SAR) and temperature rise in tissues were analyzed. Regarding the phantom, the spatial resolution is 3 mm and the material properties are defined by 40 different tissues and organs. An experimental analysis, using a Vector Network Analyzer, confirmed the main electromagnetic effects that are associated to the damage of hinges and hooks. The damage of the hinges and hooks determines the change of the frequency in correspondence to the peak of emission. Numerical and experimental evidences show that the peak tends to move toward lower frequency values as the damage increases. When the phantom was located at distances from the oven greater than 15 cm, the SAR level was under the ICNIRP basic restriction (for head and trunk) 2 W/kg even with displacements of the order of magnitude of 1 mm. The temperature increase was always below 0.1 °C.

4.2 Introduction

4.2.1 Historical view and state of the art

The most diffused high-power microwave technology is that one magnetron-based, for household appliances. The history of this technology for food heating purpose begins in 1955 when the first oven, produced by Taippan (later Westinghouse), was placed on the market under license from Raytheon. Actually, the capillary growth of sales appears 12 years later [39]. Soon, after the first phase of diffusion, scare of this technology spread over the general public [40]. Consequently, in order to improve the market-demand, new devices for the electromagnetic shielding have been developed by industries. Innovative techniques, not more based only on the mechanical contact of the walls, have been implemented. In particular, the most suitable shielding device was identified by the "choke", which is a door-seal structure that reduces electromagnetic emissions. An important proof of the improvement of shielding devices is the publication made by Osepechuk et al. where the most important successes on microwave oven safety achieved in the 70's were presented [41]. Starting from the 80's, but even more during 90's, the Information Technologies (IT) were subjected to a dramatic improvement. In particular, the wireless communication begun to play a fundamental role in the western countries. Need to reduce electromagnetic emissions became important not only for human body exposure but also for limiting interferences between devices [42]. In the end of 90's, international legislation on electromagnetic dosimetry at different frequencies have been created by scientific commissions and agencies. Relevant documentation was developed by ICNIRP [43] and Food and Drug Administration (FDA) [44]. An interesting publication, regarding the suitability of the commercial microwave ovens, has been done by Thansandate et al.; they collected a dataset of measured emissions from new and old microwave ovens, comparing the different levels of leakages. The survey included the effect of the food-masses inside the cavity and took into account the electric field intensity, but it did not include the body absorption of electromagnetic power neither thermal effects [45]. A similar analysis has been done by Alhekail Zo considering a larger and more various sample. The results showed that only a reduced portion of the considered ovens were actually out of the range defined by law [46]. So far, the emissions were quantified through evaluations of radiated power but the normative was turned not only to emitted leakages but even to Specific Absorption Rate (SAR). Consequently, need for accurate measurements of SAR appeared strongly. In 2004 Bangay et al. introduced an inovative experimental technique to measure SAR using a liquid-filled phantom with equivalent dielectric

properties of organic tissues [47]. A noteworthy work was conducted by Elder Ja, who focused onto the induced effects to eyes subjected to radiofrequency energy [17]. Regarding numerical analysis, Hirata et al., made a quantitative assessment of thermal effects at different frequencies [48]. A weakness of this work is that the leakage was not determined by a choke deficiency. Polarization and the confluence of the field lines were different with respect to real oven-emissions. Also, only the head has been implemented in the model, not considering the rest of the body trunk. In 2015 Peio Lopez-Iturri et al. have presented an in-depth analysis of oven-emissions in a complex scenario, considering both numerical and experimental aspects [30].

In the current work, a new analysis of the damage is implemented, considering the small displacements of the choke from the cavity due to mechanical slackness of hooks and hinges. The original contribution of this work is the assessment of SAR not only with a generic traveling plane-wave but considering a realistic 2.45 GHz choke, including the unavoidable effect of usage. The height and the relative distance of the phantom from the oven was considered. Temperature and SAR are reported and the actual influence of the different parameters under investigation is identified. Experimental testing was performed by measuring the scattering parameters of the system at the input port.

4.2.2 International guidelines and restrictions

International Commission on Non-Ionizing Radiation Protection

- Basic restrictions: Restrictions on exposure that are based directly on established health effects (e.g. current, specific energy absorption rate, power density).
- Reference levels: Levels that are provided whether the basic restrictions are exceeded under certain exposure conditions. These levels have been derived from direct measurements and computational techniques (e.g. electric field strength, magnetic field strength, magnetic flux density, power density).

Focusing only onto the range 100 kHz - 10 GHz, the main restriction parameter is SAR. The main effects at these frequencies are related to significant absorption of energy and temperature increases. From several studies, near-field exposure can induce high-local SAR. Separation distance between the radiating source and the exposed body can strongly influence the whole-body and local SAR. One of the most significant observations is that exposure for up to 30 minutes, under conditions in which whole-body SAR is less than 4 W kg^{-1}, can cause a body-temperature increase of less than

1°C. Therefore dividing this threshold value by a factor 10, the restriction value 0.4 W kg^{-1} provides a large safety margin for occupational exposure. An additional safety factor of 5 is whole-body SAR limit for exposure of the public, giving an average whole-body SAR limit of 0.08 W kg^{-1}. The final restrictions of SAR have been reported in Table 4.1. The related reference levels have

Exposure characteristics	Whole-body average SAR [W kg^{-1}]	Localized SAR head and trunk [W kg^{-1}]	Localized SAR limbs [W kg^{-1}]
Occupational	0.4	10	20
General public	0.08	2	4

TABLE 4.1: Basic restrictions for time varying electric and magnetic fields in the frequency range [2 GHz - 300 GHz]

been summarized in the Table 4.2, and they are referred to the undisturbed rms values. It has to be observed that the general public reference levels for electric and magnetic fields are lower by a factor 2.2 ($2.2 \approx \sqrt{5}$) than those set for occupational exposure.

Exposure characteristics	E-field strength [V m^{-1}]	H-field strength [A m^{-1}]	B-field [μT]	Equivalent plane-wave power density S_{eq} [W m^{-2}]
Occupational	137	0.36	0.45	50
General public	61	0.16	0.20	10

TABLE 4.2: Reference levels for time varying electric and magnetic fields in the frequency range [2 GHz - 300 GHz]

Food and Drug Administration

In the section 4.2.2 we have reported the restrictions based on scientific observations and analysis. In this section we report the Federal Regulation that is adopted in the United States of America, in order to have a normative reference. The legislation framework is referred to the frequencies assigned by the Federal Communications Commission in the ISM bands ranging from 890 MHz to 6 GHz. The first exposure requirement is about the power density limit: *The equivalent plane-wave power density existing in the proximity of the external oven surface shall not exceed 1 mW cm^{-2} at any point 5 cm or more from the external surface of the oven, measured prior to acquisition by a purchaser, and, thereafter, 5 mW cm^{-2} at any such point.* Moreover, the normative defines precisely the procedure that must be adopted for running the electromagnetic compatibility tests. In particular, there are indications about the load in terms of mass, the temperature, the position and shape: *Measurements*

shall be made with the microwave oven operating at its maximum output and containing a load of 275 +/- 15 mm of tap water initially at 20 +/- 5 °C placed within the cavity at the center of the load-carrying surface provided by the manufacturer. The water container shall be a low form 600 ml beaker having an inside diameter of approximately 8.5 cm and made of an electrically no-conductive material such as glass or plastic.

4.3 Materials and Methods

4.3.1 Numerical

The computational predictions have been done using Comsol Multiphysics 5.2 which is software based on Finite Element (FE) methods. The strategy that has been adopted is characterized by three main steps:

- Implementation of the FE model to analyze the leakage associated to the damage over a certain frequency band. The cavity is empty and without turntable.
- Comparison between predicted values and experimental observations.
- Numerical study of SAR and thermal effects on exposed human body. Several load masses are considered in the analysis.

The computational model is characterized by first-order shape functions. After mesh convergence analysis, the domain elements are 1201503, the boundary elements are 84996, the edge elements are 6329. Also, the number of degrees of freedom is 1337862. The used numerical solver is PARDISO which is suitable for solving large sparse symmetric linear systems of equations, in particular for distributed-memory multiprocessors. The used workstation for the computation is characterized by two processors, 16 cores Intel(R) Xeon(R) CPU E5-2620 v4 working at clock frequency 2.10 GHz and the RAM memory is 256 GB.

4.3.2 Experimental

The experimental setup was composed by a Vector Network Analyzer (VNA) which was connected to the cavity by mean of a coaxial cable and a type N connector after the remotion of the magnetron, as presented in Fig. 4.1. The magnetron slot was carefully insulated to avoid overestimation of the

leakage before analyzing the scattering parameter S_{11}. Metallic tape was applied to maximize the insulation of the connector. The analysis was performed at signal-level (low power) considering the

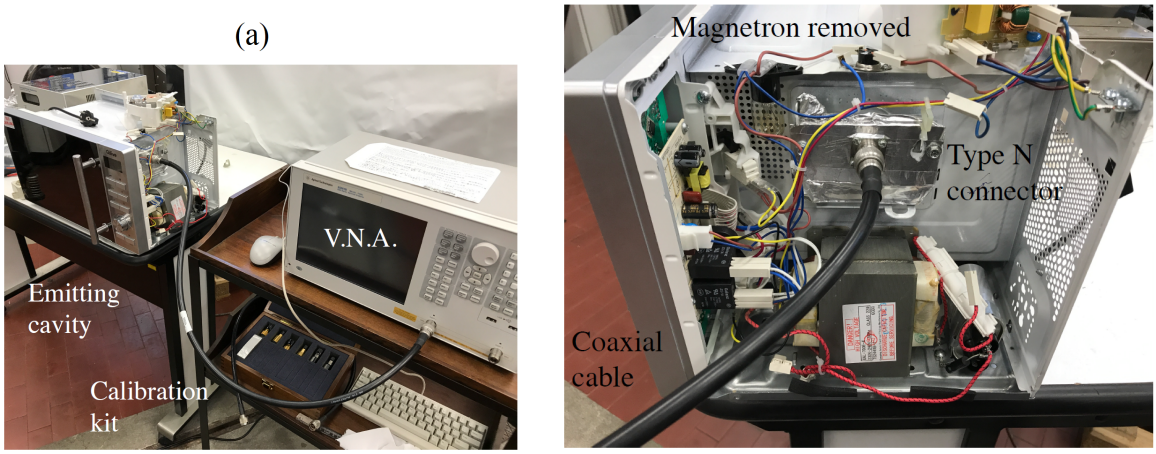

FIGURE 4.1: (a) Experimental setup used to evaluated the scattering parameter S_{11} of the cavity. (b) Substitution of the magnetron with a type-n connector which is connected to the Vector Network Analyzer.

following procedure:

- Identification of the frequency in correspondence to the resonant emission-peak.
- Restriction of the analysis, centering the band at the frequency-peak.
- Change of leakage conditions by introducing a spacer.

Depending on the actual length of the wedge-spacer that is introduced it is possible to create an artificial linear increase of the air-gap choke cavity. The oven is QILIVE Q.5645 / 875162 characterized by a 700 W magnetron, main dimensions 49.6 x 29.2 x 35.4, volume capacity 20 L, and connection hinges/hooks on the lateral sides. The VNA is Agilent Technology model n. E5061B ENA series, designed for the operative frequency band 100 kHz - 3 GHz.

4.4 Finite Element modeling of exposure on human body

The numerical model that has been developed in the current work is characterized by a realistic 2.45 GHz shielding choke and an exposed human body phantom. Regarding the choke, the effect of gradual damage of the hooks has been investigated considering the induced air-gap between the choke and the cavity. Regarding the human body phantom, a full 3D non-homogeneous model has been analyzed including the strong material non uniformity related to 40 organic tissues.

4.4.1 Non-uniformity of the organic tissues composing the phantom

The list of the material properties used in the model has been reported in Table 4.3 and Table 4.4. Regarding the reconstruction of the 3D phantom, the reader is addressed to the chapter 2. The topology of the tissues and organs derives from the database of the Visible Human Project and IT'IS Foundation [18, 49].

4.4.2 Modeling the damage

In the current analysis we consider the case of an oven door which is characterized by the presence of hinges and hooks on the lateral sides. If we include the effect of the gravity force, slackness of hinges and hooks, we can define several possible door-displacements due to appliance aging as presented in the Fig. 4.2. Considering that the structure of the hinges opposes the displacements along the vertical

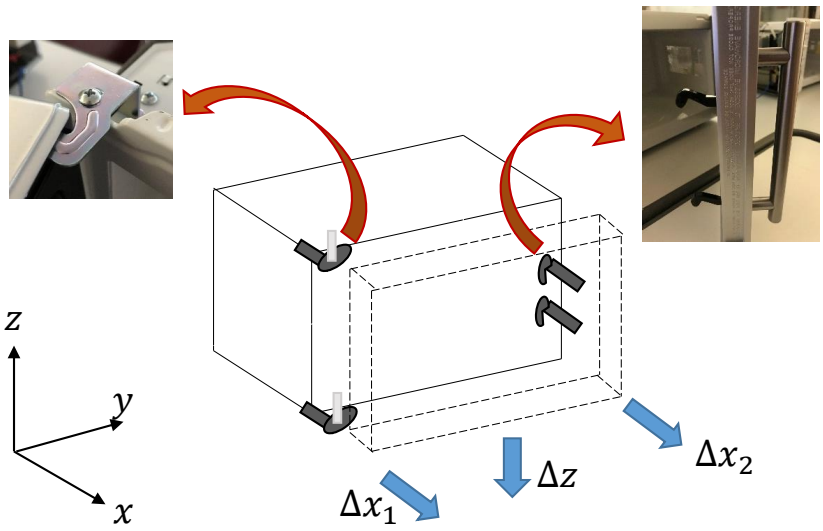

FIGURE 4.2: Representation of the hooks and hinges of a typical domestic oven, and of the possible displacements due to mechanical slackness.

direction Δz, we can just consider the displacements $\Delta x_1,\ \Delta x_2$. In general if $\Delta x_1 \neq \Delta x_2$ we get an angular rotation α around the axis z in addition to the linear shift $\langle \Delta x \rangle$ as presented in Fig. 4.3.

$$\alpha = \tan^{-1}\left(\frac{W}{\Delta x_2 - \Delta x_1}\right) \tag{4.1}$$

$$\langle \Delta x \rangle = \frac{\Delta x_1 + \Delta x_2}{2} \tag{4.2}$$

Tissue	Density [kg m^{-3}]	Specific heat [J $kg^{-1}K^{-1}$]	Thermal conductivity [W m^{-1} K^{-1}]	Blood perfusion [s^{-1}]	Metabolic heat [W m^{-3}]
Air	1.16	1003	0.02	0	0
Bile	928	4037	0.58	0	0
Urinary bladder	1086	3581	0.52	78	1.2
Blood	1049	3617	0.51	10000	0
Blood vessel walls	1101	3306	0.46	150	2.3
Water	994	4178	0.6	0	0
Bone (cancellous)	1178	2274	0.31	30	0.46
Bone (cortical)	1908	1312	0.32	10	0.15
Bone marrow (red)	1028	2666	0.28	135	2.1
Cartilage	1099	3568	0.49	35	0.54
Cerebrospinal fluid	1007	4095	0.57	0	0
Eye (cornea)	1050	3615	0.54	0	0
Eye (lens)	1075	3132	0.43	0	0
Eye (lens nucleus)	1075	3132	0.43	0	0
Eye (sclera)	1032	4200	0.58	380	5.9
Eye (vitreous humor)	1004	4047	0.59	0	0
Fat	911	2348	0.21	32.7	0.50
Gallbladder	1070	3716	0.52	30	0.46
Salivary gland	1048	3760	0.51	383	5.9
Heart muscle	1080	3686	0.56	1026	39.4
Large intestine	1088	3654	0.54	765	11.9
Small intestine	1030	3595	0.49	1026	15.9
Kidney	1066	3763	0.53	3795	18.1
Tendon (ligament)	1142	3432	0.47	29	0.45
Liver	1078	3540	0.52	860	9.9
Lung	394	3886	0.39	400	6.21
Limph	1019	4178	0.60	0	0
Mucous membrane	1102	3150	0.34	593	9.2
Muscle	1090	3421	0.50	36.74	0.9
Skin (nails)	1109	3390	0.37	106	1.65
Nerve (spine)	1075	3613	0.49	160	2.5
Brain (gray matter)	1044	3695	0.55	763	15.5
Brain (white matter)	1041	3582	0.48	212	4.32
Cerebellum	1045	3653	0.50	770	15.7
Pancreas	1086	3164	0.51	767	11.9
Skin (dermis)	1109	3390	0.34	106	1.65
Spleen	1089	3596	0.53	1556	24.1
Stomach	1088	3690	0.53	460	7.12
Penis	1101	3306	0.462	12	0.19
Tooth	2180	1255	0.59	0	0

TABLE 4.3: Thermal and biological material properties of the implemented tissues.

Tissue characteristics	Electrical permittivity [-]	Electrical conductivity [S m^{-1}]
Air	1.00	0
Bile	120	1.40
Urinary bladder	103	0.26
Blood	773	1.0
Blood vessel walls	133	0.33
Water	78	1.0
Bone (cancellous)	125	0.11
Bone (cortical)	420	0.32
Bone marrow (red)	78	0.11
Cartilage	420	0.32
Cerebrospinal fluid	109	2.0
Eye (cornea)	647	0.81
Eye (lens)	121	0.21
Eye (lens nucleus)	121	0.21
Eye (sclera)	529	0.75
Eye (vitreous humor)	72	1.5
Fat	41	0.05
Gallbladder	99	0.90
Salivary gland	84	0.67
Heart muscle	594	0.43
Large intestine	576	0.42
Small intestine	1340	1.2
Kidney	766	0.41
Tendon (ligament)	121	0.40
Liver	452	0.26
Lung	285	0.19
Limph	78	1.00
Mucous membrane	385	0.58
Muscle	385	0.58
Skin (nails)	654	0.09
Nerve (spine)	317	0.18
Brain (gray matter)	505	0.21
Brain (white matter)	254	0.13
Cerebellum	733	0.25
Pancreas	371	0.69
Skin (dermis)	654	0.09
Spleen	1020	0.36
Stomach	1020	0.36
Penis	615	0.36
Tooth	133	0.33

TABLE 4.4: Electromagnetic material properties of the implemented tissues at 2.45 GHz.

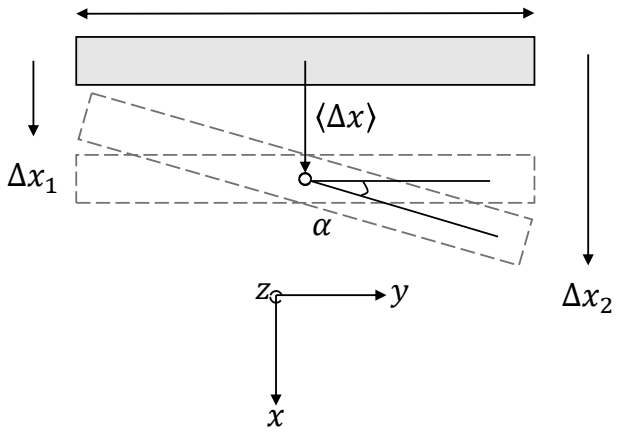

FIGURE 4.3: Composition of mechanical displacements and related degrees of freedom.

Considering that usage affects similarly the hinges and blocks, it is reasonable to assume that the $\Delta x_1 \approx \Delta x_2 \rightarrow \alpha \approx 0$. Therefore, the primary effect can be associated to a linear shift displacement which strives to distance the choke from the cavity, creating an air gap opening. It has to be observed that in case of hinges at the bottom side, the combination of gravity and slackness can induce a rotation around the axis y as primary effect.

4.4.3 Simulated physics

The governing Partial Differential Equations (PDEs) are the full-Maxwell laws and the Pennes equation. These models can be computationally solved in separate study-steps, since the characteristic time-constants have different orders of magnitude and the dielectric properties are independent from the material ones. The frequency of the electromagnetic field is $f = 2.45$ GHz, which belongs to the Industrial Scientific and Medical (ISM) spectrum. Consequently, the wavelength in the propagating medium (air) is $\lambda_0 = c/f \approx 12.2$ cm, which is smaller than the geometrical maximum length of the model, therefore the quasi-electrostatic formulation cannot be applied. The electromagnetic (PDE) is described as follows [25]:

$$\nabla \times \mu_r^{-1}(\nabla \times \boldsymbol{E}) - k_0^2 \dot{\epsilon}_r \boldsymbol{E} = 0 \tag{4.3}$$

where $\boldsymbol{E}$ is the electric field V/m, k_0 is the wave propagation number, μ_r is the relative permeability, and $\dot{\epsilon}_r$ is the complex relative permittivity. The Pennes model is solved over the time-domain, using

the classical energy balance [26, 50, 2] [1]:

$$\begin{aligned} \rho c_p \frac{\partial T}{\partial t} =& \nabla \cdot (k \nabla T) + Q_{em} + Q_{blood} + Q_{met} \\ Q_{blood} =& \rho c_b \omega_b (T_b - T) \\ Q_{em} =& 2\pi f \epsilon'' |\boldsymbol{E}|^2 \end{aligned} \tag{4.4}$$

where ρ is the density kg/m^3, c_p is the specific heat capacity J/(kg K), T is the temperature °C. The EM boundary conditions have been set as Scattering Boundary Conditions (SBCs). The metallic elements have been considered as Perfect Electric Conductors (PECs) since this approximation over the metallic surfaces is appropriate in the microwave frequency range [37]. The propagating mode TE_{10} has been assumed at the input port of the model, since the pattern due to the TE_{10} imposition is similar to that one generated by a real magnetron source [38]. The input power enters into system through port 1 injecting the power $P_{in} = P_1$. The output power is accounted for by mean of the leakage (conservation law of power), considering port 2 as the equivalent surface of radiation A_2 which is created by the choke-cavity air gap:

$$P_{out} = \int_{A_2} \Re(\boldsymbol{E} \times \boldsymbol{H^*}) \cdot \hat{n} \, dA = P_2 \tag{4.5}$$

Actually, the computation of P_2 is subjected to big numerical errors because of the presence of integration over a large surface in the air region. Therefore, it is more convenient to compute the reflection scattering parameter S_{11} in order to derive indirectly the output at port 2. In the first analysis, considering the cavity as empty:

$$S_{21} = \sqrt{P_{out}/P_{in}} = \sqrt{1 - S_{11}^2} \tag{4.6}$$

Therefore, we can compute S_{11} to derive the leakage related to S_{21}. The representation of the equivalent ports is depicted in Fig. 4.4. The thermal source is as a volumetric term which defines the connection between electromagnetic and thermal physics: Q_{em}. Q_{met} is the metabolic source term that depends on the specific tissues. Realistic geometrical sizes of the entire system, including a real 2.45 GHz choke, have been here reproduced. The overall geometry is presented in Fig. 4.5. More details about the optimization of the geometry of a choke and its shielding effect can be found in [51].

[1] Eq. 4.4 has been already presented in Eq. 2.19, but considering that any chapter should be independent, as motivated in the introduction, the equation has been explicitly shown again

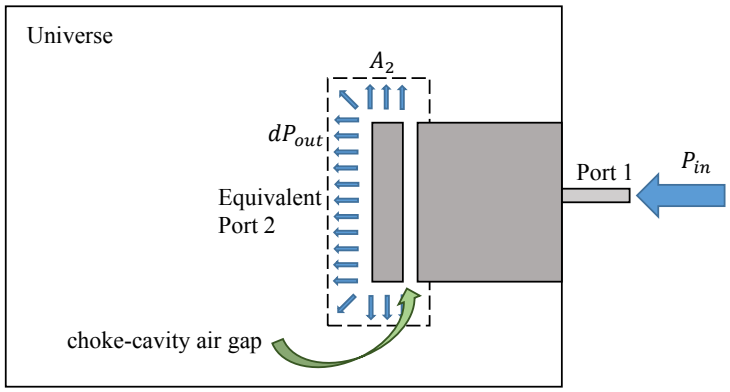

FIGURE 4.4: Scehmatic representation of the simulated system. The dashed line identifies the equivalent port due to oven age.

4.5 Results and discussion: analysis of leakage and safety

4.5.1 Influence of choke-damage and positioning

Computational predictions

It is important to evaluate the choke damage, which is mainly related to mechanical slackness. This effect can be simulated considering the gradual displacement of the choke from the original position. When this parameter changes, distributed capacities and inductances on the door-seal are modified, and therefore the electromagnetic response is influenced. In the FEM computation the displacement has been considered by $d = [0, 0.4, 0.8, 1.2]$ mm. If the displacement is bigger than 1.2 mm, the resonance peak is placed at 2.45 GHz and therefore the oven begins to radiate intensively toward the environment. In Fig. 4.6 the scattering parameter S_{21} is depicted over the frequency domain, where the port 1 is the input source and the port 2 is the output power surface. We can observe in Fig. 4.6 that the shielding behavior is strongly affected by resonance phenomena (peaks) which can be potentially very dangerous. When the displacement increases, the resonance peak moves toward lower frequency values. Therefore risks associated to choke damage are not only related to the increased radiating surface, but also to the shift of the propagation resonance. In the analysis, limited displacements guarantee shielding capability which satisfies FDA reference 1 mW/cm^2 at the distance of 5 cm for the new oven. Radiated power magnitude for several displacements is depicted in Fig. 4.7. Once that

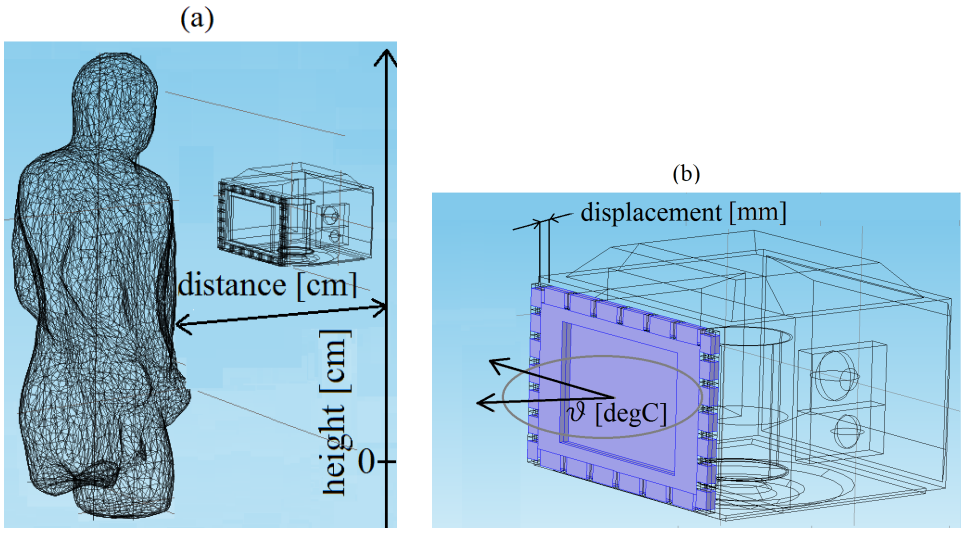

FIGURE 4.5: (a) Geometry of the model composed by the body and the oven. (b) Implemented microwave choke.

the influence of the actual emitted radiation has been considered over the choke-displacement, it is interesting to perform an evaluation of the safety zones by changing the choke-displacement d, the height of the oven h (see Fig. 4.5 for the axis reference) and the distance between the standing body and the door l. The parameters have been set considering the following ranges: $[0, 0.4, 0.8, 1.2]$ mm, $h = [-15, 5, 25, 45]$ cm and $l = [0, 8, 16, 24]$ cm. The results of the numerical analyses have been reported in Fig. 4.8. The ideal dependence between the power and the distance should be described by a quadratic law, but this is valid only for isotropic propagation, and considering concentric surfaces centered at the electromagnetic source. The results show that the maximum SAR does not exceed 2 W/kg if the considered distance is greater than 15 cm. This distance can be considered as the border of safety region. Change on the height of the oven does not induce significant difference on absorption.

Experimental observations

The experiments have been run following the procedure in section 4.3.2. The results, in terms of S_{11} and S_{21} have been reported in Fig. 4.9. From the plots, we can observe that the frequency in correspondence to the main peak moves toward lower values when the damage increases, in accordance to the numerical results. In the experimental study, the frequency-shift is reduced to a narrow band because the specific design influences the amplitude of the frequency shift. From numerical and experimental results we can deduce that the peak-frequency should be located at smaller values with respect to the operative frequency of the device.

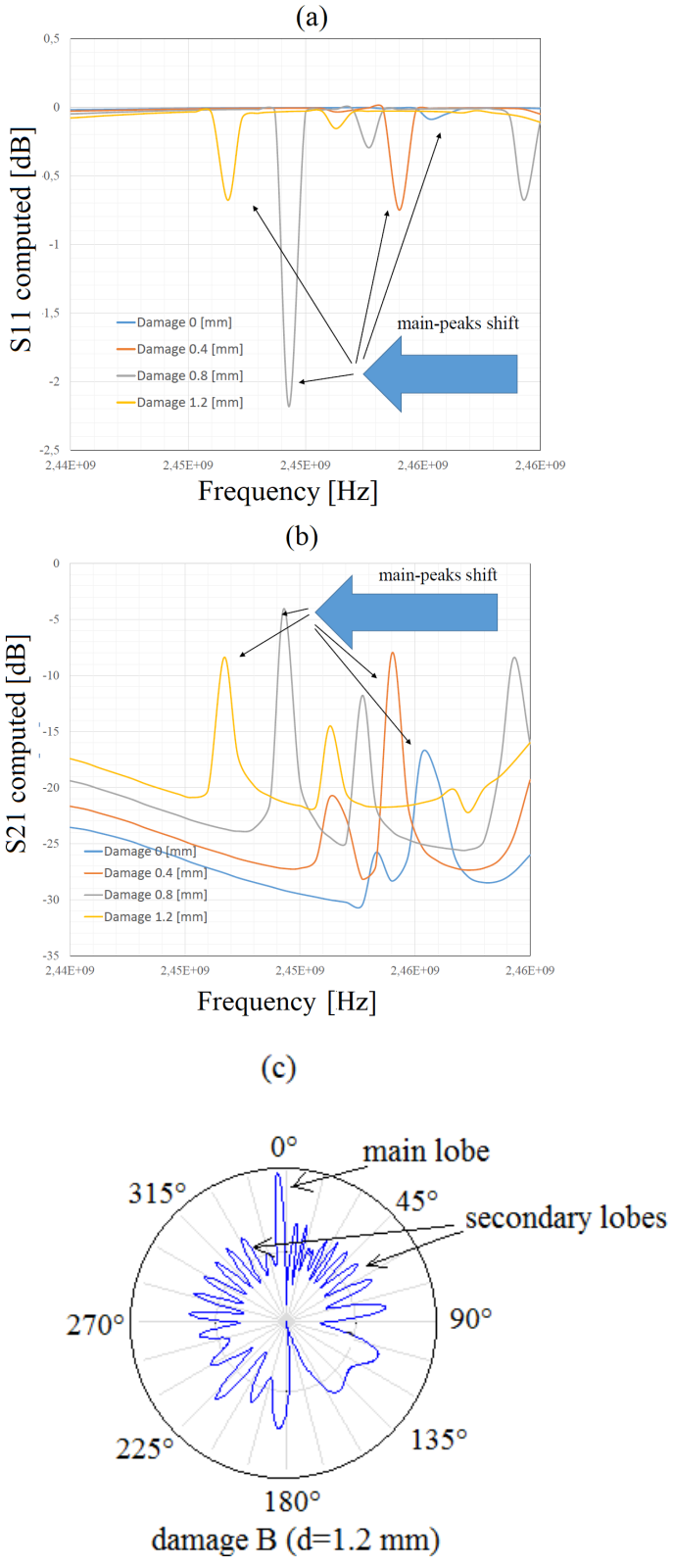

FIGURE 4.6: (a)-(b) Scattering parameters S_{11} and S_{21} respectively, over the frequency domain. (c) Normalized polar radiation pattern over the angular variable θ (case d=1.2 mm).

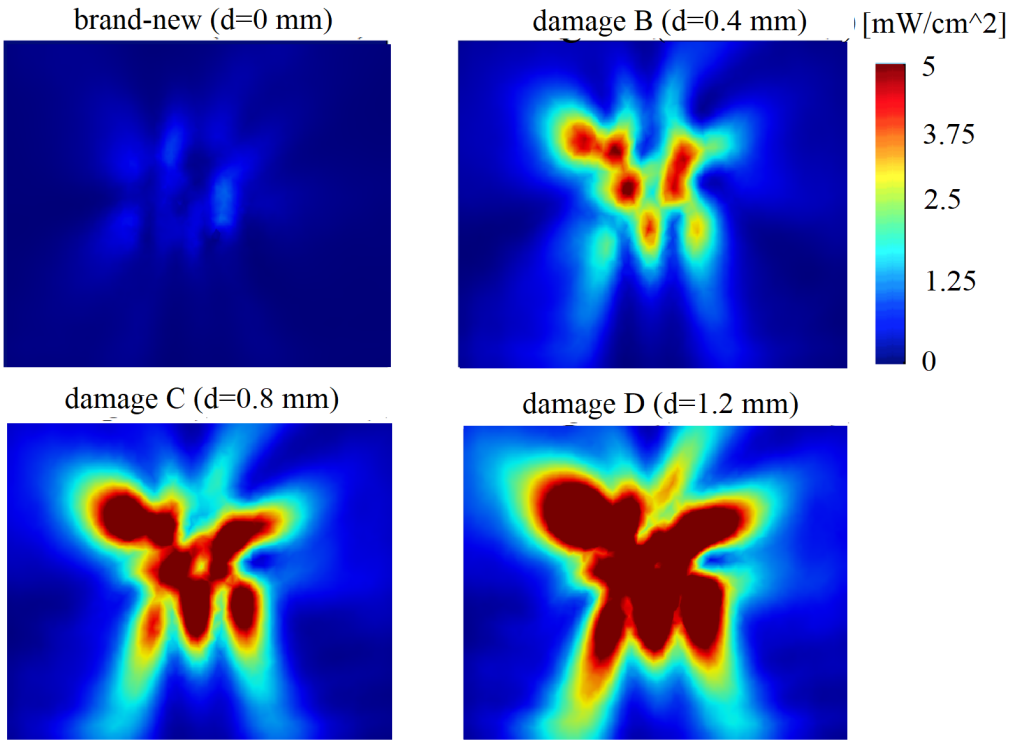

FIGURE 4.7: Magnitude of the radiating power at the distance of 5 cm from the door.

4.5.2 Influence of the absorbing mass inside the cavity

In the previous analysis, the cavity was considered empty in order to evaluate the worst possible condition. In the real case, the food is placed inside the cavity, and it absorbs a fraction of the deposited power, damping the leakage. It is not possible to analyze numerically all the different process conditions because the shape of the mass, the dielectric properties of materials, the moisture of the food and its exact position, are random variables. Therefore, in the current analysis, an equivalent mass has been considered as thermal load, and in particular the load is a water-filled cylinder ($\epsilon_r = 78 - 12.5j$) characterized by volume $v = [100, 200, 300, 400]$ mL. The height of the oven is defined by the parameter $h = [-15, 5, 25, 45]$ cm. The analysis investigates not only the SAR but also the correlated temperature raise. The initial temperature of the body is at the metabolic condition, and this is assumed as the undisturbed starting situation. The temperatures are computed at the steady state condition (worst case possible), at the distance from the choke $l = 8$ cm (5 cm is the reference value, and 3 cm is the depth of the considered oven door) and the displacement $l = 0.4$ mm. The results of the analysis are presented in Fig. 4.10 and 4.11 The results show that SAR levels and the temperature raises ΔT are very limited, in fact they are characterized by one order of magnitude less than the

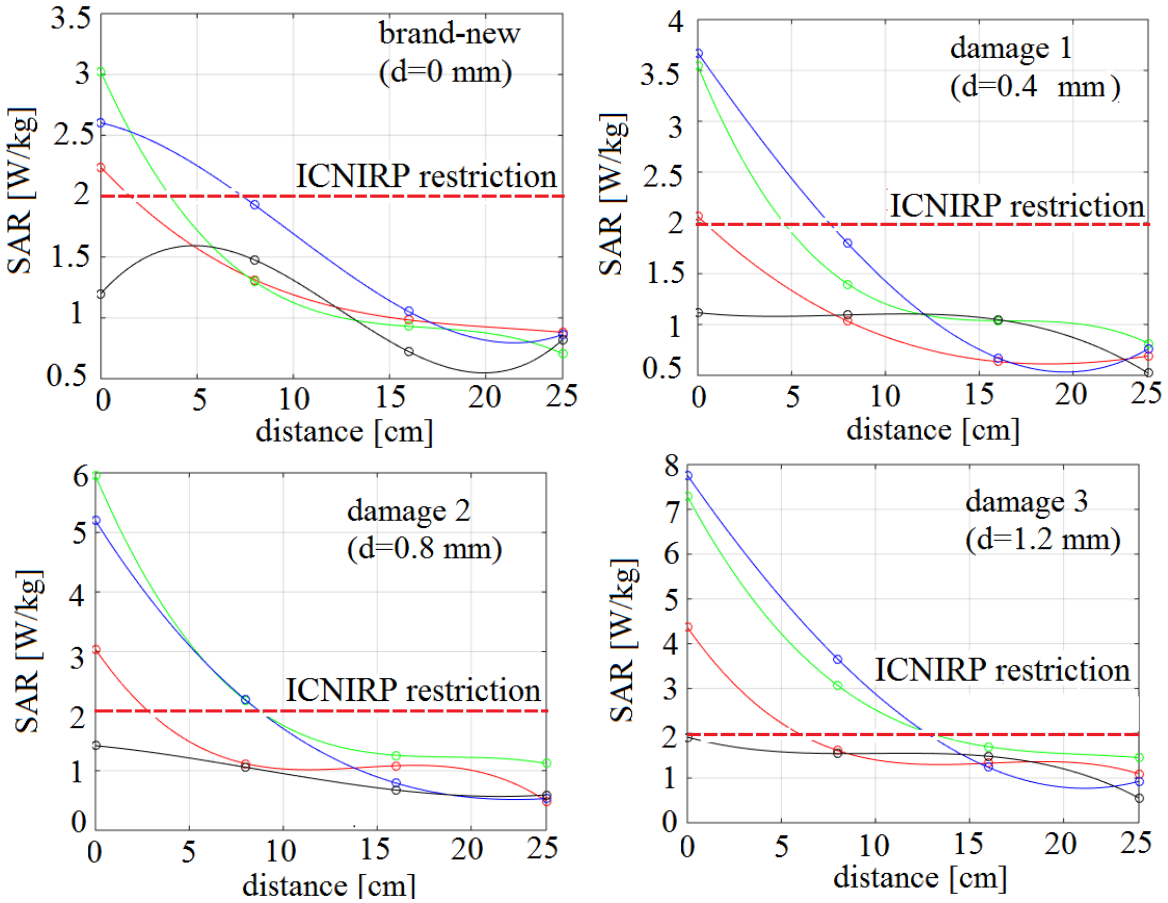

FIGURE 4.8: SAR parametrized by the height level of the oven: red-genitals; green-chest; blue-neck; black-head.

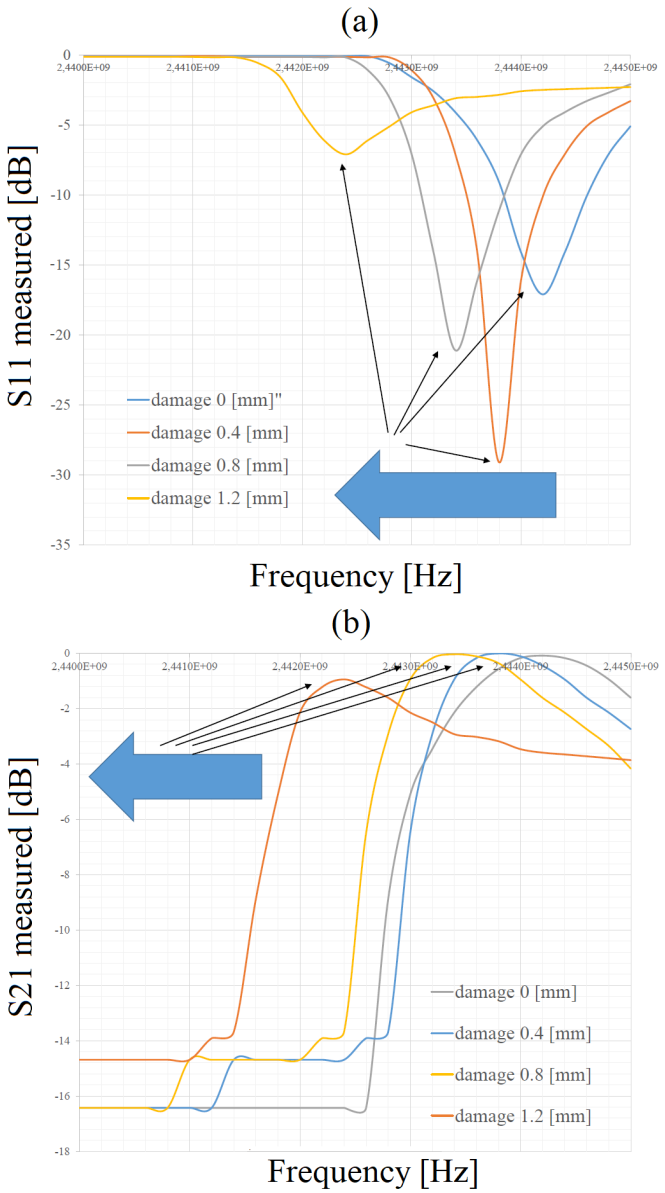

FIGURE 4.9: (a) - (b) Measured scattering parameters S_{11} and S_{21} respectively, over the frequency domain with different displacements choke-cavity.

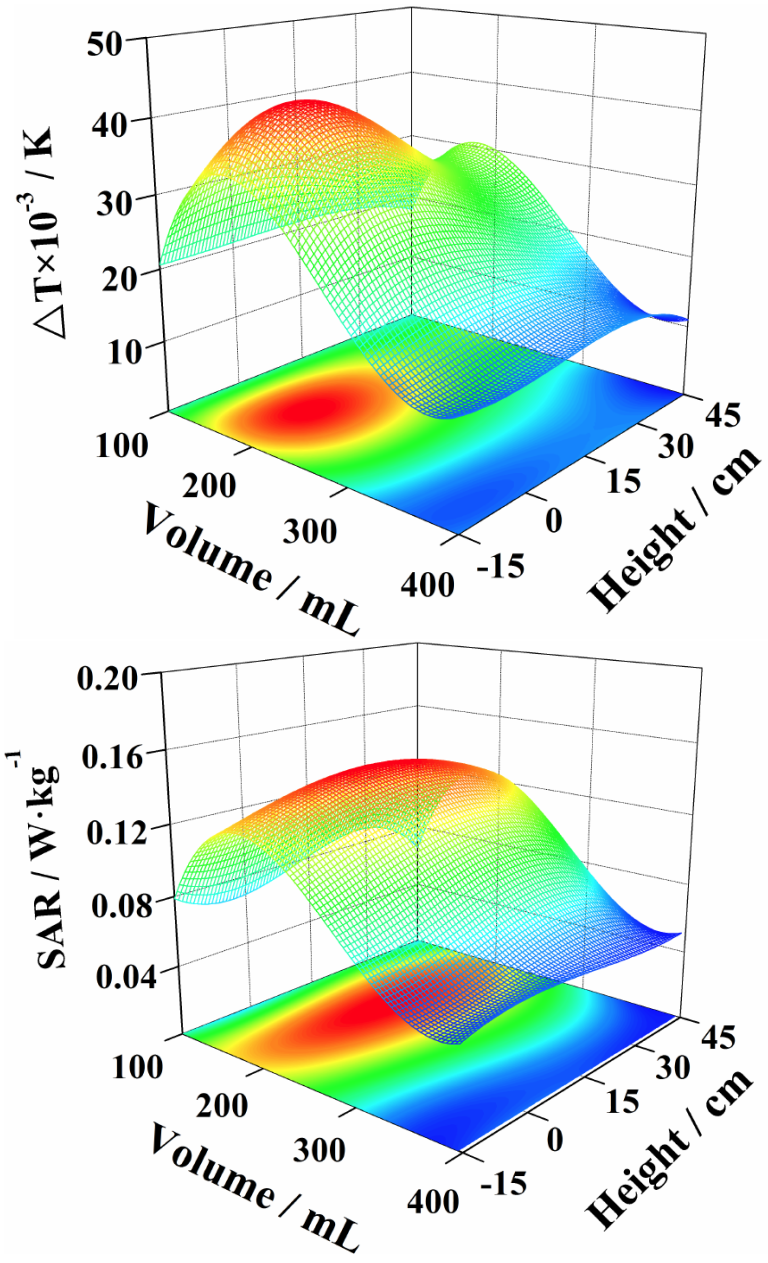

FIGURE 4.10: Values of ΔT and SAR for several load-volumes and heights.

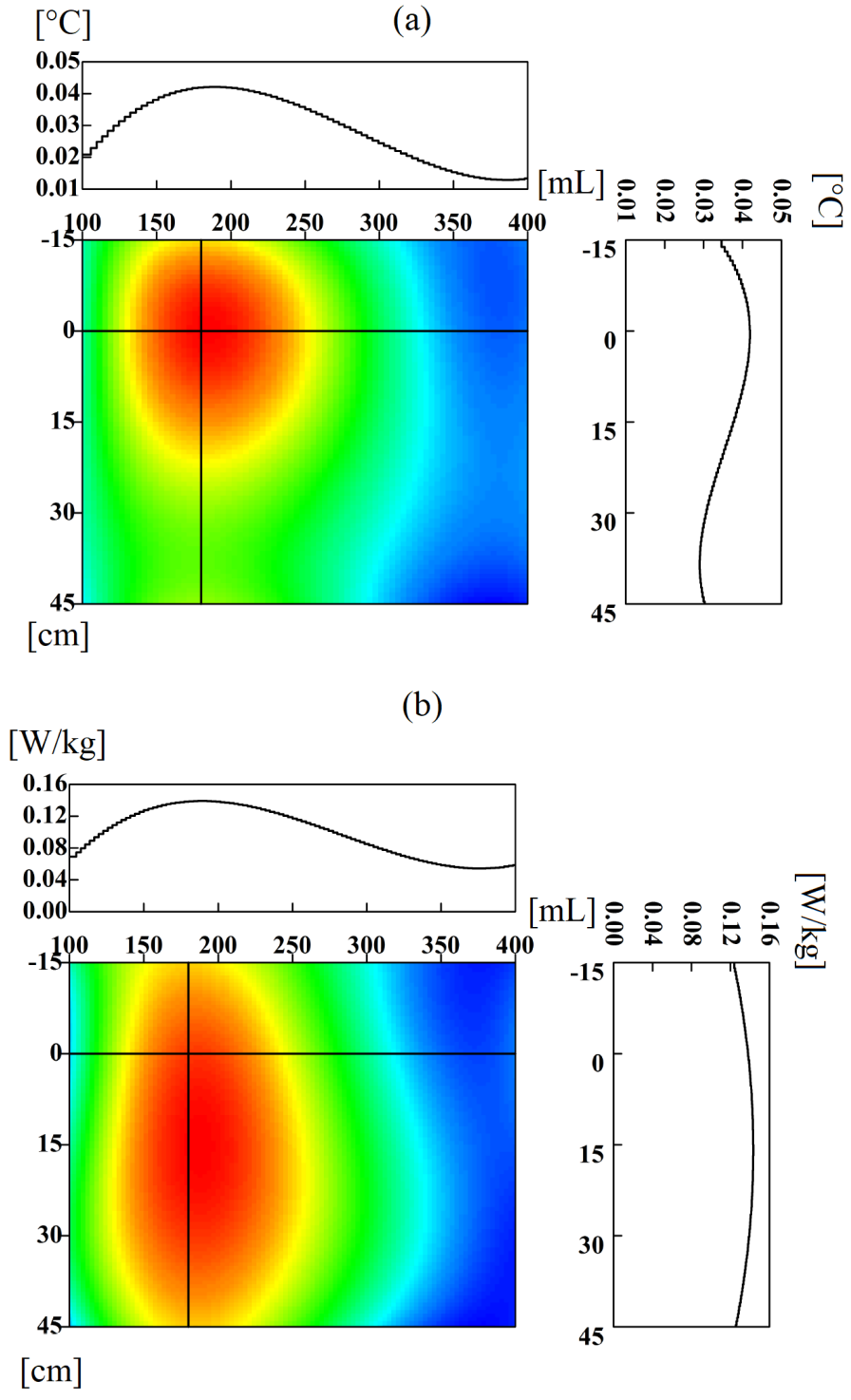

FIGURE 4.11: Representation of the most relevant ΔT (a) and SAR (b) variations.

cases with empty cavity. The maximum value of SAR is around 0.14 W/kg and the corresponding value of temperature raise is 0.04 °C. Relation between maximum SAR and ΔT is almost linear and it can be estimated by the correlation coefficient $R = 0.9535$. Peak values are not in correspondence to the minimum mass because there is a variation of the resonance condition when the shape of the load changes.

4.6 Conclusions

Leakage from a damaged MW oven was analyzed over the frequency domain, and in correspondence to the operative frequency 2.45 GHz to assess the induced thermal effects to a human body. The exposure was tested considering a realistic non-uniform 3D phantom, composed by 40 tissues. Experimental testing was performed in order to verify the numerical observations regarding the main causes of shielding failure. From a methodological point of view, the work can be divided in three stages:

- Implementation of the numerical model that can be divided in several parts:
  - modeling of the mechanical damage depending on the hinges/hooks positioning.
  - 3D non-uniform phantom modeling (not described in this manuscript).
  - implementation of the physics.
- Experimental testing, which can be characterized as follows:
  - Using a Vector Network Analyzer (VNA) in substitution of the magnetron it is possible to perform a low-power analysis of the scattering parameters of the system.
  - Artificial reproduction of the displacement using a prismatic wedge as spacer between the choke and the cavity.
- Analysis in terms of SAR and ΔT of an exposed human body, considering the distance as the main dependent variable and other influencing factors as parameters of the sensitivity analysis:
  - the mass of the absorbing thermal load (water) inside the cavity.
  - the possible hight-positioning of the appliance with respect to the exposed person.

From the point of view of the actually obtained results, we can highlight:

- The damage of the hinges/hooks determines as main effect the change of the frequency in correspondence to the peak of emission. In particular, both numerical and experimental evidences show that the peak tends to move toward lower frequency values as the damage increases.

- When the phantom was located at a distance from the oven greater than 15 cm, the SAR level was under the ICNIRP basic restriction (for head and trunk) 2 W/kg even with displacements of the order of magnitude of 1 mm. The temperature increase was always below 0.1 °C.

Considering ICNIRP reference levels and basic restrictions, with a displacement choke-cavity of the order of 1 mm it is likely that the threshold conditions can be broken. But, even in this case, a practical safety region can be actually defined standing at a distance bigger than 15 cm because SAR level decreases up to values below 2 W/kg. This restriction is tolerable by generic public without specific protections.

5 Mechanistic Understanding of Plasma Arcing in Microwave Food Processing

5.1 Abstract

While arcing during processing of food in a domestic microwave oven has been well known and has major safety implications, its mechanistic understanding is not available. A comprehensive multiphysics 3D numerical model was developed that couples electromagnetics, electrodynamics, heat transfer and moisture transfer. The model is multiscale with the electromagnetics and heat and moisture transfer at the oven cavity scale while electrodynamics at the small region around the food. The model was validated using calorimetric and temperature measurements, and reproducibility of arcing. Time evolution of arcing and factors affecting it were identified by the model. In drier air, arcing occurs at lower power level because the equilibrium between ionization and attachment is achieved at lower electric field magnitude than in moist air. Higher temperature leads to greater chances of arcing as higher temperature increases ionization more than it increases attachment. Small load of food increases the chances of arcing. Sample geometry, orientation, and placement inside the oven are also significant factors. Conditions that lead to arcing were identified in terms of maximum electric field values and temperatures. These threshold conditions can be used to identify unsafe situations for domestic microwave ovens and other microwave devices for product and process designers.

5.2 Introduction

5.2.1 The importance of understanding microwave food arcing

During 2007-2011, U.S. fire departments responded to an average of 7100 home structure fires per year in which a microwave oven was involved in ignition. These fires caused an average of fewer than 10 civilian deaths, 150 civilian injuries, and $31 million in direct property damage per year.

17% microwave oven home structure fires cited appliance housing or casing as the item first ignited [52]. Several other sources have assessed fire risks associated with home microwave oven use [53, 54]. Companies put disclaimers such as: *"It has been found that some vegetables such as green beans and carrots may cause an arcing effect/sparking (on the food product itself) when cooked in the microwave. Possible reasons why this arcing occurs: The vegetables are not covered. The types of seasoning (i.e. bacon grease, onions, etc). Little (if any) water surrounding the vegetables"* [55]. At least one Food safety agency explicitly refers to the "food arcing" phenomenon, although using completely different arguments: *"Dense vegetables such as green beans, carrots and green peppers have a higher amount of minerals in them than other food items. These minerals include iron, magnesium and selenium. The minerals act like tiny pieces of metal and create arcing effects in a microwave. The sparks result as the microwaves reflect or bounce off the metal. The arcing does not harm the food but it does prevent it from heating thoroughly"* [56]. While the risks have been documented, a mechanistic understanding of "food arcing" remains unknown.

5.2.2 Previous studies on electrical plasma discharges

The research-field of "electrically triggered plasma arcing" started in telecommunications, covering a wide range of frequencies [57, 58], in order to evaluate the maximum operative power for transmitting devices. For this reason, previous studies have been focused on the effect of specific field distributions, which are related to the electromagnetic mode of propagation and to the geometry of the transmitting waveguide or cavity [59, 60, 61]. The first focused study was conducted by MacDonald [6], giving a theoretical explanation of many physical aspects related to microwave breakdown in gases. Conditions like the presence of uniform gaseous dielectrics (e.g., air, argon, etc), which are typically non-dissipative, and the presence of metallic walls boundary conditions were commonly used [62, 63]. Propagation of the plasma discharge within solid materials and fluids have been widely studied [64]. However, only a few studies have considered the thermal aspects, and even these are far narrow temperature range [65], or their ideal geometry required strong assumption of symmetry [66]. In fact, for temperatures over 2000 K, there is a simplification of the diffusive term in the electron transport phenomena [66]. In telecommunications, humidity is not usually included in the study of breakdown since it does not play an important role with respect to other factors. Another research field that involves electrically triggered plasma is related to the chemical production of ozone and other chemicals by plasma source [67, 68]. For many of these studies, the main interest is the analysis

of the reaction kinetics in relation to the composition of the gas which is subjected to arcing [69]. In power propulsion, some studies have investigated the possibility of triggering a microwave plasma for ignition in a gas-flow [70]. Propagation of ignited plasma streamers in atmospheric air and dielectric materials have been studied [71, 72]. Only a few studies in electric power systems take into account the presence of humidity for the analysis of corona discharge since the atmospheric conditions can affect strongly the physical behavior [73, 74]. But in this case, the operative frequency is 50 Hz, and consequently the electron transport physics is not dominated by diffusion and the material properties of the metallic electrodes influence the electron population [6]. At microwave regimes, the polarization changes so quickly that the electrons do not have enough time to impinge the electrodes, so the physics is slightly different. In general, previous studies did not include the typical conditions that occur during microwave food processing. Considering the tremendous range of microwave household appliances and facts that are placed in them, it is important to obtain a mechanistic understanding of the breakdown event.

5.3 Materials and methods

The following sections are focused onto the determination of suitable food specimens for the experiments (test material), considering that the reproducibility and repeatability are the most important issues to be concerned of. The instrumentation that has been used in laboratory (equipment) and the implemented procedures for the tests (adopted protocols) have been also presented.

5.3.1 The selection of food specimen

Preliminary experiments suggest that only specific food products (e.g., carrots, grape, tomatoes, etc), with a few geometrical similarities (i.e., shape, size, cut), induce the arcing. Products exhibiting discharge-behavior are typically small, and present easy contacts between associated pieces (e.g., bunch of grapes or peas). As shown in Fig. 5.1, strawberries, carrots, tomatoes and grapefruits showed arcing. As heating starts, the induced pressure gradients tend to move the food pieces away. If the contact gets lost, the arcing disappears because the electric field in the critical zone decreases dramatically. Instead, if the connection holds, it is possible to maintain the geometrical condition for a longer period. A physical connection between pieces can be guaranteed by keeping intact the skin-layer connection. It is convenient to study a single piece which has been cut into halves leaving

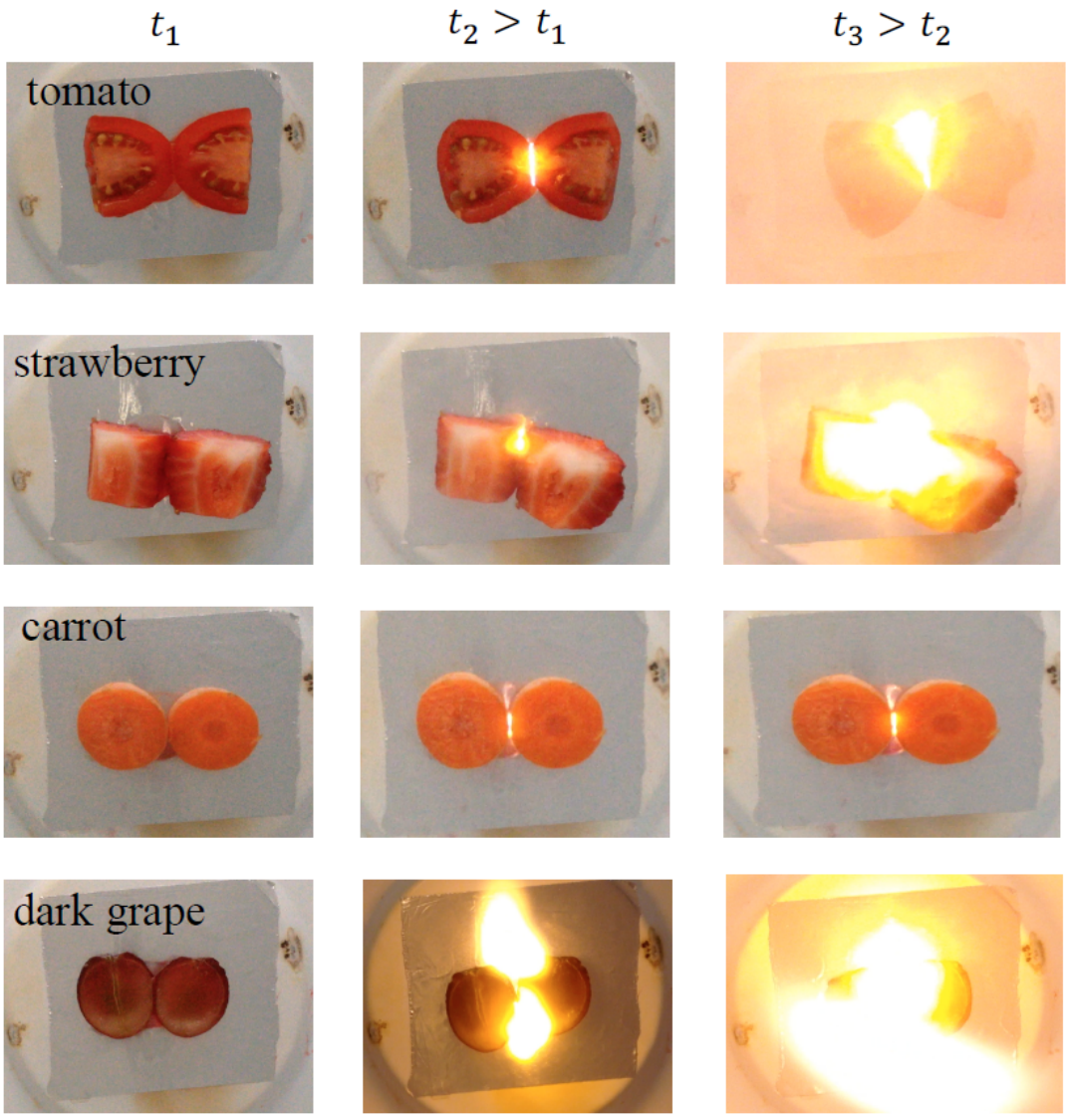

FIGURE 5.1: Several fruits and vegetables show arcing when heated in a microwave oven.

the skin connection untouched. For ease of implementation, the grape was adopted, mainly because of its regular ellipsoidal shape. The test samples were stored refrigerated at 5°C and they have been left at room temperature of 25°C for 30 minutes before running the experiments. The shape of the food specimen that has been used in laboratory is presented in Fig. 5.2.

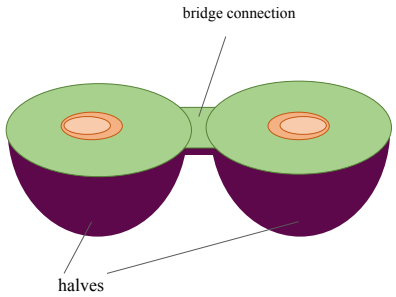

FIGURE 5.2: The bridge formed by the skin guarantees the mechanical stability of the contact between the different halves.

5.3.2 Instrumentation

The microwave oven used (ok. brand, which is a private label of Mediamarket S.p.A., model OMW-301-W), had the following specifications: rated voltage 230 V, frequency 50 Hz, rated output power 700 W, operation frequency 2450 MHz, outside dimensions 258 mm (H) x 440 mm (W) x 356 mm (D), oven capacity 20 L. In particular, the magnetron is the model 2M217J: peak anode voltage 3.9±0.2 kV, average anode current 200 mAdc, average output power 580±30 W, frequency 2456±10 MHz, filament voltage 3.3 V, typical oven power by IEC method 500∼700 W. In the the calibration stage, a water-filled glass was used as thermal load, and it has been thermally insulated using a glass-wool layer. The glass-wool was 1.5 cm thick with a thermal conductivity of 0.04 W/(m K). The glass used was made in borosilicate material, of diameter 7 cm, and this has been used for the calibration and validation tests. The camera used for recording has video resolution 640 x 480 pixel, Full-HD recording, 30 frames per second, integrated video stabilizer. The thermal measurements used a type K thermocouple, with a sensitivity of approximatively 40 μV/°C, and range -20°C to 1350 °C. The infrared thermo-camera is FLIR T420, which has temperature range from -20°C to 650 °C, frame rate 60 Hz, thermal sensitivity <0.045°C at 30°C, resolution 320 x 240 pixels, non-radiometric IR-video recording MPEG-4 to memory card. The electrical measurements have been done using a passive high voltage probe TEKTRONIX P6015A: operational frequency range from DC 75 MHz, high-voltage 20kV-DC / 40 kV Peak (100 ms Pulse Width). The used oscilloscope is Digital Phosphor

Oscilloscpe TEXTRONIX TDS5054B with a bandwidth of 500 MHz, 4 channels, sample rate 5GS/s, up to 16 M record length, and 100,000 wfms/s maximum waveform capture rate. The computer used has processors Intel(R) 2.10 GHz (16 cores) and Xeon(R) 2.10 GHz (8 cores) CPU E5-2620 v4, RAM memory 256,0 GB, 64 bit operative system. The finite element software used for implementing the physics is COMSOL Multiphysics 5.2 (COMSOL Inc. 100 District Avenue, Burlington, MA 01803, USA) with the module packages: RF module, Heat Transfer module, Chemical Reaction Engineering module and Equation-based module.

5.3.3 Experimental procedures

Two types of experiments have been conducted: arcing tests and calibration/validation tests. For arcing tests a grape was left at room temperature (around 25°C) for 30 minutes after taking out of the refrigerator. The sample was cut in two pieces maintaining the integrity of the skin connection between the pieces as described in section 5.3.1. The cut was along the middle plane, with respect to the longest axis of the grape. The grape was placed in the microwave cavity centrally (Fig. 5.4), after the removal of the turntable. The sample was placed with a specific angular orientation. The rotation has been considered, in relation to a vertical axis at the center. The default sample orientation (if not differently specified) is obtained aligning the two pieces from left to right (frontal position to the oven). Heating time was 10 seconds. The power of the magnetron is set to 100% (700 W nominal power), to avoid the effect of on-off power at various duty-cycle. In both calibration and validation tests, a mass of water has been added inside the cavity. For calorimetric tests, the water-filled glass was placed centrally inside the cavity. For the gap detection (section 5.4.2) studies, the glass was placed in the left rear corner (Fig. 5.4). This positioning during calibration tests was chosen in order to avoid distortions of the electric field in the critical zone of the grape-contact. Temperatures were measured using a k-type thermocouple after mixing the fluid to obtain a mixed mean value. The calorimetric tests have been repeated four times for different load-masses of 100 mL, 200 mL, 300 mL and 400 mL.

5.4 Model development

5.4.1 Formulation

The governing equations for the electromagnetics, heat transfer, moisture transfer and electrodynamics, and their coupling are presented here.

Schematic

The three regions (Fig. 5.3) are: the food domain Ω_1, the surrounding air Ω_2, and the remaining cavity Ω_3. It is convenient to separate the borders of the domains in sub-borders, in order to facilitate the definition of the boundary conditions:

$$\xi_1 = \gamma_1 \cup \gamma_2 = \partial\Omega_1 \tag{5.1}$$

$$\xi_2 = \gamma_3 \cup \gamma_4 = \partial\left(\Omega_1 \cup \Omega_2\right) \tag{5.2}$$

$$\xi_3 = \gamma_3 \cup \gamma_5 \cup \gamma_6 = \partial\left(\Omega_1 \cup \Omega_2 \cup \Omega_3\right) \tag{5.3}$$

The actual geometry is shown in Fig. 5.4. Various physics are implemented in the domains as:

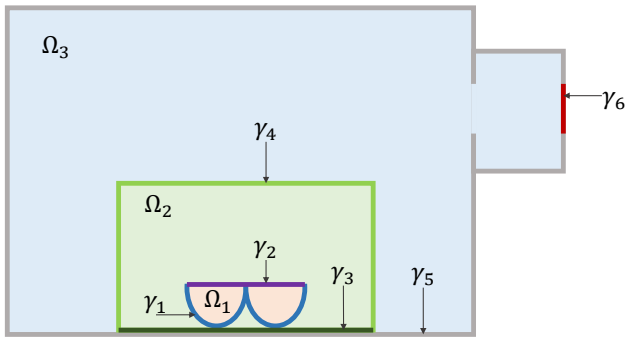

FIGURE 5.3: General schema showing the computational domain and sub-domains.

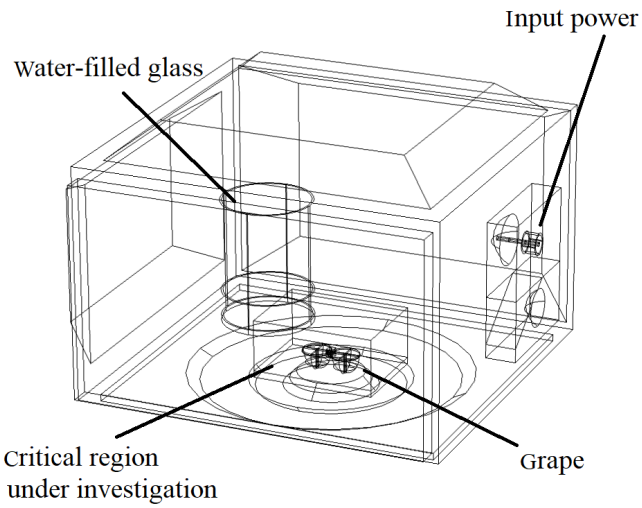

FIGURE 5.4: Computational domains used in the finite element software.

(Electromagnetism (EM), Heat Transfer (HT), Moisture Transfer (MT) and Electrodynamics (ED)):

$$\text{EM} : \Omega_1 \cup \Omega_2 \cup \Omega_3 \tag{5.4}$$

$$\text{HT} : \Omega_1 \cup \Omega_2 \tag{5.5}$$

$$\text{MT} : \Omega_1 \cup \Omega_2 \tag{5.6}$$

$$\text{ED} : \Omega_2 \tag{5.7}$$

Input parameters

All the input parameters for the model are in Table 5.1. The input power functions, which have been obtained experimentally, have been discussed in section 5.5.1.

Electromagnetics

The governing Maxwell's equations of the electromagnetics are considered in the frequency domain, known as Helmholtz equation [25]:

$$\nabla \times \mu_r^{-1} (\nabla \times \mathbf{E}) - k_0^2 \left(\dot{\epsilon_r} - j \frac{\sigma}{\omega \epsilon_0} \right) = 0 \tag{5.8}$$

Parameter	Value	Source
Oven dimensions (m)	$0.275 \times 0.26 \times 0.175$	
grape sample (semi-ellipse) axis (m)	$0.01 \times 0.01 \times 0.014$	
Electromagnetics		
Frequency (GHz)	2.45	
Power (avg) (W)	$P_{steady}\ m_{avg}$	(5.5.3)
Complex dielectric permittivity (1)		
Air	1	
Grape	(interpolated data)	[75]
Heat transfer		
Thermal conductivity (W/(m K))		
Air	0.026	[76]
Grape	0.57	[76]
Specific heat capacity (J/(kg K))		
Air	1006	[76]
Grape	4178	[76]
Density (kg/(m^3))		
Air	(Ideal gas law)	
Grape	998	[76]
Vapor diffusivity in air (m^2/s)	(interpolated data)	[26]
Vapor pressure (Pa)	(Eq. 5.17)	[77]
Convective heat coefficient (W/(m^2 K))	2257	[26]
Latent heat of evaporation (kJ/(kg))	15	
Electron transport		
Peaks to average factor (-)	r_k	(5.5.3)
Velocity (V/(cm Torr))→(cm/s)		
Air	$0.9 \times 10^5 + 2173.9(E/P)$	[73]
Vapor	$0.25 \times 10^5 + 625(E/P)$	[73]
Attachment		
[V/(cm Torr)]→[1/(cm Torr)]		
Air	$0.01298 - 0.54 \times 10^{-3}(E/P)...$ $... + 0.87 \times 10^{-5}(E/P)^2$	[73]
Vapor $(E/P) < 40$	$-3.67 \times 10^{-5}(E/P)^2...$ $... + 0.026(E/P) - 0.2732$	[73]
$(E/P) \geq 40$	$-2.5 \times 10^{-5}(E/P)^2...$ $... - 2.5 \times 10^{-4}(E/P) + 0.235$	
Ionization		
[V/(cm Torr)]→[1/(cm Torr)]		
Air	$4.7786 \exp(-221(P/E))$	[73]
Vapor	$0.001(E/P)^2 - 0.06(E/P) + 1.0$	[73]
Initial conditions		
Ambient pressure (Pa)	101325	
Temperature(°C)	20	
Moisture concentration (mol/m^3)	0.96415	
Electron density (1/m^3)	5×10^9	[4]

TABLE 5.1: Input parameters for simulation purpose.

where the angular frequency is related to the propagation frequency $\omega = 2\pi f$. The quantity k_0 is called wave number and it is strictly related to the material properties of the propagation mean:

$$k_0 = \omega\sqrt{\mu_0\mu_r\epsilon_0\epsilon_r} \tag{5.9}$$

The boundary conditions of the model are defined by the presence of metallic material of the oven wall. At microwave frequencies the walls can be considered as perfect conductors, allowing the use of Perfect Electric Conductors (PEC) [37]:

$$\vec{\mathbf{n}} \times \mathbf{E} = 0 \tag{5.10}$$

Equation 5.10 implies that the electric field has no tangential component at the metallic surface. The electromagnetic port is defined by a coaxial shape where the propagation mode TEM is imposed. At the input port, a nominal input power has been set as $P_{EM} = P_{input}$. The electromagnetic and thermal models are coupled through the dissipated power that is the heat source. The reverse coupling is through the temperature dependent complex electric permittivity of the material:

$$\dot{\epsilon_r} = \epsilon_r' - j\epsilon_r'' \tag{5.11}$$

Heat transfer

The governing equation for the the thermal model is the heat equation [26]:

$$\rho c_p \frac{\partial T}{\partial t} + \nabla \cdot (-k\nabla T) = Q \tag{5.12}$$

A heat flux boundary condition is used that includes convective heat exchange (almost natural convection),

$$\vec{\mathbf{q}} = h\,(T - T_0) \tag{5.13}$$

and evaporation at the wet surface:

$$\vec{\mathbf{q}} = \Delta H_m \vec{\mathbf{j}}_{\mathbf{vap}} \tag{5.14}$$

The initial temperature of the system is set at the environmental value (293.15 K) in the air domain. Initial temperature within the food is variable corresponding to storage condition. The coupling

between the thermal and the electromagnetic model is mainly due to the converted power density induced by dielectric polarization of the material:

$$Q = \omega \epsilon'' |\vec{\mathbf{E}}|^2 \tag{5.15}$$

Eq. 5.11 and Eq. 5.15 represent the two way coupling between the electromagnetic and thermal models.

Moisture transfer

The humidity contained within the air affects the composition of the weakly ionized gas. The moist air is considered as a mix of dry air and vapor, and each of these components has a different electrodynamic behavior. The overall pressure is fixed at the atmospheric level (760 Torr) and it is equal to the sum of the partial pressures of dry air and vapor.

$$P_{atm} = p_{vap} + p_{air} \tag{5.16}$$

Concentration of vapor is calculated from saturation vapor pressure data for water as [77]:

$$c_{vap} = \frac{p_{sat}(T)}{R_b T}$$

$$p_{sat}(T) = a + b \ln T + c (\ln T)^2 + d (\ln T)^4 + e (\ln T)^5 \tag{5.17}$$

where the coefficients of Eq. 5.17 are reported in Table 5.2. The condition presented in Eq. 5.17 behaves as a boundary source term for moisture transfer in air. Ignoring convection inside the

a	b	c	d	e
9.567 56	−5.398 06	−6.161 83	1.495 72	0.433 00

TABLE 5.2: Coefficients for the interpolation function of saturation vapor pressure over temperature.

oven cavity, moisture transfer occurs mainly by diffusion and thus described by the Fick's law. The governing equation for diffusive moisture transfer in the air domain is:

$$\nabla \cdot (-D_{air} \nabla c_{vap}) = 0 \tag{5.18}$$

At a far away location, the boundary condition is set at the undisturbed initial value:

$$c_{vap}|_{bc} = c_0 \tag{5.19}$$

with the wall, the floor of the oven and the uncut surfaces of the food with skin present, being impermeable

$$\nabla c_{vap} \cdot \vec{\mathbf{n}} = 0 \tag{5.20}$$

Coupling between the moisture and the heat transfer models comes from Eq. 5.14 and Eq. 5.17, and it is a two-way coupling.

Electron mean free path in the gas components

The ionization in a gas is primarily influenced by three critical parameters: the required ionization energy, the applied electric field magnitude and the electron mean free path in the gas [6]. In particular, the electron mean free path determines the average distance that can be traveled by electrons between collisions. Therefore, this parameter is related to the number of possible ionizing events along the path of any electrons, given certain thermodynamic conditions. The electron mean free path in the gases is obtained as follows. Consider the ionization term [74]:

$$\alpha = \frac{1}{\lambda_e} e^{-\left(\frac{V_i}{\lambda_e |\mathbf{E}|}\right)} \tag{5.21}$$

the dependence of the mean free path onto the characteristics of the gas [78]:

$$\lambda_e = \frac{k_b T}{P \sigma_{coll}} \tag{5.22}$$

The dependence of the ionization term on the reduced electric field (for both dry air and vapor), which is shown from literature in Table 5.3 [78]. From Eq.s 5.21 and 5.22 we can explicitly show the dependence of the reduced ionization (α/P) over the reduced electric field $(|\mathbf{E}|/P)$ as:

$$\frac{\alpha}{P} = \frac{\sigma}{k_b T_e} e^{-\left(\frac{V_i \sigma}{k_b T_e} \frac{P}{|\mathbf{E}|}\right)} \tag{5.23}$$

Fitting the available tabular data with the analytical expression of ionization, we derive the effective electron mean free paths for vapor and air. Equation 5.23 shows that the term (α/P) depends strictly

$\frac{\|\mathbf{E}\|}{P}$	$\left(\frac{\alpha}{P}\right)_{vap}$	$\left(\frac{\alpha}{P}\right)_{air}$
30	1.000E-1	3.0E-3
35	1.250E-1	8.7E-3
40	2.000E-1	1.90E-2
45	3.250E-1	3.52E-2
50	5.000E-1	5.75E-2

TABLE 5.3: Computed ionization coefficient as corresponding to the reduced electric field for vapor and dry air.

on $(|\mathbf{E}|/P)$. Therefore, it is possible to derive an expression for λ_e imposing the equality of the ionization terms. From equation 5.21:

$$e^{\ln(\alpha\lambda_e)} = e^{-\left(\frac{V_i}{\lambda_e|\mathbf{E}|}\right)}$$

$$\ln(\alpha\lambda_e) = -\frac{V_i}{\lambda_e|\mathbf{E}|}$$

$$\lambda_e = \frac{V_i}{\frac{|\mathbf{E}|}{P}P\left[\ln\lambda_e + \ln\left(\frac{\alpha}{P}P\right)\right]} \tag{5.24}$$

Equation 5.24 allows iterative computation of λ_e for a pair of values $\left\{\frac{|\mathbf{E}|}{P}, \frac{\alpha}{P}\right\}$ by minimizing the error:

$$\epsilon(\lambda_e) = \sum_{\frac{|\mathbf{E}|}{P}=1}^{n}\left[\frac{1}{\lambda_e P}e^{-\left(\frac{V_i}{\lambda_e|\mathbf{E}|}\right)} - \frac{\alpha}{P}\left(\frac{|\mathbf{E}|}{P}\right)\right]^2 \tag{5.25}$$

Using the values in Table 5.3, we can obtain λ_e for each gas at a particular temperature. Considering Eq. 5.21, dividing by P, and making explicit the linear relation of λ_e over T, we derive as follows:

$$\frac{\alpha}{P} = \frac{1}{\lambda_e P}e^{-\left(\frac{V_i}{\lambda_e|\mathbf{E}|}\left(\frac{T_0}{T}\right)\right)} \tag{5.26}$$

Spanning the values of λ_e as independent variable of equation 5.26 we can obtain multiple curves of α/P, at a given temperature and pressure. Considering the environmental temperature and the atmospheric pressure, the obtained data fit the values in Table 5.3, given the appropriate equivalent value of λ_e. The (α/P) curves over $(|\mathbf{E}|/P)$ have been depicted in Fig. 5.5 for vapor (top) and dry air (bottom). At the standard conditions T_0, P_0, several curves have been reported, given multiple values of λ_e (Fig. 5.5 (a)-(c)). Considering different values of temperature at the atmospheric pressure, the

(α/P) curves over $(|\mathbf{E}|/P)$ have been reported, considering the value of λ_e such that minimizes the error (Fig. 5.5 (b)-(d)). Minimizing the error we obtain the equivalent λ_e in vapor and in dry air: $(\lambda_e)_{vap} = 0.986594 \cdot 10^{-4}$ cm, $(\lambda_e)_{air} = 1.2707 \cdot 10^{-4}$ cm. The range of maximum and minimum values are $(\lambda_e)_{vap} \in \left[0.986 \cdot 10^{-4}; 1.170 \cdot 10^{-4}\right]$ cm and $(\lambda_e)_{air} \in \left[1.224 \cdot 10^{-4}; 1.317 \cdot 10^{-4}\right]$ cm.

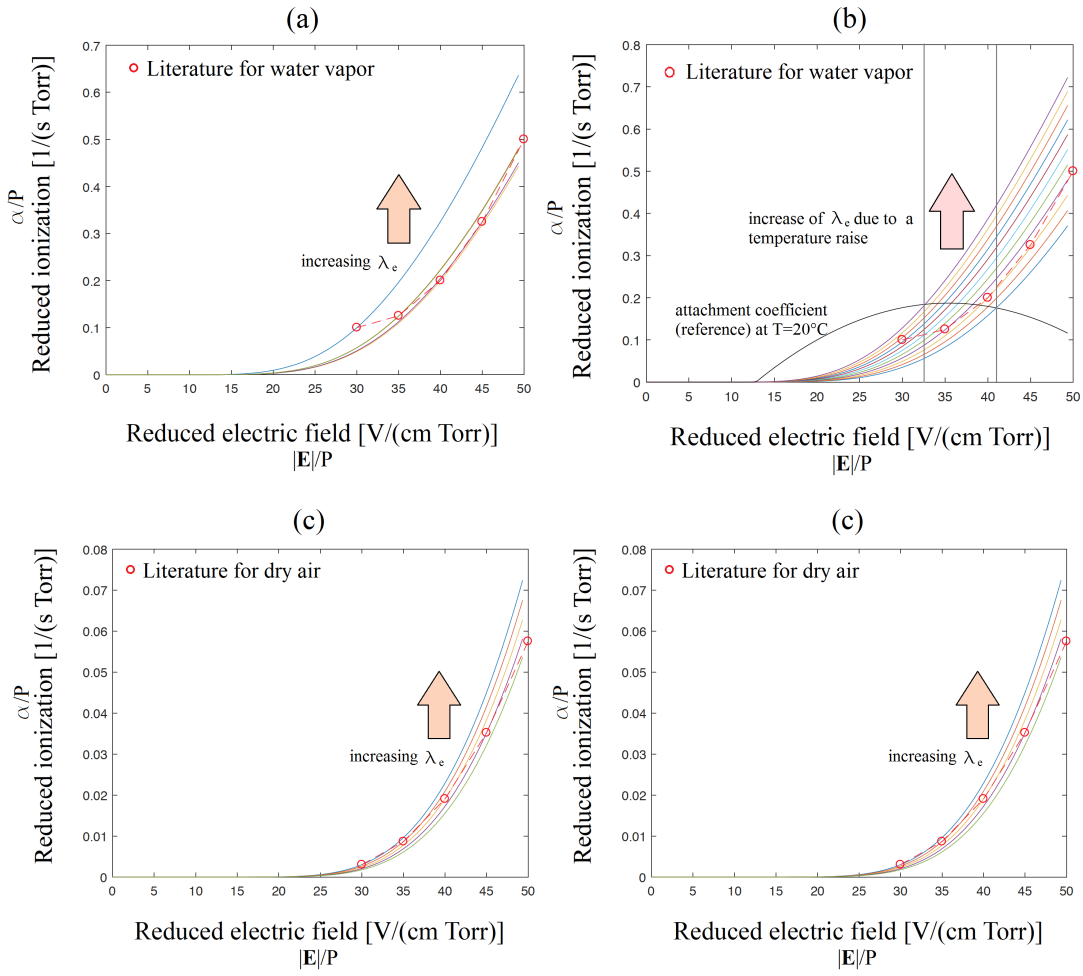

FIGURE 5.5: (a) - (c) Reduced ionization as function of reduced electric field, parameterized by different λ_e. (b) - (d) For a fixed value of λ_e, reduced ionization as function of reduced electric field, parameterized by the temperature of the gas. The top figures are for vapor and the bottom figures are for dry air.

Electron transport and discharge formation

In order to analyze the evolution over time of the electron population, we must take into account all the electron transport phenomena as diffusion, electron density variation, and the source and sinks

terms like ionization and attachment. Recombination can be neglected in the conditions of the current analysis [66]. The star indicates that we are dealing with an equivalent pressure, because the physical dependence over the reduced electric field is with $(|\mathbf{E}|/n)$, but since $n = P/(RT)$, we can adopt the equivalent value $P_* = P(T/T_0)$. Velocities of the electrons as a function of the reduced electric field $(|\mathbf{E}|/P_*)$ for both dry air and vapor (Table 5.1 for the general expressions or data sources) [79, 80] are:

$$(v_e)_{vap} = f_{vap}\left(\frac{|\mathbf{E}|}{P_*}\right) \quad (v_e)_{air} = f_{air}\left(\frac{|\mathbf{E}|}{P_*}\right) \tag{5.27}$$

and similarly, we can consider the ionization and attachment dependencies over the reduced field for both the gas components [4]:

$$\eta_{vap} = g_{vap}\left(\frac{|\mathbf{E}|}{P_*}\right) \quad \eta_{air} = g_{air}\left(\frac{|\mathbf{E}|}{P_*}\right) \tag{5.28}$$

$$\alpha_{vap} = h_{vap}\left(\frac{|\mathbf{E}|}{P_*}\right) \quad \alpha_{air} = h_{air}\left(\frac{|\mathbf{E}|}{P_*}\right) \tag{5.29}$$

The diffusive transport of water vapor (Eq. 5.18) provides the partial pressures of vapor p_{vap} and dry air p_{air} at any location. Electron mobilities are given by:

$$(K_e)_{vap} = \frac{(v_e)_{vap}}{|\mathbf{E}|} \quad (K_e)_{air} = \frac{(v_e)_{air}}{|\mathbf{E}|} \tag{5.30}$$

The electron mobility is not influenced in a relevant way by the alternative polarization of the electric field, considering that the operative angular frequency is much smaller than the collision frequency [81]:

$$\nu_c = 5.3\ 10^9 P \ \rightarrow \ \nu_c \gg \omega \tag{5.31}$$

where the pressure P is defined in Torr. Regarding the electric field magnitude there is not any influence at the operative frequency.

$$E_{eff} = \frac{E_{rms}}{\sqrt{1 + \left(\frac{\omega}{\nu_c}\right)^2}} \approx E_{rms} \tag{5.32}$$

The electron mobility for AC regime can be written explicitly in terms of the angular frequency [6]:

$$K_e = \frac{(e/m_e)\,\nu_c}{\nu_c^2 + \omega^2} \approx \frac{(e/m_e)}{c} \tag{5.33}$$

So K_e does not depend on the angular frequency and can be well approximated by the electron mobility for static fields (until the condition in Eq. 5.31 holds). The electron mobility of the gas mixture (water vapor and air) is estimated from the electron mobilities of the individual gases (at atmospheric pressure) as:

$$\frac{1}{(K_e)_{mix}} = \frac{p_{vap}}{P_0}\left(\frac{1}{(K_e)_{vap}}\right) + \frac{p_{air}}{P_0}\left(\frac{1}{(K_e)_{air}}\right) \tag{5.34}$$

Like in Eq. 5.34, the average value of the electron mean free path in the gas mixture, is estimated as:

$$\frac{1}{(\lambda_e)_{mix}} = \frac{p_{vap}}{P_0}\left(\frac{1}{(\lambda_e)_{vap}}\right) + \frac{p_{air}}{P_0}\left(\frac{1}{(\lambda_e)_{air}}\right) \tag{5.35}$$

which can be derived starting from the mean free paths in the insulated gas components at atmospheric pressure λ_{vap}, λ_{air} [74]. It is important to observe that the electron mean free path in the gas is strongly influenced by the thermodynamic conditions of pressure and temperature (Eq. 5.22 in the section 5.4.1) The electron diffusivity in the gas is computed from electron mobility as [74]:

$$D_e = \frac{1}{3}(\lambda_e)_{mix}(v_e)_{mix} = \frac{1}{3}(\lambda_e)_{mix}(K_e)_{mix}\,|\mathbf{E}| \tag{5.36}$$

The other important parameters that determine the electron transport phenomena are the ionization and the attachment coefficient. These parameters are strictly related to the partial pressures and the temperature as presented in Eq. 5.37 and Eq. 5.38:

$$\alpha_{mix} = \frac{T}{T_0}\left[\alpha_{vap}\left(\frac{p_{vap}}{P_0}\right) + \alpha_{air}\left(\frac{p_{air}}{P_0}\right)\right]$$

$$\nu_{ion} = (v_e)_{mix}\alpha_{mix} \tag{5.37}$$

$$\eta_{mix} = \frac{T}{T_0}\left[\eta_{vap}\left(\frac{p_{vap}}{P_0}\right) + \eta_{air}\left(\frac{p_{air}}{P_0}\right)\right]$$

$$\nu_{att} = (v_e)_{mix}\eta_{mix} \tag{5.38}$$

Using these electron transport parameters, the governing electron transport equation is given by [6]:

$$\frac{\partial n_e}{\partial t} = \nabla\cdot(D_e\nabla n_e) + (\nu_{ion} - \nu_{att})\,n_e \tag{5.39}$$

Equation 5.39 provides the evolution of the electron population in the gas mixture during the microwave heating. In this way, all the variations related to the thermodynamic changes can be accounted for, since D_e, ν_{ion} and ν_{att} are functions of p_{vap} and p_{air} (Eq. 5.34, 5.35, 5.37, 5.38), and T (Eq. 5.27, 5.29, 5.37 5.38). Also, included in the electrodynamics (Eq. 5.27, 5.30, 5.36). A classical threshold condition for breakdown is the Townsend's criterion that states that the plasma discharge occurs when the rate of the supplied electrons (new electrons for ionization) is equal to the rate of the subtracted electrons (diffused and attached electrons) [6]. This criterion can be written as:

$$\frac{\partial n_e}{\partial t} \geq 0 \rightarrow \nabla \cdot (D_e \nabla n_e) + \nu_{ion} n_e = \nu_{att} n_e \tag{5.40}$$

While this criterion can be suitable for steady state analysis, it needs to modified for an evolutionary dynamics. The easiest way to modify this criterion is by introducing a temporal condition. The changes in the system cannot affect the growth-chain after a certain period:

$$\exists t_* : \forall t > t_* \quad \frac{\partial n_e}{\partial t} \geq 0 \tag{5.41}$$

Therefore, this condition corresponds to the more compact expression:

$$\lim_{t \to \infty} \frac{\partial n_e}{\partial t} \geq 0 \tag{5.42}$$

The condition in Eq. 5.40 is now suitable for an evolutionary system, but still, it is not adequate for numerical implementation. Therefore, it is convenient to define a threshold level n_e^* of the electron density that must be reached to obtain a discharge. So, Eq. 5.38 must be satisfied until the condition in Eq. 5.43 is achieved. The threshold value of the electron population density to induce an irreversible electron build-up is $n_e^* = 10^{14}$ [1/m^3] [82, 83]:

$$n_e \geq n_e^* \tag{5.43}$$

Considering that the background electron population is mainly related to cosmic radiation and photoionization, the depletion of the electron population is actually compensated by these natural sources [4]. Therefore, it is possible to consider the background electron population at a steady level, since the attached electrons are replaced continuously. This background level can be considered as the initial condition of any electrodynamic micro-scale time-domain analysis.

Electrodynamic boundary conditions at the dielectric interfaces

The computation of boundary conditions for a weakly ionized gas at any dielectric surface is necessary to obtain an expression for the electron density (Dirichlet condition), which can be applied at any surface of food. The general condition regarding the charge density change over time is [84]:

$$\frac{\partial \rho_{ch}}{\partial t} = e\left(\frac{1}{4} n_e v_{e_{th}} - \frac{1}{2} n_i v_{i_{th}}\right) \tag{5.44}$$

Since the gas in the cavity is weakly ionized, we can assume that the electron density approaches the ion density (quasi-neutrality) [5]:

$$n_e \approx n_i \tag{5.45}$$

The thermal velocities of electrons and ions can be expressed respectively, as function of temperature and mass as [85]:

$$v_{e_{th}} = \sqrt{\frac{2k_b T_e}{m_e}} \tag{5.46}$$

$$v_{i_{th}} = \sqrt{\frac{2k_b T_i}{m_i}} \tag{5.47}$$

In normal conditions, the electron temperature is much higher than the ion temperature $T_e >> T_i$ and since the electron mass is much smaller than the ion mass $m_e << m_i$:

$$v_{e_{th}} >> v_{i_{th}} \tag{5.48}$$

If we substitute Eq.s 5.45 and 5.48 into Eq. 5.44, we can derive a simplified equation for the ion density as:

$$\frac{\partial \rho}{\partial t} = \frac{1}{4} n_e e v_{e_{th}} \tag{5.49}$$

Finally, substituting the term related to electron thermal velocity (Eq. 5.46) into Eq. 5.49, the boundary condition is obtained for the model:

$$n_e = \frac{4}{e v_{e_{th}}} \frac{\partial \rho}{\partial t} = \frac{2\sqrt{2} m_e}{e\sqrt{k_b T_e}} \frac{\partial \rho}{\partial t} \tag{5.50}$$

The term $\partial\rho/\partial t$ is obtained from the electromagnetic computation, the electron temperature in presence of a microwave field is computed from [86]:

$$T_e = T + \frac{m_i e^2 \left|\mathbf{E}\right|^2}{3k_b m_e^2 \omega^2} \tag{5.51}$$

where the ion mass of the gas m_i, which is assumed equal to the molecular mass, can be derived through the weighted average of the mass of the molecules [87]:

$$m_i = m_m = \left[x_{O_2}\left(\frac{W_{O_2}}{N_a}\right) + x_N\left(\frac{W_N}{N_a}\right)\right] \tag{5.52}$$

5.4.2 Numerical aspects

The model was implemented using the finite element software Comsol Multiphysics 5.2. Critical issues related to the implementation of the physics are here presented and discussed drawing particular attention to the physical coupling, the handling of numerical singularities and the necessary calibration of critical elements in the model.

Numerical implementation

In principle, EM can be performed in the frequency domain. But, since the material properties depend strongly on HT+MT, which must be solved in the time domain, the physics EM+HT+MT must be solved through a frequency-transient analysis. Because of the evaporation, HT and MT are related by a two-way coupling, instead EM can be solved in a segregated step to save computational burden. ED can be solved in the time-domain and it is characterized by a much smaller inertia of the frequency-transient physics. Therefore, at any step, it is possible to perform a multiscale one-way coupling to evaluate if the Townsend's criterion is verified as presented in Eq. 5.42 and Eq. 5.43. The general schema of the couplings has been depicted in Fig. 5.6.

Halves connection and geometrical singularities

From a physical point of view, the arcing phenomenon occurs when the proximity between the food pieces is sufficiently small that the created electric field is intense enough to trigger the discharge. In order to guarantee mechanical stability and reproducibility, as already described in the section 5.3,

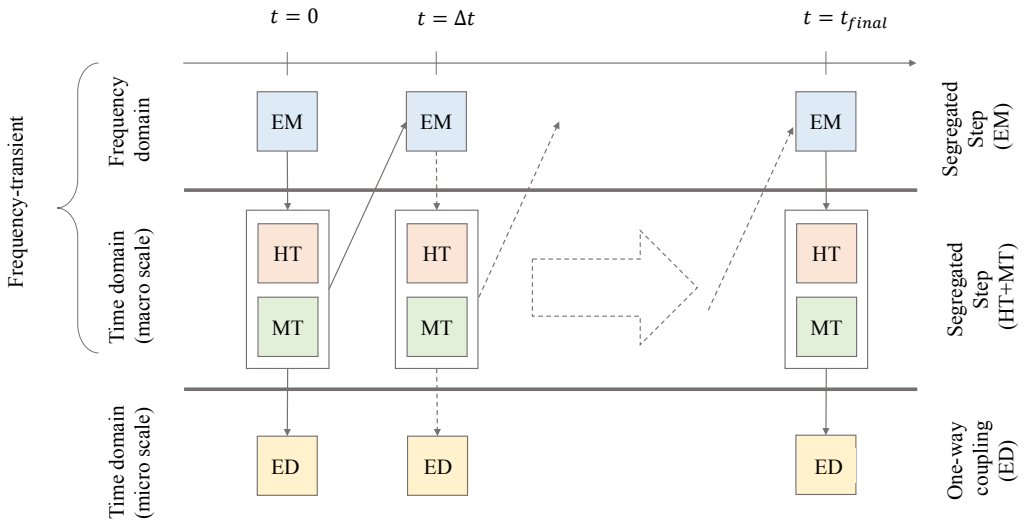

FIGURE 5.6: Coupling between the different physics and computational steps in the multiscale simulation.

the configuration characterized by the skin connection has been adopted. For geometrical implementation, the connection can be can be obtained through boolean operations between ellipses and parallelepipeds. Unfortunately, this series of operations generates sharp edges and sharp corners very close to the critical zone that can introduce geometrical singularities, and consequently, the correspondent numerical results in these zones can be strongly affected. If the connection is removed and the pieces are separated by a gap g the singularity can be avoided. Unfortunately, the case $g = 0$ rises again numerical issues because we are actually introducing material singularities. In fact, in this case, three material regions (grape piece 1 - air - grape piece 2) collapse in one point, which is in the critical zone. Instead, if we consider the case $g > 0$, we are introducing a non-physical condition which tends to monotonically decrease the electric field magnitude. Consequently, it is necessary to define a certain distance g that reproduces the physical observations, thus must be found through an experimentally based calibration. This calibration process can be run identifying a threshold condition for the discharge. A water-filled glass is introduced into the cavity, as described in section 5.3. The mass of water m must be varied until the minimum inception condition is achieved. This mass value is $\hat{m}_* = 65$ g (the hat indicates that the value has been found experimentally) and the experimental behavior has been also presented for the cases $m = 60$ g and $m = 70$ g in Fig. 5.7. The threshold mass $\hat{m}_*$ is sufficiently big to absorb the electromagnetic power and consequently to reduce

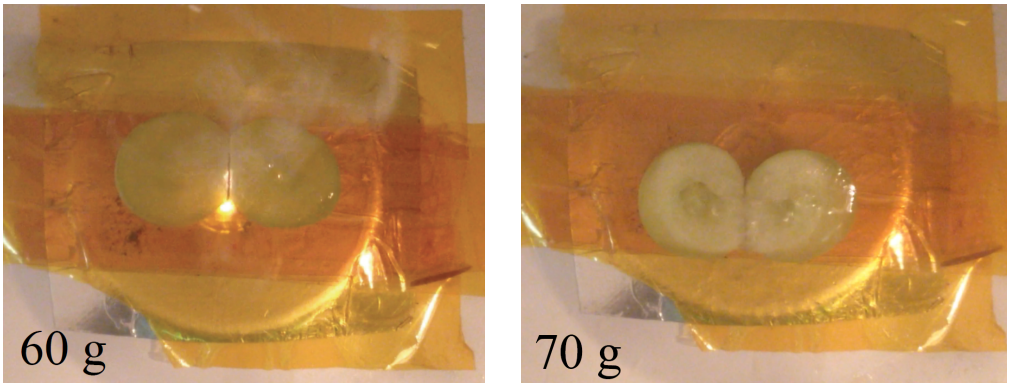

FIGURE 5.7: The mass of water added in the oven is 60 g on the left (showing arcing) and on the right is 70 g (sowing no arcing).

the electric field magnitude in the critical zone at the minimum triggering value. From a numerical point of view, the configuration that is characterized by the water-filled glass of mass $\hat{m}_*$, and the threshold gap distance g, must satisfy the lower case Townsend's criterion. This value of the gap distance can be identified as $\tilde{g}_*$ (the tilde indicates that the value has been found numerically) and it allows to align the threshold conditions between numerical model and experimental trials. The process of identification of $\tilde{g}_*$ is a calibration process and it is fundamental to guarantee the reliability of numerical predictions. The numerical results at the threshold conditions have been presented in Fig. 5.8, given the critical mass $\hat{m}_* = 65$ g and the corresponding threshold gap $\tilde{g}_* = 32\mu$m. Also, in the same figure, the cases $m = 60$ g and $m = 70$ g have been reported.

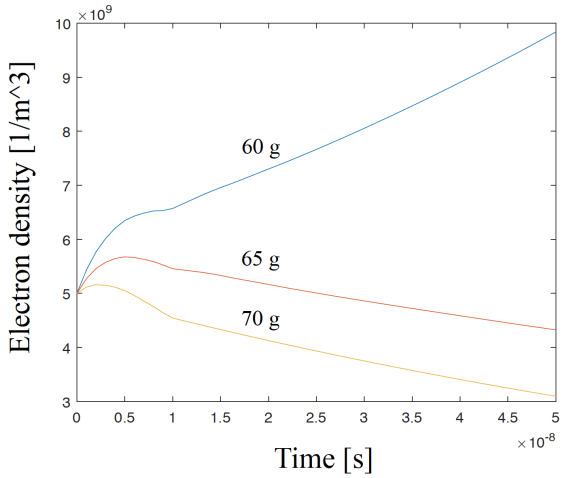

FIGURE 5.8: The evolution of the electron population over time near grapes for different amounts of added water that absorb energy.

5.5 Results and discussion

To develop the numerical model, some experiments must be done to perform calibration. In section 5.4.2 the calibration of the gap between the halves has been presented. Following cases are reported here: identification of power levels (data acquisition), calorimetric tests with different load-masses (calibration and validation), prediction and identification of threshold conditions for arcing (validation) and comparison of the temperature distributions from the model and experiments (validation).

5.5.1 Estimation and experimental validation of input power

The input power must be determined indirectly through calorimetric tests (calibration). A calorimetric experiment can be run considering a thermally insulated (by a glass-wool layer) glass, which has been filled by a water mass m, as thermal load. Then the glass should be located in a specific position of the cavity (e.g, central position). Here, it is possible to make measurements of the temperature rise over several incremental time periods. Before getting the measured value, the liquid is stirred to obtain the average temperature. When the calibration is concluded, it is independently validated by changing the thermal mass m and comparing the numerically predicted temperature with the experimental values. This validates the thermal model as shown in Fig. 5.9.

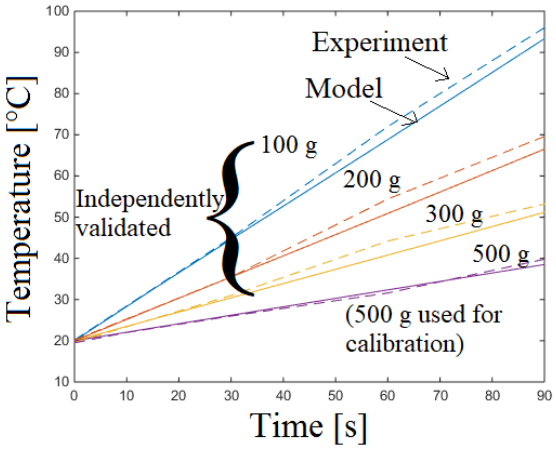

FIGURE 5.9: The model was calibrated using the water mass 500 g. The comparison between model and experiment for 100 g, 200 g and 300 g validates the coupled EM+HT model.

5.5.2 Experimental validation of the temperature

Figure 5.10 shows that the observed temperature rise magnitude and distributions are well predicted by the model.

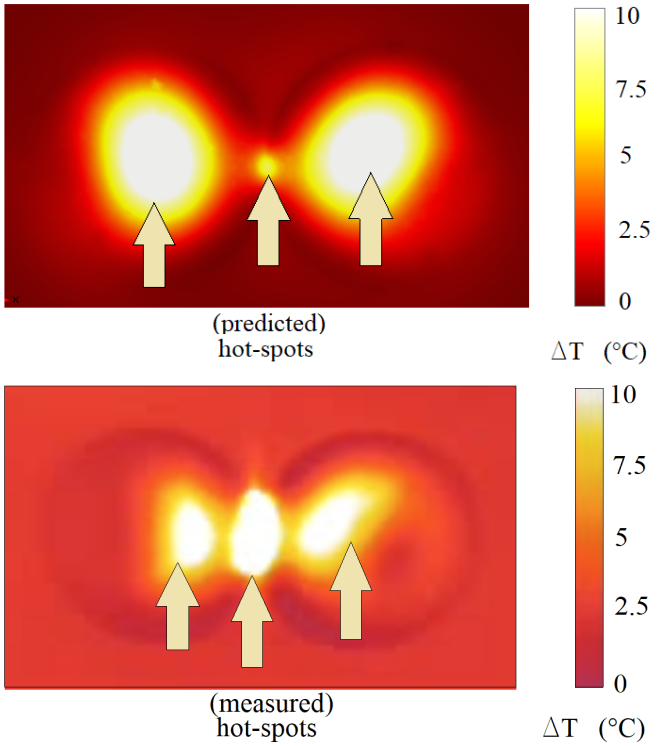

FIGURE 5.10: Comparison between the measured temperature distribution and the predicted values for validation of the thermal model.

5.5.3 Obtaining input power for electromagnetic calculation

From electrodynamics, it is important to consider the temporal evolution of the peaks of the electric field, since the peaks are the actual responsible for arcing. We can consider a discrete set of values that identify the evolution of the electric field peaks over time (discretization, n, finer discretization, m, $m >> n$):

$$p_{peaks_k} = \max_{t \in [k\Delta t,(k+1)\Delta t]} (p(t)) \qquad k = 1, ..., m \tag{5.53}$$

Also, considering that the relation between the power and the electric field is $p \propto |\mathbf{E}|^2$, we can introduce a new discrete function r_k as follows:

$$r_k = \sqrt{\frac{p_{peaks_k}}{p_{avg_j}}} \qquad k = 1, ..., m \quad \text{(corresponding: } j = 1, ..., n) \tag{5.54}$$

Here, the relation between the computed electric field within the electromagnetic physics can be inserted into the electrodynamics (one-way coupling), by introducing the discrete function r_k as peaks-to-average factor (the subscripts identify the physics of reference):

$$\mathbf{E}_{(ED)} = r_k \mathbf{E}_{(EM)} \tag{5.55}$$

In this way it is possible to guarantee the numerical stability of the solver and at the same time assess the dynamic evolution from an electrical as well as an electrodynamic point of view. All the experimentally measured power functions and the corresponding input functions have been reported in Fig. 5.11.

5.5.4 Influence of sample orientation

The position of the load inside the cavity influences strongly the distribution and the magnitude of the electric field within the material. Therefore, the position of the grape can be considered as a relevant parameter for the current validation. The simplest idea is to shift the grape on the base of the oven, but there are two practical difficulties. First, the base of the oven is not flat and therefore it is not possible to guarantee the mechanical stability in any position. Second, opening in the oven for interior viewing allows just a limited focus angle. There is another possibility to change the position of the grape avoiding the shifting, and this is through the change of the grape orientation θ. As already described in the section 5.3, we can take the grape and rotate it along the vertical rotation axis which must be centered in the barycenter of the food. By mean of numerical analysis, it is possible to determine the threshold arcing conditions in a few steps, in terms of the angular rotation θ_*. In the section 5.4.2, the arcing conditions of the system have been determined experimentally and numerically. In particular, it is possible to estimate the electric field magnitude in the critical region to triggering the breakdown at the maximum power level ($t \approx 0.9$ s; see Fig. 5.11 (b)). Considering the evolution of the power level (Fig. 5.11), we can extrapolate the corresponding initial value ($t = 0$ s) of the threshold electric field. This value is strongly influenced by λ_e and can be described as a function $|\boldsymbol{E}_*| = f(\lambda_e)$.

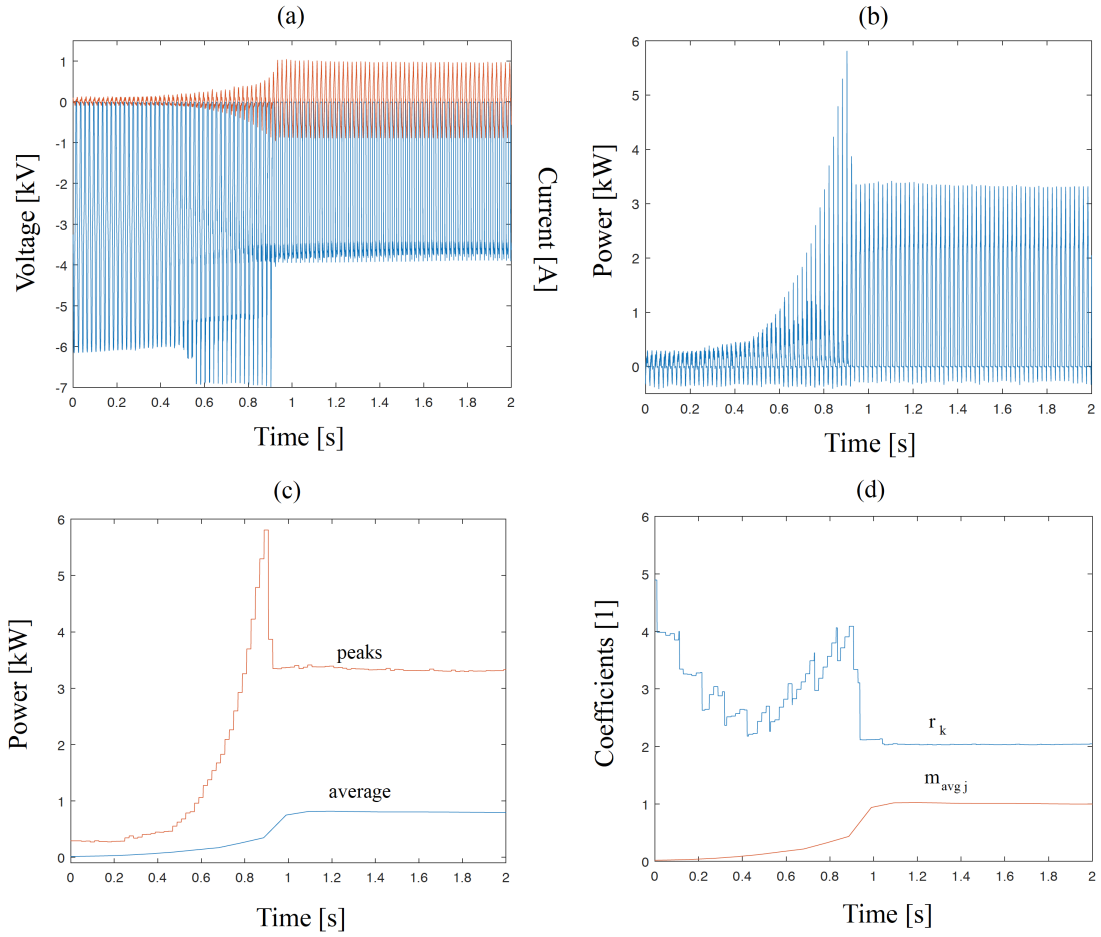

FIGURE 5.11: (a) Magnetron voltage (blue) and anode current (red). (b) Instantaneous power absorbed by the magnetron. (c) Power peaks evolution (red) and to the power average evolution (blue). (d) Implemented coefficients r_k and m_{avgj} as simulation input.

Therefore, in correspondence to the bounds of the electron mean free path determined in section 5.4.1, we can determine the bounds in terms of triggering electric field magnitude. The mass of the sample influences the intensity of the electric field peak, so, the variability of the mass was included in the model considering a size factor s ($s \in [0.9, 1.1]$). The electric field peak is a function of the angular rotation and size, and it can be described as $\max(|\boldsymbol{E}|) = f(\lambda_e, s)$. Computing these functions, it is possible to infer the bounds of the threshold conditions in terms of angular rotation as depicted in Fig. 5.12. Successively, an investigation through a complete (not only at $t = 0$ s)

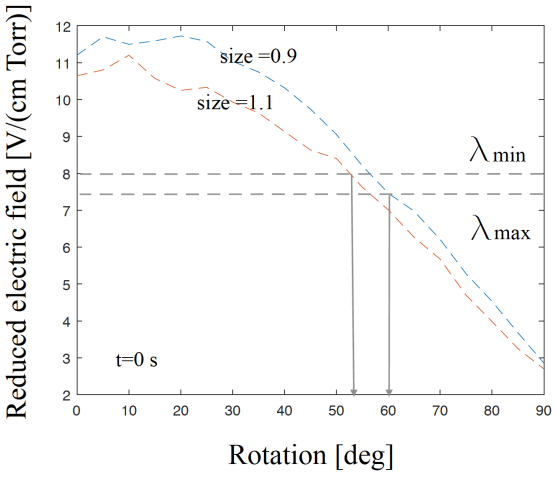

FIGURE 5.12: Maximum electric field in the contact position for various angular positions of the grape. Variability of the grape size and the uncertainty on the values of electron mean free path define the bounds of the arcing threshold in terms of angular position.

numerical analysis has been made setting $\theta = 50°$, $\theta = 53°$ and $\theta = 55°$. The results regarding the discharge occurrence have been reported in Fig. 5.13. Based upon experiments, it is possible to identify the experimental threshold rotation angle $\hat{\theta}_*$. This value has been estimated by $\hat{\theta}_* = 55°$ and it is in agreement with the corresponding value of $\tilde{\theta}_* \approx 53°$ that has been numerically found (Fig. 5.13). The experimental cases at $\theta = 55°$ have been reported in Fig. 5.14, showing that this angular rotation corresponds to an unstable arcing condition. The numerical predictions are consistent with the experimental observations, thus validating the model.

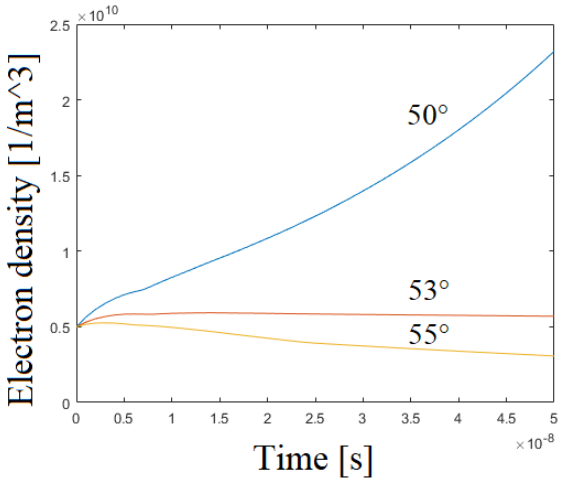

FIGURE 5.13: The evolution of the electron population over time near grapes for different sample orientations.

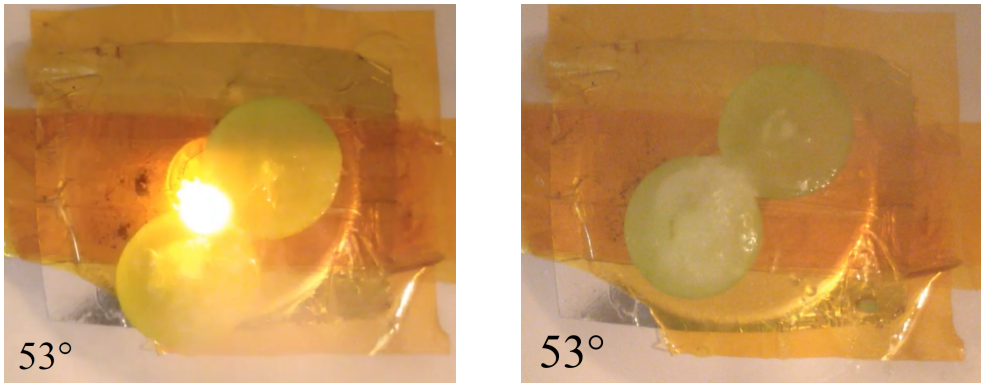

FIGURE 5.14: For an angular position of 53°, the two figures demonstrate an unstable threshold condition.

5.5.5 Sensitivity analysis

The numerical model is used to predict discharge conditions in different situations and identify a practical safety condition for avoiding arcing. Influences of other environmental parameters on the plasma breakdown has been presented. Since the electric field peaks are the actual responsible of the electron chain-growth, in Fig. 5.15 there are several slices depicting the electric field values. We can observe that the most intense electric fields are at the contact position between grape pieces and between the support and the grape. In fact, in certain conditions (e.g., presence of only one half), the bottom-zones can be characterized by electric field magnitudes such that it is possible to achieve the breakdown conditions even without contact between food pieces. Therefore, we can state that the critical regions are primarily the contact zones between different food-pieces, but the contact zones between the metallic support and the food are also important. This behavior has been experimentally observed by the presence of highly localized burns in the bottom positions of several specimens (an example can be seen in Fig. 5.16).

Prediction of discharge formation

This section predicts the ambient conditions that would lead to arcing. The physical parameters that determine the discharge are the temperature T, the humidity c_{vap} and the electric field magnitude $|\mathbf{E}|$ (the pressure is considered atmospheric). In principle, the discharge is determined by three important variables which correspond to three degrees of freedom, but, considering that the phenomenon occurs only at the surface of food, two simplifications can be made. First, since at the external surface of food the Eq. 5.17 holds, we can eliminate one degree of freedom because $c_{vap} = f(T)$. Second, since the temperature is a continuous function over space, the temperature at the surface of the food in the air side is actually the same of the temperature at the solid side. In this way, the analysis can be run considering the temperature in the range $T \in [273.15; 373.15]$ K as the only independent environmental parameter. Moreover, in the current analysis we can consider that the distribution of the electric field is fixed, so we can just modulate the maximum value of the field using a scalar coefficient $\alpha \in [0.5; 1]$, assuming as reference value $E_{ref} = 3.80 \times 10^6$ (V/m) (This value is the threshold electric field magnitude to induce arcing at any food temperature). Given these conditions, we can assess the discharge formation just computing the electrodynamics and assuming T and $|\mathbf{E}|$ as independent variables. The results of this analysis are shown in Fig. 5.17 where the color blue identifies the non-discharge zone, and the remaining colors identify the zone where the electron population increases in

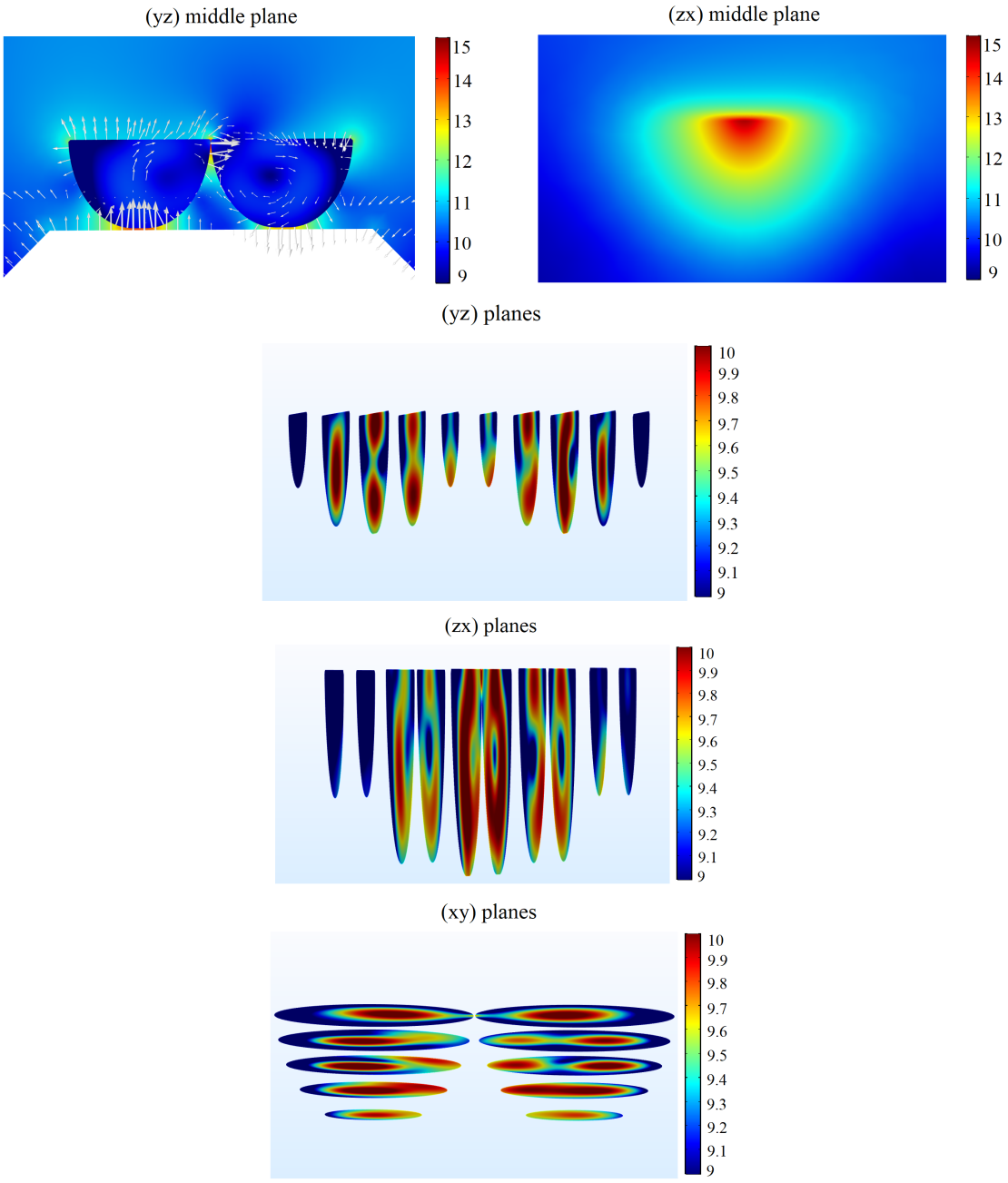

FIGURE 5.15: The electric field magnitude (V/m) in logarithmic scale, since the levels in air and within the grape differ by several orders of magnitude.

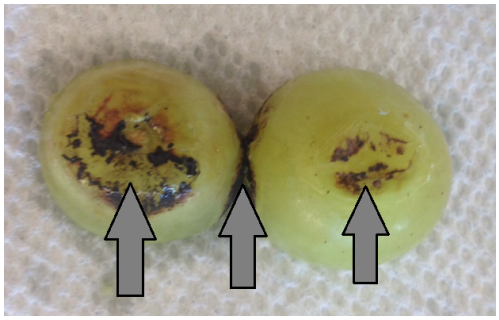

FIGURE 5.16: Burns at the bottom contact with the floor from large electric field.

irreversible way. From the figure, for $\alpha > 0.95$ discharge occurs at any food temperature, while for

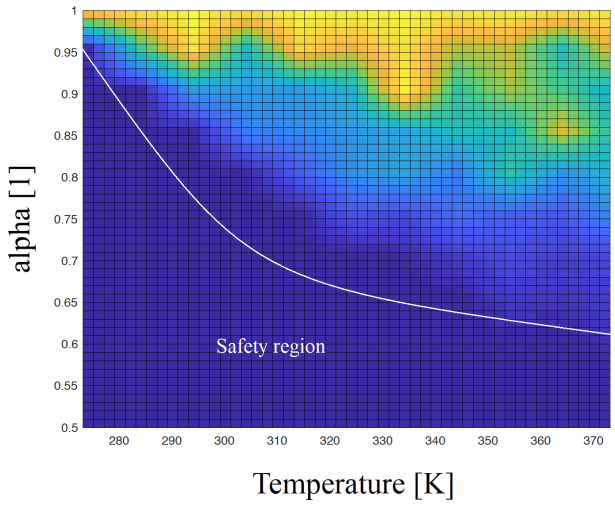

FIGURE 5.17: Dependence of the discharge occurence on temperature and electric field magnitude. The blue zone represents the safe region since the electrodynamic conditions do not satisfy the dynamic Townsend's criterion.

$\alpha < 0.65$ the discharge cannot occur even at the boiling temperature. From these considerations, we can define an empirical safety condition for practical purpose as follows:

$$E_{contact} < (0.95 \cdot E_{ref})\, e^{-4.16\times10^{-3}\left(T_{food}-273.15\right)} \tag{5.56}$$

where $E_{contact}$ (measured in (V/m)) is the maximum value of the electric field in the location of contact between different food pieces or between the bottom and the support, and T_{food} (measured in K) is the temperature in the food at the closest position to the contact.

Influence of the main environmental parameters

This section analyzes the influence of the main environmental parameters (temperature, T and humidity, c_{vap}) and external factors (electric field magnitude $|\mathbf{E}|$) onto the discharge occurrence. For a positive increase on the electric field magnitude, Table 5.1 shows that the electron velocity increases linearly. Also, from Eq. 5.36, 5.37, 5.38 we can note that there is a linear relation between the velocity v_e and all the terms $D_e, \nu_{ion}, \nu_{att}$, giving an overall effect of increasing the dynamics of the electron population, but not directly affecting the arcing. On the other hand, if the electric field magnitude increases, there is a strong influence on the ionization and attachment coefficients (Eq. 5.28 and 5.29 respectively). Eq. 5.21, shows the exponential relation between the electric field and the ionization rate. For the attachment coefficient, the behavior is not monotonic since there is a maximum level at a certain reduced electric field value. Therefore, for small electric field increases the discharge can be obstructed, but for bigger changes, the discharge is strongly favored. For positive ΔT, there are several correlated effects on the electrodynamics. First, the effective pressure can be linearly augmented proportionally to T, which corresponds actually to an equivalent rise on the field which triggers the ionization and the attachment. Second, Eq. 5.22 shows that the higher the temperature, the longer the electron mean free path. This has two main consequences – the electron diffusion D_e gets bigger, which means that the local electron build up is discouraged. In this way, the growth of the effective electric field is compensated by the increased diffusion, just affecting the dynamics but not leading to discharge. On the other hand, the electron mean free path can directly influence the ionization rate (Eq. 5.21). This relation is exponential and therefore it can strongly reduce the energy gap necessary for achieving the electron chain growth. Considering these three aspects, the overall effect of temperature increase is facilitation of the discharge. Finally, even the moisture concentration in air, which can be quantified by the partial pressure p_{vap}, influences the discharge occurrence. Comparing the plots related to ionization and attachment for the gas components dry-air and vapor, we can observe that the intersection point between the curves (Fig. 5.5, on the right) can be obtained at lower electric field magnitudes for dry-air with respect to vapor. Plasma discharge can occur more easily in drier air. Fig. 5.18 shows the interrelation between the physical quantities influencing the electron population. Fig. 5.19 shows the general schema of the main factors affecting the arcing.

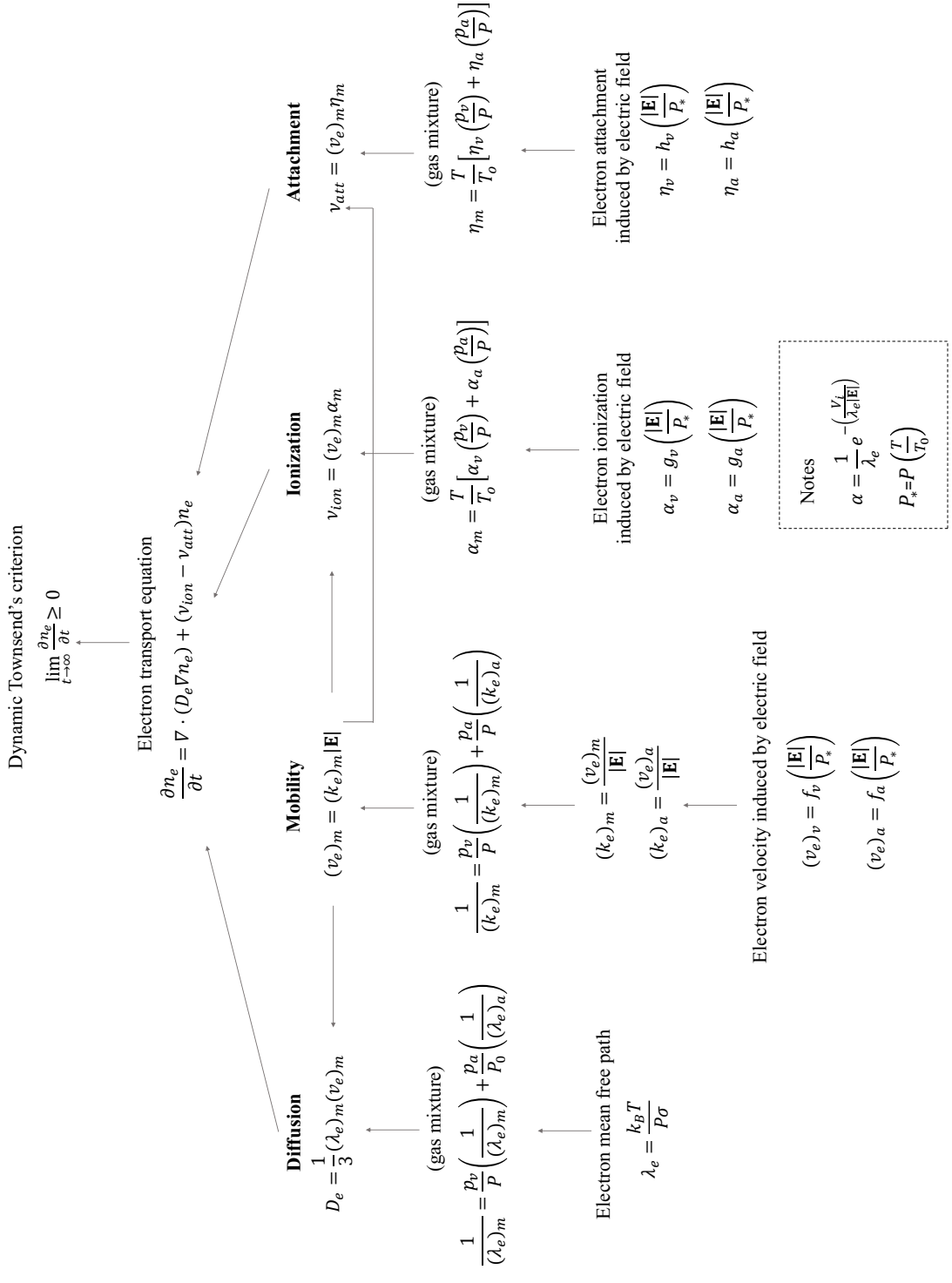

FIGURE 5.18: Relative influence of the electrodynamic physical variables and their mutual connection.

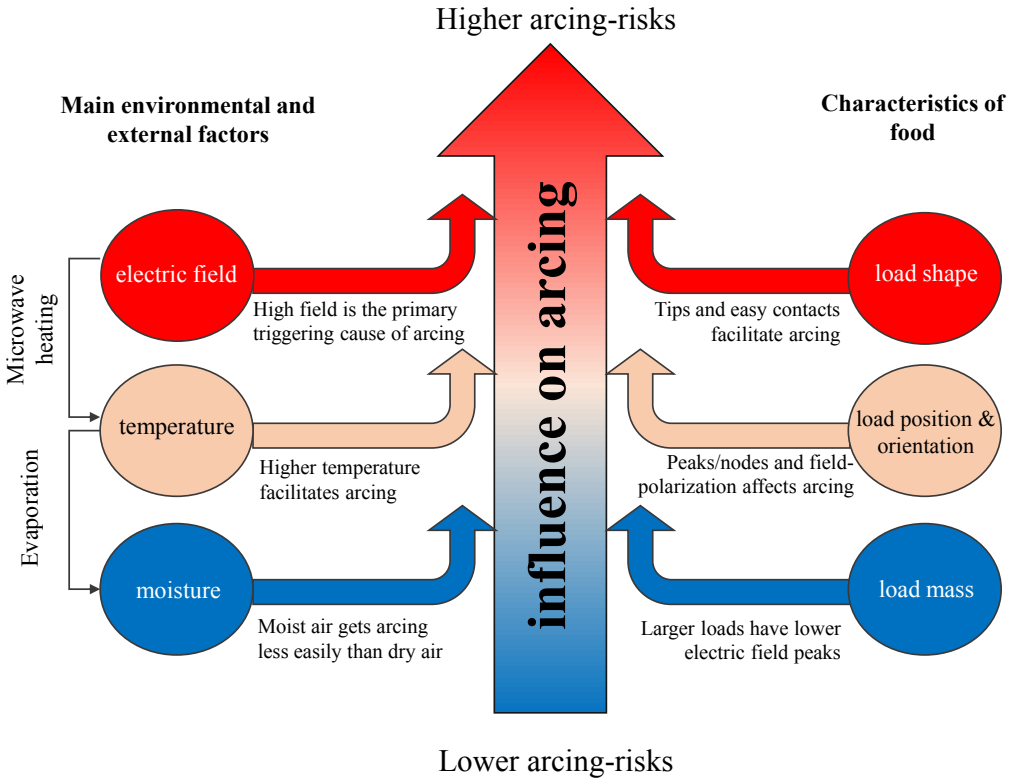

FIGURE 5.19: Schematic summarizing the main factors influencing the arcing.

5.6 Conclusions

A comprehensive multiphysics model that includes electromagnetics, electrodynamics, heat transfer and moisture transfer that is also multiscale (oven cavity and the small region around the food) was developed and validated. The model is less restrictive in being full 3D and with respect to parameters such as range of temperature and microwave frequencies over which it is valid. The mechanistic understanding allows us to more precisely identify the important factors leading to arcing. For example, based on this understanding, it is unlikely that that minerals in the food are the primary cause for discharge, as has been reported in some sources [55, 56]. In drier air, arcing would occur at lower power level as the equilibrium between ionization and attachment is achieved at lower electric field magnitude than in moist air. Higher temperature leads to greater chances of arcing as higher temperature increases ionization more than it increases attachment. If the food load is too small, additional load such as a glass of water should be included in the oven to reduce the chances of arcing—while this was partly known from experience, the relationships between various parameters leading up to arcing for small volume heating are shown here. Sample geometry, orientation, and placement inside the oven are also some of the significant factors. A safe zone for operation has been identified in terms of maximum electric field values and temperatures. These threshold conditions can be used to identify unsafe situations for domestic microwave ovens. For example, knowing the maximum electric field (e.g., from a simulation), an oven manufacturer can estimate the minimum mass necessary inside the oven to avoid discharge. These conditions would be useful for testing other microwave devices at specific operating conditions.

6 Enhanced Power Density Uniformity for Microwave Catalytic Reactions Adopting Solid-State Generators: Comparison with Magnetron Technology

6.1 Abstract

Endothermic processes at high temperature are typically implemented through heat transfer techniques based on thermal conduction from the surface. This situation implies non-uniform radial temperature within the load causing a lower quality process. The microwave (MW) based volumetric heating is the ideal alternative to improve these processes, but axial-thermal gradients appear for the presence of resonant standing waves. In the current research, a laboratory-prototype has been developed to experimentally validate an implemented Finite Element (FE) model. The efficiency and the non-uniformity have been assumed as objective functions, and the Pareto-fronts have been evaluated to compare Magnetron Based Systems (MBS) and Solid-state Based Systems (SBS). The physical effects related to the porosity of the subsceptor (SiC) have been numerically evaluated in the range from 0 to 0.6. The higher the porosity the more uniform the heating pattern. At equal efficiency conditions, the SBS can achieve a 20% reduction of non-uniformity with respect to MBS. The statistical distribution of the electric field in SBS is right-skewed quasi-Gaussian, meaning that the most frequent power density level is close to the mean value. SBS defines Pareto-configurations that are dominant with respect to those based on MBS.

6.2 Introduction

Steam reforming is the most widespread and sustainable process for the production of synthesis gas ($CO+H_2$) from hydrocarbons. For a long time, hydrogen plays a fundamental role in the chemical industry, since it is largely used in many processes [88]. Nowadays, hydrogen has increasing importance in new fields. One of these promising applications is the fuel cell technology, mainly related to the motion of vehicles or small-scale power generators. However, some obstacles related to the storage and the distribution of hydrogen induce the development of compact generator systems [89]. Nickel based catalysts are generally employed in this catalytic heterogeneous process, which is leaded in tubular reactors. The conventional process is carried out at high temperature (650-1000 °C), and it is typically conducted in large central plants which are mostly based on combustion. Despite this process has already achieved the technological maturity, it presents a major drawback related to the inability of exploiting uniformly the catalytic bed because of the presence of thermal non-uniformities. The temperature gradients occur since the heat transfer is supplied from the reactor walls, and therefore the heat absorption rate in the core cannot be compensated by the radial diffusion from the walls. The more the reaction is endothermic and the more the problem is severe. For this reason, dielectric volumetric heating, which is characterized by direct energy conversion within the material, seems to be an ideal candidate to overcome this limit on an industrial scale. The resolution of this problem could extend the life of the catalyst thanks to the minor deposition of carbon, which generally appears at lower temperatures [90]. Microwave heating is a well-known energy conversion process, largely used in domestic scale and also increasingly used in industry. Although microwave applications for low temperature processes in chemical industries are currently adopted, high-temperature systems of this technology need further developments [91, 92], in particular regarding some issues on homogeneity [93]. The microwave-heating pattern is strictly correlated to the pattern of the electric field in the material, and in general, it is non-uniform because of the presence of resonant electromagnetic standing waves. These waves are associated to the shape of the resonant cavity and they arise as a series of electromagnetic modes, selected by the propagation wavelength. Therefore, the choice of using a dielectric heating for achieving more temperature uniformity, thanks to a direct energy-conversion within the material, seems to become ineffective for the presence of non-uniformities over the entire volume. The idea of adopting microwave technology in catalytic processes for limiting thermal gradients is actually quite old, and a remarkable work on this topic has been done by Perry and Brown [94]. In the mentioned work, there is a numerical and experimental comparison of radial gradients which

appear in tubular reactors, considering microwave and conventional processes. From the results of Perry and Brown, the radial temperature uniformity can be much better achieved with microwave processing than with conventional one. Despite this apparent success, after twenty years the conventional process is still the most widespread used in industry, and just a few lab-scale magnetron based prototypes have been constructed [95, 96, 97, 98, 99, 100]. It is important to observe that there are also other minor difficulties that are obstructing the development of microwave-based reforming processes, even if some of them have been successfully overcome. Let us point out the main obstacles, making a short recap. On one hand, there are several restrictions to achieve an energy efficient scale-up related to the relation between the adopted cavity and the mass of the sample [101]. On the other hand, if the load-mass is too small, there are several problems to couple efficiently the electric field with the matter. Also, regarding real-time temperature measurement, using metallic thermocouples, there are some problems related to electromagnetic compatibility. Therefore, non-standard thermometers must be developed. An interesting investigation has been assessed by Farag & Chouki on a thermometric technique for the specific use in microwave cavities [102]. Another delicate issue is due to the fact that the reagents should behave as microwave absorber substances, and this feature is mainly related to the presence of polar molecules. Unfortunately the reagents are in gas-phase, and the typical catalyst (Ni/Al2O3) is not a good microwave absorber. In recent works, carbon has been mixed with alumina-supported catalyst [88, 95]; also, silicon carbide (SiC) particles have been used in order to create a microwave absorbent bed [96]. Making an overall evaluation, we have to consider that magnetron technology for generating microwaves has already achieved the economical and technological maturity, even because the production on industrial scale started more than fifty years ago. Therefore, the probabilities that large magnetron based reforming plants can penetrate into the market, are decreasing over time. But still, the issues related to radial temperature gradients have not been solved. In fact, a very recent communication investigates the problem regarding the formation of a thermal boundary layer for endothermic reactions with convective heating [103]. Although many difficulties, since the dawn of the marriage of microwave heating and catalysis, the potential for high-temperature endothermic processes was evidently clear [104]. So, a spontaneous question arises: is there still today the possibility to create new microwave-based systems, which can really become competitive with the conventional technology? Even if the answer is far from being given, a recent technological innovation can play a major role in the future scenario. This innovation is available thanks to the development of solid state electronics at microwave frequency suitable to handle

several hundred watts of power. Since the description of operating principles of this new microwave technology is out of the purpose of the current work, the interested reader is addressed to the works [105, 106, 107]. Instead, the advancements derived from this technology are very important to understand the new degrees of freedom in terms of possible resulting electric field patterns. And so, these new electric field patterns can be properly determined to maximize the performances. Let us point out the related novelties. First, at any electromagnetic port, it is possible to control the initial phase of the varying field. Therefore, it is possible to superimpose the fields and to modify the resulting electric field in real time, giving the possibility to change the position of the nodes and anti-nodes. Second, it is possible to change the power of any port independently, increasing further the number of feasible electric field patterns. Third, it is possible to change dynamically the frequency in a certain range, which must comply the ISM band, giving the possibility to change the number of resonant modes. In the current study, just the first two cases have been considered, because the authors will investigate the possible patterns related to the dynamic frequency-shift in a separate research. It is clear that the use of numerical and mathematical modeling is a necessary wherewithal and an invaluable resource to exploit the renovated potential of microwave heating [108].The purpose of this study is to investigate several aspects related to high temperature applications, setting up an equipment to provide uniform microwave heating to yield high quality endothermic reactions. The thermal conditions considered in this work are referred to the methane steam reforming process. The main focus is turned to define a novel setup for microwave-assisted reactors, which can reduce not only radial gradients, but also axial ones. In fact, the presence of axial gradients is one of the major limitations to the potential of the industrial diffusion of microwave based reactors, affecting the competitiveness with respect to traditional heating technology. The investigation takes into account the porosity of the granular material through a systematical numerical analysis. The Pareto fronts of Magnetron Based Systems (MBS) and Solid-state Based Systems (SBS) technologies have been identified and compared. The optimal settings at any port for controlling the SBS system are given for different porosities of the granular subsceptor. Particular attention has been turned to the capability of improving the performances, exploiting the feasible electric field patterns, which correspond to the available degrees of freedom of each technology.

6.3 Materials and Methods: overall configuration

The initial prototype is derived from a commercial microwave oven for domestic use. The microwave oven adopted is characterized by a 700 W magnetron. In order to transfer thermal energy to the reagents, the walls of the reactor must be transparent to microwaves. A quartz tube can be used as tubular reactor, since it can face typical temperatures of steam reforming (greater than 650 °C). The internal diameter of the reactor is 16 mm, with a wall thickness of 2 mm. Since the reaction involves reagents in gas phase, which cannot be directly heated by microwave radiation, it is necessary to fill the reactor with a microwave absorbent porous bed. The materials forming the bed must have high thermal conductivity to properly transfer thermal energy to the gas reagents. A material that satisfies the requirements is silicon carbide (SiC), and it can be employed in granular shape. One of the necessary modifications to reach temperature over 600 °C is the reduction of heat losses by an improvement of the thermal insulation. Quartz wool can be employed to create an insulation layer around the reactor. Since the reflected electromagnetic power is directly absorbed by the magnetron, inducing dangerous overheating, an external air-cooling system is necessary. The inlet and the outlet regions, as the door-seal opening, can be potentially subjected to electromagnetic leakages, involving hazards for human safety. Fine electromagnetic insulation is required, and it can be obtained using metallic foils. All the circular gaps, with a radius smaller than the cutoff length in Eq. 6.1 for the lowest order mode TE_{11}, radiate an electromagnetic field which decays exponentially as evanescent wave [25]:

$$l_c = \frac{1.8412\ c}{2\pi f} \tag{6.1}$$

Where is the speed of light, is the frequency (2.45 GHz), giving the cut-off size 3.6 cm. Therefore, the radius of inlet and outlet cross-sections must be smaller than this value to avoid electromagnetic leakages toward the external environment. Considering the operative frequency, the European legislation has defined the guidelines for power density leakage [43]. The power control of domestic magnetrons is made by setting a duty-cycle, which determines the actual average output of the microwave source. Therefore, it is convenient to implement an hysteresis controller in order to handle the magnetron with two state-levels control (on/off). The operative range of electric signals is from 0 to 5 Volts, which corresponds to the pressure range (transducer connected to the air-thermometer exposed in 2.1) from 0 to 7 bar. All the data are delivered in parallel to a computer that stores them. We can observe from Fig. 6.1 that a branch connects the solid-state relay with the magnetron, to in-

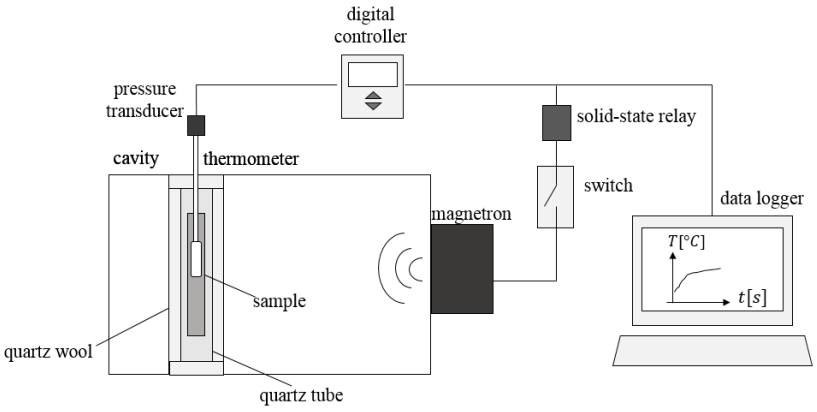

FIGURE 6.1: Schematic representation of the overall system configuration.

ject the modulated power. Therefore, this relay works as a switch that is driven directly by the digital controller during the normal functioning of the system. This connection is in series with the general switch which is activated just in case of overheating of the electronics, therefore for normal operation the general switch must be closed. The glass-wool insulation, not only reduces the heat losses but also slows down the temperature variation, implying benefits for the control system. The general equipment is depicted in Fig. 6.2, also the air-thermometer and the catalyst support are presented in section 2.1 and 2.2. Other fundamental aspects that have been considered in the presented work are related to the apparatus for measuring and controlling the temperature.

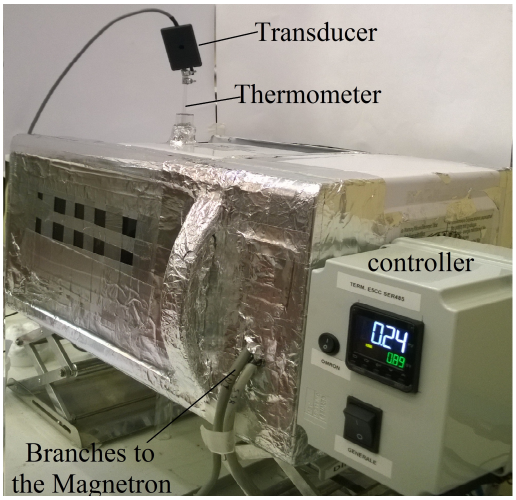

FIGURE 6.2: Experimental setup of the preliminary prototype, controller, and thermometer.

6.3.1 Air-thermometer

One of the most difficult tasks related to microwave heating is to obtain a real-time monitoring of temperature. Although several researchers use metallic thermocouples [95, 96, 97, 98], in the current work, an air-thermometer optimized for microwave conditions is here introduced. This tool permits to obtain precise measurements avoiding problems as electromagnetic interference, corona discharges and electromagnetic leakages due to the interaction microwave-metal [63]. An in-depth analysis of these problems can be found in the work edited by Datta and Anantheswaran [109]. As previously stated, if a circular hole is characterized by a radius smaller than l_c, then the opening does not induce radiation toward the external environment. If a metallic thermocouple is inserted into the hole, the dielectric cross section (air) becomes an annulus. This annular shape can sustain the electromagnetic propagation mode TEM (transverse electric and magnetic field), which can be transmitted even at lower frequencies. The actual behavior of the thermocouple becomes similar to that one of a radiating antenna. For this reason, the development of a pneumatic thermometer can be useful for avoiding electromagnetic compatibility issues [102]. An application of such a device can be found in a recent work [99]. In the current work, an air-thermometer has been developed based on the same principles (relation between temperature and pressure following the ideal gas law), taking care of maximizing the accuracy (considering the limits for mechanical brittleness). The most important components are a glass probe and a pressure transducer. The glass probe is composed by a bulb (actual sensitive element), which is welded with a capillary (branch). On the terminal part of the capillary there is a connection to the transducer. The pressure transducer allows to measure the rate of expansion of the air inside the bulb, which is linearly proportional to the temperature of the sample under test. The system has been previously calibrated in a laboratory stove, since both temperature and pressure are known. The prototype thermometer has been built using borosilicate glass, considering that the best material for this kind of applications is quartz. The sensitivity of the thermometer is strongly influenced by the ratio between the air volume in the bulb and the air volume in the capillary. The bigger the volume-ratio, the better is the accuracy. Since the internal diameter of the branch capillary cannot be reduced without affecting the mechanical properties, the only volume reduction can be applied to the fitting system between the glass capillary and the pressure transducer. From Fig. 6.3 we can observe the importance of increasing the volume ratio between the actual sensitive element and the branch element, where the theoretical pressure is given by the ideal gas law. The geometrical characteristics of the experimental setup have been presented in the Table 6.1. The air thermometer

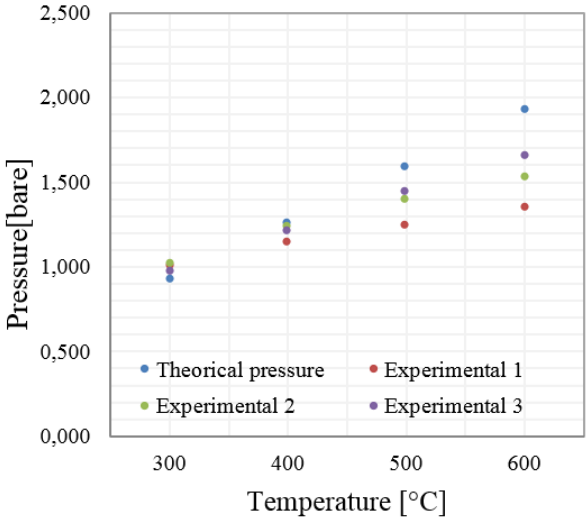

FIGURE 6.3: Calibration curves for the air-thermometer.

Trial	$V_{in\ bulb}[mm^3]$	$V_{in\ capillary}[mm^3]$	$V_{in\ junction}[mm^3]$	$V_{ratio}[-]$
1	2543.4	29.4	96.2	20.3
2	2543.4	29.4	48.1	32.8
3	2543.4	29.4	<1	86.5

TABLE 6.1: Section volumes of the three cases shown.

has been built with the configuration presented in the experimental trial 3. The final design of the equipment, which has been used for the experiments, is presented in Fig. 6.4.

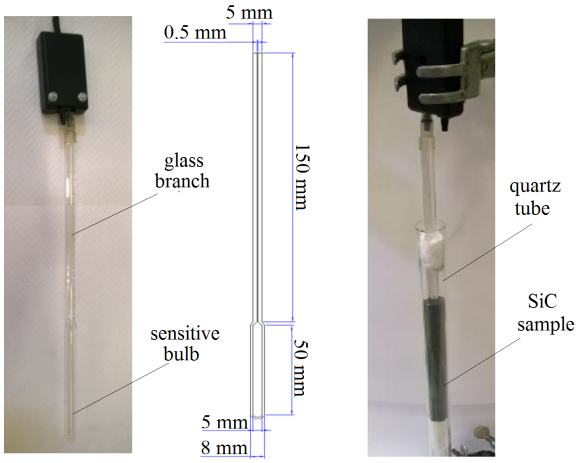

FIGURE 6.4: Air thermometer in the final configuration and its insertions into the sample.

6.3.2 Catalyst support

In the traditional methane steam-reforming process, the typical adopted catalyst is nickel-based, and the typical catalyst support is porous alumina. For microwave heating processes, the reduced capability of alumina to absorb microwave radiation [110] induces some difficulties for dielectric heating. A technique that can be useful to facilitate the electromagnetic heating is the mixing of the actual catalyst with a microwave subsceptor. Following this way, it is possible to achieve a satisfactory heat exchange between the reagents in gas phase and the porous bed. SiC can be employed as microwave subsceptor to be mixed with the catalyst, since it is inert with respect to the reaction, and it is characterized by notable resistance to high temperature. An inconvenient of this kind of mixing is due to the fact that the volume of the reactor must be increased because of the addition of inert material. An example of innovative use of a of Pt/SiC support for catalytic reactions can be found in the work developed by Fang et al [111]. If we consider the crystalline structure of β-SiC, it is characterized by enlarged superficial area BET [112]. Therefore, the β-SiC structure can be considered as an ideal candidate for the role of catalyst support in these applications. A comparison of the microwave heating capabilities between SiC, Ni/Al_2O_3 and Al_2O_3 has been tested in laboratory. The results are reported in the Fig. 6.5, considering the output power 700 W and a sample volume of 100 cm^3. From Fig.

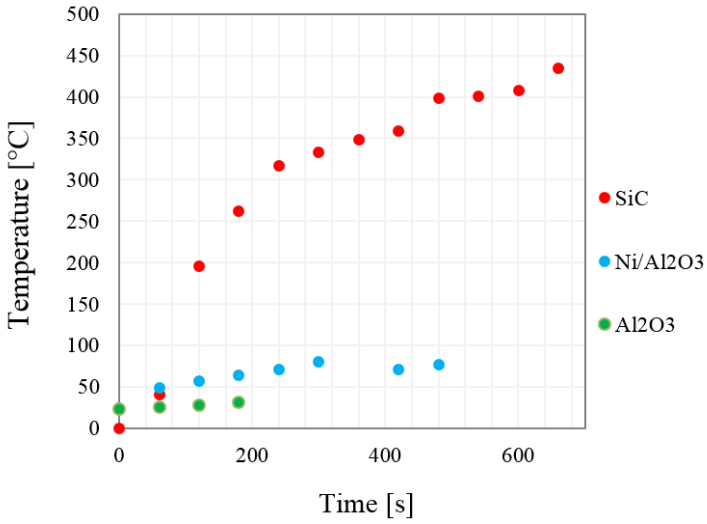

FIGURE 6.5: Microwave heating comparison between SiC, Al_2O_3, and conventional catalyst Ni/Al_2O_3.

6.5, we can observe the high capability of the SiC sample to be heated with respect to the other two materials. Since β-SiC shows good performances, and since it has superficial area similar to that one of alumina, it could be employed successfully also for catalytic-microwave processes. In this way, it is possible to make functional the entire volume of the reactor because porous β-SiC assumes at the same time the role of catalyst support and microwave subsceptor.

6.4 FEM-assisted design and experimental validation

The purpose of this section is to analyze all the numerical aspects, applying a Finite Element Method (FEM) software, which are related to the implementation of the physical model: governing equations, boundary conditions (BCs), geometry and materials. The governing Partial Differential Equations (PDEs) are the full-Maxwell's laws and the heat transfer law for the preliminary magnetron based prototype (model i), and for the validation case (model ii). These models have been solved with a fully-coupled frequency transient analysis, in order to assess the change of the electromagnetic material properties in relation with temperature. Therefore, these models include electromagnetic (EM) and thermal (HT) aspects in order to assess the temperature gradients. Instead, the performances of MBS (model iii) and SBS (model iv) have been computed focusing only onto the electromagnetic aspects. The linearity of the material properties has been assumed around the operative temperature (600 °C). The assumption of linearity allows to apply the superimposition principle, which can be

effectively adopted to reduce the need for FEM computation. So, the cylindrical reactors have been considered only from an electromagnetic point of view, just focusing onto the power density distributions and conversion-efficiencies. Implementation and experimental validation in laboratory have been also discussed in the following sections.

6.4.1 Implementation of the computational model

The adopted frequency of the electromagnetic (EM) field is GHz, which belongs to the Industrial Scientific and Medical (ISM) spectrum. Consequently, the EM wavelength in the propagating medium (air) is 12.2 cm, which is comparable with the geometrical maximum length of the cavity. The EM model is analyzed over the frequency domain, and considering the phasorial transformation, it can be described as follows (Helmholtz equation):

$$\nabla \times \mu_r^{-1}(\nabla \times \boldsymbol{E}) - k_0^2 \dot{\epsilon_r} \boldsymbol{E} = 0 \tag{6.2}$$

The EM boundary conditions have been set as Perfect Electric Conductors (PECs), due to the presence of the metallic walls of the cavity and waveguide. The PEC approximation over the metallic surfaces is appropriate in the microwave frequency range [37] and it is implemented as :

$$\hat{n} \times \boldsymbol{E} = 0 \tag{6.3}$$

The quantity is the unit vector over the entire metallic surface. At the general i-th port, regarding the electromagnetic propagation, the scattering coefficient can be computed as:

$$S = \frac{\int_{Port\ i} (\boldsymbol{E} - \boldsymbol{E_i}) \cdot \boldsymbol{E_i}}{\boldsymbol{E} - \boldsymbol{E_i}} \tag{6.4}$$

where becomes the scattering parameter in case of just one port active (any remaining port off). Regarding case (i), (iii) and (iv), the diffusion scattering boundary conditions are imposed over the inlet and outlet faces of the apertures (crossing sections of the quartz tube):

$$\hat{n} \times (\nabla \times \boldsymbol{E}) - jk_0 \hat{n} \times (\boldsymbol{E} \times \hat{n}) = 0 \tag{6.5}$$

This imposition derives from the Sommerfeld condition at a finite distance from a radiating source. Therefore, in order to truncate the computational domain, imposing the absence of reflection, we can

approximate properly in this way. Even if this imposition is just an approximation of the Sommerfeld radiation (e.g. tangential components of the electric field cannot be totally scattered), it is very accurate because the leakage toward the external space is very limited. Let us remind that the hole has been designed to avoid excessive leakage. For more details, any interested reader can be addressed to the following reference [27]. Regarding the model sources, for models (i) and (i) a coaxial cable has been implemented, maintaining similar geometrical dimensions of the terminal part of the magnetron antenna. The definition of the coaxial port has been considered in order to increase the accuracy of the model, instead of assuming the propagating electromagnetic mode TE_{10} at the port [38]. Instead, for models and , the approximation of the input mode TE_{10} at the ports has been assumed. The thermal source is related to the converted EM energy inside the material due to polarization phenomena and molecular friction, and it appears as a volumetric term which determines the connection between the electromagnetic and thermal models [2]. The volumetric power density can be quantified as:

$$P_{em} = 2\pi f \epsilon'' E_{rms}^2 \tag{6.6}$$

the thermal models (i) and (ii) have been solved over the time-domain, using the classical heat equation presented in Eq. 6.7:

$$\rho c_p \frac{\partial T}{\partial t} = \nabla \cdot (k \nabla T) + P_{em} \tag{6.7}$$

The adiabatic boundary condition is imposed over the external surface of the glass-wool. this assumption is valid only for the model (ii). The reason is that the temperature difference between the water domain and the external environment is smaller than 80°C, so the 1.5 cm thickness of insulating material ($k = 0.04$ W/(m K)) can guarantee reliability on the mentioned approximation. Eq. 6.8 represents the condition of absence of thermal flux:

$$\hat{n} \cdot \boldsymbol{q} = 0 \tag{6.8}$$

Instead, in the model (i), the adiabatic condition is not valid (the temperature gradient is much higher), and therefore, the thermal conduction through the insulator and also the convection toward the external environment must be considered. The natural convection law is imposed at the external faces of the glass-wool insulation (convective heat coefficient equal to 15 W/(m^2 K)). Still, considering the

model (i), at the external surface of the silicon carbide the Stefan-Boltzmann law holds as:

$$\hat{n} \cdot \boldsymbol{q} = \epsilon_{sic} k_b (T^4 - T_{room}^4) \tag{6.9}$$

Where the initial temperature is $T_{room} = 20$ °C, $\epsilon_{sic} = 0.85$ is the emissivity of silicon carbide and k_b is the Boltzmann's constant. In order to clarify the boundary conditions of each model, all the previous aspects have been graphically depicted in Fig. 6.6. The geometry of the domestic cavity has been presented in Fig. 6.7 (the geometry of MBS and SBS will be presented in the dedicated section 4). The internal diameter of the reactor is 16 mm, the wall thickness is 2 mm, the main dimensions of the cavity are 275 mm, 260 mm, 175 mm, respectively along x,y,z. The position of the quartz tube is 70 mm and 130 mm (the 0-reference is placed in the bottom-frontal corner on the left). The glass-wool insulation layer is 15 mm thick. The radius of the cylindrical glass is 45 mm, the height is 125 mm, and the thickness of the glass is 2 mm. The water-filled glass is placed in the center of the cavity. PEC condition is imposed. The implemented materials are air, quartz, silicon carbide and water (the last one only for model (ii)), and their properties can be summarized as follows: quartz (quartz-wool) $\mu_r = 1$, $\sigma = 0$ S/m, $\dot{\epsilon_r} = 4 - j0.0104$ [113], ($\rho = 15$ kg/m^3 from technical data-sheet), $k = 0.04$ W/(m K) , $c_p = 3460$ J/(kg K) [114]; silicon carbide $\mu_r = 1$, $\sigma = 0.01$ S/m, $\rho = 3217$ kg/m^3 (bulk material) [115], $c_p = 3460$ J/(kg K). Also it is important to consider thermal conductivity and specific heat of the SiC sample as functions of temperature as presented in Eq. 6.10 and Eq. 6.11 [116]:

$$k(T) = 72 - (0.13)T + (1.23 \cdot 10^{-4})T^2 - (4.4 \cdot 10^{-8})T^3 \tag{6.10}$$

$$c_p(T) = -107.98 + (0.828)T + (0.0172)T^2 - (5.450 \cdot 10^{-5})T^3 \tag{6.11}$$

Since the SiC sample is granular, an effective value of complex electrical permittivity, depending on the grade of porosity, can be computed as [117]:

$$3\nu_b \frac{\dot{\epsilon_b} - \dot{\epsilon_g}}{2\dot{\epsilon_g} + \dot{\epsilon_b}} + (1 + \nu_b) \frac{\dot{\epsilon_i} - \dot{\epsilon_g}}{\dot{\epsilon_g} + L_i(\dot{\epsilon_i} - \dot{\epsilon_g})} = 0 \tag{6.12}$$

Where $\dot{\epsilon_b}$ is the electrical permittivity of the background material (air), $\dot{\epsilon_i}$ is the electrical permittivity of the inserted material (bulk SiC), $\dot{\epsilon_g}$ is the effective electrical permittivity of the granular material (porous SiC), ν_b is the air volume fraction and $L_i = 0.08$ is a geometrical-based constant. The grade of porosity of the silicon carbide sample in laboratory is $\nu_b = 0.5$. The complex permittivity of the

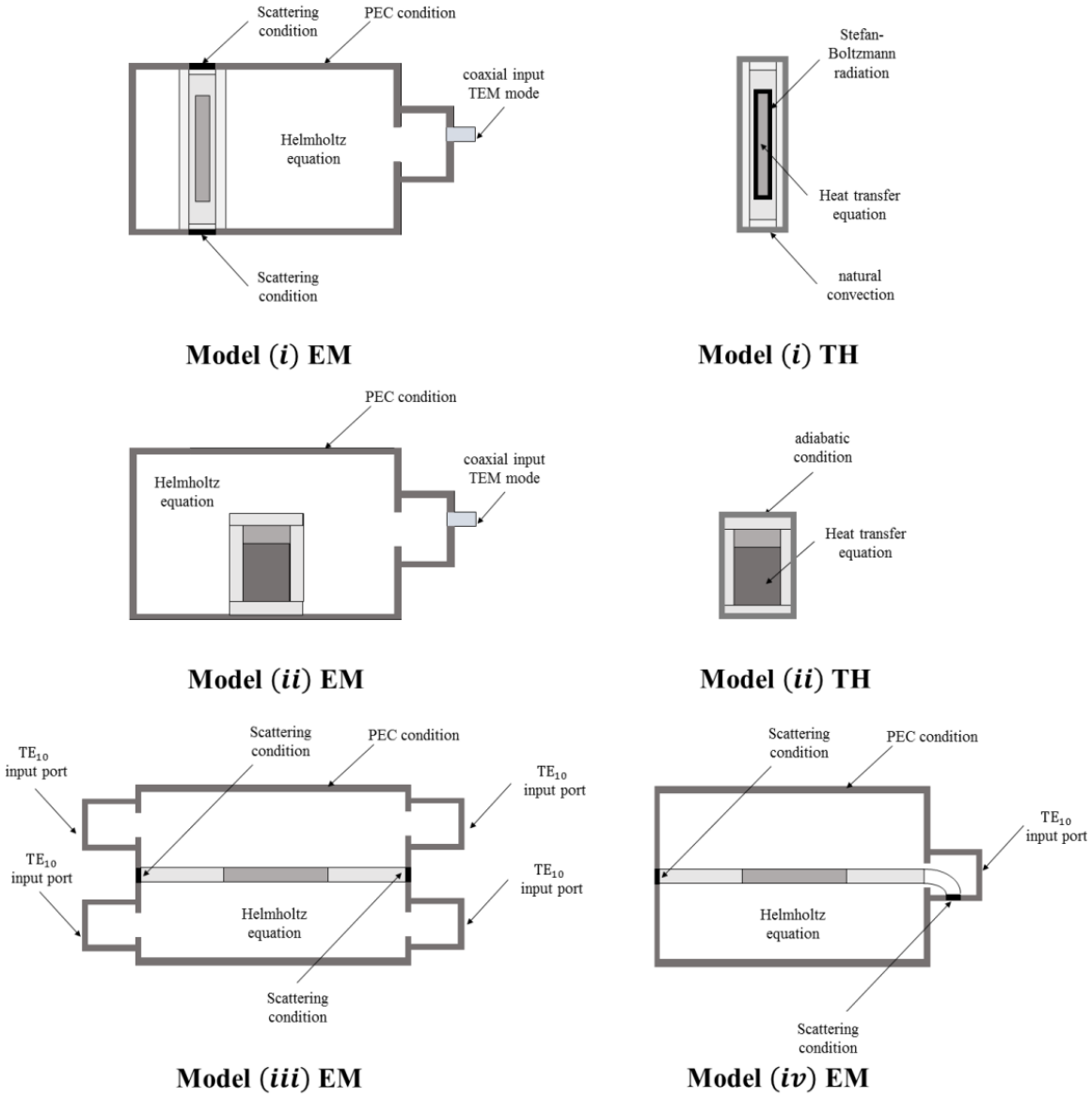

FIGURE 6.6: Governing equation and boundary for each model, and for each implemented physics.

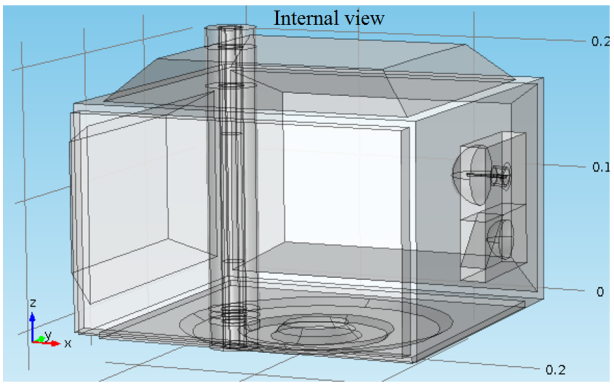

FIGURE 6.7: Geometry of the cavity and quartz tube containing the insulated silicon carbide sample.

silicon carbide over temperature for different grades of porosity is reported in the Fig. 6.8 [118, 119]: Regarding the numerical resolution of the electromagnetic and thermal models, they have been solved applying a direct solver. This solver is PARDISO and it is suitable for solving large sparse symmetric linear systems of equations, in particular for distributed-memory multiprocessors.

6.4.2 Experimental validation of the computational model

The determination of the reliability of an implemented model is a fundamental issue before to proceed with any numerical analysis. Validation can be done, confirming the capability to numerically predict observable and measurable results. In this work, calorimetric tests have been conducted, considering as thermal load several water-filled glasses, which have different masses $m_1 = 100$ g, $m_2 = 200$ g, $m_3 = 300$ g and $m_4 = 500$ g. The supplied power is continuous and has been fixed at the level $P_{in} = 700$ W (maximum power of the magnetron). Regarding the temperature, the thermal measurements have been done with a K-thermocouple. In this phase, in order to assess the average temperature of the liquid, the mixing of the fluid is required. The electromagnetic model is validated indirectly, because its thermal effect appears with the converted power, as stated in Eq. 6.6. A quartz-wool layer covers the glass to reduce thermal convection and to reduce the uncertainties related to the heat loss. The schema of the validation setup is depicted in Fig. 6.9. Considering the space occupied by the glass as control volume (CV), we can explicitly make the thermal balance presented in Eq. 6.7, so we can derive the following expression:

$$P_{abs} = P_{in} - P_{refl} - P_{loss} = \rho c_p \int_{cv} \frac{\partial T}{\partial t} dV = \int_{cv} 2\pi f \epsilon'' |\boldsymbol{E}|^2 dV \tag{6.13}$$

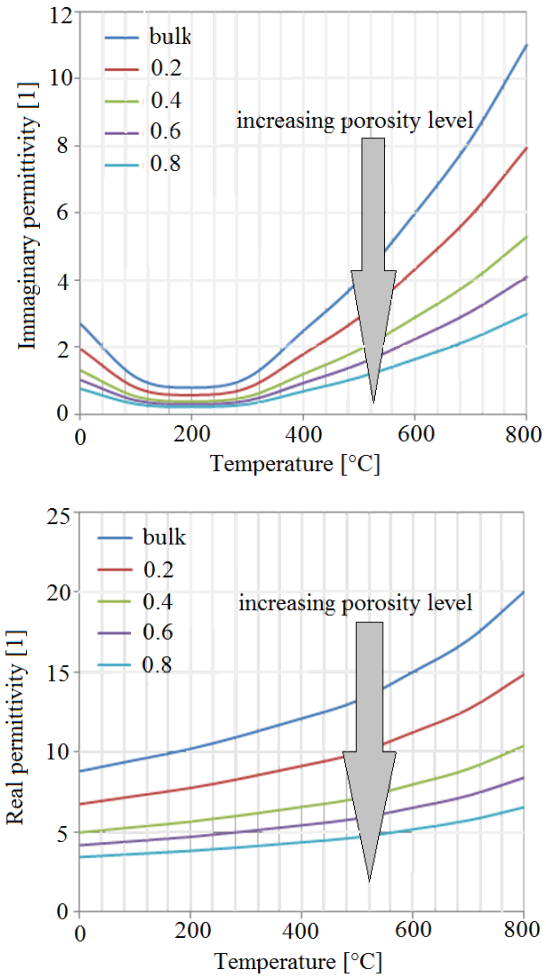

FIGURE 6.8: Complex dielectric permittivity over temperature for different porosities.

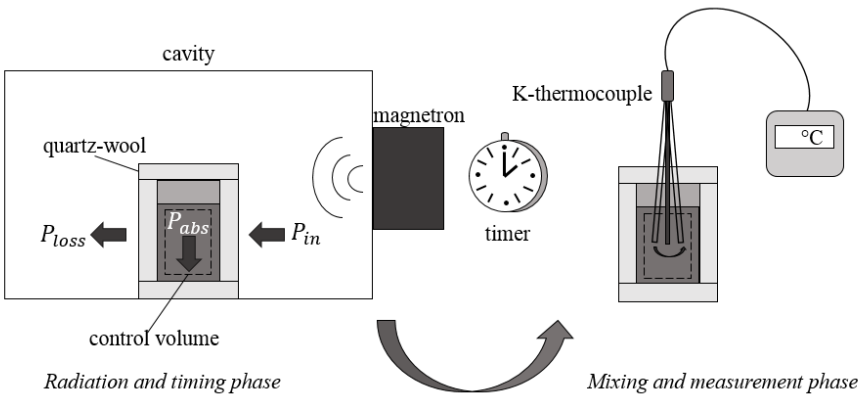

FIGURE 6.9: Schema of the experimental setup applied for the model validation.

The term P_{refl} represents the reflected power, and it depends on the coupling between the electromagnetic field and the quantity of the load-mass. The term corresponding to the heat loss is almost zero ($P_{loss} \approx 0$ W), since the boundary are quasi-adiabatic. The increase of internal energy is uniquely determined by the magnitude of the electric field all over the control volume. The electromagnetic field, in its turn, is uniquely defined by the mass, since the radiating power is fixed. Consequently, the increase of temperature is related only to the load-mass m_i with $i = 1, ..., 4$. The average temperature is assessed starting from Eq. 6.13 in a few simple steps, dividing by the control volume, inverting the order of space-integration and time-derivation, assuming the homogeneous initial temperature $T_{room} = 20$ °C, and finally integrating over time, we obtain as follows:

$$\langle T \rangle_i = T_{room} + \frac{P_{abs}(m_i)}{\Delta V_i \rho c_p} \Delta t \quad i = 1, ..., 4 \tag{6.14}$$

The Eq. 6.14 represents the linear increase of average temperature for the different analyzed cases. The quantity $P_{abs}(m_i)$ must be numerically computed with the FEM model. The comparison between the numerical and experimental average temperatures is plotted in Fig. 6.10 (left): The curves in Fig.

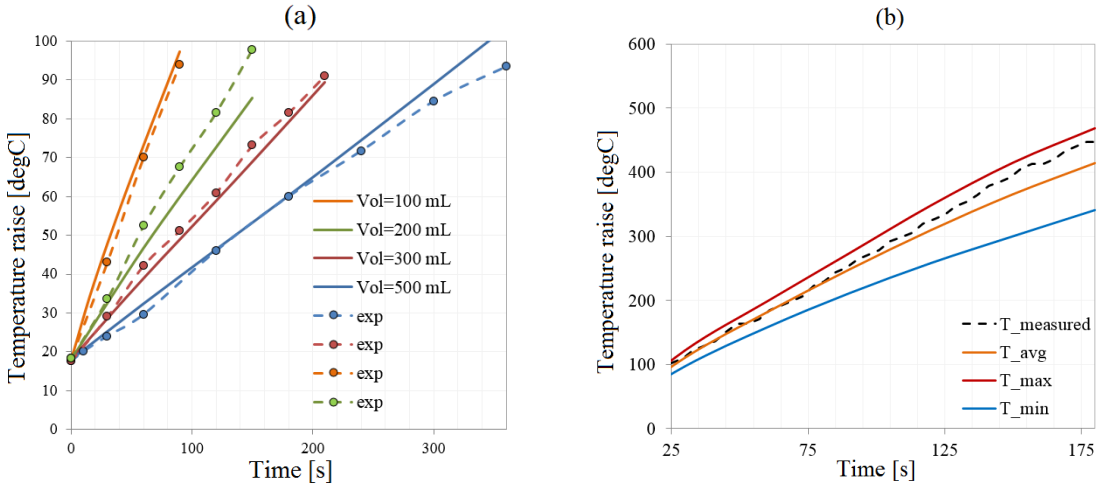

FIGURE 6.10: (a) Comparison between numerical (solid lines) and experimental results (dashed lines) with water-filled glasses. (b) Validation of the FE model comparing numerical and measured values of the temperature in the SiC sample.

6.10 (left) clearly show the compatibility of the results obtained from the FEM model with the results obtained experimentally. Moreover, another important issue that must be considered, is the adequacy of the real-time temperature performance, assessing its inertia and precision during a transient state. The FEM model, with the quartz tube reactor and silicon carbide as thermal load, is here evaluated

over the time domain $t = 25$ s. The experimental evaluation of the thermometer is more accurate above 100 °C (for calibration issues), therefore the first set of measurements up to 25 s has been excluded. It is possible to observe from Fig. 6.10 (right) that the measured and numerical values match properly, confirming the suitability of the computational model and of the air-thermometer as well. In Fig. 6.11 the temperature distribution and power density have been depicted to show the effect of the axial gradients due to the electromagnetic standing waves. This effect is intrinsically present for radiation at frequencies around a few GHz [120]. This is one the most critical limits for the applications in the industrial scale since it reduces any achieved advantage of the volumetric heating. Therefore, in the next sections a particular interest will be turned to the reduction of such intrinsic electromagnetic phenomenon. Despite the axial thermal gradients, From Fig. 6.11 it is evident that the volumetric heating allows to achieve homogeneous temperature distributions along the different cross sections of the gas flow.

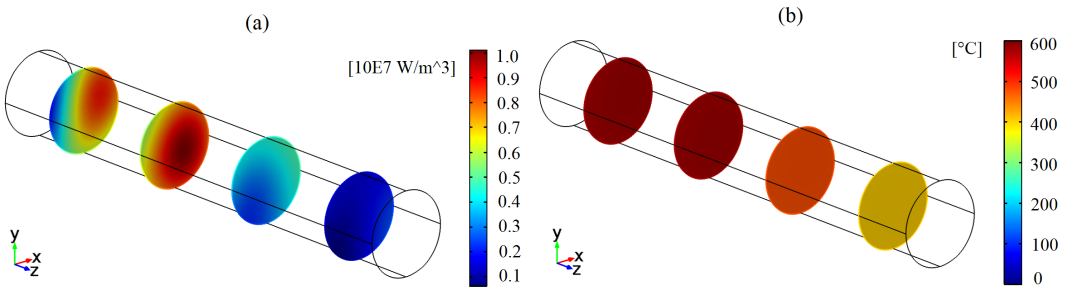

FIGURE 6.11: (a) Power density distribution over different cross sections along the x-axis with an oven cavity at $t = 180$ s. (b) Temperature distribution over the corresponding cross sections.

6.5 Novel configuration to achieve an uniform field distribution

All the previous sections were devoted to the construction of a device capable to heat up a sample of SiC and automatically control the load temperature. Once that the implemented model has been validated with experimental measurements, the model will be used to predict physical behaviors of new possible reactors, which are based on the same physics. An open challenge is related to overcome difficulties related to non-uniform electromagnetic patterns along the reactor-axis, which generate axial thermal gradients. In order to overcome this problem related to the presence of resonant standing waves inside the cavity, it is necessary to handle the electromagnetic pattern. The electromagnetic pattern is defined by three factors: the material properties, the geometry, and the microwave-source

input. The first factor is restricted by the chemistry of the reaction, while the second factor can be properly modified, even if it alone cannot prevent the formation of standing waves. Instead, the change of microwave input can be investigated to take advantage of the constructive and destructive interference phenomena [121]. Several recent works have proposed algorithmic techniques to optimize SBS systems but presenting a few limitations, e.g. the uniformity is not considered [121, 122, 123]. In the following sections the MBS and SBS technologies have been compared, considering that the first one can apply mostly for the geometry-factor, while the second one can easily exploit the interference of waves just controlling the phases of the input fields.

6.5.1 Numerical and semi-analytical modeling of MBS and SBS technology

To prevent the inconvenient of axial-gradients due to the presence of microwave standing waves, a new tubular cavity has been designed, and it is characterized by four microwave ports. The geometrical characteristics of the cavity are reported in Fig. 6.12: The length of the reactor is 20 cm, the

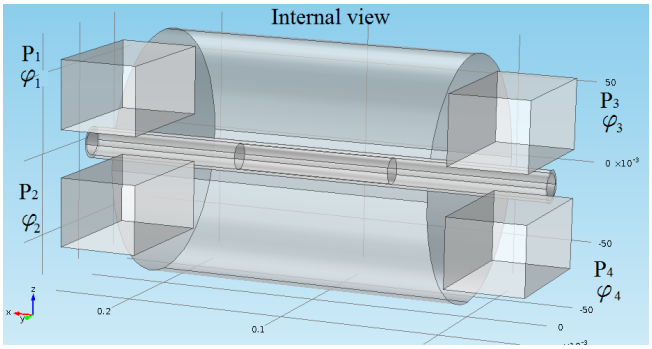

FIGURE 6.12: Geometry of the four ports cavity assisted by solid-state generator (SBS technology).

radius is 7.5 cm, the rectangular ports are defined by edges 8.6 cm and 4.3 cm, the distance between the barycenter of two same-sided ports is 7.3 cm, the quartz-tube radius is 1 cm and the SiC is distributed over a 10 cm length. The grade of porosity of the sample is 0.5. Considering the recent developments of high power solid state transistors, which has been already started in 90's [124], it is possible to generate microwaves in a more controllable way [105, 106, 107]. In particular, the SBS technology allows to increase the number of degrees of freedom of an electromagnetic system. The meaning of degrees of freedom is the number of possible electric field patterns which can be obtained changing the setup at the ports or the geometrical features of the system. Therefore, at any degree of freedom corresponds a specific field distribution over space. Using this technology it is possible

to change, at each of the m electromagnetic ports, the frequency (not considered in this article), the magnitude of the radiated fields, and the phase. In order to clarify how SBS can create new electric field patterns exploiting constructive and destructive interference, let us consider a microwave device characterized by m ports. The field distribution that is generated by each independent port can be written in phasorial form as presented in Eq. 6.15 (the subscript $_*$ is referred to the case in absence of modulation), and therefore including the modulation we get as:

$$\dot{\boldsymbol{E}}_{*i} = \dot{\boldsymbol{E}}_{0i}(x,y,z)e^{j\theta_i} \quad i = 1,...,m \tag{6.15}$$

$$\dot{\boldsymbol{E}}_{i} = \alpha_i\dot{\boldsymbol{E}}_{*i}(x,y,z)e^{j\phi_i} \quad i = 1,...,m \tag{6.16}$$

also we can derive the total field (assuming linearity of material), and expressing the field in the exponential (Eulerian) form:

$$\dot{\boldsymbol{E}}_{tot} = \sum_{i=1}^{m} \dot{\boldsymbol{E}}_{i}(x,y,z)e^{j\phi_i} = \sum_{i=1}^{m} \alpha_i\dot{\boldsymbol{E}}_{0i}(x,y,z)e^{j\theta_i}e^{j\phi_i} \tag{6.17}$$

Now it is convenient to express the fields in the rectangular form in order simplify the summation as depicted here:

$$\begin{aligned}\dot{\boldsymbol{E}}_{tot}(x,y,z) &= \sum_{i=1}^{m}\left[\alpha_i\dot{\boldsymbol{E}}_{i0}(x,y,z)\cos(\theta_i+\phi_i)\right] + j\sum_{i=1}^{m}\left[\alpha_i\dot{\boldsymbol{E}}_{i0}(x,y,z)\sin(\theta_i+\phi_i)\right] \\ &= a(\boldsymbol{\alpha},\boldsymbol{\phi}) + jb(\boldsymbol{\alpha},\boldsymbol{\phi})\end{aligned} \tag{6.18}$$

From Eq. 6.18, we derive that the resulting electric field distribution can be determined by changing the phases and the amplitudes at any port. It is important to observe that the initial distributions determine in a critical way the possible resulting patterns. This flexibility is not present with the MBS since it is characterized by fixed frequency radiation and extremely complicated active control of phase shifts. The purpose of this section is to compare the heating performances of a MBS device with SBS one. The conventional magnetron-based reactor has been implemented considering a fixed cavity geometry (same main dimensions of the previous case) as presented in Fig. 6.13, and spanning different possible positions of the quartz tube ($0 < r_{pos} < 6$ cm, $0 < \theta_{pos} < 337.5$). On one hand, the magnetron based device is supplied by only one ($m = 1$) electromagnetic port (400 W power). In the case of having more than one port for MBS, there could be the possibility of connecting one

magnetron at each port. In principle, the generated fields must be superimposed giving the resultant field. But anyway, the magnetron has two major limitations: 1) the frequency is not exactly 2.45 GHz, but actually, it belongs to a narrow band around 2.45 GHz. Therefore, if the harmonics are not the same, the superimposition principle cannot be applied. So, only the power density derived from the independent fields can be summed up, but not the fields themselves. 2) Let us assume to have the same exact frequency generated by the magnetrons. Therefore, in this condition, the superposition principle can be adopted. But even in this case, the magnetrons do not have the possibility to be synchronized because the oscillations of resonant electrons in the lobes cannot be triggered at the same time. So, the initial phase-sifts between independent ports becomes actually an uncontrollable random variable. The only way to change dynamically the phase shifts between the ports is changing the path of the waveguides (connected to only one magnetron) to create a specific phase-shift, but this means that it is necessary to introduce mechanical changes of the waveguide shape (e.g. inserting gates to select the path, or stubs). Therefore, the complexity of the system would increase dramatically, but above all, the mechanical changes cannot be quick enough to face promptly the electromagnetic variations at the ports that can be imposed by a controller. For this reason, in case of MBS, considering just one port, or more ports characterized by fixed phase shifts, the number of degrees of freedom does not increase. On the other hand, the solid state system is supplied by four ($m = 4$) ports, which are fully controllable in phase and amplitude. In the current work, the numerical evaluation is done considering the non-uniformity of the electric field distribution u_E over the n mesh-nodes, and the rate of transferred energy to the load η (the remaining energy is backward reflected). It has to be clearly

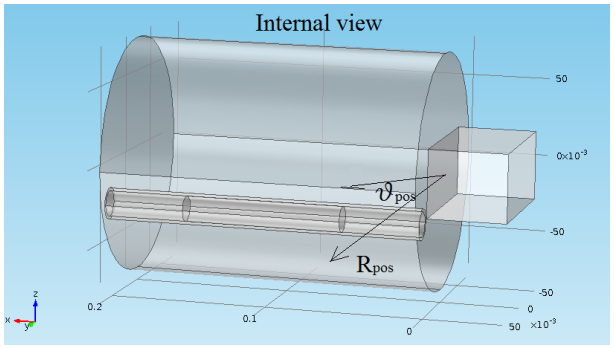

FIGURE 6.13: Geometry of the one port cavity assisted by conventional magnetron based generator (MBS technology).

stated that the efficiency is related to a single step conversion, but since the reflected electromagnetic power could be again used, the overall efficiency should be determined by a cascade series of reactors

as presented in Fig. 6.14 and Fig. 6.15. The performances of a single reactor can be quantified by Eq. 6.19 (non-uniformity) and Eq. 6.20 (conversion efficiency):

$$u_E = \frac{\sqrt{\frac{\sum_{i=1}^{n} \left(|\boldsymbol{E}_i| - \langle|\boldsymbol{E}|\rangle\right)^2}{n}}}{\langle|\boldsymbol{E}|\rangle} \tag{6.19}$$

$$\eta = \frac{P_{load}}{\sum_{i=1}^{m} P_{port\ i}} \tag{6.20}$$

In order to present an example of how the system can be created by mean of a cascade series of reactors, it is necessary to use the 3-ports microwave circulator which is characterized by the scattering matrix presented in Eq. 6.21:

$$\boldsymbol{S}_{circ} = \begin{bmatrix} 0 & 0 & 1 \\ 1 & 0 & 0 \\ 0 & 1 & 0 \end{bmatrix} \tag{6.21}$$

The circulator allows to swap the input to output power between the ports: $(1 \rightarrow 2)$, $(2 \rightarrow 3)$, $(3 \rightarrow 1)$. The basic principle is that the injected power comes from 1 to 2 which is connected to the electromagnetic port. Then, the reflected power goes from 2 to 3, which is connected to the input power of the next reactor. The ports of last reactor element are connected to a matched dissipative element. In this way, the safety can be guaranteed because the overall power can be always dissipated or transmitted to the following reactor. Also, at the same time, there is a one-direction power flow regime that prevents the power-reflection toward the solid state generator. The general schema of multi step conversion SBS has been depicted in Fig. 6.14 and Fig. 6.15. For MBS, the degrees of freedom are related to the position of the tubular reactor (oriented on the x-axis), changing the radial and angular position R_{pos}, θ_{pos}, of the quartz-tube (geometrical spanning). The chosen actual number of the degrees in the current analysis is 49. Instead, the degrees of freedom for SBS are related to the possible configurations of power at the ports P_1, P_2, P_3, P_4 with the constrain of the fixed total power P_{tot} (400 W) as follows:

$$\sum_{i=1}^{m} P_{port\ i} = P_{tot} \tag{6.22}$$

Also, the possible configurations are based on the shifts between the phases ϕ_1, ϕ_2, ϕ_3, ϕ_4, considering the phase $\phi_4 = 0°$ as reference (in this case the reactor position is kept fixed). The total number of

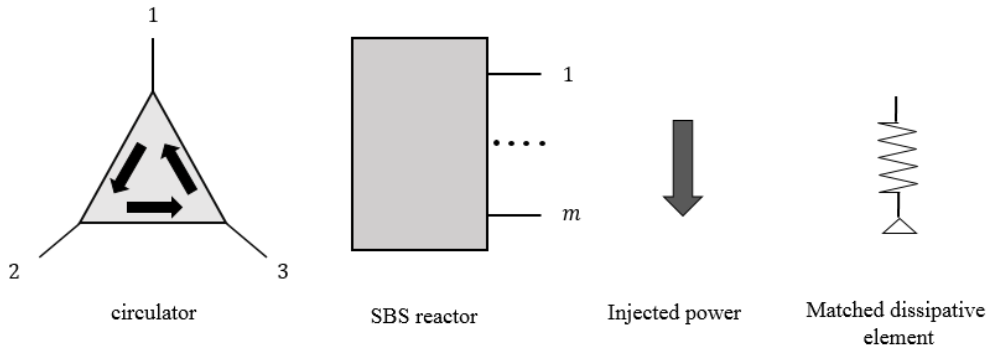

FIGURE 6.14: Main elements composing the microwave circuit of the system.

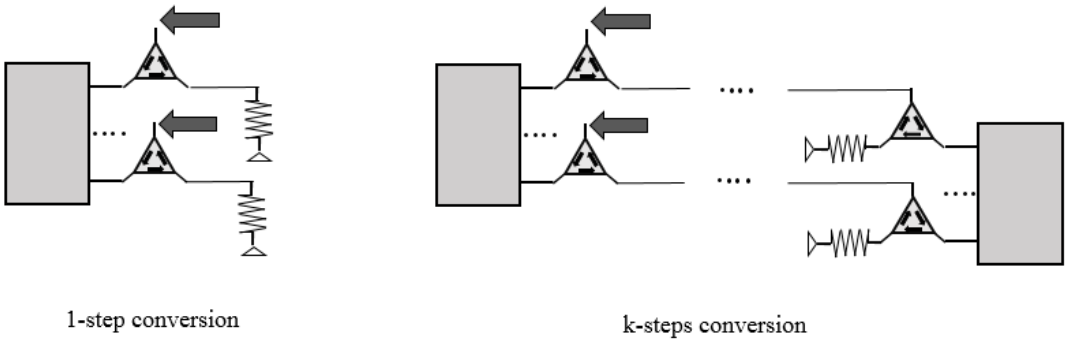

FIGURE 6.15: Microwave schema of 1-step conversion and multi-step conversion reactors.

degrees of freedom is 36.047.592. This value derives from the particular adopted setting (e.g. minimum power at each port $P_{min} = 0$ W, maximum power at each port $P_{max} = 200$ W, the step between different power settings $\Delta P = 10$ W, the degrees of shifting $\phi = 20°$). Since this number is huge, considering the computational cost of FEM models, a semi-analytical approach has been adopted. First, four ($m = 4$) FEM simulations must be run, where only one port at a time is active, in order to obtain the entire scattering matrix of the system which is depicted in Eq. 6.23. Also, we can consider the input power vector $\boldsymbol{P_\phi}$ as :

$$\boldsymbol{S} = \boldsymbol{S}_{m\times m} = \begin{bmatrix} S_{11} & \dots & S_{1m} \\ \vdots & \ddots & \vdots \\ S_{m1} & \dots & S_{mm} \end{bmatrix} \tag{6.23}$$

$$\boldsymbol{P_\phi} = \boldsymbol{P} \circ \boldsymbol{\phi} = \begin{bmatrix} \sqrt{P_1} \\ \vdots \\ \sqrt{P_m} \end{bmatrix} \circ \begin{bmatrix} e^{j\phi_1} \\ \vdots \\ e^{j\phi_m} \end{bmatrix} = \begin{bmatrix} \sqrt{P_1}e^{j\phi_1} \\ \vdots \\ \sqrt{P_m}e^{j\phi_m} \end{bmatrix} \tag{6.24}$$

Where the symbol $\circ$ denotes the Hadamard product. For a comprehensive description of the assessment of a microwave network basing upon the scattering parameters, the reader is addressed to the work of Dobrowolski [125]. The independent electric field distributions, which are generated by each independent port, must be computed. The power set in the simulation has been fixed at an arbitrary reference P_{ref}, and the same for the phases ϕ_{ref}, since the actual values will be defined by the semi-analytical model. In order to adopt the semi-analytical model, the superimposition principle must be applied and then the resultant electric field (at each i-th mesh-node) distribution and the efficiency are presented in Eq. 6.25 and Eq. 6.26 respectively [126]:

$$\dot{\boldsymbol{E}}_{tot\ i}(\boldsymbol{P}, \boldsymbol{\phi}) = \sum_{k=1}^{m} \left(\frac{P_k}{P_{ref}} \right) \dot{\boldsymbol{E}}_k e^{j(\phi_k - \phi_{ref})} \quad i = 1, \dots n \tag{6.25}$$

$$\eta(\boldsymbol{P}, \boldsymbol{\phi}) = \left(\frac{P_k}{P_{ref}} \right) \left[\boldsymbol{P'_\phi} \cdot \left[\boldsymbol{I} - \boldsymbol{S'S} \right] \cdot \boldsymbol{P_\phi} \right] \tag{6.26}$$

6.5.2 Results and discussion

The linearity of materials has been assumed since the complex permittivity does not varies strongly with respect to the temperature. The last condition can be well approximated if we consider Fig. 6.7

with a grade of porosity ν_b and assuming $T = 150$ °C, around the operating point of the reforming process $T = 650$ °C. Considering all the previous aspects, the results of the analysis have been reported in Fig. 6.16 (a), depicting a comparison of the performances. Moreover, it is interesting to

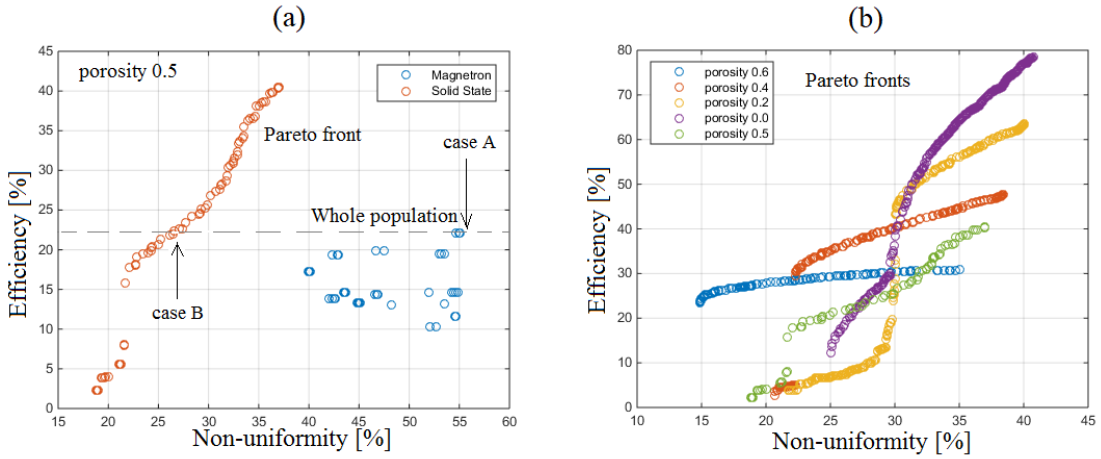

FIGURE 6.16: (a) Comparison of performances between the SBS and the MBS. (b) Pareto fronts of the SBS, considering many porosity levels of the sample.

compare the behaviors at different porosity levels of the SiC sample. We can observe from Fig. 6.16 (b) that the Pareto fronts are strongly dependent on the porosity. On one hand the bigger the porosity the higher the uniformity (but lower efficiencies); on the other hand, the smaller the porosity the higher the efficiency (but less homogeneous heating). Therefore, in the design phase of the system, it is very important to consider these aspects to increase the quality of the process. When the heating process is optimized, the numerical analysis can be done including mass transfer in porous media, flow-dynamics and phase-change, like presented by Rakesh et al. [127] and by Hou et al. [128] for the kinetics. Let us consider the case with the highest efficiency for MBS (case A: $r_{pos} = 0.06$ m, $\theta_{pos} = 225°$), and let us compare it with the corresponding SBS case, which presents the same efficiency (case B: $P_1 = 100$ W, $P_2 = 100$ W, $P_3 = 80$ W, $P_4 = 120$ W, $\phi_1 = 60°$, $\phi_2 = 180°$, $\phi_3 = 340°$, $\phi_4 = 0°$). The comparison can be developed assessing the distribution of the power density along the x-axis for a few cross-sections, and also assessing the magnitude of the electric field over the entire SiC sample. These results have been depicted in Fig. 6.17 and Fig. 6.18 respectively. In particular, from Fig. 6.17, it is evident that the uniformity in case B is higher than in case A. In case A there is not any complete cold spot while in case B the majority of the elements correspond to the cold zone. Also, the case B presents more intense hot-zones with a maximum value which is almost the double of the case A. The shape of case A is quasi-Gaussian, meaning that the most

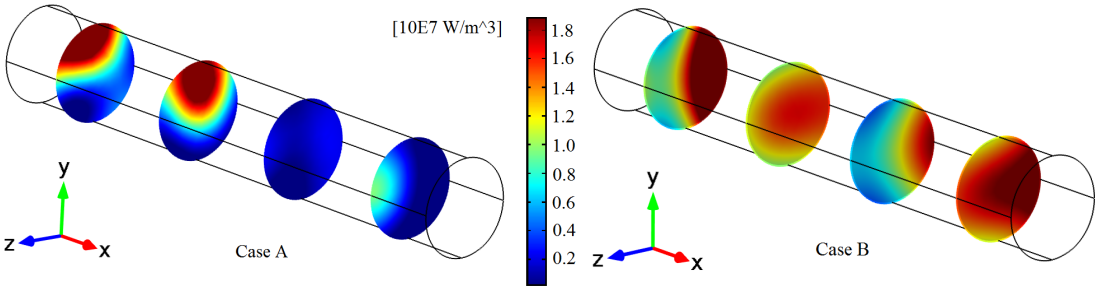

FIGURE 6.17: Power density over different cross sections along the x-axis. Case A: magnetron-based system, and case B: solid-state based system.

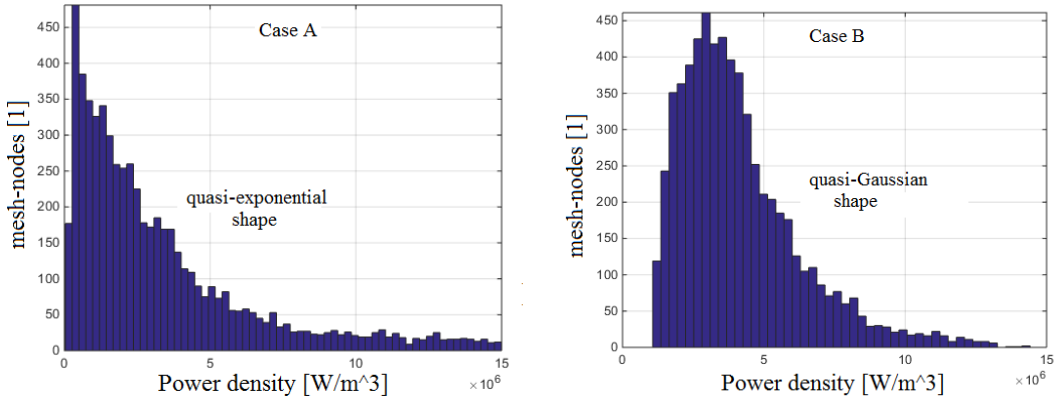

FIGURE 6.18: Power density histograms for a tubular cavity. Case A: magnetron-based system. Case B: solid-state based system.

frequent power-density is close to the mean value. On the other hand, the MBS is characterized by a quasi-exponential distribution implying that the most frequent power-density is close to zero. All the previous results are referred to the outcomes, therefore, it is also important to identify the optimal solutions which belong to the optimization domain. Let us remind that the constraint presented in Eq. 6.22 has been chosen to compare only the input-settings, assuming of having the same total injected power. This kind of analysis is oriented to the case of an industrial production of hydrogen, where the input power is fixed to maximize the possible output. In general, this constraint is not considered, and the investigation could be extended including an entire range of overall power values. Therefore, new Pareto solutions can be found. This other investigation can be more automotive-oriented because it is suitable to modulate the hydrogen production rate, including multilevel-power solutions in case of different working velocities. This premise is important to understand how the Pareto solutions depend strictly on the specific case under investigation. When the Pareto solutions of the reactor have been identified, it is necessary to implement a control algorithm which must be capable of selecting the appropriate setting at any electromagnetic port in real time. The required setting can be determined including other aspects, and we list a few of the most important practical cases. In transient state, it is more convenient to have high efficiency solutions rather than high uniformity solutions, in order to reduce the transient period. In case of combined heating (conventional and microwave), a compensation of the radial non-uniformity can be achieved with low microwave power (and higher quality heating pattern), because the main power supply can be based on conventional technology. Therefore, an high uniform Pareto setting can be suitable to provide just a small heating amount. In case of a steady state, it is possible to use a negative feedback control, considering a set of Pareto solutions at different output power. Indeed, if the input power is fixed when the efficiency changes, the outcome is actually modulated. Summarizing, the SBS can provide the possibility to face many practical situations in a very flexible way and at the same time it provides dominant performances with respect to MBS. In Fig. 6.19, the Paretian electromagnetic settings at each port, for the reactor under investigation have been presented in the power-phase domain, for different levels of porosity. Observing the results in Fig. 6.19, we must note that for any reported configuration there are three other homologue ones due to the geometrical and electromagnetic symmetry of the system. These configurations have been explicitly reported in Table 6.2. In the analysis, only the phase spanning $0^\circ < \phi_i < 360^\circ$ has been considered, therefore the cases 2, 3, 4 do not appear in the presented results, but they can be obtained applying the relations in Table 6.2. In order to actually implement a

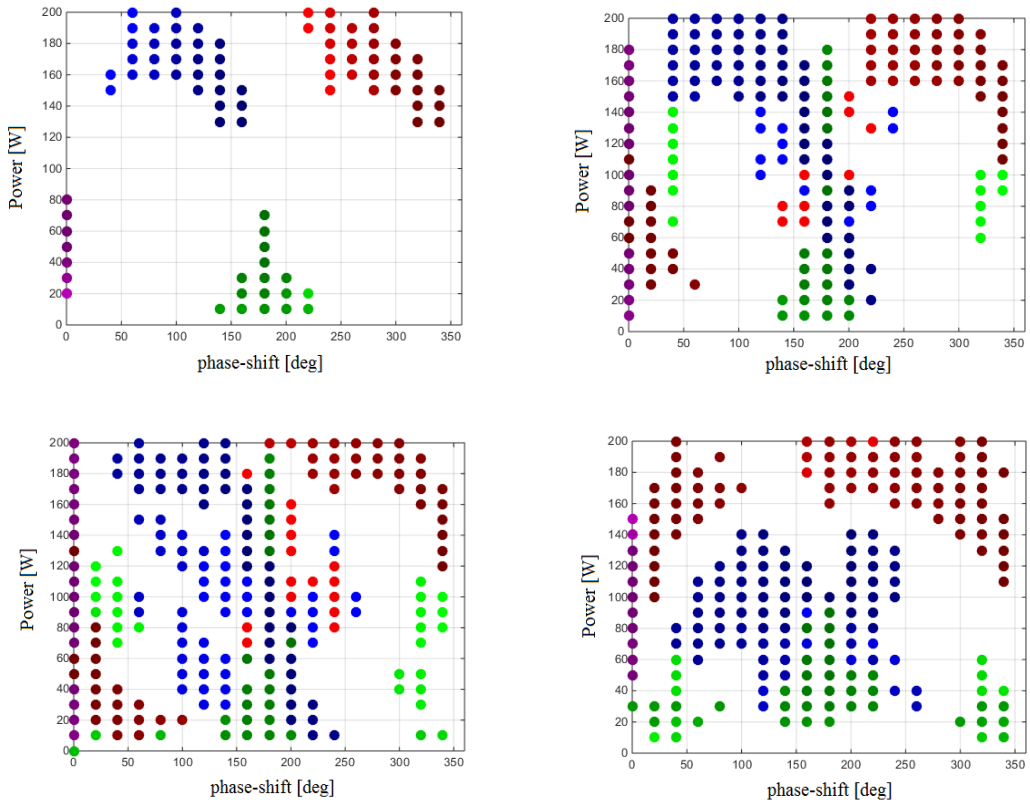

FIGURE 6.19: Power-phase diagrams for different levels of porosity: $\nu_b = 0.6$, $\nu_b = 0.4$, $\nu_b = 0.2$ $\nu_b = 0$, respectively from left to roght and from top to bottom. The marker colors are referred to the specific port: ϕ_1-red, ϕ_2-green, ϕ_3-blue, ϕ_4-purple.

Configuration	Port 1	Port 2	Port 3	Port 4
1	P_1, ϕ_1	P_2, ϕ_2	P_3, ϕ_3	$P_4, 0$
2	$P_3, (\phi_3 - \phi_2)$	$P_4, (-\phi_2)$	$P_1, (\phi_1 - \phi_2)$	$P_2, 0$
3	$P_2, (\phi_2 - \phi_3)$	$P_1, (\phi_1 - \phi_3)$	$P_4, (-\phi_3)$	$P_3, 0$
4	$P_4, (-\phi_1)$	$P_3, (-\phi_1)$	$P_3, (\phi_2 - \phi_1)$	$P_1, 0$

TABLE 6.2: Section volumes of the three cases shown.

four ports SBS reactor, the reader is addressed to the appendix, where the power-phase setting at each port is presented in tabular format for the all investigated Pareto fronts. These data can be used to set a control algorithm at the ports when a specific target of uniformity and efficiency are required as described above, considering a SiC sample as thermal load and a reactor with geometrical similarity. For different reactors and loads, specific settings can be obtained just following the methodology and computational strategy presented in the previous sections.

6.6 Conclusions

The purpose of the current work is the investigation in a rigorous and systematic way on improving the performances of high temperature endothermic processes, by mean of new generation solid state microwave technology. So far, there has been evidence that microwave systems based on magnetron can induce advantages for making a radially uniform heating in case of tubular reactors, especially with respect to conventional techniques. In spite of this improvement, one of the major limitations of Magnetron-Based Systems (MBSs) is the inability of providing a uniform heating along the main axis in case of extended loads. For this reason, the achievement of uniform volumetric heating is the major open challenge to actually spreading microwave technology across chemical industry. Consequently, an analysis of the performances that can be achieved adopting new generation Solid-state Based Systems (SBSs) has turned out as necessary to assess their actual potential. From a methodological point of view, the current work can be divided in three stages:

- Creation of a preliminary prototype (magnetron-based) with two main scopes:
  - Testing several elements of the system, in particular, the adequacy of using an air-thermometer, and the use of β-SiC as catalyst support and subsceptor.
  - Defining an experimental reference which can be used to validate a Finite Element (FE) electromagnetic and thermal model.

- Development of a numerical FE model, which can be used to investigate on the following aspects:
  - The quality of magnetron-based heating, analyzing the electromagnetic and thermal patterns on several cross-sections along the main axis.
  - The sensitivity of the systems in relation to a change of thermal load properties, in particular the porosity of the microwave subsceptor.
- Basing upon a semi-analytical approach, an electromagnetic comparison between MBS and SBS has been developed, considering a cylindrical reactor as benchmark. The Pareto fronts for both the technologies have been computed, defining the efficiency and the uniformity as objective functions. The configurations of SBS have been obtained through phase-shift and power modulation of any independent electromagnetic port. The configurations of MBS have been obtained by mean of changing the position of the thermal load inside the cavity.

From a physical and technological standpoint, we can highlight the most relevant results which have been obtained.

- The SBS technology is characterized by a Pareto front which is composed by dominant solutions with respect to the entire population of MBS. Therefore, the improvement of the performances, using new generation electronics, has been demonstrated through a systematical comparative analysis of the field patterns and power conversion.
- If the complex electric permittivity changes, because of its dependence on the porosity of the subsceptor, it induces strong changes onto the Pareto front. In particular, if the process is more oriented to high-uniformity, it is convenient to use high level of porosity. On the other hand, if the process is more oriented to a high-efficiency conversion, it is more suitable to reduce the porosity level.

Finally, we can conclude by observing that this comparative analysis should be considered just as a starting point for the investigation on solid state technology in the sector of endothermic reactions. In fact, the actual renovated potential of microwave heating through this new technology is far from being completely explored. The future developments should strive toward the creation of new shapes of reactors, since the geometry can increase fundamentally the degrees of freedom achievable with a generic SBS n-ports device. In this way, the possibility of spreading the microwave processing

in chemical industry can become feasible from a technical, and considering the cost reduction of electronic components on large scale, even from an economical point of view.

7 Probabilistic Approach to Pilot Solid-State Sources to Optimizing the Heating Pattern for Continuous Flow Microwave Processing

7.1 Abstract

Thanks to the recently developed high-power and efficient solid-state based generators at microwave frequencies, it is possible to drive multiple electromagnetic ports, controlling power and phase at each of them. Completely new opportunities are now available, since it is possible to exploit constructive and destructive interferences, obtaining a much more controlled heating pattern in the thermal load during microwave processing. In order to properly utilize this technology, it is important to know how to control in a suitable way the electromagnetic ports. The purpose of the current work is to develop a probabilistic algorithm that allows to improve the quality of the heating pattern. The analysis was done considering a continuous flow process within a tubular reactor. The development of the algorithm is followed by the analysis of a test-case by mean of a finite element software. In the test-case the objective heating shape was defined as constant function, which corresponds to uniform heating. This choice is justified by the fact that one of the most difficult challenges in microwave processing is the reduction of thermal non-uniformities due to the presence of resonant standing waves. An experimental 2-ports SBS prototype was developed in laboratory and tested to increase the possible degrees of freedom in terms of electric field patterns. Numerical results confirm the capability of improving the temperature pattern quality. The current work represents just a starting point to exploit the entire renovated potential of microwave heating.

7.2 Introduction

One of the most challenging and still unresolved issues in microwave heating processes is the capability of improving the heating pattern and temperature distribution qualities. Systems based on magnetron technology can mainly rely on mechanical stirrers or on the variation of cavity geometry to modify the heating pattern [129]. At microwave frequencies, non-uniformity is intrinsically due to the presence of electromagnetic resonant standing waves in closed cavities. Despite the enormous potential of microwave heating, thanks to the possibility to convert energy directly within the material, many limitations restrict industrial diffusion and large-scale development. Even tough, microwave processing was subjected to an increasing attention of many scientific communities, from food scientists to chemical and environmental engineers [130, 131]. It is interesting to observe that the number of scientific publications in the field of microwave heating is increased in an exponential way over the last couple of decades [132]. The augmented attention of the scientific community does not correspond in a proportional way to the actual diffusion of microwave technology for large scale applications. The recent advancements on microwave electronics for high-power applications define new scenarios which are still unexplored. [105, 106, 107]. Multi-ports solid state MW generators allow to create new possible patterns of the electric field through controlling constructive and destructive interference. The purpose of this paper is to provide a new algorithmic probabilistic strategy to optimize the temperature distribution within the load. The development of the algorithm is based upon mechanistic laws of microwave radiation, superimposition principle and volumetric heating due to dielectric polarization. In order to assess the capability of improving the heating quality, a benchmark test-case was numerically analyzed, considering uniform heating as objective target. The comparison was made taking under investigation a cylindrical reactor, comparing the performances of probabilistically controlled Solid State based System (SBS) and a traditional Magnetron Based System (MBS).

7.3 Materials and methods

The structure of the entire work can be briefed as follows:

- Development of a microwave processing system based on solid-state technology.

- Implementation of a numerical model that reproduces the physics and the power-phase control capability of solid-state technology.
- Validation of the model by comparing numerical predictions with experimental observations.
- Theoretical development of innovative probabilistic controller.
- Numerical comparison of the quality patterns between solid-state technology and classical magnetron technology.

7.3.1 Experimental

Hardware and equipment

The system splits a low power signal into several components, and by mean of an externally controlled electronic buffer, it is possible to create appropriate phase-shifts between the divided channels (2-ports in the current experimental SBS). The signals are amplified by solid state generators, and the resulting output is injected into waveguides that deliver the power to the cavity. The used DC power supply (for the electronic buffer) is a Virtual Bench of National Instruments with the following features: voltage range [0, +6] V, current range [0,1] A, programming accuracy $\pm$ 0.1 % of reading $\pm$ 5 mV offset. The DAQ driver is National Instruments USB-9162 with the following features: 4 channels $\pm$ 10 V 16-Bit Analog output, $\pm$ 10 V Ch-to-COM, 250 Vrms CAT II Ch-to-earth isolation. The signal generator is Mini-Circuit USB Synthesized Signal Generator SSG-4000HP, which works in the dynamic range 70 dB, output power from -50dBm to +20dBm in 0.25dB steps at the frequency band [250, 4000] MHz. The splitter is Mini-Circuits splitter ZFSC-2-372-S+ with the following features: band [10, 3700] MHz, insertion loss 0.6 dB, amplitude unbalance 0.2 dB, phase unbalance 1.0 °. The I/Q modulators are Marki microwave IQ1545MMP with the following features: frequency band [1.5, 4.5] GHz, conversion loss 5.5 dB, image rejection 25 dB, amplitude deviation 0.3 dB, phase deviation 3°. The solid-state generator is Emblation ISYSconnect (prototype equipment R&D use only) characterized by the following features: Output [0-100] W at 2.45 GHz, characteristic impedance 50 Ω, voltage [100,240] V, Power 255 VA, frequency 50/60 Hz. The cavity is characterized by an ad-hoc design for the current research, made by Whirlpool. The cavity is connected to 2 rectangular waveguides. The control software of the system is a proprietary software which was developed with C sharp. The used infrared thermo-camera is FLIR T420 characterized by: temperature range from -20°C to 650 °C, frame rate 60 Hz, thermal sensitivity <0.045°C at 30°C, resolution 320 x 240 pixels,

non-radiometric IR-video recording MPEG-4 to memory card. The setup of the system is presented in Fig. 7.1 and Fig. 7.2.

Procedures

Experimental tests were run changing the electromagnetic phase-shifts between the 2 ports of the system. The adopted thermal load was water inside a squared container composed by 25 cubes (edges of 5 cm). The container was made with low-dissipative plastic (at microwave frequencies $\tan(\delta_{plas}) \ll \tan(\delta_{wat})$). The adopted steps during the tests are listed as follows:

- The container was filled by 1 L of water.
- The load was left at the room temperature ($\approx$ 25 °C) for 20 minutes to achieve the equilibrium temperature.
- The load was placed centrally in the cavity and the power setting was fixed at 100 W (both the channels) with phase shift [0, 90, 180] deg. Each experiment was 300 s long.
- After heating phase, the load was taken off and thermo-metrically measured by mean of infrared camera.

It was not necessary to steer the fluid since convective movements within any cubes allowed to homogenize the temperature distribution of the cells.

7.3.2 Finite Element modeling

Physics laws and implemented conditions

In the current work we should distinguish two Finite Element models: first, the model that reproduces the behavior of the experimental device in laboratory; second, the model that makes comparative predictions regarding different physical responses of magnetron based technology (MBS) and solid-state based technology (SBS). The first model is characterized by electromagnetics and thermal transfer, instead the second model is characterized by electromagnetics, heat transfer and fluid dynamics. Considering that electromagnetic waves propagate at 2.45 GHz as monochromatic harmonic functions, the full Maxwell's laws have been rewritten adopting the Steinmetz transformation, giving the following equation:

$$\nabla \times \mu^{-1} \nabla \times \boldsymbol{E} - k_0 \dot{\epsilon_r} \boldsymbol{E} = 0 \tag{7.1}$$

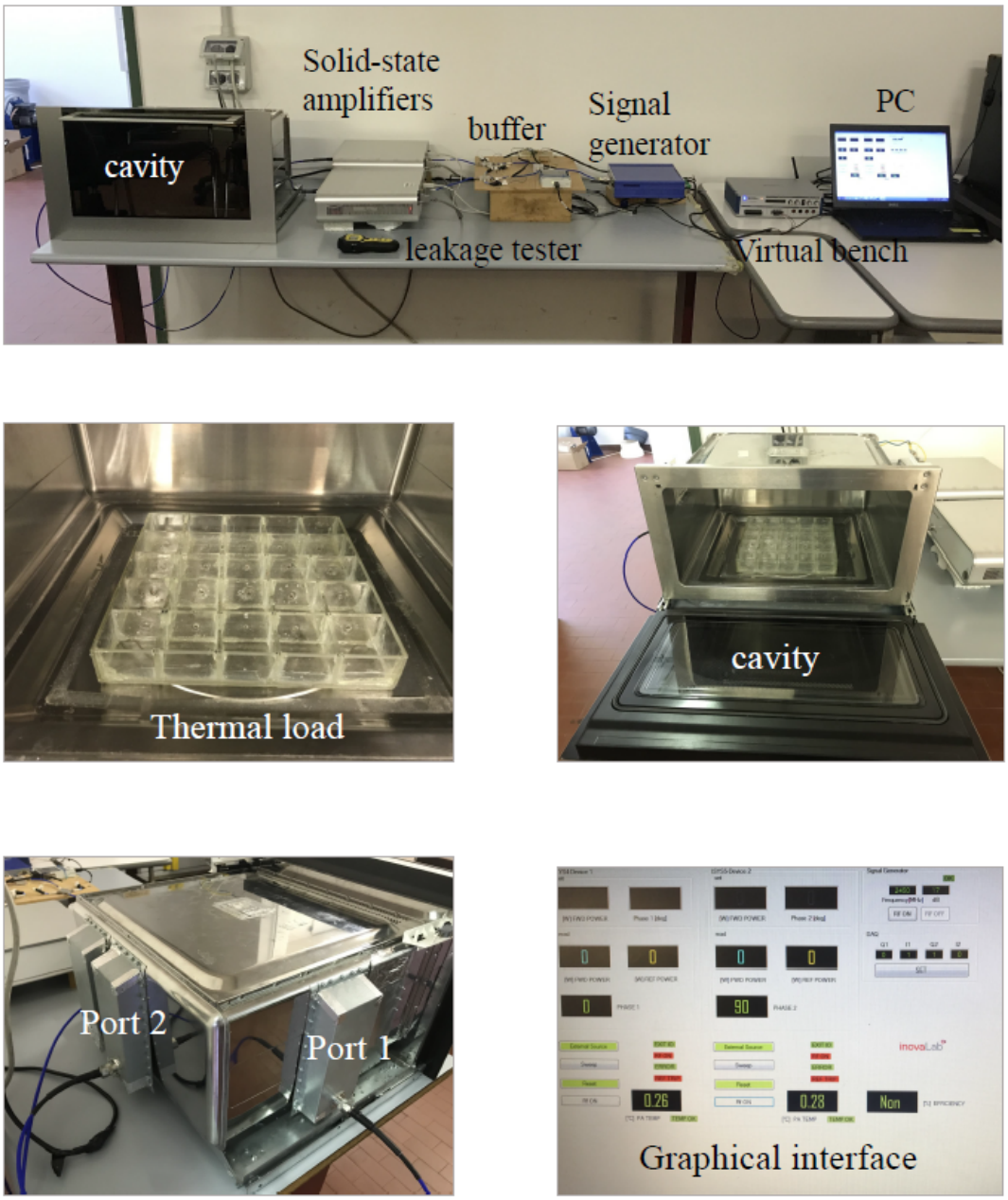

FIGURE 7.1: On the top, the experimental setup of the two-ports SBS is presented. In the central pictures, the container and the cavity are shown. In the bottom, the waveguides and the GUI of the proprietary software are reported.

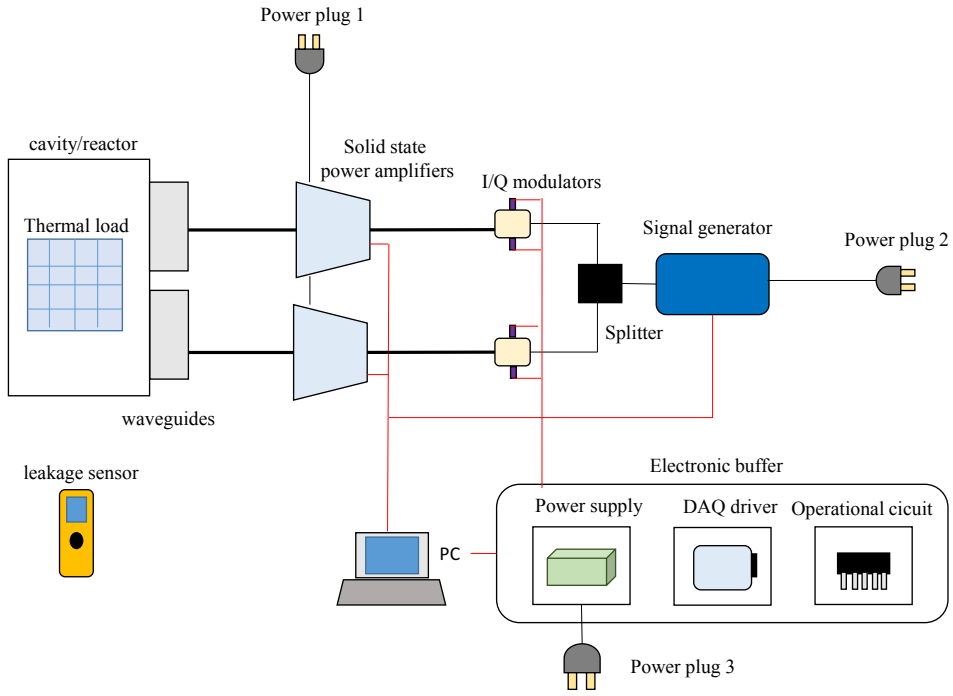

FIGURE 7.2: Schema of the experimental setup that was adopted to run the tests.

$$\dot{\epsilon_r} = \epsilon' - j\epsilon'' \tag{7.2}$$

$$k_0 = \omega\sqrt{\mu_0\epsilon_0} \tag{7.3}$$

where $\dot{\epsilon_r}$ is the complex electrical permittivity and k_0 is the propagation constant in free space. The apertures of the cavity are supplied by rectangular waveguides. At the extremities of the guides the propagation mode TE_{10} is imposed for both SBS and MBS. This assumption is valid even for magnetron based systems [38]. The metallic walls are characterized by the Perfect Electric Conductor (PEC) condition, which corresponds to normal directionality of the field over wall surfaces. This condition is suitable at microwave frequencies [37]:

$$\hat{n} \times \boldsymbol{E} = 0 \tag{7.4}$$

The volumetric power density can be quantified as:

$$Q_{em} = 2\pi f \epsilon'' E_{rms}^2 \tag{7.5}$$

thermal models were solved over the time-domain, using the classical heat equation [26]:

$$\rho c_p \frac{\partial T}{\partial t} = \nabla \cdot (k_{th} \nabla T) + Q_{em} \tag{7.6}$$

In the first model, the natural convection law was imposed at the external boundaries of the load:

$$\boldsymbol{q} \cdot \hat{n} = h(T - T_{room}) \tag{7.7}$$

where $h \approx 15$ W/(m^2 K) is the convective coefficient. In the second model, the walls were considered as thermally insulated, and therefore the adiabatic condition was imposed:

$$\boldsymbol{q} \cdot \hat{n} = 0 \tag{7.8}$$

The initial temperature of the system was considered as $T_{room} = 25°$C.

Computational aspects

The Finite Element model was created using Comsol Multiphysics 5.2. The computational model is characterized by second-order shape functions. The implemented geometry is presented in Fig. 7.14. After mesh convergence analysis, there were 458673 domain elements, 95040 boundary elements and 10085 edge elements. The number of degrees of freedom was 410416 (+ 251335 internal DOFs). The used numerical solver was PARDISO, which is suitable for solving large sparse symmetric linear systems of equations, in particular for distributed-memory multiprocessors. The used workstation for the computation is characterized by two processors, 16 cores Intel(R) Xeon(R) CPU E5-2620 v4 working at clock frequency of 2.10 GHz and RAM memory of 256 GB.

7.4 Analysis of thermal patterns using solid-state technology

The purpose of this section can be divided in two parts: first, demonstration of capability to reproduce different electric field patterns by mean of setting modulation and phase; second, verification of compatibility between experimental observations and numerical predictions. FE models were used to compare MBS with SBS. Experimental tests can be subjected to power unbalance between the ports due to the leakage-losses of the cables. Therefore, the injected power can be slightly lower than the

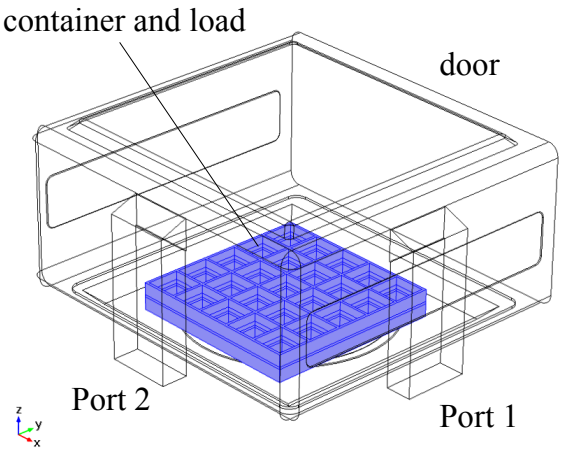

FIGURE 7.3: The implemented cavity is here reported, highlighting the thermal load and the two input-ports.

theoretical value. The main consequence of this phenomenon is that the ports can be differently electromagnetically charged. Beyond the reduction of the total injected power, unbalance can induce to change the resulting electric field pattern. In order to clarify the main effect due to power unbalance, an illustrative picture is reported in Fig. 7.4. From a numerical point of view, it is important to make another observation: temperature is related to the convective motion of the fluid that occurs within any cube. Since the heating time is quite long ($\approx$ 300 s), the main induced effect is the homogenization of the temperature in any cells. To accurately compute the temperature pattern we should take into account the buoyancy effect. This introduction would increase significantly the computational cost without augmenting the actual comprehension and the interpretation of the obtained results. From Fig. 7.5 we can make a few assessments in terms of the temperature:

- Temperature pattern variation depending of the phase-shift $\Delta\phi = [0, 90, 180]$ degrees (columns 1, 2 and 3 of the frame in Fig. 7.5).
- Reproducibility of experimental patterns (comparison between row 1 and 2).
- Matching between experimental measurements and numerical results.

Variation of the phase-shift influences the positioning of the main hot-spots and cold-spots. In case of $\phi = 0°$, the field is more intense in correspondence to the lateral sides, instead, in the case $\phi = 90°$, on the right, there is an intensification of the angular hot-spot and a splitting of the band. In

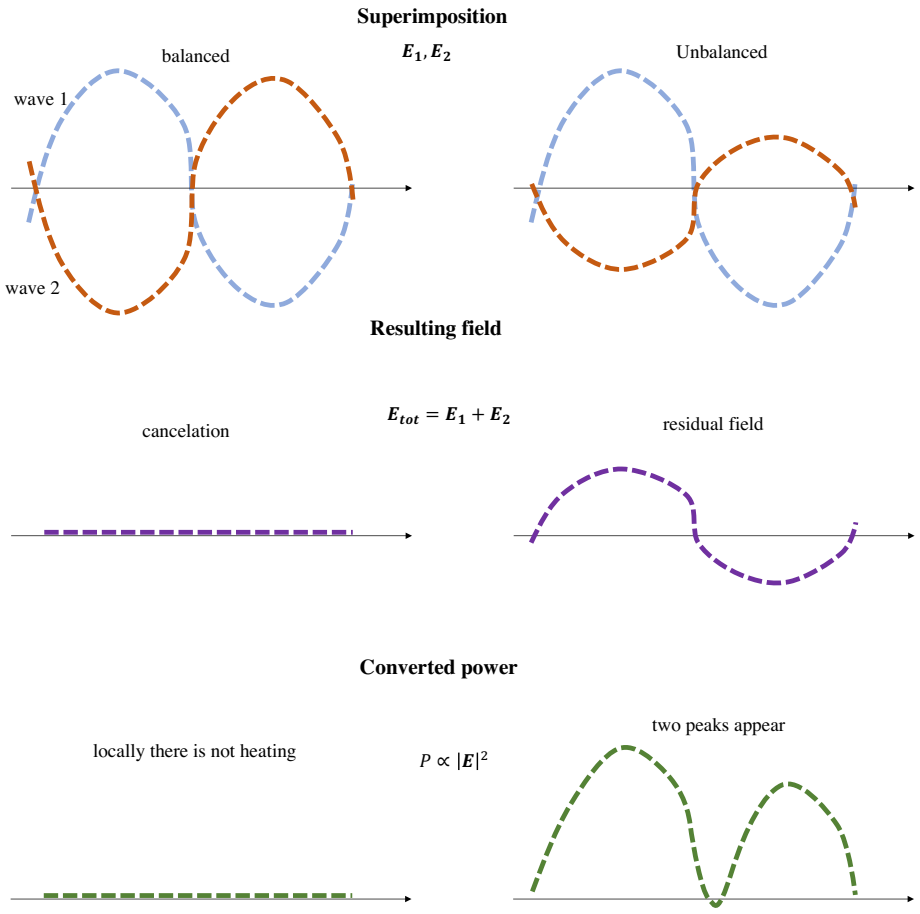

FIGURE 7.4: The illustration explains the main discrepancy in terms of power density that occurs between the case of a perfectly balanced and unbalanced radiation.

case of $\phi = 180°$, we observe strong predominance of heating in the left side and in the bottom. Comparing the rows 1 and 2, the high-quality to reproduce the same heating pattern experimentally is verified. Therefore, the experimental setup was appropriately prepared to guarantee repeatability of the experiments. We can observe in Fig. 7.5 by mean of several markers, the matching of the predicted and observed patterns (circles). A few discrepancies can be identified (crosses), but they can be considered as acceptable, considering the mismatching between perfectly balanced and unbalanced cases as already illustrated.

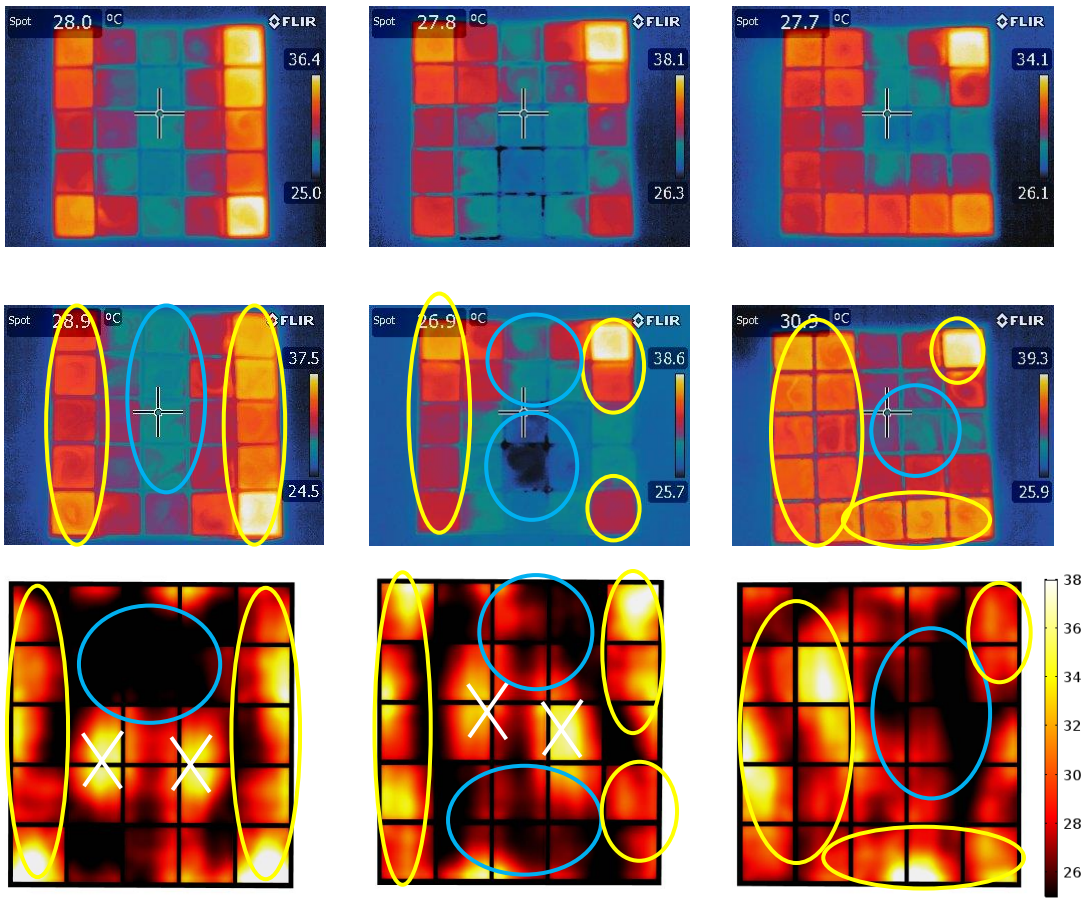

FIGURE 7.5: Experimental (row 1 and 2) and numerical (row 3) results in terms of the superficial temperature of the load, related to the different phase-shifts of the input-ports $\Delta\phi = [0°, 90°, 180°]$ (columns 1, 2 and 3).

7.5 Probabilistic determination of the electromagnetic setting

7.5.1 Formal definition of the system

Let us consider an extended thermal load that is laying in the region Ω, and which must be processed by microwave radiation. We assume that the microwave source is a k-ports, solid-state based generator (SBS). This recent technology allows to change the radiation conditions through a control of power $\boldsymbol{P} = (P_1, ..., P_k)$ and of phase $\boldsymbol{\phi} = \phi_1, ..., \phi_k$ at all the electromagnetic ports. The configurations of the system can be defined by a series of $j = 1, ..., n$ possible states. At any j-th vectorial set of $\{\boldsymbol{P}, \boldsymbol{\phi}\}_j$, an electric field pattern $\mathbf{E}_j = f_j(x, y, z)$ is uniquely defined in the load, and it depends only onto the j-th setting [25]. Consequently, also the electromagnetic power dissipation $w_j = h_j(x, y, z)$ inside the material is uniquely defined when the j-th configuration is set. We assume that the dependence of the material properties on the temperature is analytically known as a series of p functions that depend on the physics under investigation (e.g electromagnetics, heat transfer, chemical kinetics, fluid dynamics etc.):

$$m_1 = f(T), ..., m_p = f(T) \tag{7.9}$$

7.5.2 Constructive and destructive interference

In the section 7.5.1 we have stated that the electric field pattern can be modified just setting the powers and the phases at each electromagnetic port. In order to clarify this effect, let us analyze what happens within the material in the region Ω. The field distribution can be expressed in the phasorial form through the Steinmetz transformation. We can explicitly define the coefficients that modulate the independent electric fields with $\alpha_1, ..., \alpha_k$ ($P \propto \alpha^2$) and so we can write as follows:

$$\alpha_1 \dot{\boldsymbol{E}}_1(x, y, z) e^{j\phi_1}, ..., \alpha_k \dot{\boldsymbol{E}}_k(x, y, z) e^{j\phi_k} \tag{7.10}$$

Here, assuming the linearity, we can sum up the fields in the Eulerian form:

$$\begin{aligned} \dot{\boldsymbol{E}}(x, y, z) &= \sum_{i=1}^{m} \alpha_i \dot{\boldsymbol{E}}_i(x, y, z) e^{j\phi_1} = \sum_{i=1}^{m} \alpha_i \dot{E}_{0i}(x, y, z) e^{j\theta_i} e^{j\phi_i} \\ &= \sum_{i=1}^{m} \alpha_i \dot{E}_{0i}(x, y, z) e^{j(\theta_i + \phi_i)} \end{aligned} \tag{7.11}$$

where $\dot{E}_{0i}$ and θ_i are the amplitudes and the phases of the phasors. Now we can express the fields in the algebraic form in order to simplify the summation:

$$\begin{aligned}\dot{\boldsymbol{E}}(x,y,z) &= \sum_{i=1}^{m}[\alpha_i \dot{E}_{0i}(x,y,z)\cos(\theta_i+\phi_i)] + \sum_{i=1}^{m}[\alpha_i \dot{E}_{0i}(x,y,z)\cos(\theta_i+\phi_i)] \\ &= a(\boldsymbol{\alpha},\boldsymbol{\phi}) + jb(\boldsymbol{\alpha},\boldsymbol{\phi})\end{aligned} \tag{7.12}$$

from Eq. 7.12 we can observe that the electric field pattern is strongly dependent on the settings at the ports, in any point of the load. Power density is directly given by the classical equation for polarized dielectrics [2], as already presented in Eq. 7.5 [1]:

$$w = 2\pi f \epsilon_0 \epsilon'' |\dot{\boldsymbol{E}}| \tag{7.13}$$

7.5.3 Discretization

It is convenient to consider that the spatial region Ω can be discretized by a series of m nodes that cover the entire volumetric load space. Let us draw the attention to a generic internal i-th node of this series, and since the relations $f_j(x,y,z)$ and $h_j(x,y,z)$ can be defined at any point in Ω, we can express them in a discrete form $\mathbf{E}_j^i = f_j^i$ and $w_j^i = h_j^i$. In general, we can define an objective target function $T_* = o(x,y,z,t)$ in Ω that represents the desired temperature pattern over time. Considering the nodal discretization of the load, we have a correspondent target function $T_*^i = o^i(t)$. Given the discrete distribution w_j^i, the actual determination of the temperature T^i depends strongly on the specific physical conditions of the system (thermal diffusion, velocity of the flow, endothermic phenomena, etc.). For this reason, the objective target function in terms of power density must be determined on a physics-basis as will be presented in section 7.6. Let us define the target functions in terms of power density $w_* = h_*(x,y,z)$ and its correspondent discrete form $w_*^i = h_*^i$.

7.5.4 Probabilities of any settings at the ports

Let us assume that w_*^i is already available[2]. It is possible to asses at any i-th point the suitability of the j-th configuration just comparing the discrepancy between the functions w_j^i and w_*^i. Suitability of the j-th configuration throughout Ω is assumed as reference to define the configuration probability

[1] Two symbols are used for the electromagnetic power density (Q_{em} and w). Q_{em} is referred to the physical quantity (same convention of other books). w is referred to the variables used for the algorithmic controller.

[2] The identification of w_*^i will be treated in the section 7.6.

distribution. Let us formalize the discrete probability as follows:

$$p_j^i = \frac{1}{(n-1)}\left(1 - \frac{|w_*^i - w_j^i|}{\sum_{j=1}^n |w_*^i - w_j^i|}\right) \quad j = 1, ..., n \quad i = 1, ..., m \tag{7.14}$$

It is possible to check that through the definition in Eq. 7.14, summing up for all the configurations, we cover the full probability-spectrum:

$$\begin{aligned} p^i = \sum_{j=1}^n p_j^i &= \sum_{j=1}^n \frac{1}{(n-1)}\left(1 - \frac{|w_*^i - w_j^i|}{\sum_{j=1}^n |w_*^i - w_j^i|}\right) \quad i = 1, ..., m \\ &= \frac{1}{(n-1)}\left(n - \frac{\sum_{j=1}^n |w_*^i - w_j^i|}{\sum_{j=1}^n |w_*^i - w_j^i|}\right) \\ &= \frac{n-1}{n-1} = 1 \end{aligned} \tag{7.15}$$

If we consider the definition in Eq. 7.14 but we want to account for all the nodes, it is possible to define the total probability of any configurations through a weighted average that includes the nodal weights f^i

$$p_j = \frac{\sum_{i=1}^m f^i p_j^i}{\sum_{i=1}^m f^i} \tag{7.16}$$

Similarly to the previous case, let us check that, including the weighted average for all the nodes, we still fully cover the probability-spectrum:

$$\begin{aligned} p = \sum_{j=1}^n p_j &= \sum_{j=1}^n \left(\frac{\sum_{i=1}^m f^i p_j^i}{\sum_{i=1}^m f^i}\right) = \frac{1}{\sum_{i=1}^m f^i} \cdot \sum_{j=1}^n \left(\sum_{i=1}^m f^i p_j^i\right) \\ &= \frac{1}{\sum_{i=1}^m f^i} \cdot \sum_{i=1}^m \left(\sum_{j=1}^n f^i p_j^i\right) \\ &= \frac{1}{\sum_{i=1}^m f^i} \cdot \sum_{i=1}^m f^i \sum_{j=1}^n p_j^i \\ &= \frac{\sum_{i=1}^m f^i}{\sum_{i=1}^m f^i} = 1 \end{aligned} \tag{7.17}$$

Eqs.7.14 and 7.16 determine the discrete probability distribution that has to be set at all the possible configurations of the electromagnetic ports. All the nodes contribute to decide the best configuration, based upon an independent judgment of suitability.

7.6 Physical determination of the target power density

7.6.1 Distinction of the time scales

The definition of the discrete probabilities as presented in section 7.5 is characterized by the presence of the term w_*^i, which must be determined considering the physics of the system. Before starting the analysis, it is important to make a comment about the target power density function. In general, the system can be analyzed and optimized in a time-variant state, and therefore, all the expressions that have been defined in section 7.5 should be expressed as functions over time. In order to keep compact the notation, only the temperature target function $T_*^i = o^i(t)$ was explicitly expressed in dependence to time in the previous section. Let us distinguish two time domain scales. First, there is the scale related to the thermal evolution of the system is characterized by a sufficiently small time step Δt_{th}, where all the thermal properties presented in Eq. 7.9 do not change. Second, there is the scale related to the time necessary to change the electromagnetic settings at the ports, and it is characterized by the time step Δt_{em}. Within a thermal time step there is a fixed set of l electromagnetic time steps, and therefore $\Delta t_{th} = l\Delta t_{em}$ as presented in Fig. 7.6 . Therefore, we can distinguish three different

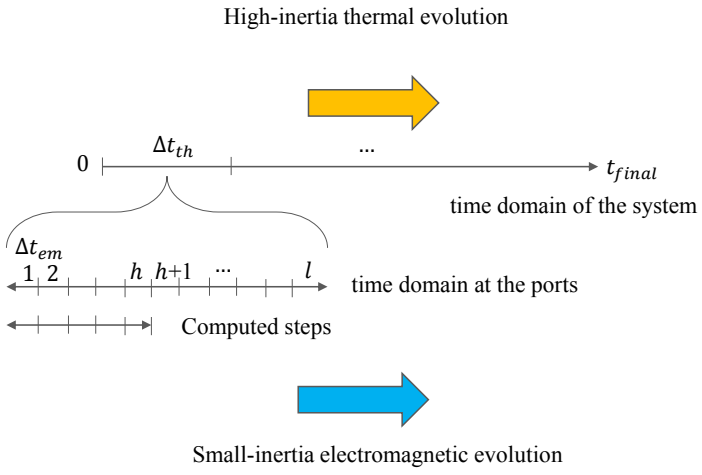

FIGURE 7.6: Time scales related to the thermal evolution and to the electromagnetic changes at the ports.

power density functions: w_c^i which is the computed power density after the probabilistic extraction process at any Δt_{em}; w_*^i which is the actual target function updated after any extraction, and it has to be updated at any Δt_{em}; w_r^i which is the physically required function and that must be updated at any Δt_{th}. The definition of the target function w_*^i can be computed in such a way that it is possible to

compensate the discrepancies between the already computed extractions and the physically required function. Considering the case where h extractions have been already done, we impose the following condition:

$$\begin{aligned} w_r^i &= \frac{\sum_{t=0}^{h}(w_c^i)_t + (w_*^i)_{h+1}(l-h)}{l} \quad h = 1,...,l-1 \quad i = 1,...,m \\ \rightarrow (w_*^i)_{h+1} &= \frac{l w_r^i - \sum_{t=0}^{h}(w_c^i)_t}{l-h} \end{aligned} \tag{7.18}$$

thanks to Eq. 7.18 it is possible to compute the value of $(w_*^i)_{h+1}$ at any step Δt_{em}, just knowing the previously extracted set of power densities $\{(w_c^i)_1, ..., (w_c^i)_h\}$ and the physically required power function w_r^i.

7.6.2 Determination of the physically required power function

In this section, the calculation of the required physical power function is presented. Let us recall that the actual objective function is temperature $T_*^i = o^i(t)$ and that we must identify the function w_r^i such that it can induce the desired temperature. Without loosing generality of the method, we make several assumptions that are present in practical situations, allowing to get a few simplifications. Let us consider the case where the thermal load is a fluid that is passing through a microwave cavity, and we assume that the fluid is characterized by a known velocity-field $\boldsymbol{V}(x,y,z)$. We assume that the fluid has already achieved the steady-state condition, and therefore $\partial \boldsymbol{V}(x,y,z)/\partial t = 0$. We consider the case where the objective temperature pattern is a fixed function over time and $\partial T_*/\partial t = 0$. Now, we can consider the energy transport equation [26]:

$$\rho c_p \frac{\partial T}{\partial t} + \rho c_p \nabla \cdot (T\boldsymbol{V}) = k_{th}\nabla^2 T + Q \tag{7.19}$$

and given the vectorial identity [133]:

$$\nabla \cdot (\phi \boldsymbol{A}) = \phi \nabla \cdot \boldsymbol{A} + \boldsymbol{A} \cdot \nabla \phi \tag{7.20}$$

we derive the following relation:

$$\rho c_p \nabla \cdot (T\boldsymbol{V}) = \rho c_p (T \nabla \cdot \boldsymbol{V} + \boldsymbol{V} \cdot \nabla T) \tag{7.21}$$

Let us consider that we are dealing with in incompressible fluid, and so we can describe this condition as $\nabla \cdot \boldsymbol{V} = 0$ [134]. Therefore, considering the incompressibility and by substitution of Eq. 7.21 into Eq. 7.19, we derive:

$$Q = \rho c_p \frac{\partial T}{\partial t} + \rho c_p (\boldsymbol{V} \cdot \nabla T) - k_{th} \nabla^2 T \tag{7.22}$$

Eq. 7.22 states that the term Q can be assumed as the necessary power density to induce three physical effects:

- The increment of the local temperature over time: $\rho c_p \frac{\partial T}{\partial t}$.
- The compensation of losses/acquisitions of diffusive heat (it depends on the temperature gradient): $-k_{th} \nabla^2 T$.
- The creation of a thermal gradient along flow direction: $\rho c_p (\boldsymbol{V} \cdot \nabla T)$.

Therefore, it is reasonable to identify the function w_r^i with a quantity which has the same structure of Eq. 7.22. So, now we can derive an expression for w_r^i as follows[3]:

$$w_r^i = \left(\frac{T_* - T}{T_*} \right) \rho c_p \dot{T}_\dagger + \rho c_p (\boldsymbol{V} \cdot \nabla T) - k_{th} \nabla^2 T \tag{7.23}$$

Where $\dot{T}_\dagger$ is a parameter that must be set "a priori". Eq. 7.23 is similar to Eq. 7.22, excepted for the first term. In fact the first term in Eq. 7.22 goes to zero when the temperature has achieved the steady-state. Instead, the first term in Eq. 7.23 goes to zero when the temperature has achieved the objective temperature function. If the temperature pattern achieves $T = T_*$, the required power density function strives to maintain the temperature level, compensating the thermal diffusion and providing the necessary energy to increment the temperature along the flow-streams.

7.6.3 Convection at the superficial nodes

The expression for w_r^i, which is presented in the section 7.6 can be applied for internal nodes of the domain Ω. Regarding superficial nodes, it is important to include the effects related to thermal convection as boundary condition. If we consider that natural convection occurs at the surface of thermal load, we have to derive an expression for superficial w_r^i. Let us consider an infinitesimal element, which has one face that corresponds to the local border of Ω. The element has an infinitesimal volume $dV = dl\ d\rho\ d\delta$, and the $d\delta$ is the infinitesimal depth. The differential element is depicted in Fig.

[3] It has to be noted that the differential operators are in the discrete form since the function w_r^i is discrete.

7.7 . The infinitesimal heat losses for thermal convection can be accounted for as follows:

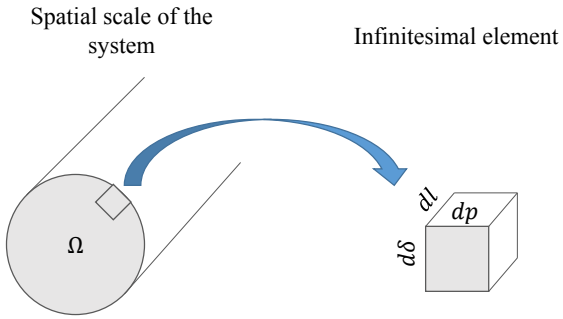

FIGURE 7.7: Superficial infinitesimal element which is subjected to natural thermal convection.

$$dQ = (dl\ dp)h(T - T_0) \tag{7.24}$$

Here, if we consider that the required power density should be expressed as a volumetric term, we can impose the following relations:

$$w_r^i\ dV = dQ \tag{7.25}$$

$$\rightarrow w_r^i = \frac{h}{d\delta}(T - T_0) \tag{7.26}$$

Therefore, from Eq. 7.26 we can derive another expression just considering the finite depth δ:

$$w_r^i = \frac{h}{\delta}(T - T_0) \tag{7.27}$$

Eq. 7.27 should be applied for all the nodes that are within the finite superficial layer which is characterized by the depth δ.

7.6.4 Computational strategy

So far, we have developed through a probabilistic and mechanistic approach the main expressions that should be implemented in an overall algorithmic strategy. In the Table 7.1, the equations have been reported following the sequential computational order. There are two possible uses of the presented computational schema. First, the development of an open-loop control for a real system after a stage

Step	Computation	Note
$\forall \Delta t_{th}, \quad \forall i = 1, ..., m$		
$i = 1, ..., d$	$w_r^i = \left(\frac{T_* - T}{T_*}\right) \rho c_p \dot{T}_\dagger + \rho c_p (\boldsymbol{V} \cdot \nabla T) - k_{th} \nabla^2 T$	
$i = d+1, ..., m$	$w_r^i = w_r^i = \frac{h}{\delta}(T - T_0)$	
-	$\dot{\boldsymbol{E}}_1, ..., \dot{\boldsymbol{E}}_k$	independent ports
$\forall \Delta t_{em}, \quad \forall i = 1, ..., m,$		
	$(w_*^i)_{h+1} = \frac{l w_r^i - \sum_{t=0}^{h} (w_c^i)_t}{l - h}$	$h \in [0; l-1]$
$\forall j = 1, ..., n$		
	$\dot{\boldsymbol{E}}_j = f_j^i \rightarrow w_j^i$	
	$p_j^i = \frac{1}{(n-1)} \left(1 - \frac{\lvert w_*^i - w_j^i \rvert}{\sum_{j=1}^{n} \lvert w_*^i - w_j^i \rvert}\right)$	
-	$p_j = \frac{\sum_{i=1}^{m} f^i p_j^i}{\sum_{i=1}^{m} f^i}$	
-	$\{\boldsymbol{P}, \boldsymbol{\phi}\}_j \rightarrow w^i \rightarrow T$	identify optimum
-		start over

TABLE 7.1: Computational steps in sequence.

of data-acquisition by mean of a numerical finite element analysis. Second, the strategy can be used to pilot in real-time a system through a close-loop control. In this work we consider only the first case because further investigation is needed to reconstruct the temperature inside the cavity at a speed that must be comparable with the thermal evolution. An interesting approach of internal thermometry was already developed by researchers, but the required computation does not allow to have a real time reconstruction [135]. Therefore, the current work is oriented to an open-loop strategy, starting from the algorithmic and numerical analysis, in order to derive the optimal "recipe" of the port settings. These two different approaches are reported in Fig. 7.8 and 7.9.

7.7 Test-case: uniform heating pattern

One of the most important open challenges in microwave processing is the achievement of uniform heating pattern, we report a simple case where the required power density w_r^i is a constant function. The obtained results with probabilistic control through solid state technology (SBS) will be compared with the results of the correspondent case which is based on magnetron (MBS). First of all, we have to point out a few important considerations:

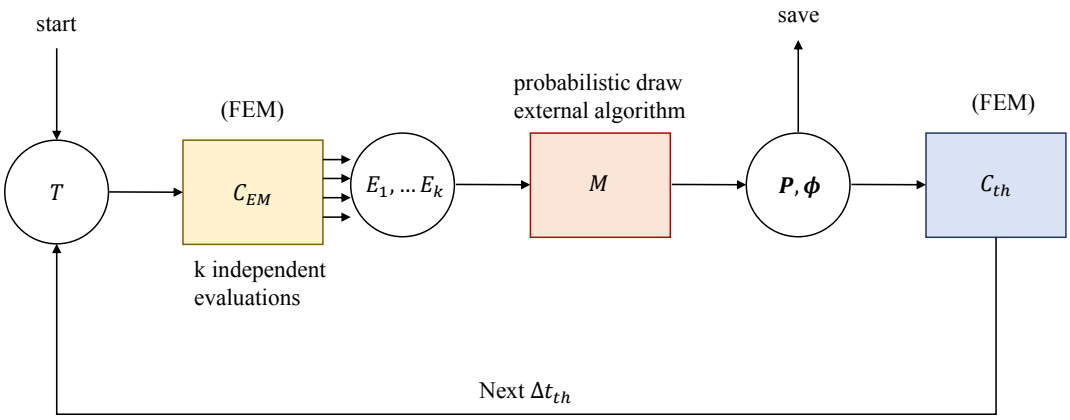

FIGURE 7.8: Data-flow that must be performed in order to create the recipe. The probabilistic algorithm can be considered as the driver of microwave heating.

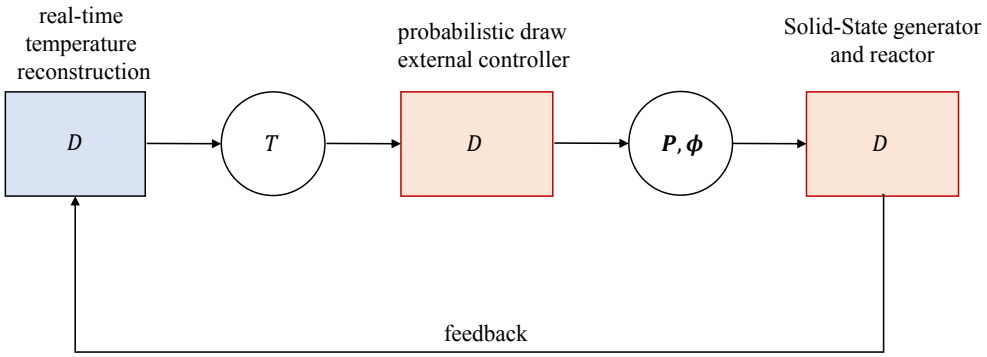

FIGURE 7.9: The probabilistic algorithm is directly implemented in the control system and it determines in real-time the optimal configuration for microwave heating.

- We consider the power density as the actual target function (not the temperature)in order to impose that the total power dissipation within the load is the same in both the cases:

$$\iiint_{\Omega}(w^i)_{\text{MBS}}dV = \iiint_{\Omega}(w^i)_{\text{SBS}}dV \tag{7.28}$$

- The reactor under investigation was not previously optimized, so the results are not particularized to a specific reactor shape.

- The efficiency of the system was not considered in the current test-case. SBS is characterized by dominant Pareto configurations with respect to MBS considering uniformity and efficiency as objective functions [136].

- The pipe walls are adiabatic to maximize the achievement of thermal uniformity, since the convection at the walls would tend to level out the temperature to the room level.

the reactor shapes and tubular loads are depicted in Fig. 7.10. The input parameters of the tested simulations are reported in Table 7.2.

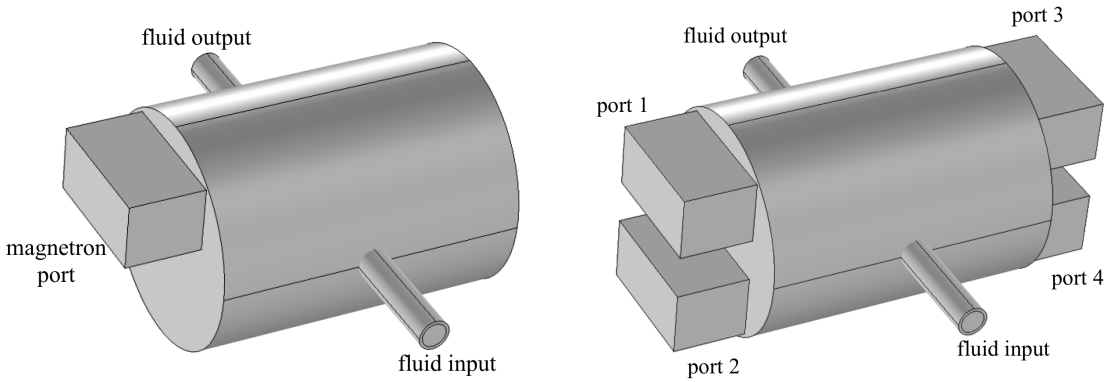

FIGURE 7.10: Geometry of the 1-port MBS and 4-ports SBS reactors.

The plot (a) and (b) in Fig. 7.11, regard the SBS reactor, depicting the histogram of the computed probability function p_j of all the possible configurations. Since the plot (a) is strongly asymmetric, we can state that the algorithm avoids the worst configurations rather than stand out a few selected ones. This fact is reasonable, considering that the reactor has not been previously optimized, and therefore there is not any configurations which is significantly better than others. In Fig. 7.11 (b), we can observe that the histogram of the relative error function ϵ^i, is presented. This function is defined

Input parameters for simulation purpose

Parameter	Value	Source
Reactor dimensions (cylinder) (m)	(r) 0.075; (h) 0.2	
Waveguide apertures (m)	0.8636×0.04318	
Thermal load (cylinder) (m)	(r) 0.01; (h) 0.3	
Electromagnetics		
Frequency (GHz)	2.45	
Total dissipated power (W)	100	
Complex dielectric permittivity (1)		
Air	1	
Fluid (water)	(interpolated data)	[137]
Heat transfer		
Convective heat coefficient (W/(m^2 K))	0	
Thermal conductivity (W/(m K))		
Air	0.026	[76]
Fluid (water)	0.57	[76]
Specific heat capacity (J/(kg K))		
Air	1006	[76]
Fluid (water)	4178	[76]
Density (kg/(m^3))		
Air	1.25	[138]
Fluid (water)	998	[76]
Fluid dynamics		
Dynamic viscosity (Pa s)	$1.0089 \times 10^{-}3$	[138]
Specific heat ratio (1)	1	
Input velocity (m/s)	0.001	
Output pressure (Pa)	101325	
Initial & Boundary conditions		
Ambient pressure (Pa)	101325	
Temperature (K)	293.15	
Metallic walls	PEC	[37]
Tubular load walls	no-slip	

TABLE 7.2: Input parameters for simulation purpose.

as follows:

$$\epsilon^i = 100 \left(\frac{w_r^i - w^i}{w_r^i} \right) \tag{7.29}$$

The ϵ^i function is monotonically decreasing, which means that there is not any systematical phase-shift (offset) between required power density and actually achieved level throughout the load. In Fig.7.12 (a) and (b) there are the actual power density functions w^i in Ω for SBS and MBS respectively. The red line indicates w_r^i. Despite there are two hot-spots in both the cases, the majority of the points are much more smoothly heated in SBS than in MBS, since the values are more confined around the required level w_r^i. Fig.7.12 (c) and (d) show that the distribution shape for SBS is much more elongated at the required power level w_r^i, than in the MBS case, indicating that the required value level is more frequently occurred in SBS. Fig. 7.13 shows the temperature distribution patterns of the fluid at several cross sections of the flow. The temperature pattern is much more homogeneous for probabilistic based controlled SBS than for traditional MBS, especially regarding the core. MBS is characterized by several colder regions at the core with respect to the superficial levels. This behavior is quite evident in the cross sections which are close to the entrance of the fluid. Instead, the SBS temperature distributions for SBS are characterized by a more uniform heating of the core at all the cross sections (7.11 (a) - (b)). In general, the results indicate that an improvement of heating pattern was achieved by using the combination of solid state technology (SBS) and a probabilistic control algorithm, with respect to the case based on traditional magnetron source.

7.8 Conclusions

The purpose of this work is turned to the development of a new probabilistic algorithm, based upon the new generation of solid state microwave sources for high power applications, which allows to optimize the heating pattern within the thermal load in microwave processing. In this work we have reported the theoretical and computational strategy to improve the heating pattern quality. A significant test-case was considered as benchmark for comparing the performances between magnetron based system (MBS) and solid state based system (SBS). An experimental 2-ports SBS prototype was developed in laboratory and tested to demonstrate the efficacy into create different electric field patterns. The prototype was adopted to validate the numerical FE model, which was used to make comparative predictions between MBS and SBS. The SBS reactor was driven by an innovative probabilistic algorithm. The results confirm the capability of improving the temperature pattern quality

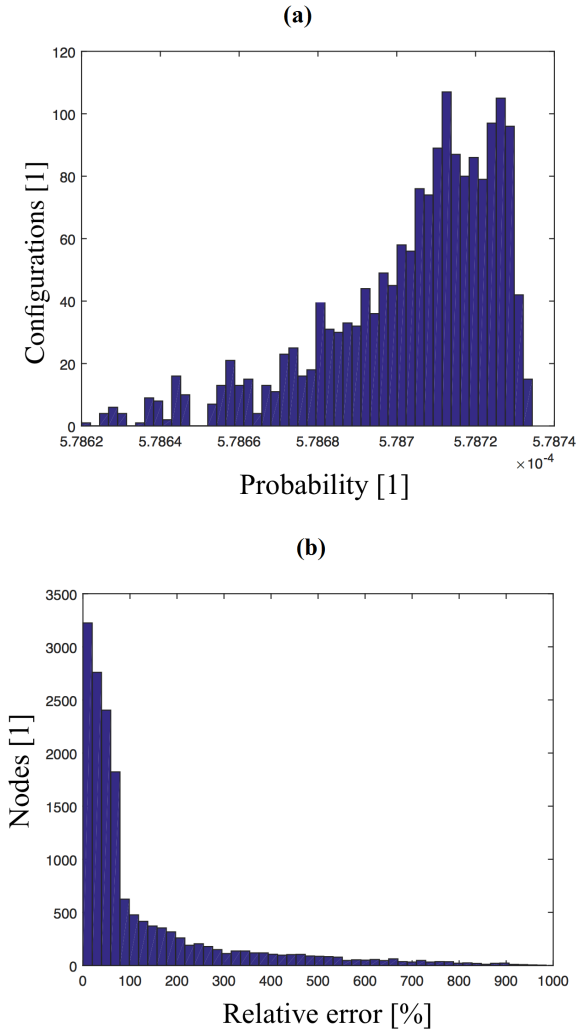

FIGURE 7.11: The figures are referred to the probability function (a) and relative error (b) of SBS.

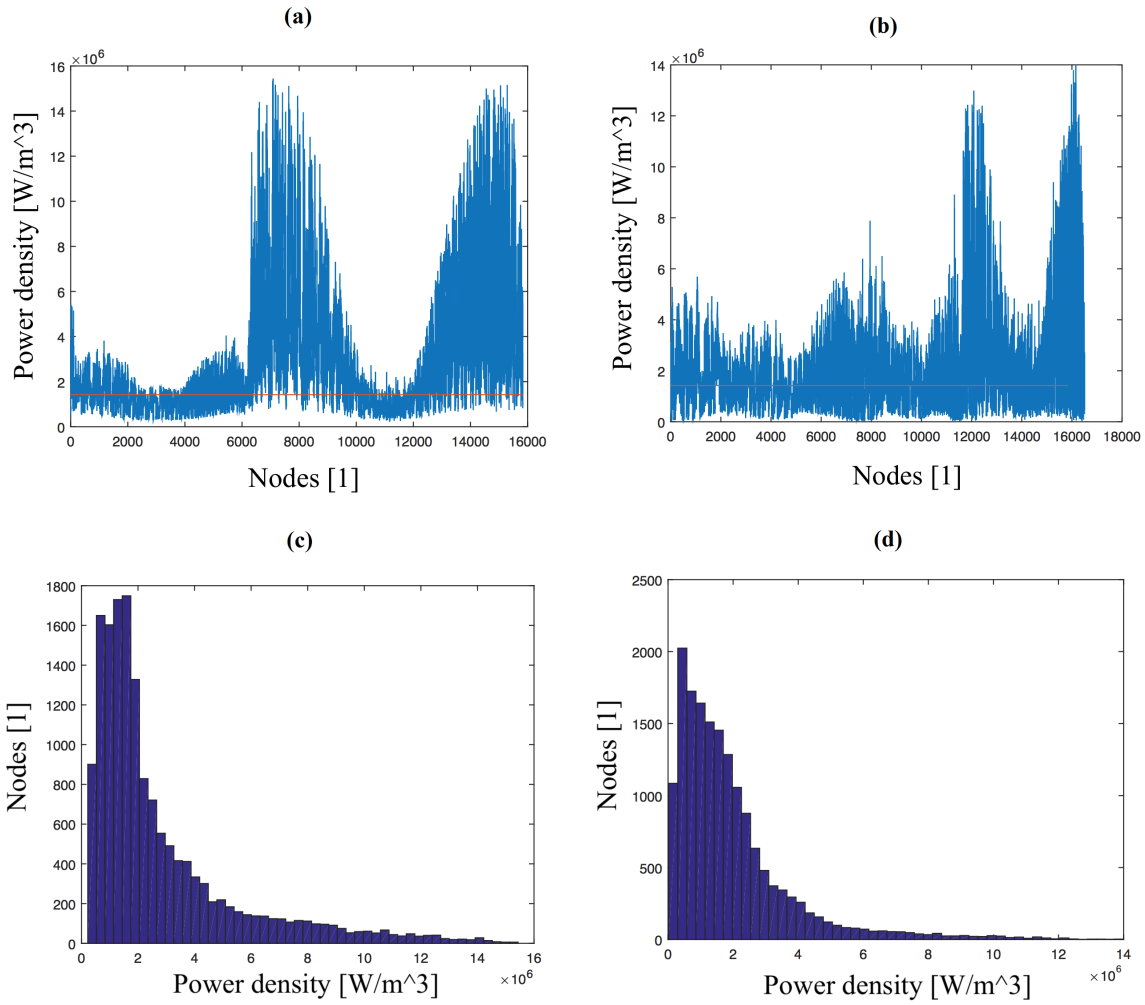

FIGURE 7.12: Plots (a) - (c) are referred to SBS, while plots (b) - (d) are referred to MBS.

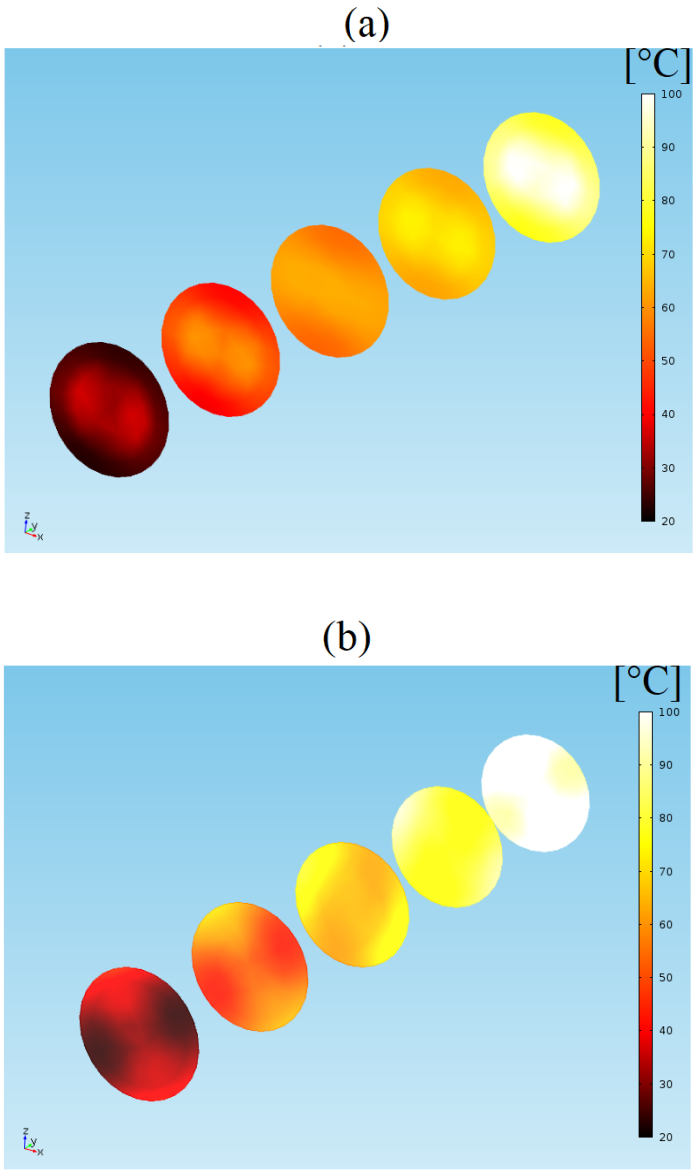

FIGURE 7.13: (a) SBS technology: uniform heating along the the different cross sections of the gas-flow. (b) MBS technology: strong non-uniform heating since the core is colder then the surface at several positions.

even without optimizing the reactor geometry. New generation reactors can further exploit the characteristics of SBS (e.g. phase-shift control, power modulation, high-speed reconfiguration, etc). New scenarios for microwave heating should be explored in the future, considering that further advancements of solid state electronics can be achieved even in economical terms. Considering the reduction of costs for massive industrial productions of electronic components, solid state microwave sources combined with suitable algorithmic controllers can become competitive with traditional MBS technology in lab-scale as well as in industrial-scale.

8 Conclusions

8.1 RF biomedical treatment - Electrothermal dosimetry

After a series of procedures for the CE marking request, the medical device was considered suitable for carrying out the therapeutic treatment. The regulatory conditions have been verified (93/42/EC, 2007/47/EC, IEC EN 60601- 1) and the device has met the essential requirements (Annex I of the standard 93/42/EC) and it is classified as class II A, as it falls into the category *active therapeutic medical device intended to release or exchange energy with the human body in a potentially non-dangerous form*. Based on this classification, Directive 93/42/EC and S.M.I. 2007/47 EC requires a certification process based on the risk class. According to Annex II it was necessary to carry out a guarantee process by a notified body to assess the quality system's dossier and functioning. The therapy has already been tested for some clinical trials in Italy at the San Raffaele Hospital in Milan and in some other Italian eye clinics, also in Germany and in England. The next steps will be related to the improvement of the mask electrode, shaping and positioning in the most appropriate way the two metal electrodes, thus, continuing the research carried out in the framework of this thesis.

8.2 MW shielding design - Novel strategy

Thanks to the strategy in the work presented here it was possible to develop a complete 915 MHz operational choke, that is ready for commercialization. This product was developed in collaboration with an industrial partner (Illinois Tool Works), allowing the diffusion of the here developed device in the American market. As previously noted, among the results obtained, there is an electromagnetic configuration whereby the device exhibits a physical behavior independent from the choke-cavity distance. So, it is conceivable that in the future we can develop new generation shields that allow protection without suffering the effect of aging due to mechanical failures. Further research must

be carried out to identify the electromagnetic characteristics that guarantee this condition and subsequently increase the shielding effectiveness to normative values.

8.3 MW leakage and human exposure - Safety implications

After more than fifty years since the introduction of microwave ovens in the market, this technology has become widespread in both industrialized and developing countries. Categories of people belonging to the weakest groups are subject to greater risks for electromagnetic emissions if they are outside the regulatory levels. For example, when the shielding effectiveness is limited by the mechanical wear of the door hooks, the proximity of the body to the appliance can become critical (e.g. often children observe cooking at very short distances from the door, exposing the eyes to fields that are potentially intense). With the results presented in this thesis, even if there are limits due to the enormous variability of the possible cases, safety intervals have been defined even if the device is subject to aging. Therefore, until a shielding system has been developed that minimizes the influence of aging, it is possible to eliminate health risks through responsible use.

8.4 MW food arcing - Theoretical study and safety implications

Thanks to the results obtained from these researches it is possible to argue with scientific reasons what are the causes of the formation of discharges in food during heating at microwave frequencies. Some agencies such as the Canadian Food Inspection Agency or producers like General Electrics have observed and declared the presence of this phenomenon, even if not strictly justifying the real physical causes. As a result there is less effective communication to citizens and/or customers to reduce risk factors. Moreover, these phenomena have been empirically observed by many people and can be easily verified due to the high diffusion of amateur video on social networks about plasma discharges that are generated in microwave ovens. This phenomenon has aroused much curiosity in the general public. Now, a scientific based explanation of the physical mechanism that leads to a discharge in microwave food processing has been provided.

8.5 MW chemical processing - Comparing magnetron and solid-state sources

Microwave technology has enormous potential for the chemical industry, but despite many attempts have already been made, large-scale development has not yet completely taken place. Through the research developed in this thesis, the technical-scientific superiority of solid-state technology compared to magnetron has been verified in terms of efficiency and uniformity. This means that a new possibility of relaunching can pass through a path so far unexplored. Applications can also be addressed to the automotive sector, as well as to the chemical production sector. The market currently shows a reduction in the costs of solid-state electronics at high frequency and high power that seems to allow rapid growth of the learning curve. As long as the market is not yet ready for real dissemination, research must also insist on a possible hybridization of this technology to allow a gradual replacement.

8.6 MW heating - Probabilistic strategy using solid-state source

After demonstrating the superiority of solid state technology for high frequency and high-power applications, it was necessary to identify an optimized management of these systems. If we consider that the new potentials are based on the ability to increase the available configurations of the electric field, it is necessary to invest on artificial intelligence to control these configurations. Between the two main strands there are the algorithmic control and the reactor design. In the current thesis, a probabilistic control algorithm has been developed that maximizes the quality of a solid-state RF/MW process. Therefore, it is already possible to implement such systems also for reactors, or in general traditional cavities. This can bridge the gap between conventional and new generation technology, facilitating hybridization rather than substitution.

8.7 Final comment

In order to avoid repetition of the previous conclusions, this final section is turned to make some comments on the potential of the research achievements on the long run. The findings in chapters 3, 4 and 5 can be considered as immediately usable. Indeed, safe behavior of microwave oven users

and indications for designers are formulated in such a way to be directly available. Instead, the results achieved in chapters 2, 6 and 7 are just a starting point to opening new research scenarios. Dry eye treatment by mean of radiofrequency stimulation was tested with a few experimental trials. The procedure to achieve the approval from the European Community is quite long and complex. Safety and ethical issues must be considered as fundamental research drivers, and therefore, numerical techniques are the only available instruments to overcome these obstacles. Research findings in chapter 2 provide quantitative results that would be inaccessible experimentally. They provide information on new potential protocols to improve the effectiveness of the therapy. Many investigations are still necessary to achieving regular adoption of this promising therapy in hospitals and clinics, but the results obtained so far are extremely encouraging.

The results in chapters 6 and 7 address chemical engineering researchers and designers to investigate on new microwave solid-state systems as a competitive alternative of conventional heating. The advantages can be expressed in terms of process efficiency since chemical reactions can occur with improved uniformity. Many other technical aspects should be considered to assess the possibility of integrating microwave solid state technology with traditional power sources. Power Electronics at high frequency has not achieved industrial maturity yet, and therefore cost drivers determine an economical gap that still must be compensated. Higher quality in chemical processing implicates reduction on consumption of chemicals and energy. Considering the increased sensitivity of people to environmental pollution, probably as a consequence of climate changes, more restrictive regulation on emissions and temporal subsidizes could play a major role in the future to implement on large scale green technologies that are already available today.

Christian Bianchi

9 Appendix

9.1 Chapter 2: Matlab files

9.1.1 Reconstruction of the material properties

```
1
2  clc
3  clear all
4  close all
5
6  zz=2;
7  %NUMERO DI CUBETTI CHE VIENE ANALIZZATO AD OGNI SLICE
8  sezionamenti=100;
9  %indicare fino a dove sezionare il corpo
10 effettuate=0;
11 %indicare se si ï£¡ giï£¡ in possesso di un sezionmento
       precedentemente effettuato
12 CORPO_files=sezionamenti;
13 %in generale questo valore puï£¡ essere diverso,
14 %ma conviene lasciarlo pari all'ultimo numero di elementi sezionati
15 percorso='C:\Users\christian\Desktop\HUMAN BODY\Algoritmi\CORPO';
16 %impostare la corrente directory di lavoro
17
18
19 for slice_fatte=effettuate:sezionamenti-1
20
21 tic
```

```
22
23 m = 1;                % = meter
24 mm = 1e-3*m;
25
26 %% QUI SI CARICA UN TENSORE CONTENENTE I DATI DEL CORPO
27
28
29 %% Loads the description of the different tissues
30 %(each tissue correspond to a 8-bit value)
31 [name, id] = textread ('tissues_matlab.txt', '%s %d');
32 % = name and ID of all the tissus
33 %% Load the model of the human body (resolution = 3mm).
34 fid = fopen ('a_man_3mm_196x114x626.raw', 'r');
35 Nx = 196; Ny = 114 ; Nz = 626;
36 rawdata = reshape (fread (fid, inf, 'uint8=>uint8'), [Nx Ny Nz]);
37 fclose (fid);
38
39 %%%%%%%%%%%%%%%%%%%%%%%%%%%%%%%%%%%%%%%%%%%%%%%%%%%%%%%%%%%%%%%%%%%%
40
41 ciccio=rawdata(1:196, 1:114, (slice_fatte*zz+1):(slice_fatte*zz+zz)
      );
42 %TENSORE DI APPOGGIO
43
44 %%%%%%%%%%%%%%%%%%%%%%%%%%%%%%%%%%%%%%%%%%%%%%%%%%%%%%%%%%%%%%%%%%%%
45
46 clear rawdata
47
48 rawdata=ciccio;
49
50 xx=numel(rawdata(:,1,1));
51 yy=numel(rawdata(1,:,1));
```

```
52 zz=numel(rawdata(1,1,:));
53
54 %COSTRUZIONE DEL TENSORE CORPO E ARIA
55
56 posizione=zeros(xx*yy*zz,4);
57 index=zeros((xx*yy*zz),3);
58
59 cont=1;
60 contat=1;
61 contatore=1;
62
63 for jj=1:numel(rawdata(:,1,1))
64    % tic
65
66     for kk=1:numel(rawdata(1,:,1))
67
68         for ll=1:numel(rawdata(1,1,:))
69
70             if rawdata(jj,kk,ll)~=0;
71
72                corpo(contat,1:3)=3*mm*[jj, kk, slice_fatte*zz+ll];
73
74             contat=contat+1;
75             end
76
77             if rawdata(jj,kk,ll)==0;
78
79                aria(contatore,1:3)=3*mm*[jj, kk, slice_fatte*zz+ll
                      ];
80
81             contatore=contatore+1;
```

```
82              end
83
84              index(jj,kk,ll)=cont;
85
86          cont=cont+1;
87          end
88
89      cont=cont+1;
90      end
91
92  cont=cont+1;
93  end
94
95  %STAMPA A VIDEO
96
97  slice_fatte
98  tempo1=toc
99
100 %%%%%%%%%%%%%%%%%%%%%%%%%%%%%%%%%%%%%%%%%%%%%%%%%%%%%%%%%%%%%%%%%%%%%%%
101 %CALCOLO DEL FRONTE DI INTERFACCIA TRA CORPO E ARIA DELLA SINGOLA
       SLICE
102
103 tic
104
105 kont=1;
106
107  for ii=1:numel(corpo(:,1))
108
109      for jj=1:numel(aria(:,1))
110
111          dist=norm(corpo(ii,:)-aria(jj,:));
```

```
112
113         if dist<0.0031 & dist>0.0029
114
115            fronte_corpo_aria(kont,:)=corpo(ii,:);
116
117         kont=kont+1;
118         end
119
120     end
121
122  end
123
124 %STAMPA A VIDEO
125
126 fronte_corpo_aria
127 slice_fatte
128 tempo2=toc
129
130 %%%%%%%%%%%%%%%%%%%%%%%%%%%%%%%%%%%%%%%%%%%%%%%%%%%%%%%%%%%%%%%%%%%%%%%
131
132 %SALVATAGGIO DEI FILE TXT PARZIALI
133
134 stringhetta=num2str(slice_fatte+1);
135 ext='.txt';
136 nome_salvataggio=strcat('CORPO',stringhetta,ext);
137 fid = fopen(nome_salvataggio,'wt')
138
139 for ind=1:numel(fronte_corpo_aria(:,1))
140
141     fprintf(fid,'%5.5f %5.5f %5.5f\n',fronte_corpo_aria(ind,1),...
142     fronte_corpo_aria(ind,2),fronte_corpo_aria(ind,3) );
```

```
143
144 end
145
146 fclose(fid)
147
148 end
149
150 %%%%%%%%%%%%%%%%%%%%%%%%%%%%%%%%%%%%%%%%%%%%%%%%%%%%%%%%%%%%%%%%%%%%%%%
151
152 %SALVATAGGIO DEI VARI FILE DEL CORPO IN UN UNICO ELEMENTO
153
154 for k=1:CORPO_files
155
156 indice=num2str(k);
157 ext='.txt';
158 nome_completo=strcat(percorso,indice,ext);
159
160 filename = nome_completo;
161 formatSpec = '%7f%8f%f%[^\n\r]';
162 fileID = fopen(filename,'r');
163 dataArray = textscan(fileID, formatSpec, 'Delimiter', '',...
164     'WhiteSpace', '',  'ReturnOnError', false);
165 fclose(fileID);
166
167 X_provv = dataArray{:, 1};
168 Y_provv = dataArray{:, 2};
169 Z_provv = dataArray{:, 3};
170
171 clearvars filename formatSpec fileID dataArray ans;
172
173     if k==1
```

```
174
175         X=X_provv;
176         Y=Y_provv;
177         Z=Z_provv;
178
179     end
180
181    if k>1
182
183         XX=X;
184         YY=Y;
185         ZZ=Z;
186
187         X=[XX;X_provv];
188         Y=[YY;Y_provv];
189         Z=[ZZ;Z_provv];
190
191    end
192
193 end
194
195 CORPO_completo=[X, Y, Z];
196
197 %%%%%%%%%%%%%%%%%%%%%%%%%%%%%%%%%%%%%%%%%%%%%%%%%%%%%%%%%%%%%%%%%%%%%%%%
198
199 %SALVATAGGIO DEI FILE TXT
200
201 ext='.txt';
202 nome_salvataggio=strcat('CORPO_completo',ext);
203 fid = fopen(nome_salvataggio,'wt')
204
```

```
for ind=1:numel(CORPO_completo(:,1))

    fprintf(fid,'%5.5f %5.5f %5.5f\n',CORPO_completo(ind,1),...
    CORPO_completo(ind,2),CORPO_completo(ind,3) );

end

fclose(fid)
```

9.1.2 Reconstruction of the phantom geometry

```
clc
clear all
close all

zz=3; % NUMERO DI CUBETTI CHE VIENE ANALIZZATO AD OGNI SLICE
sezionamenti=125;
effettuate=0;

%%%%%%%%%%%%%%%%%%%%%%%%%%%%%%%%%%%%%%%%%%%%%%%%%%%%%%%%%%%%%%%%

%AQUISIZIONE DELLE PROPRIETA'

filename = 'D:\HUMAN BODY RECONSTRUCTION\Algoritmi\Dati_completi.
   txt';
delimiter = '\t';

formatSpec = '%s%s%s%s%s%s%s%s%s%s%s%s%s%s%s%s%s%s%s%s%s%s%s%[^\n\r]';

fileID = fopen(filename,'r');

dataArray = textscan(fileID, formatSpec,'Delimiter', delimiter, ...
```

```
    'ReturnOnError', false);

fclose(fileID);

raw = repmat({''},length(dataArray{1}),length(dataArray)-1);
for col=1:length(dataArray)-1
    raw(1:length(dataArray{col}),col) = dataArray{col};
end
numericData = NaN(size(dataArray{1},1),size(dataArray,2));

for col=[1,3,4,5,6,7,8,9,10,11,12,13,14,15,16,17,18,19,20,21]
    % Converts strings in the input cell array to numbers....
    ...Replaced non-numeric
    % strings with NaN.
    rawData = dataArray{col};
    for row=1:size(rawData, 1);
        % Create a regular expression to detect and remove ...
        ...non-numeric prefixes and
        % suffixes.
        regexstr = '(?<prefix>.*?)(?<numbers>([-]*(\d+[\.]*)
           +[\,]{0,1}...
        \d*[eEdD]{0,1}[-+]*\d*[i]{0,1})|([-]*(\d+[\.]*)*[\,]{1,1}\
           ...
            d+[eEdD]{0,1}[-+]*\d*[i]{0,1}))(?<suffix>.*)';
        try
            result = regexp(rawData{row}, regexstr, 'names');
            numbers = result.numbers;

            % Detected commas in non-thousand locations.
            invalidThousandsSeparator = false;
            if any(numbers=='.');
```

```
                thousandsRegExp = '^\d+?(\.\d{3})*\,{0,1}\d*$';
                if isempty(regexp(thousandsRegExp, '.', 'once'));
                    numbers = NaN;
                    invalidThousandsSeparator = true;
                end
            end
            % Convert numeric strings to numbers.
            if ~invalidThousandsSeparator;
                numbers = strrep(numbers, '.', '');
                numbers = strrep(numbers, ',', '.');
                numbers = textscan(numbers, '%f');
                numericData(row, col) = numbers{1};
                raw{row, col} = numbers{1};
            end
        catch me
        end
    end
end

rawNumericColumns = raw(:, [1,3,4,5,6,7,8,9,10,11,12,13,14,15,...
    16,17,18,19,20,21]);
rawCellColumns = raw(:, 2);


%% Allocate imported array to column variable names
tissue = cell2mat(rawNumericColumns(:, 1));
labels = rawCellColumns(:, 1)

VarName1 = cell2mat(rawNumericColumns(:, 2));
            ...%DENSITA' [kg/m^3]
VarName2 = cell2mat(rawNumericColumns(:, 3));
```

```
81              ...%CALORE SPECIFICO [J/(Kg*K)]
82 VarName3 = cell2mat(rawNumericColumns(:, 4));
83              ...%CONDUTTIVITA' TERMICA [W/(m*K)]
84 VarName4 = cell2mat(rawNumericColumns(:, 5));
85              ...%PERFUSIONE SANGUIGNA [mL/(min*Kg)]
86
87 blood_density=1049.75; % [Kg/m^3]
88 VarName4=VarName4*((10^-6)/60)*blood_density;  %PERFUSIONE
      SANGUIGNA [1/s]
89
90 VarName5 = cell2mat(rawNumericColumns(:, 6));
91              ...%GENERAZIONE TERMICA METABOLICA [W/kg]
92 VarName5=VarName5.*VarName1;
93              ...%GENERAZIONE TERMICA METABOLICA [W/m^3]
94
95 f=4*10^6;
96 omega=2*pi*f;
97
98 VarName6 = cell2mat(rawNumericColumns(:, 7)); %PERMITTIVITA'
      ELETTRICA [1]
99 VarName7 = cell2mat(rawNumericColumns(:, 8)); %CONDUTTIVITA'
      ELETTRICA [S/m]
100
101
102 TypesVar=['DENSITA [kg/m^3]','CALORE SPECIFICO [J/(Kg*K)]',...
103     'CONDUTTIVITA TERMICA [W/(m*K)]',...
104     'PERFUSIONE SANGUIGNA [1/s]',...
105     'GENERAZIONE TERMICA METABOLICA [W/m^3]',...
106     '%PERMITTIVITA ELETTRICA [1]','CONDUTTIVITA ELETTRICA [S/m]']
107
108 %% Clear temporary variables
```

```
109 clearvars filename delimiter formatSpec fileID dataArray ans raw
       col...
110     numericData rawData row regexstr result numbers ...
111     invalidThousandsSeparator thousandsRegExp me ...
112     rawNumericColumns rawCellColumns;
113
114 data=zeros(max(tissue),7);
115
116 for kk=1:numel(tissue)
117
118     data(tissue(kk),:)=[VarName1(kk),VarName2(kk),VarName3(kk),...
119     VarName4(kk),VarName5(kk),VarName6(kk),VarName7(kk)] ;
120
121 end
122
123 %%%%%%%%%%%%%%%%%%%%%%%%%%%%%%%%%%%%%%%%%%%%%%%%%%%%%%%%%%%%%%%%
124
125 %INIZIZALIZZO I CONTATORI FUORI DAL CICLO FOR
126
127 m = 1;
128 mm = 1e-3*m;
129
130 for hh=1:7
131
132 cont=1;
133 contat=1;
134
135 %% QUI SI CARICA UN TENSORE CONTENENTE I DATI DEL CORPO
136
137 corpo=zeros(30*145907,4);
138
```

```
139 for slice_fatte=effettuate:sezionamenti-1
140
141
142 %% Loads the description of the different tissues
143 ...(each tissue correspond to a 8-bit value)
144 [name, id] = textread ('tissues_matlab.txt', '%s %d');
145 ...% = name and ID of all the tissus
146 %% Load the model of the human body (resolution = 3mm).
147 fid = fopen ('a_man_3mm_196x114x626.raw', 'r');
148 Nx = 196; Ny = 114 ; Nz = 626;
149 rawdata = reshape (fread (fid, inf, 'uint8=>uint8'), [Nx Ny Nz]);
150 fclose (fid);
151
152 %%%%%%%%%%%%%%%%%%%%%%%%%%%%%%%%%%%%%%%%%%%%%%%%%%%%%%%%%%%%%%%%%%%%
153
154 ciccio=rawdata(1:196, 1:114, (slice_fatte*zz+1):(slice_fatte*zz+zz)
       );
155 ...%TENSORE DI APPOGGIO
156
157 %%%%%%%%%%%%%%%%%%%%%%%%%%%%%%%%%%%%%%%%%%%%%%%%%%%%%%%%%%%%%%%%%%%%
158
159 clear rawdata
160
161 rawdata=ciccio;
162
163 xx=numel(rawdata(:,1,1));
164 yy=numel(rawdata(1,:,1));
165 zz=numel(rawdata(1,1,:));
166
167 %COSTRUZIONE DEL TENSORE CORPO E ARIA
168
```

```
posizione=zeros(xx*yy*zz,4);
index=zeros((xx*yy*zz),3);

tic
for jj=1:numel(rawdata(:,1,1))
   % tic

    for kk=1:numel(rawdata(1,:,1))

        for ll=1:numel(rawdata(1,1,:))

            if rawdata(jj,kk,ll)~=0;

               corpo(contat,1:3)=3*mm*[jj, kk, slice_fatte*zz+ll];
               corpo(contat,4)=data(rawdata(jj,kk,ll),hh);

            contat=contat+1;
            end

            index(jj,kk,ll)=cont;

        cont=cont+1;
        end

    cont=cont+1;
    end

cont=cont+1;
end

tempo=toc
```

```
200
201 %STAMPA A VIDEO
202 slice_fatte
203
204 end
205
206 corpo=corpo(1:contat-1,:);
207
208 %SALVATAGGIO DEI FILE TXT
209
210 ext='.txt';
211 num=num2str(hh)
212 nome_salvataggio=strcat('MATERIALI',num,ext);
213 fid = fopen(nome_salvataggio,'wt')
214
215 for ind=1:numel(corpo(:,1))
216
217     fprintf(fid,'%5.5f %5.5f %5.5f %5.5f\n',corpo(ind,1),corpo(ind
        ,2),...
218     corpo(ind,3),corpo(ind,4) );
219
220 end
221
222 fclose(fid)
223
224 end
```

9.2 Chapter 6: Results in tabular form

9.3 Chapter 7: Matlab files

9.3.1 Main

u_E [%]	η [%]	ϕ_1 [deg]	ϕ_2 [deg]	ϕ_3 [deg]	ϕ_4 [deg]	P_1 [W]	P_2 [W]	P_3 [W]	P_4 [W]
14.90	23.56	220	160	40	0	200	20	150	30
15.17	24.91	240	200	60	0	190	10	170	30
15.93	25.83	260	220	80	0	170	10	170	30
17.14	26.62	260	180	80	0	190	10	170	30
18.16	27.01	260	160	80	0	180	10	180	30
18.90	27.28	280	200	100	0	170	20	180	30
20.77	28.09	280	180	100	0	170	10	170	50
22.24	28.42	300	200	120	0	170	20	180	30
23.18	28.74	300	200	120	0	180	10	160	50
24.38	29.21	300	180	120	0	170	20	170	40
26.24	29.61	300	160	120	0	160	20	170	50
28.19	29.90	320	200	140	0	160	30	150	60
29.70	30.34	320	180	140	0	150	40	160	50
31.23	30.56	320	180	140	0	140	50	140	70
34.28	30.76	340	180	160	0	140	60	140	60

TABLE 9.1: Power phase-shift data at each port in tabular form for Pareto front at porosity 0.6.

u_E [%]	η [%]	ϕ_1 [deg]	ϕ_2 [deg]	ϕ_3 [deg]	ϕ_4 [deg]	P_1 [W]	P_2 [W]	P_3 [W]	P_4 [W]
20.65	2.57	180	340	160	0	100	100	100	100
21.77	4.76	140	320	120	0	70	70	140	120
22.48	31.01	220	160	40	0	200	20	160	20
23.56	33.28	260	200	80	0	170	20	200	100
24.73	34.69	240	140	60	0	200	20	170	10
25.97	36.07	300	220	120	0	190	20	180	10
27.88	38.09	280	160	100	0	180	20	170	30
29.68	39.80	300	180	120	0	170	20	170	40
30.94	41.22	320	180	140	0	180	20	180	20
33.37	43.21	320	160	140	0	160	30	170	40
34.28	43.95	40	180	200	0	50	160	40	150
34.89	44.54	340	180	160	0	160	50	160	30
35.99	45.50	20	180	200	0	70	140	40	150
36.93	46.36	340	180	160	0	130	80	130	60
38.03	47.04	0	180	180	0	80	130	60	130

TABLE 9.2: Power phase-shift data at each port in tabular form for Pareto front at porosity 0.4.

u_E [%]	η [%]	ϕ_1 [deg]	ϕ_2 [deg]	ϕ_3 [deg]	ϕ_4 [deg]	P_1 [W]	P_2 [W]	P_3 [W]	P_4 [W]
21.70	3.89	180	340	160	0	100	100	110	90
23.99	6.57	180	40	220	0	90	110	90	110
25.17	7.00	160	40	200	0	100	130	70	100
26.83	8.41	160	60	180	0	150	100	90	60
28.70	12.54	180	20	120	0	200	60	60	80
29.99	27.63	180	40	60	0	200	30	90	80
30.48	46.53	240	140	60	0	190	10	180	20
31.95	50.82	80	180	240	0	20	170	10	200
33.12	53.15	320	200	140	0	170	20	200	10
34.14	54.53	60	180	220	0	30	170	20	180
35.37	56.82	320	180	140	0	170	30	170	30
36.57	58.34	340	180	160	0	170	40	170	20
37.97	60.56	20	180	200	0	60	160	40	140
39.17	61.76	20	180	180	0	60	140	70	130
39.76	62.57	0	180	180	0	130	70	140	60

TABLE 9.3: Power phase-shift data at each port in tabular form for Pareto front at porosity 0.2.

u_E [%]	η [%]	ϕ_1 [deg]	ϕ_2 [deg]	ϕ_3 [deg]	ϕ_4 [deg]	P_1 [W]	P_2 [W]	P_3 [W]	P_4 [W]
25.02	12.20	180	340	160	0	200	10	100	90
27.33	23.25	180	320	140	0	200	30	60	110
28.97	27.41	180	320	140	0	190	50	40	120
30.23	40.58	160	60	180	0	190	20	50	140
31.88	52.20	180	20	140	0	190	20	70	120
33.09	57.96	180	20	100	0	180	30	70	120
34.14	61.36	240	180	60	0	200	20	70	110
35.08	64.37	260	160	80	0	200	30	90	80
36.18	66.92	300	200	120	0	150	50	120	80
36.87	68.85	300	160	120	0	180	30	100	90
37.62	70.72	300	160	120	0	150	40	140	70
38.41	72.21	40	180	220	0	190	30	110	70
38.99	74.32	40	180	200	0	160	60	120	60
39.64	76.00	20	180	200	0	130	50	120	100
40.30	77.49	20	180	200	0	140	60	110	90

TABLE 9.4: Power phase-shift data at each port in tabular form for Pareto front at porosity 0 (bulk).

```
clc
clear all
close all

path='C:\POSS Probabilistic Optimal Solid State\Modelli FEM\'

%PARAMETRI DI CONTROLLO

global ricetta

frequency=2.45e9;
epsilon_0=8.85418781762e-12;
omega=2*pi*frequency;
n_th=10
n_em=10
delta_th=1
delta_em=delta_th/n_em
ordine=1;

ricetta=zeros(n_th,n_em);

min_porta=0
max_porta=200
step=10;
step_fi=30;

valore=100;
Potenze=[valore, valore, valore, valore]

%%%%%%%%%%%%%%%%%%%%%%%%%%%%%%%%%%%%%%%%%%%%%%%%%%%%%%%%%%%%%%%%%%%%%%%%%%%%

```

```
32 %ACQUISIZIONE DELLE COMPONENTI DEL CAMPO ELETTRICO A FASE 0 CON
      CIASCUNA
33 %PORTA SINGOLA ACCESA
34
35 import_data
36 potenza_req=1.4230e+06*ones(1,numel(x1));
37
38 %%%%%%%%%%%%%%%%%%%%%%%%%%%%%%%%%%%%%%%%%%%%%%%%%%%%%%%%%%%%%%%%%%%%
39
40 %INTRODUZIONE DEGLI SFASAMENTI
41
42 for vv=1:numel(Potenze(:,1))
43
44  tic
45  POW=Potenze(vv,:)';
46  cont=1;
47  fasi=zeros((360/step_fi)^3,4);
48  fasi_=zeros((360/step_fi)^3,4);
49  FI4=0;
50
51 for FI1=0:step_fi:360-step_fi;
52
53     for FI2=0:step_fi:360-step_fi;
54
55         for FI3=0:step_fi:360-step_fi;
56
57
58             fasi(cont,:)=(pi/180)*[FI1, FI2, FI3, FI4];
59             %FASI IN [deg]
60             fasi_(cont,:)=exp(1).^((j*fasi(cont,:)));
61             %FASI COMPLESSE [1]
```

```
62
63          a_power=rand; %COEFFICIENTI PER RANDOMIZZARE
64                        ...LE AMPIEZZE DELLE PORTE
65          b_power=rand;
66          c_power=rand;
67          d_power=rand;
68
69          a_power=1; %COEFFICIENTI PER RANDOMIZZARE
70                     ...LE AMPIEZZE DELLE PORTE
71          b_power=1;
72          c_power=1;
73          d_power=1;
74
75          Px1_=sqrt(a_power*POW(1)/100)*x1*exp(FI1*(pi*j/180));
76          Px2_=sqrt(b_power*POW(2)/100)*x2*exp(FI2*(pi*j/180));
77          Px3_=sqrt(c_power*POW(3)/100)*x3*exp(FI3*(pi*j/180));
78          Px4_=sqrt(d_power*POW(4)/100)*x4*exp(FI4*(pi*j/180));
79
80          Ex_tot=Px1_+Px2_+Px3_+Px4_;
81
82          Py1_=sqrt(a_power*POW(1)/100)*y1*exp(FI1*(pi*j/180));
83          Py2_=sqrt(b_power*POW(2)/100)*y2*exp(FI2*(pi*j/180));
84          Py3_=sqrt(c_power*POW(3)/100)*y3*exp(FI3*(pi*j/180));
85          Py4_=sqrt(d_power*POW(4)/100)*y4*exp(FI4*(pi*j/180));
86
87          Ey_tot=Py1_+Py2_+Py3_+Py4_;
88
89          Pz1_=sqrt(a_power*POW(1)/100)*z1*exp(FI1*(pi*j/180));
90          Pz2_=sqrt(b_power*POW(2)/100)*z2*exp(FI2*(pi*j/180));
91          Pz3_=sqrt(c_power*POW(3)/100)*z3*exp(FI3*(pi*j/180));
92          Pz4_=sqrt(d_power*POW(4)/100)*z4*exp(FI4*(pi*j/180));
```

```
93
94              Ez_tot=Pz1_+Pz2_+Pz3_+Pz4_;
95
96              E_tot=((abs(Ex_tot)).^2+(abs(Ey_tot)).^2+(abs(Ez_tot)
                    ...
97                   ).^2).^0.5;
98
99              %DISTRIBUZIONE DEL MODULO DEL CAMPO ELETTRICO DOPO
100             ...APPLICAZIONE PSE
101
102             conf_tot=((360/step_fi))^3;
103             potenza_dissipata((vv-1)*conf_tot+cont,:)=-epsilon_0*
                    ...
104                  omega*eps_ii.*(E_tot).^2;
105             nodi=numel(potenza_dissipata(1,:));
106
107             for pp=1:numel(fasi_(1,:)) %SCAMBIA RIGA CON COLONNA
                    SENZA
108                  ...FARE IL COMPLESSO CONIUGATO
109
110                  FAS(pp,1)=fasi_(cont,pp);
111
112             end
113
114         setting_P_F((vv-1)*conf_tot+cont,:)=[a_power*POW(1) b_power*
                ...
115              POW(2) c_power*POW(3) d_power*POW(4) FI1 FI2 FI3 FI4];
116
117         cont=cont+1;
118         end
119
```

```
120     end
121
122 end
123
124 frase_tempo=strcat('tempo_1=toc');
125 eval(frase_tempo);
126 clear frase_tempo
127
128 vv
129
130 end
131
132 %%%%%%%%%%%%%%%%%%%%%%%%%%%%%%%%%%%%%%%%%%%%%%%%%%%%%%%%%%%%%%%%%%%%%%%
133
134 potenza_accumulata=zeros(1,nodi);
135 for xxx=1:n_em;
136
137 estr_fatte=xxx-1;
138
139 if estr_fatte<0.001;
140
141     potenza_asterisco=potenza_req;
142
143 else
144
145     potenza_asterisco=(n_em...
146         *potenza_req-potenza_accumulata)/(n_em-estr_fatte);
147
148 end
149
150 %%%%%%%%%%%%%%%%%%%%%%%%%%%%%%%%%%%%%%%%%%%%%%%%%%%%%%%%%%%%%%%%%%%%%%%
```

```
151
152 %CALCOLO LE PROBABLITA' DELLE CONFIGURAZIONI CONSIDERANDO I SINGOLI
        NODI
153
154             configurazioni=numel(potenza_dissipata(:,1));
155             prob=zeros(configurazioni,nodi);
156
157             for iii=1:nodi
158
159                  cacchio(iii)=(sum(abs(   potenza_dissipata...
160                      (:,iii)  -  potenza_asterisco(iii)'  ).^ordine)
                           );
161                  prob(:,iii)=(1/(configurazioni-1))*...
162                      (1-(abs(potenza_dissipata...
163                      (:,iii)-potenza_asterisco(iii)').^ordine/
                           cacchio...
164                      (iii)));
165
166             end
167
168  %CALCOLO LE PROBABILITA' DELLE CONFIGURAZIONI CONSIDERANDO
169  ...UNA MEDIA PESATA DEI NODI
170
171  for kkk=1:numel(prob(:,1))
172  prob_avg(kkk,:)=mean(prob(kkk,:))    ;
173  end
174
175 extractions=linspace(1,numel(prob_avg),numel(prob_avg));
176 probability=prob_avg(:)';
177
178 sommo=sum(probability);
```

```
179 probability=probability/sommo;
180 [drawn]=discrete_probability(1,probability,extractions);
181
182 ricetta(1,xxx)=drawn;
183
184 %%%%%%%%%%%%%%%%%%%%%%%%%%%%%%%%%%%%%%%%%%%%%%%%%%%%%%%%%%%%%%%%%%%%%%%
185
186 %CALCOLIAMO IL VALORE DELLA POTENZA AGGIORNATO PER LA
187 ...SUCCESSIVA ITERAZIONE
188
189             Px1_=sqrt(setting_P_F((ricetta(1,xxx)),1)/100)*x1*...
190                 exp(setting_P_F((ricetta(1,xxx)),5)*(pi*j/180));
191             Px2_=sqrt(setting_P_F((ricetta(1,xxx)),2)/100)*x2*...
192                 exp(setting_P_F((ricetta(1,xxx)),6)*(pi*j/180));
193             Px3_=sqrt(setting_P_F((ricetta(1,xxx)),3)/100)*x3*...
194                 exp(setting_P_F((ricetta(1,xxx)),7)*(pi*j/180));
195             Px4_=sqrt(setting_P_F((ricetta(1,xxx)),4)/100)*x4*...
196                 exp(setting_P_F((ricetta(1,xxx)),8)*(pi*j/180));
197
198             Ex_tot=Px1_+Px2_+Px3_+Px4_;
199
200             Py1_=sqrt(setting_P_F((ricetta(1,xxx)),1)/100)*y1*...
201                 exp(setting_P_F((ricetta(1,xxx)),5)*(pi*j/180));
202             Py2_=sqrt(setting_P_F((ricetta(1,xxx)),2)/100)*y2*...
203                 exp(setting_P_F((ricetta(1,xxx)),6)*(pi*j/180));
204             Py3_=sqrt(setting_P_F((ricetta(1,xxx)),3)/100)*y3*...
205                 exp(setting_P_F((ricetta(1,xxx)),7)*(pi*j/180));
206             Py4_=sqrt(setting_P_F((ricetta(1,xxx)),4)/100)*y4*...
207                 exp(setting_P_F((ricetta(1,xxx)),8)*(pi*j/180));
208
209             Ey_tot=Py1_+Py2_+Py3_+Py4_;
```

```
210
211             Pz1_=sqrt(setting_P_F((ricetta(1,xxx)),1)/100)*z1*...
212                 exp(setting_P_F((ricetta(1,xxx)),5)*(pi*j/180));
213             Pz2_=sqrt(setting_P_F((ricetta(1,xxx)),2)/100)*z2*...
214                 exp(setting_P_F((ricetta(1,xxx)),6)*(pi*j/180));
215             Pz3_=sqrt(setting_P_F((ricetta(1,xxx)),3)/100)*z3*...
216                 exp(setting_P_F((ricetta(1,xxx)),7)*(pi*j/180));
217             Pz4_=sqrt(setting_P_F((ricetta(1,xxx)),4)/100)*z4*...
218                 exp(setting_P_F((ricetta(1,xxx)),8)*(pi*j/180));
219
220             Ez_tot=Pz1_+Pz2_+Pz3_+Pz4_;
221
222             clear E_tot
223             E_tot=((abs(Ex_tot)).^2+(abs(Ey_tot)).^2+(abs...
224                 (Ez_tot)).^2).^0.5;
225
226             %DISTRIBUZIONE DEL MODULO DEL CAMPO ELETTRICO DOPO
227             ...APPLICAZIONE PSE
228
229             potenza_estratta(xxx,:)=-epsilon_0*omega*eps_ii.*(E_tot
                    ).^2;
230             potenza_accumulata=potenza_accumulata+potenza_estratta(
                    xxx,:);
231
232             mean(abs((100*((potenza_req-potenza_estratta...
233                 (xxx,:))./potenza_req))))
234             xxx
235
236 clear potenza_asterisco
237 end
238
```

```
239 figure
240 hist(probability,50)
241
242 mean(abs((100*((potenza_req-potenza_accumulata/n_em)./potenza_req))
    ))
243
244 figure
245 hist(abs((100*((potenza_req-potenza_accumulata/n_em)./potenza_req))
    ),50)
246
247 figure
248 plot(potenza_accumulata/n_em)
249 hold on
250 plot(potenza_req)
251 figure
252 hist(potenza_accumulata/n_em,50)
253
254 ricetta(1,5)
255 setting_P_F(944,:)
256
257 %SALVATAGGIO DEL FILE TXT ASSEMBLATO
258
259 ext='.txt';
260 nome_salvataggio=strcat('potenza_accumulata',ext);
261 fid = fopen(nome_salvataggio,'wt')
262 for ind=1:numel(potenza_accumulata(:))
263
264     fprintf(fid,'%5.5f %5.5f %5.5f %5.5f\n',x(ind),y(ind),z(ind),
        ...
265         potenza_accumulata(ind)/n_em );
266
```

```
267 end
268 fclose(fid)
269
270 ext='.txt';
271 nome_salvataggio=strcat('Setting_P_F',ext);
272 fid = fopen(setting_P_F,'wt')
273
274 for ind=1:numel(setting_P_F(:,1))
275
276 fprintf(fid,'%5.5f %5.5f %5.5f %5.5f %5.5f %5.5f %5.5f %5.5f\n',...
277     setting_P_F(ind,1),setting_P_F(ind,2),setting_P_F(ind,3),...
278     setting_P_F(ind,4),setting_P_F(ind,5),setting_P_F(ind,6),...
279     setting_P_F(ind,7),setting_P_F(ind,8));
280
281 end
282
283 fclose(fid)
284 figure
285 plot(density_mag)
286 plot(density_mag)
```

9.3.2 Function: discrete probabilty

```
1 function [sample]=simdiscreta(npoints,pdf,val)
2
3 if (sum(pdf)>1.001)||(sum(pdf)<0.999)   error('le probabilitïf¡
     devono sommare a 1'); end
4 n=length(pdf);
5 if (nargin==2) val = [1:n]; end
6 cumprob= [0 cumsum(pdf)];
7 runi=rand(1, npoints);
8 for j=1:n
```

```
9       ind = find((runi>cumprob(j)) & (runi<cumprob(j+1)));
10      sample(ind)= val(j);
11  end
```

Bibliography

[1] S. Fujii, S. Kawamura, D. Mochizuki, M. M. Maitani, E. Suzuki, and Y. Wada. “Microwave sintering of Ag-nanoparticle thin films on a polyimide substrate”. In: *AIP Advances* 5 (12 2015).

[2] A. C. Metaxas and R. J. Meredith. *Industrial Microwave Heating*. IET, 1995. Chap. Theoretical aspects of volumetric heating.

[3] S. Lupi. *Appunti di Elettrotermia*. Edizione Progetto, 2005.

[4] G. Wormeester, S. Nijdam, A. Luque, and U. Ebert. “How Photo-ionization and Background Ionization Affect Streamers and Sprites”. In: *XIV International Conference on Atmospheric Electricity*. 2011.

[5] M. A. Lieberman and A. J. Lichtenberg. *Principles of Plasma Discharges and Material Processing*. John Wiley & Sons, 2005.

[6] A.D. MacDonald. *Microwave Breackdown in Gases*. John Wiley & Sons, 1966.

[7] F. Chen. *Introduction to Plasma Physics and Controlled Fusion*. third. Springer, 2016.

[8] No authors listed. “Methodologies to diagnose and monitor dry eye disease: report of the diagnostic methodology subcommittee of the international dry eye workshop”. In: *The Ocular Surface* 5.2 (2007).

[9] M. Rolando, G. Geerling, HS Dua, J. M. Benitez del Castillo, and C. Creuzot-Garcher. “Emerging treatment paradigms of ocular surface disease: proceedings of the Ocular Surface Workshop”. In: *British Journal of Ophtalmology* 94.1 (2010), pp. 1–9.

[10] S. Tedesco. “Design of an ocular surface protection system from overtemperatures during the treatment with em fields”. In: *Master’s Thesis (University of Padua)* (2016).

[11] J. J. Gicquel and D. Bremond-Gignac. “Emerging treatments for dry eye: some like it hot, while others may prefer a good stimulation”. In: *British Journal of Ophtalmology* 97 (2013), pp. 539–540.

[12] P. Aragona and M. Rolando. “Towards a dynamic customised therapy for ocular surface dysfunctions”. In: *British Journal of Ophtalmology* 97 (2013), pp. 955–960.

[13] D. Bremond-Gignac, J.J. Gicquel, and F. Chiambaretta. “Pharmacokinetic evaluation of diquafosol tetrasodium for the treatment of Sjogren’s syndrome”. In: *British Journal of Ophtalmology* 97 (2013), pp. 539–540.

[14] J. E. Lee, N. M. Kim, J. W. Yang, S. J. Kim, J. S. Lee, and J.E. Lee. “A randomised controlled trial comparing a thermal massager with artificial teardrops for the treatment of dry eye”. In: *British Journal of Ophtalmology* 98 (2014), pp. 46–51.

[15] J. M. Benitez del Castillo, T. Kaercher, K. Mansour, E. Wylegala, and H. Dua. “Evaluation of the efficacy, safety, and acceptability of an eyelid warming device for the treatment of meibomian gland dysfunction”. In: *Clinical Ophtalmology* 8 (2014), pp. 2019–2027.

[16] E. Pedrotti, F. Bosello, A. Fasolo, A. C. Frigo, I. Marchesoni, A. Ruggeri, and G. Marchini. “Transcutaneous periorbital electrical stimulation in the treatment of dry eye”. In: *British Journal of Ophtalmology* 0 (2016), pp. 1–6.

[17] J. A. Elder. “Ocular effects of radiofrequency energy”. In: *Bioelectromagnetics* 24.6 (2003), pp. 148–161.

[18] U.S. National Library of Medicine. *Visible Human Project*. Ed. by USA.gov. URL: https://www.nlm.nih.gov/research/visible/visible_human.html.

[19] M. Kazhdan, M. Bolitho, and H. Hoppe. “Poisson surface reconstruction”. In: *Proceedings of the Symposium on Geometry Processing* (2006), pp. 11–21.

[20] M. Garland and P. S. Heckbert. “Surface simplification using quadric error metrics”. In: *Proceedings of the 24th annual conference on Computer graphics and interactive techniques* (1997), pp. 209–216.

[21] A. K. Datta and V. Rakesh. *An introduction to modelling of transport processes. Applications to biomedical systems*. Cambridge University Press, 2010.

[22] P.A. Hasgall, F. Di Gennaro, C. Baumgartner, E. Neufeld, M. C. Gosselin, D. Payne, A. Klingenbock, and N. Kuster. "IT'IS Database for thermal and electromagnetic parameters of biological tissues (Version 3.0)". In: (2015). DOI: 10.13099/VIP21000-03-0.

[23] No authors listed. "Commission Directive (EU) 2015/565: amending Directive 2006/86/EC as regards certain technical requirements for the coding of human tissues and cells". In: *Official Journal of the European Union* 93 (2015), pp. 43–55.

[24] Nicola Zoppetti. "Dosimetria numerica in condizioni quasi-statiche e problemi collegati". In: *Ph.D Thesis (University of Florence)* (2008).

[25] David M. Pozar. *Microwave Engineering*. John Wiley & Sons, 2011.

[26] Ashim K. Datta. *Biological and Bioenvironmental Heat and Mass transfer*. Marcel Dekker, Inc., 2002.

[27] Comsol Multiphysics. *https://www.comsol.com/blogs/using-perfectly-matched-layers-and-scattering-boundary-conditions-for-wave-electromagnetics-problems/*. 2017. URL: https://www.comsol.com/blogs/using-perfectly-matched-layers-and-scattering-boundary-conditions-for-wave-electromagnetics-problems/.

[28] J. D. Romano and R. H. Price. "The conical resistance conundrum: a potential solution". In: *American Association of Physics teachers* 64.9 (1996), pp. 1150–1153.

[29] K. Tomiyasu. "Minimizing radiation leakage from microwave ovens". In: *IEEE Microwave Magazine* 9.1 (2008).

[30] P. Lopez-Iturri, S. De Miguel-Bilbao, E. Aguirre, L. Azpilcueta, F. Falcone, and V. Ramos. "Estimation of radiofrequency power leakage from microwave ovens for dosimetric assessment at nonionizing radiation exposure levels". In: *BioMed Research International* (2014).

[31] V. D'Ambrosio and F. Dughiero. "Numerical model for RF capacitive regional deep hyperthermia for pelvic tumors". In: *Medical & Biological Engineering & Computing* 45 (5 2007), pp. 459–466.

[32] M. Kirscheneck, D. Rixen, and H. Polinder. "Model reduction methods for magnetic fields-based modal analysis". In: *IEEE Transaction on Magnetics* 50.11 (2014).

[33] A. Canova, F. Dughiero, F. Fasolo, M. Forzan, F. Freschi, L. Giaccone, and M. Repetto. "Simplified approach for 3-D nonlinear induction heating problems". In: *IEEE Transactions on Magnetics* 45.3 (2009).

[34] T. Wittij, I. Munteanu, R. Schumann, and D. Weiland. "Two-steps Lanczos algorithm for order model reduction". In: *IEEE Transactions on Magnetics* 38.2 (2002).

[35] A. M. Rocha, M. Facao, J. P. Sousa, and A. Viegas. "Optimization of a door seal structure of a microwave oven using a FDTD method". In: *International Jounal of Numerical Modeling* 21 (2008), pp. 507–513.

[36] P. Di Barba. "Evolutionary multiobjective optimization methods for the shape design of industrial electromagnetic devices". In: *IEEE Transactions on Magnetics* 45.3 (2009).

[37] P. Kildal and A. Kishk. "EM modeling of surfaces with stop or go characteristics - Artificial magnetic conductors and soft and hard surfaces". In: *Applied Computational Electromagnetics Society Journal* 18.1 (2003), pp. 32–40.

[38] K. Iwabuchi, T. Kubata, and T. Kashiwa. "Analysis of electromagnetic fields in a mass-produced microwave oven using the finite-difference time-domain method". In: *Journal of Microwave Power and Electromagnetic Energy* 31.3 (1996), pp. 188–196.

[39] J. M. Osepchuk. "The hystory of the microwave oven: a critical review". In: *IEEE Conference: Boston, MA, USA* (2009), pp. 1397–1400.

[40] J. M. Osepchuk. "A hystory of microwave heating applications". In: *IEEE Transactions on MIcrowave Theory and Techniques* 32.9 (1984), pp. 1200–1224.

[41] J. M. Osepchuk and J. E. Simpson. "Advances in choke design for microwave oven door seals". In: *Journal of Microwave Power* 8 (3 1973), pp. 296–302.

[42] J. M. Osepchuk. "Impact of the EMF controversy on emerging technologies: good or bad". In: *IEEE Conference, Philadelphia, PA, USA* (1994), pp. 167–170.

[43] I.C.N.I.R.P. "ICNIRP guidelines: for limiting exposure to time-varying electric magnetic and electromagnetic fields (up to 300 GHz)". In: *Health Physics* 74.4 (1998), pp. 494–522.

[44] FDA. *CFR - Code of Federal Regulations Title 21*. 2017. URL: https://www.accessdata.fda.gov/scripts/cdrh/cfdocs/cfcfr/CFRSearch.cfm?FR=1030.10.

[45] A. Thansandote, D. W. Lecuyer, and G. B. Gajda. “Radiation leakage of before-sale and used microwave ovens”. In: *Microwave World* 21.1 (2000), pp. 4–8.

[46] O. Zeyad and I. Alhekail. “Electromagnetic radiation from microwave ovens”. In: *Journal of Radiological Protection* 21 (2001), pp. 251–258.

[47] M. Bangay and C. Zombolas. “Advanced measurements of microwave oven leakage”. In: (2004).

[48] A. Hirata, S. I. Matsuyama, and T. Shiozawa. “Temperature rises in the human eye exposed to em waves in the frequency range 0.6-6 GHz”. In: *IEEE Transactions on Electromagnetic Compatibility* 42.4 (2000), pp. 386–393.

[49] IT’IS Foundation. *Virtual Population Database: https://www.itis.ethz.ch/virtual-population/tissue-properties/database/*. Ed. by IT’IS Fondation. URL: https://www.itis.ethz.ch/virtual-population/tissue-properties/database/.

[50] H. H. Pennes. “Analysis of Tissue and Arterial Blood Temperatures in the Resting Human Forearm”. In: *Journal of Applied Physiology* 1.2 (1948), pp. 93–122.

[51] C. Bianchi, F. Bressan, F. Dughiero, and R. Hunter. “Novel efficient strategy to design an optimized microwave shield”. In: *IEEE Transactions on Magnetics* 52.3 (2016).

[52] National Fire Protection Agency. *Home Fires involving Cooking Equipment*. Research Report. National Fire Protection Association (NFPA), Sept. 1, 2015.

[53] National Institutes of Health. *Fire Safety Tips for Using Microwave Ovens*. National Institutes of Health (Office of management). 2016. URL: https://www.ors.od.nih.gov/News/Pages/Using_Microwave_Ovens.aspx.

[54] R. F. Shiffmann. *Fires in microwave and RF heating systems: causes and prevention*. Tech. rep. R.F. Schiffmann Associates, Inc., 2016.

[55] General Electrics. *Microwave arcing in cavity*. General Electric. 2016. URL: http://products.geappliances.com/appliance/gea-support-search-content?contentId=16605.

[56] Canadian Food Inspection Agency. *Why Sparks Occur When Cooking Vegetables in a Microwave*. Canadian Food Inspection Agency (CFIA). 2016. URL: http://www.inspection.gc.ca/food/information-for-consumers/fact-sheets-and-infographics/products-and-risks/fruits-and-vegetables/sparks-when-cooking/eng/1332278105073/1332278331477.

[57] T. Olsson, U. Jordan, D.S. Dorozhkina, V. Semenov, D. Anderson, M. Lisak, J. Puech, I. Nefedov, and I. Shereshevskii. "Microwave Breakdown in RF devices containing sharp corners". In: *IEEE MTT-S International Microwave Symposum Digest* (2006), pp. 1233–1236.

[58] M. Nakamura, T. Saito, and M. Kuramoto. "Characteristics of high-power breakdown at 28 GHz". In: *IEEE Transactions on Microwave Theory and Techniques* 26.5 (1978), pp. 354–356.

[59] H. K. Malik and A. K. Aria. "Microwave breakdown for the TE10 mode in a rectangular waveguide". In: *Physics of Plasmas* 20.082125 (2013).

[60] R. Tomala, U. Jordan, D. Anderson, and M. Lisak. "Microwave breakdown of the TE11 mode in a circular waveguide". In: *Journal of Physics D: Applied Physics* 38 (2005), pp. 2378–2381.

[61] D. Anderson, U. Jordan, M. Lisak, T. Olsson, and M. Ahlander. "Microwave Breakdown in Resonators and Filters". In: *IEEE Transactions on Microwave Theory and Techniques* 47.12 (1999), pp. 2547–2556.

[62] Y. A. Lebedev, M. V. Mokeev, A. V. Tatarinov, V. A. Shakhatov, and I. L. Epstein. "Physics and microstructure of electrode microwave discharge". In: *Journal of Physics D: Applied Physics* 41 (2008).

[63] J. Sun, W. Wang, Q. Yue, C. Ma, J. Zhang, X. Zhao, and Z. Song. "Review on microwave-metal discharges and their applications in energy and industrial processes". In: *Applied Energy* 175.4 (2016), pp. 494–522.

[64] F. Peruani, G. Solovey, E. E. Mola, I. Irurzun, A. J. Marzocca, and J. L. Vicente. "Dielectric breakdown model for composite materials". In: *Physical Review E* 67.066121 (2003).

[65] D.G. Anderson, M. Lisak, and P. T. Lewin. "Thermal Lowering of the Threshold for Microwave Breakdown in Air-Filled Waveguides". In: *IEEE Transactions on Microwave Theory and Techniques* MTT-35.7 (1987).

[66] J. Rasch, V. E. Semenov D. Anderson, M. Lisak, and J. Puech. "On the microwave breakdown stability of a spherical hot spot in air". In: *Journal of Physics D: Applied Physics* 43 (2010).

[67] B. Held and R. Peyrous. "Physical and chemical studies of corona discharge in air". In: *Czechoslovak Journal of Physics* 49.3 (1999).

[68] R. J. Van Brunt. "Physics and Chemistry of Partial Discharge and Corona". In: *IEEE Transactions on Dielectrics and Electrical Insulation* 1.5 (1994), pp. 761–784.

[69] B. Eliasson and U. Kogelshaltz. "Modeling and applications of silent discharge plasmas". In: *IEEE Transcations on Plasma Science* 19.2 (1991), pp. 309–323.

[70] V. M. Shibkov, A. F. Aleksandrov, V. A. Chernikov, A. P. Ershov, and L. V. Shibkova. "Microwave and Direct-Current Discharges in High-Speed Flow: Fundamentals and Application to Ignition". In: *Journal of Propulsion and Power* 25.1 (2009), pp. 123–137.

[71] D. P. Lymberopulos and D. J. Economou. "Two-dimensional self consistent radio frequency plasma simulations relevant to the gaseous electronics conference RF reference cell". In: *Journal of Research of the National Institute of Standards Technology* 100.4 (1995), pp. 473–494.

[72] A. Larsson, A. B. Clergerie, and I. Gallimberti. "Numerical modelling of inhibited electrical discharges in air". In: *Journal of Physics D: Applied Physics* 31 (1998), pp. 1831–1840.

[73] M. Abdel-Salam. "Positive Wire-to-Plane Coronas as Influenced by Atmospheric Humidity". In: *IEEE Transactions on Industry Applications* IA-21.1 (1985), pp. 35–40.

[74] M. Abdel-Salam, H. Anis, A. El-Morshdey, and R. Radwan. *High-Voltage Engineering*. Marcel Dekker, Inc., 2000.

[75] T.N. Tulasidas, G.S.V. Raghavan, F. Van de Voort, and R. Girard. "Dielectric Properties of Grapes and Sugar Solutions at 2.45 GHz". In: *Journal of Microwave Power and Electromagnetic Energy* 30.2 (1995), pp. 117–123.

[76] Y. Choi and M.R. Okos. "Thermal properties of liquid foods review". In: *Physical and Chemical Properties of Food* (1986), pp. 35–77.

[77] M. Affandi, N. Mamat, S.N. Kanafiah, and N. Syahirah. "Simplified Equations for Saturated Steam Properties for Simulation Purpose". In: *Procedia Engineering* 53 (2013), pp. 772–776.

[78] X. Wen, X. Yuan, L. Lan, M. Long, and L. Hao. "Study on the Effective Ionization Rate of Atmospheric Corona Discharge Plasmas by Considering Humidity". In: *IEEE Transactions on Plasma Science* 44.12 (2016), pp. 3386–3391.

[79] *Drift velocity of electrons and ions in dry and humid air in water vapour*. Vol. 85. 1965, pp. 1283–1295.

[80] W. T. Wyatt. *Computed Electron Drift Velocity*. Research rep. U.S. Army Engineer Research and Development Laboratories, Fort Belvoir, Virginia, 1967.

[81] Bhaskar Chaudhury and Jean-Pierre Boeuf. "Computational Studies of Filamentary Pattern Formation in a High Power Microwave Breakdown Generated Air Plasma". In: *IEEE Transactions on Plasma Science* 38.9 (2010), pp. 2281–2288.

[82] K. Frigui, D. Baillargeat, S. Verdeyme, S. Bila, and A. Catherinot. "One dimensional numerical modelling of microwave breakdown in OMUX filters". In: *Microwave Symposium*. IEEE, July 2, 2007, pp. 2121–2124.

[83] K. Frigui, S. Bila, D. Baillargeat, A. Catherinot, S. Verdeyme, J. Puech, L. Estagerie, D. Pacaud, and H. Dillenbourg. "Modeling and Characterization of microwave breakdown at atmospheric pressure in OMUX filters". In: *International Journal of Microwave and Computer-Aided Engineering* 24.1 (2014), pp. 46–54.

[84] T. Paunska, A. Shivarova, and K. Tarnev. "Comments on the boundary conditions for metal and dielectrics walls in the fluid-plasma modelling". In: *30th International Conference on Phenomena in Ionized Gases*. 2011.

[85] P. Chabert and N. Braithwaite. *Physics of Radio-Frequency Plamsas*. Cambridge University Press, 2011.

[86] A. A. Dougal and L. Goldstein. "Energy Exchange between Electron and Ion Gases through Coulomb Collisions in Plasmas". In: *The Physical Review*. II 109.3 (Feb. 1, 1958), pp. 615–624.

[87] M. E. Wieser. "Atomic Weights of the Elements". In: *Pure and Applied Chemistry* 78.11 (2006), pp. 2051–2066.

[88] K. Aasberg-Petersen, J. Bak Hansen, T. Christensen, I. Dybkjaer, P. S. Christensen, C. S. Nielsen, S. W. Madsen, and J. Rostrup-Nielsen. "Technologies for large scale conversion". In: *Applied Catalysis A: General* 221.1-2 (2001), pp. 379–387.

[89] M. A. Khairurrijal, F. Noor, A. Marully, and M. Sanny. "Design of steam reforming reactor for converting methanol into hydrogen using an ultrasonic nebulizer as liquid feeder and polymer liquid processed CuO/ZnOAl2O particles as catalyst". In: *Journal of Sustainable Energy 1* (2010), pp. 11–15.

[90] M. Annesini, V. Piemonte, and L. Turchetti. "Carbon formation in the steam reforming process: a thermodynamic analysis based on the elemental composition". In: *Chemical Engineering Transactions* 11 (2007), pp. 21–26.

[91] G. Stefanidis, A. Munoz, G. Sturm, and A. Stankiewicz. "A helicopter view of microwave application to chemical processes: reactions, separations, and equipment concepts". In: *Reviews in Chemical Engineering* 30.3 (2014), pp. 233–259.

[92] L. Estel, M. Poux, N. Benamara, and I. Polaert. "Continuous flow-microwave reactor: Where are we?" In: *Chemical Engineering and Processing: Process intensification* 113 (2017), pp. 56–64.

[93] T. Durka, T. Van Gerven, and A. Stankievicz. "Microwaves in heterogeneous gas-phase catalysis: experimental and numerical approaches". In: *Chemical Engineering & Technology* 32.9 (2009), pp. 1301–1312.

[94] W.L. Perry and L.F. Brown. "Mirowave heating of endothermic catalytic reactions: reforming of methanol". In: *AIChE Journal* 48.4 (2002), pp. 820–831.

[95] B. Fidalgo and J. Menendez. "Study of energy consumption in laboratory pilot plant for microwave assisted CO2 reforming of CH4". In: *Fuel Processing Technology* 95 (2012), pp. 55–61.

[96] Q. Xie, F. Borges, Y. Cheng, Y. Wan, Y. Lin, Y. Liu, F. Hussain, P. Chen, and R. Ruan. "Fast microwave assisted catalytic gasification of biomass for syngas production and gas removal". In: *Bioresource Technology* 156 (2014), pp. 291–296.

[97] B. Fidalgo, A. Dominguez, J. Pis, and J. Menendez and. "Microwave-assisted dry reforming of methane". In: *International Journal of Hydrogen Energy* 13.16 (2008), pp. 4337–4344.

[98] W. Chen and B. Lin. “Hydrogen production and thermal behaviour of methanol autothermal reforming and steam reforming triggered by microwave heating”. In: *International Journal of Hydrogen Energy* 38.24 (2013), pp. 9973–9983.

[99] S. Farag, D. Fu, J. Jessop, and J. Chouki. “Detailed comositional analysis and structural investigation of a bio-oil from microwave pyrolisis of kraft lignin”. In: *Journal of Analytical and Applied Pyrolisis* 109 (2014), pp. 249–257.

[100] S. Gunduz and T. Dogu. “Hydrogen by steam reforming of ethanol over Co-Mg incorporated novel mesoporous alumina catalysts in tubular and microwave reactors”. In: *Applied Catalysis B: Enironmental* 168-169 (2015), pp. 497–508.

[101] J. Bermudez, D. Beneroso, N. Rey-Raap, A. Arenillas, and J. Mendez. “Energy consumption estimation in the scaling-up of microwave heating processes”. In: *Chemical Engineering and Processing* 9 (2015), pp. 1–8.

[102] S. Farag and J. Chouki. “A modified microwave thermo-gravimetric analyzer for kinetic purposes”. In: *Applied Thermal Engineering* 75 (2015), pp. 65–72.

[103] Y. Feng, S. Zhang, K. Wu, J. Qin, Y. Cao, and H. Huang. “Numerical investigation of distribution of reaction rate during convective heat transfer with endothermic chemical reaction”. In: *International Communications in Heat and Mass Transfer* 83 (2017), pp. 1–7.

[104] J. Wann. “Microwave and chemistry: the catalysis of an exciting marriage”. In: *Proceeding from the 14-th National Industrial Energy Technology Conference* (1992), pp. 105–109.

[105] D. Calvillo-Cortes, M. Van der Heijden, M. Acar, M. De Langhen, R. Wesson, F. Van Rijs, and L. De Vreede. “A package-integrated chireix outphasing RF switch-mode high power amplifier”. In: *IEEE Transactions on Microwave Theory and Techniques* 61.10 (2013), pp. 3721–3732.

[106] C. Huang, K. Buisman, P. Zampardi, and L. Larson L. De Vreede. “On the compression and blocking distortion of semiconducto-based varactors”. In: *IEEE Transactions on Microwave Theory and Techniques* 60.12 (2012), pp. 3699–3709.

[107] D. Calvillo-Cortes, K. Shi, M. De Langen, F. Van Rijs, and L. De Vreede. “On the design of package integrated RF high-power amplifiers”. In: *IEEE Conference Publications*. 2012.

[108] R. Kaur, M. Newborough, and S. Probert. “Multi-purpose mathematical model for electromagnetic-heating process”. In: *Applied Energy* 44 (1993), pp. 337–386.

[109] A. Datta and R. Anantheswaran. *Handbook of microwave technology for food application*. Marcel Dekker, Inc., 2001, pp. 279–298.

[110] J. Krupka, K. Derzakowsly, B. Ridlle, and J. Baker-Jarvis. “A dielectric resonator for measurement of complex permittivity as a function of temperature”. In: *Measurement Science and Technology* 9 (1998), pp. 1751–1756.

[111] L. Fang, X. Huang, F. Vidal-Iglesias, Y. Liu, and X. Wang. “Preparation, characterization and catalytic performance of a novel Pt/SiC”. In: *Electrochemistry Communications* 13 (2011), pp. 1309–1312.

[112] J. Diaz, M. Calvo-Serrano, A. De La Osa, A. Garcia-Minguillan, A. Romero, A. Giroir-Fendler, and J. Valverde. “Beta-silicon carbide as a catalyst support in the Fisher-Tropsch synthesis: influence of the modification of the support by a pore agent and acidic treatment”. In: *Applied Catalysis A: General* 475 (2014), pp. 82–89.

[113] B. Mitchell. *An introduction for Materials Engineering and Science for Chemical and Materials Engineers*. 2004. Chap. Thermal conductivities of selected materials, pp. 874–879.

[114] O. Zmeskal, M. Buchnicek, M. Nezadal, P. Stefkova, and R. Capousek. “Thermal properties of fractal structure materials”. In: *(Researchgate)* (2014), pp. 84–88.

[115] V. V. Komarov. *Handbook of dielectric and thermal properties of materials at microwave frequencies*. Artech House, 2012. Chap. Ceramics.

[116] V. Koschenko, Y. K. Grinberg, and R. Koschenko. In: *Inorganic Materials* 15.7 (1985), p. 197.

[117] B. Jia, W. Lin, and S. Liu. “The study of effective medium parameters for granular media”. In: *Progress in Electromagnetic Research (PIER)* 8 (1994), pp. 89–108.

[118] O. Wiedenmann, R. Ramakrishnan, P. Saal, P. Kilic, U. Siart, T. Eibert, and W. Volk. “Local microwave heating of sand molds as a means to overcome design limitations in sand mold casting”. In: *Advances in Radio Science* 12 (2014), pp. 21–28.

[119] H. Sugawara, K. Kashimura, M. Hayashi, S. Ishihara, T. Mitani, and N. Shinohara. “Behaviour of microwave-heated silicon carbide particles at frequencies of 2.0-13.5 GHz”. In: *Applied Physics Letter* 105 (2014).

[120] M. Regier and H. Shubert. *Microwave Processing*. CRC press, 2001, pp. 178–204.

[121] P. Korpas, A. Wieckowski, M. Krysicki, and M. Celuch. "Application study of a new solid-state high power microwave sources for efficiency improvement of commercial domestic oven". In: *IMPI's 47-th Microwave Power Symposium* (2013).

[122] A. Wieckowski, P. Korpas, M. Krysicki, F. Dughiero, M. Bullo, F. Bressan, and C. Fager. "Efficiency optimization for phase controlled multi-source microwave oven". In: *International Journal of Applied Electromagnetics and Mechanics* 44 (2014), pp. 235–241.

[123] F. Bressan, F. Dughiero, M. Bullo, and P. Di Barba. "Efficiency optimization of a two-port microave oven: a robust automated procedure". In: *The international Journal for Computation and Mathematics in Electrical and Electronic Engineering* 44 (2015), pp. 235–241.

[124] A. Metaxas. *Foundations of electroheat: a unified approach*. Wiley, 1996.

[125] J. Dobrowolski. *Microwave network design using the scattering matrix*. Artech House, 2010. Chap. Wave variables and the scattering matrix.

[126] S. Orfanidis. *Electromagnetic waves and antennas*. 2010. Chap. S-Parameters, pp. 526–529.

[127] V. Rakesh, A. Datta, J. Walton, and K. McCarthy. "Microwave combination heating: coupled electromagnetics-multiphase porous media modeling and MRI experimentation". In: *AIChE Journal* 58.4 (2012), pp. 1262–1278.

[128] K. Hou and R. Huges. "The kinetics of methane steam reforming over a Ni/alpha-Al2O catalyst". In: *Chemical Engineering Journal* 82 (2001), pp. 311–328.

[129] E. T. Thostenson and T. W. Chou. "Microwave processing: fundamentals and applications". In: *Composites part A: Applied Science and Manufacturing* 30 (1999), pp. 1055–1071.

[130] D. A. Jones, T.P. Lelyveld, S. V. Mavrofidis, S. W. Kingman, and N. J. Miles. "Microwave heating applications in environmental engineering - a review". In: *Resources, Conservation and recycling* 34 (2 2002), pp. 75–90.

[131] S. M. Bradshaw, E. J. Van Wyk, and J. B de Swardt. "Microwave heating principles and the application to the regeneration of granular activated carbon". In: *The Journal of the South African Institute of Minining and Metallurgy* 98.4 (1998), pp. 201–210.

[132] K. Boodhoo and A. Harvey. *Process Intensification for green chemistry. Engineering Solutions for Sustainable Chemical Processing*. Wiley, 2013. Chap. Green Chemistry Principles.

[133] R. B. Bird, W. E. Stewart, and E. N. Lightfoot. *Transport Phenomena*. Revised Second. Wiley, 2007.

[134] B. R. Munson, A. P. Rothmayer, T. H. Okiishi, and W. Huebsch. *Fundamentals of Fluid Mechanics*. 7th. Wiley, 2013.

[135] V. D'Ambrosio, P. Di Barba, F. Dughiero, M. E. Mognaschi, and A. Savini. "Non-invasive thermometry for the thermal ablation of liver tumor: A computational methodology". In: *International Journal of Applied Electromagnetics and Mechanics* 25.1-4 (2007), pp. 407–412.

[136] C. Bianchi, P. Bonato, F. Dughiero, and P. Canu. "Enhanced power density uniformity for microwave catalytic reactions adopting solid-state generators: comparison with magnetron technology". In: *Chemical Engineering Processing: Process Intensifaction* 120 (2017), pp. 286–300. DOI: http://dx.doi.org/10.1016/j.cep.2017.07.006.

[137] V. Komarov, S. Wang, and J. Tang. "Permittivity and Measurements". In: *Encyclopedia of RF and Microwave Engineering* (Apr. 15, 2005), pp. 3693–3711.

[138] W.M. Haynes, ed. *Handbook of Chemistry and Physics (91-st Edition)*. CRC, 2010-2011.